Propagation des ondes : approches espace et ondelette

Bernhard Hustedt

UNIVERSITE DE NICE-SOPHIA ANTIPOLIS - UFR SCIENCES
L'ECOLE DOCTORALE SCIENCES FONDAMENTALES ET APPLIQUEES

THÈSE

Présentée pour obtenir le titre de

Docteur en SCIENCES
de l'Université Nice-Sophia Antipolis

Discipline: Sciences
Mention: Sismologie

Bernhard HUSTEDT

Propagation des ondes: approches espace et ondelette

A soutenir le 17 décembre 2002 devant le jury composé de

G. C. Herman (Professeur, TU Delft)	Rapporteur
R. Madariaga (Professeur, ENS Paris)	Examinateur
S. Operto (Chargé de Recherche, CNRS)	Examinateur
D. Rodrigues (Ingénieur de Recherche, CEA)	Examinateur
J.-P. Vilotte (Physicien du Globe, IPGP)	Rapporteur
J. Virieux (Professeur, UNSA)	Directeur de thèse

à 14h30, à Sophia Antipolis

UNIVERSITE DE NICE-SOPHIA ANTIPOLIS - UFR SCIENCES
L'ECOLE DOCTORALE SCIENCES FONDAMENTALES ET APPLIQUEES

THESIS

Submitted in accordance
with the requirements for the degree of

Doctor of PHILOSOPHY
The Université Nice-Sophia Antipolis

Department of Earth Sciences
Speciality : Seismology

Bernhard HUSTEDT

Wave Propagation Modelling: Space and Wavelet Approaches

The viva voce will take place on the 17th of December in front of the jury

G. C. Herman (Professor, TU Delft)	Rapporteur
R. Madariaga (Professor, ENS Paris)	Examiner
S. Operto (Researcher, CNRS)	Examiner
D. Rodrigues (Researcher, CEA)	Examiner
J.-P. Vilotte (Physicist of the Globe, IPGP)	Rapporteur
J. Virieux (Professor, UNSA)	Thesis Director

14h30, Sophia Antipolis

Abstract

In seismology, numerical wave propagation modelling is an essential tool to e.g., quantify local seismic risk or to invert multi-source seismic data. Realistic phenomena are accounted for when three-dimensional (3D) models with complex heterogeneous structures are simulated using sophisticated techniques on irregular grids.

In this thesis, I investigate frequency domain finite difference (FDFD) modelling for efficient space discretization optimization algorithms in order to render 3D FDFD modelling feasible.

I compare FDFD acoustic wave simulations in heterogeneous media by a staggered cross stencil analysis with a grid rotation approach. For two-dimensional (2D) modelling, grid rotation is superior in terms of CPU-time and memory requirements. Therefore, I propose that space discretization by grid rotation shall be investigated for 2D time domain FD modelling. Moreover, 3D discretizations lead to 27-points rotation star, and 19-points staggered cross stencils. I suggest that both shall be examined with respect to numerical accuracy and computer resources requirements.

I propose a multi-level direct and iterative solver combination for realistic 3D FDFD wave simulations. Exact coarse-grid wave solutions are computed by a direct LU matrix factorization. The coarse-grid solution is prolongated on a fine-resolution grid and subsequently used as preconditioner for an iterative solver scheme. I investigate two multi-level approaches based on nested iteration, denoted by Direct-Iterative-Space Solver (DISS), and a multi-scale wavelet expansion, called Direct-Iterative-Wavelet Solver (DIWS). DISS and DIWS wave simulations in 2D and 3D heterogeneous media are compared with respect to their CPU-time and memory performance.

The DISS approach provides fast and efficient matrix construction algorithms. The convergence of the iterative scheme is strongly dependent on efficient suppression of phase-shift artefacts caused by bilinear interpolation. Either large numbers of iteration steps or V- and W-cycles need to be performed to provide dispersion-free wave simulations.

Wavelet-based DIWS preconditioning leads to optimal iterative behaviour at the cost of wavelet projections. Matrix constructions become expensive due to convolution-type computations. Furthermore, non-zero DIWS matrix entries increase and therefore slow down matrix-vector product performances. Nevertheless, the multi-scale wavelet formulation gives fast and stable iterative constructions simultaneously on a series of approximation grids of decreasing resolution, where difficult grid interactions are accounted for naturally. Therefore, DIWS preconditioning is superior. Moreover, wavelet formulations provide adaptive optimization strategies for efficient implementation schemes.

Wave simulation examples are illustrated for several homogeneous and heterogeneous 2D and 3D models. The 3D applications are limited in size by restrictions to sequential computations. Extensions to parallel algorithms on distributed memory computer structures are discussed.

Résumé

Dans le domaine de la sismologie, la modélisation numérique de la propagation des ondes est un outil essentiel pour, par exemple, la quantification du risque sismique ou l'imagerie du sous-sol par inversion de données sismiques. Ces applications géophysiques nécessitent le développement de méthodes numériques sophistiquées de modélisation des ondes dans des milieux de propagation 3D hétérogènes. Parmi les approches possibles, les méthodes directes fondées sur la représentation du milieu sur des grilles numériques permettent la prise en compte de toute la complexité du champ d'onde dans des milieux fortement hétérogènes. Dans ce contexte, la représentation optimale du milieu de propagation et du champ d'onde propagé sur des grilles numériques irrégulières est actuellement un axe de recherche fortement dévelppé car elle permet d'atteindre le meilleur compromis entre la précision et la rapidité d'exécution des simulations dans des grilles numériques de taille considérable.

Dans cette thèse, je propose une nouvelle méthode de modélisation de la propagation des ondes acoustiques par différences finies dans le domaine des fréquences. Le problème numérique associé est la résolution d'un système matriciel. L'approche développée propose une discrétisation spatiale optimisée de l'équation d'onde rendant possible des modélisations en 3D.

Premièrement, je compare des modélisations acoustiques en milieu hétérogène calculées avec des schémas aux différences finies en quinconce et des schémas optimisés, discrétisés suivant deux systèmes d'axe tournés de 45 degrés (schémas tournés). Pour des modélisations 2D, la seconde approche montre des performances supérieures en terme de temps calcul et de stockage mémoire. J'en conclus que la discrétisation suivant des grilles tournées doit être utilisée pour des simulations 2D. Dans le cas 3D, les schémas utilisant les deux types de discrétisation contiennent 19 coefficients dans le cas des grilles en quinconce et 27 coefficients dans le cas des schémas tournés. Je suggère que les performances, en termes de précision numérique et de stockage mémoire, des deux types de discrétisation doivent être examinées dans le futur.

Deuxièmement, je propose une approche mixte multi-échelles combinant une méthode directe et itérative de résolution du système matriciel qui permet d'effectuer des modélisations réalistes dans des milieux 3D. Dans un premier temps, le champ d'onde exact est calculée *via* la factorisation LU de la matrice sur une grille de résolution grossière. Deuxièmement, ce champ d'onde approché est interpolé sur une grille numérique de résolution fine pour être injecté comme estimé initial dans l'algorithme de résolution itérative. J'ai exploré deux approches multi-échelles fondées respectivement sur une "*nested iteration*", appellée méthode "*Direct-Iterative-Space Solver*" (DISS), et une décomposition multi-grilles en ondelettes, appellée méthode "*Direct-Iterative-Wavelet Solver*" (DIWS). Les performances respectives, en termes de temps-CPU et de stockage mémoire, de ces deux méthodes de modélisation des ondes en milieu 2D et 3D sont comparées. L'algorithme de la méthode DISS permet la construction rapide du système matriciel. La convergence de l'algorithme itératif dépend fortement de sa capacité à éliminer des artefacts

numériques associés à des phénomènes déphasage. L'importance de ces artefacts dépend fortement de la précision de la solution initiale et de la discrétisation numérique du champ modélisé dans l'algorithme itératif. Un nombre important d'itérations ou l'utilisation de cycles en V et W sont nécessaires pour supprimer ces phénomènes. Dans la méthode DIWS, une représentation multirésolution du système matriciel est développée par projection sur une base d'ondelettes. Malgré le coût induit pour transformer le système dans le domaine spectral, la représentation multirésolution a fourni un outil numérique de préconditonnement permettant de stabiliser et d'accélérer significativement l'algorithme itératif. L'accélération de la convergence est attribuée à la représentation du système sur plusieurs grilles numériques de résolution différente dont les interactions sont prise en compte au cours des itérations. Par ailleurs, la formulation en ondelettes ouvre des perspectives d'optimisation sous forme d'adaptation spatial du maillage en fonction des propriétés locales du milieu et du champ propagé.

Plusieurs exemples de simulation d'ondes dans des milieux 2D et 3D de complexité variable sont présentés pour illustrer les performances respectives des méthodes DISS et DIWS. La taille des applications 3D présentées a été limitée par l'utilisation de programmes séquentiels. Finalement, des stratégies de parallélisation en mémoire distribuée des codes sont proposées.

Contents

List of Figures

List of Tables

Abbreviations

Numerical Methods

PDE(s)	Partial Differential Equation(s)
FD	Finite difference method
FDFD	Frequency Domain Finite Difference method
TDFD	Time Domain Finite Difference method
FE	Finite Element method
SE	Spectral Element method
FV	Finite Volume method

Discretization

FMG	Full Multi-Grid method
CGC	Coarse Grid Correction
NI	Nested Iteration
MRM	Mesh Refinement Methods
AMR	Automatic Mesh Refinement

Wavelet Transform

WT	Wavelet Transform
DWT	Discrete Wavelet Transform
OWT	Orthogonal Wavelet Transform
MRA	Multi-Resolution Analysis
W	Forward orthogonal wavelet transform operators
W^T	Transpose (inverse) orthogonal wavelet transform operator
Daub4	Daubechies-4 wavelets
STF	Standard Form of an operator in a wavelet basis
NSF	Non-Standard Form of an operator

Programming

MPI	Message Passing Interface
HPF	High Performance Fortran
MUMPS	MUltifrontal Massively Parallel Solver method
UMFPACK	Unsymmetric-pattern Multifrontal PACKage
GMRES	Generalized Minimum RESidual method
LU	Matrix factorization (lower- and upper-triangulars)
RHS	Right-Hand Side
CSR	Compact Sparse Row storage
HB	Harwell-Boeing storage

Solver Schemes

DIS	Direct-Iterative Solver strategy
DISS	Direct-Iterative-Space Solver approach
DIWS	Direct-Iterative-Wavelet Solver approach
DISS-3D	Direct-Iterative-Space Solver approach in 3D
DIWS-3D	Direct-Iterative-Wavelet Solver approach in 3D

General

PML	Perfectly Matched Layers
FT	Fourier Transform
SH-wave	Shear wave, which has only a horizontal component of motion
P-wave	Pressure wave (acoustic wave equation)
CPU	Computer Processor Unit
PC	Personal Computer

Acknowledgements

At first I would like to acknowledge Jean Virieux for all the help during the four years of my studies in Nice. He always supported my desire to start a PhD in France despite of all the difficulties encountered. Jean Virieux had to find financing for the PhD project and to assure that my Master degree would be sufficient for entering a French PhD program. Furthermore, he did not know me personally, neither my university education, or my former supervisor at the University of Leeds, but still he offered to start working with him and Stephane Operto on finite-difference modelling using wavelet theory.

Moreover, I would like to thank Jean Virieux and Stephane Operto for the supervision of my PhD project. Their critical comments and ideas on my work and sometimes endlessly seeming discussions concerning my project significantly improved not only the outcome of my work, but also the way I reason and address scientific problems in general. Together with them, my research work was a pleasure and I am happy to have chosen to come to Nice four years ago.

I also would like to thank all researchers at Géosciences Azur for the numerous fruitful discussions *on the corridor* and for the nice and pleasant working environment. Especially, I appreciate the possibility to participate in several field-work experiences in far away countries.

My special thanks go to Dominique Rodrigues (DASE/CEA), Luc Giraud (CERFACS), Stephane Lanterie (INRIA-Sophia Antipolis) and Patrick Amestoy (ENSEEIHT-IRIT). Their advice and suggestions concerning topics such as general numerical modelling, direct and iterative matrix solvers, parallel programming, and so on guaranteed the successful progress of my work. Besides, Luc Giraud and Patrick Amestoy are also acknowledged for providing me with a direct and a iterative matrix solver software packages, together with all the necessary support to get them running on sequential and parallel computing environments.

Many thanks go to Caroline Ramel for continuous help and useful support of computer software and hardware related problems.

My friends in Nice with whom I worked at Géosciences Azur, went to play hockey and tennis, or went hiking and snowboarding on the mountains, are thanked very much: Alain, Arnd, Barbara, Carine, Giuseppe, Isabella, Jean-Mathieu, Jan, Julia, Karim, Mathilde, Max, Neda, Pierre, Raffaella, Sergio, Sophie, Ulla, and Victor. Very special thanks to my friends in Germany with whom I often had the pleasure of exchanging long email communications or profit from short but intensive visits: Bert, Frieder, Horscht, Jens, and Reinsieg.

I also would like to thank Cristina for helping out in any difficult situation I encountered and for her personal advice whenever it was needed. I could always count on her and I am very grateful for her support throughout the years I spent in Nice. Of course, her proof readings of large parts of the present thesis significantly improved my otherwise loose English writing style.....

Grateful thanks go to my parents and family in Germany. They always supported my studies abroad and tried to help whenever I needed it.

Chapter 1

Introduction

1.1 Résumé

En recherchant la signification du mot *seismology* dans un dictionnaire d'anglais classique, on trouvera typiquement une définition du type: *The scientific study and recording of earthquakes and related phenomena.* L'objet de la recherche scientifique est la Terre. La sismologie est l'outil mis en oeuvre pour déterminer sa structure interne qui fournit de précieux indices pour la compréhension des processus géodynamiques actifs qui s'y produisent. Les implications géodynamiques que l'on peut déduire de la connaissance de la structure de la Terre dépendent principalement de l'échelle d'observation. En première approximation, on fait généralement l'hypothèse que la Terre se compose de plusieurs enveloppes, telles que le noyau, le manteau, le croûte, etc., supposées de composition homogène (voir le Figure 1.1). Cependant, une inspection plus détaillée de la structure de la Terre révèle que les interfaces séparant les enveloppes sont plutôt complexes, que la structure interne des enveloppes peux être fortement hétérogène (croûte terrestre) et subir des variations importantes au cours du temps.

Les données sismologiques sont sensibles aux différentes échelles auxquelles se produisent les phénomènes tectoniques. En d'autres termes, l'échelle des temps de l'observation sismologique est liée aux échelles caractéristiques des processus géodynamiques actifs. Typiquement, nous trouvons deux échelles de temps distinctes qui sont associées d'une part à l'excitation sismique de la source (de l'ordre de la milliseconde jusqu'à plusieurs secondes), et d'autre part au temps nécessaire aux ondes sismiques pour se propager jusqu'au capteur (de quelques secondes à quelques heures).

Depuis plusieurs décennies, les sismologues ont tenté d'interpréter une masse de données sismologiques de plus en plus volumineuse. L'accumulation continue des données et les avancées des techniques de traitement et de modélisation des signaux sismologiques ont permis d'améliorer de manière significative la connaissance de la structure de la terre. Les thèmes de recherche en sismologie sont à caractère académiques, tel que l'étude de la structure du noyau constituant le coeur de la Terre mais peuvent aussi avoir des implications économiques et anthropiques fondamentales en relation avec la gestion et l'exploitation des ressources énergétiques (recherche du pétrole et du gaz), la surveillance

des explosions nucléaires souterraines, la compréhension de l'aléa sismique. Dans ces derniers cas, la sismologie fournit un outil incontournable pour obtenir une reproduction la plus exacte possible de la structure et de la composition des premiers kilomètres de l'écorce terrestre.

Propagation d'onde

En raison du manque d'accessibilité directe à l'intérieur de la terre, les sismologues utilisent les ondes sismiques comme outil indirect d'exploration. L'information sur la structure de la Terre véhiculée par les ondes sismiques est particulièrement riche, la difficulté résidant dans l'extraction de cette information indirecte. Les ondes sismiques se propagent de la position de la source (par exemple, un tremblement de terre ou une explosion artificielle) jusqu'à la surface de la terre où elles sont enregistrées par un capteur sismique. Par conséquence, les ondes sismiques contiennent une signature non seulement du processus de nucléation des ondes mais aussi des propriétés physiques du milieu dans lequel elles se sont propagées. Parmi toutes les méthodes géophysiques, les méthodes sismiques sont sans aucun doute celles qui disposent du pouvoir de résolution le plus élevé en terme de taille des structures imagées et de diversité de paramètres étudiés (vitesses de propagation, densité, atténuation). L'analyse des temps arrivés, de l'amplitude, de la phase, et de l'atténuation des ondes sismiques fournit des informations importantes sur la composition pétrologique des milieux et sur la géométrie et la nature des discontinuités tectoniques traversées.

A titre d'illustration, considérons l'enregistrement d'un tremblement de terre représenté sur la Figure 1.2. En fonction de la résolution choisie pour l'enregistrement et l'analyse, nous pouvons considérer différents trains d'onde (par exemple **S** et **R2-3**), des arrivées individualisées (**P**), ou l'amplitude et la phase d'une seule arrivée (**R1**). La question posée par la sismologue est de comprendre comment les ondes ont été excitées et modulées lors de leur propagation jusqu'à la surface de la terre, et quelles enseignements géologiques peut on tirer de cette analyse.

Une séquence classique d'étude sismique commence par l'acquisition des données sismologiques, suivie par la modélisation des ondes dans un modèle synthétique prédéfini de la terre. La confrontation de la simulation synthétique des ondes avec les données enregistrées permet d'évaluer la pertinence du modèle de Terre prédéfini et de le modifier si nécessaire par itérations successives pour améliorer la correspondance entre données observées et calculées . L'interprétation des données sismologiques nécessite la mise au point dŠoutils numériques précis de modélisation de la propagation des ondes dans un modèle de Terre, afin de pouvoir explorer les différents scénarios géologiques possibles pouvant expliquer les données géophysiques enregistrées.

Modélisation

La modélisation et la compréhension des phénomènes de propagation des ondes nécessitent la mise au point d'outils numériques performants de simulation des ondes. La simulation des ondes permet la construction de sismogrammes qui seraient enregistrés pour

une géométrie d'acquisition donnée, une excitation de source, et un modèle physique de la terre. Idéalement, les outils de modélisation doivent pouvoir prendre en compte des modèles de Terre réalistes, fortement hétérogènes et de rhéologie complexe, et fournir des simulations précises capables de prendre en compte toute la complexité des phénomènes de propagation. Au cours de ces années, un grand nombre de techniques de simulation ont été développées. Toutes ont des avantages et des domaines d'application qui leur sont propres.

La modélisation numérique est largement utilisée pour comprendre des phénomènes complexes de propagation des ondes dans des structures hétérogènes complexes, supposées de rhéologie linéaire ou non linéaire. Les photographies de la propagation des ondes à un temps de propagation donné, appelées *instantanés de propagation*, fournissent un outil nécessaire pour comprendre les interactions complexes des différents types d'ondes. D'autres applications nécessitent des modélisations pour comparer des sismogrammes observés et calculés dans un modèle prédéfini. Des conclusions sur la précision du modèle testé peuvent être tirées de ces comparaisons.

Ces dernières années, la modélisation de la propagation des ondes a été employée pour le contrôle et la surveillance des emplacements de déchets, de la recherche des couches aquifères proches de la surface, et de la détection des matériaux enterrés ayant des paramètres physiques contrastés (par exemple, la densité) par rapport au sol environnant. Beaucoup d'applications nécessitent la simulation des phénomènes des ondes afin de trouver un modèle représentatif de la terre qui explique les données rassemblées. Les méthodes d'inversion (tomographie sismique, imagerie sismique) nécessitent des algorithmes de modélisation rapides et efficaces de sorte que des comparaisons entre données observées et calculées puissent être calculées de manière répétée dans un processus itératif. L'industrie pétrolière a besoin d'images haute résolution des réservoirs souterrains afin d'optimiser l'extraction du pétrole. Puisque les forages sont extrêmement chers et fournissent seulement des informations locales, l'industrie pétrolière acquiert des données sismiques réflexion multitrace 3D. Après le traitement des signaux, les données sismiques fournissent une image 3D du réservoir à partir de laquelle une stratégie de forage peut être élaborée.

Afin d'éviter des erreurs irrémédiables pendant l'acquisition de données sismique, la modélisation numérique est en grande partie utilisée pour définir la géométrie optimale du dispositif d'acquisition à mettre en oeuvre. Les expériences sismiques répétées à intervalles de temps réguliers, appelées "*4D time-lapse seismic*", combinées avec des simulations du champ d'onde 3D permettent de suivre l'évolution du réservoir et de ce fait d'optimiser l'extraction du pétrole.

Motivation

Comme nous l'avons mentionné, les simulations synthétiques de la propagation des ondes sont cruciales pour de nombreuses applications sismologiques. Au cours des années, différents algorithmes et techniques de modélisation ont été développés par les sismologues et d'autres scientifiques (par exemple, mathématiciens, ingénieurs électriciens, etc.), qui fournissent des approches de simulation des ondes pour des problématiques plus ou moins

spécifiques.

Grâce à l'augmentation de la puissance des ordinateurs, les sismologues peuvent calculer de nos jours des simulations du champ d'onde dans des modèles tridimensionnels à grande échelle de la terre en utilisant les architectures de super calculateurs. Des modélisations de la propagation d'onde qui prennent en compte une rhéologie proche de la réalité dans des modèles de grande taille sont loin d'être évidentes à calculer, en raison des difficultés de construire des algorithmes optimisés des points de vue de l'analyse numérique, de la précision, du temps CPU, et de la gestion de la mémoire. Typiquement, pour les applications mentionnées ci-dessus, nous devons pouvoir traiter des modèles 3D avec une rhéologie hétérogène complexe de dimensions spatiales d'environ $30 \times 30 \times 10 Km$ et une excitation de source ayant une bande de fréquence de $0 - 10 Hz$ (voir la Figure 1.3). Développer une approche numérique permettant de calculer ce type de simulations constitue l'objectif de cette thèse.

Les outils mathématiques les plus répandus pour optimiser les codes numériques de modélisation des ondes ont pour objectif de fournir des représentations adaptées de la propagation des ondes dans des espaces d'approximations hiérarchiques. Un des outils numériques définissant de manière naturelle une hiérarchie des espaces de résolution est la transformée en ondelettes et les analyses multirésolution associées. Beaucoup d'applications performantes et intéressantes de la transformée en ondelettes, par exemple, dans les domaines du traitement d'images, de la compression d'informations numériques, des simulations non linéaires complexes des écoulements turbulents, etc., ont été présentées ces dernières années. Bien que selon moi plusieurs des développements fondés sur la transformée en ondelettes n'aient pas remplacé des techniques standards existantes, le développement des applications de la transformée en ondelettes méritent d'être poursuivi. La transformée en ondelettes est une extension d'autres procédures hiérarchiques plus classiques et pourrait de ce fait fournir des informations supplémantaires qui était non détectées ou invisibles précédemment.

Dans cette thèse, je présente une nouvelle méthode de modélisation des ondes sismiques acoustiques qui est basé sur la transformée en ondelettes. L'approche développée dans cette thèse a pour objectif de surmonter les limites des méthodes de simulation classiques en rendant possibles des simulations de propagation des ondes à grande échelle dans des modèles complexes 3D fortement hétérogènes pour un grand nombre des fréquences et de sources. D'une part, le nouvel algorithme se fonde, sur des formulations fortes bien connues, stables, et puissantes des équations aux dérivés partielles qui sont employées pour des problématiques 3D de petites tailles. L'extension proposée doit permettre de manipuler des rhéologies physiques plus complexes pour des modèles à grande échelle de la terre en tirant profit de la décomposition hiérarchique fournie par la transformée en ondelettes.

Les ondelettes ont été largement utilisées pour modéliser la propagation des ondes, bien que beaucoup d'applications n'exploitent selon moi que partiellement la décomposition multirésolution fournie par les ondelettes pour, par exemple, calculer les dérivés partielles numériquement, ou pour effectuer du seuillage numérique dans le but de construire des grilles numériques non uniformes. Le nouvel algorithme de modélisation développé dans cette thèse est plus ambitieux: la modélisation des ondes est complètement résolue

dans le domaine des ondelettes afin de tirer un profit optimal de la décomposition multi-grilles fournie par la transformée en ondelettes tout en évitant les allers-retours coûteux entre les domaines physiques et spectraux propres aux approches classiques.

Les applications envisagées de cette nouvelle approche sont le calcul de simulations pour des expériences multi sources telles que celles mises en oeuvre dans le contexte de l'exploration pétrolière. En outre, l'étude des effets de site pour la prévention des catastrophes naturelles dans des secteurs fortement peuplés comme par exemple, les marges continentales convergentes menacés par le risque sismique élevé, devient de plus en plus importante. Ces études sont largement fondées sur la modélisation des ondes sismique en 3D à grande échelle afin de prévoir les scénarios possibles du mouvement du sol.

Plan de la thèse

La thèse est subdivisée en sept chapitres. Dans le chapitre 2, je discute et illustre la nécessité de définir une approximation numérique de l'équation d'ondes. J'expose un bref panorama des différentes discrétisations possibles, ainsi que les avantages et inconvénients de ces approches pour la modélisation des ondes à grande échelle. Ce chapitre traite de l'approximation des dérivés partielles spatiales de l'équation d'onde. Des discrétisations en temps de l'équation d'ondes sont brièvement commentées à la fin du chapitre, parce que la dimension temporelle joue un rôle mineur dans le travail présenté ici, l'approche choisie étant implémentée dans le domaine des fréquences.

Dans le Chapitre 3, je présente l'approche par différences-finies dans le domaine des fréquences (FDFD) utilisée actuellement pour les simulations. La formulation classique par rotation des grilles en FDFD est comparée à une discrétisation FD de l'équation d'ondes basée sur une géométrie des grilles en quinconce plus classiquement utilisée dans les formulations temporelles. Le schéma à 13-points, qui combine des grilles en quinconce dans le domaine de fréquence, est examiné du point de vue de la précision et de la rapidité numériques dans des milieux 2D homogènes et hétérogènes.

Afin de surmonter les limites des stratégies de modélisation FDFD par rotations des grilles et des grilles en quinconce, je développe dans le chapitre 4 un nouveau algorithme de modélisation FDFD fondé sur une approche multigrille. Le chapitre 4 débute par un état de l'art des méthodes de construction de grilles numériques qui ont été développées pour la résolution numérique d'équations aux dérivés partielles. Je discute des avantages et inconvénients des techniques existantes qui mèneront à la conclusion qui a motivé mon travail. La nouvelle approche de modélisation par FDFD est basée sur une combinaison des solutions du champ d'onde calculées sur des grilles de résolutions grossière et fine. Une première solution est calculée exactement sur une grille de résolution grossière par une méthode directe. Deuxièmement, ce champ d'onde est utilisé pour construire une solution initiale injectée dans une méthode de résolution itérative. Je développe deux méthodes différentes qui sont fondées sur une combinaison spatiale de grilles numériques de résolutions différentes (approche multigrille). Dans la première approche, les transferts entre les différentes grilles sont effectués par interpolation bilinéaire et injection (approche "*Direct-Iterative-Space Solver*" (DISS)). Dans la deuxième approche, les transferts entre grilles sont gérés par la décomposition multigrille fournie par la transformée en ondelettes

(approche "*Direct-Iterative-Wavelet Solver*" (DIWS)). Les deux approches sont développées pour calculer des propagations d'ondes SH dans des milieux 2D hétérogènes.

Le chapitre 5 présente plusieurs applications des outils développés au chapitre 4 pour des milieux homogènes et hétérogènes. Les performances respectives en termes de précision et de rapidité des approches DISS et DIWS sont comparées et interprétées dans le contexte des méthodes multigrilles.

Dans le chapitre 6, les stratégies de DISS et de DIWS sont étendues aux cas des milieux 3D acoustiques. Les codes 3D sont d'abord examinés pour des petits modèles 3D en utilisant une exécution en mode séquentielle. Par ailleurs, je discute en détail des problèmes associés à l'extension en mode parallèle du code séquentiel.

Le chapitre 7 récapitule le travail présenté dans la thèse. Finalement, je clôture la discussion en proposant plusieurs perspectives de développements ayant pour objectifs de poursuivre mes travaux.

1.2 Seismology

Looking up the meaning of *seismology* in a standard English language dictionary, one typically finds a definition of the type: *The scientific study and recording of earthquakes and related phenomena.* The object under scientific investigation is the Earth and seismology is the tool applied to discover the inner Earth structure and processes, as-well-as the understanding of how the Earth has been formed and its actual state. The description of the Earth's structure and processes depends mainly on the scale we are looking at. It is commonly known that the Earth consists of several onion-like shells, such as core, mantle, crust, etc., where each shell is assumed to be a more or less homogeneous body (see Figure 1.1). However, a more detailed inspection of the Earth's structure reveals rather complex interfaces between shells, and spatially varying heterogeneous and dynamic structure in the interior of the shells.

The non-uniform and scale-dependent processes in the Earth create scale-dependent seismological data. In other words, the time-scale of *seismological* observation is related to the characteristic scales of processes in the Earth. Typically, we find two distinct time scales, that are related to the seismic source excitation (the order of milliseconds up to seconds), and the time required for seismic waves to propagate to the receiver station (few seconds up to hours).

For many years, seismologists tried to interpret the wide range of recorded seismological information. The continuing accumulation of data and advances in signal processing techniques significantly improved the knowledge of the Earth's structure. The insights gained are, on one hand, related to academic problematics, such as discovering the structure of the innermost core of the Earth. On the other hand, research investigations, such as the search for oil and gas, the control and understanding of underground nuclear explosions, or seismic risk analysis, use seismology as a tool to obtain an as-exact-as-possible reproduction of the near surface Earth's structure composition.

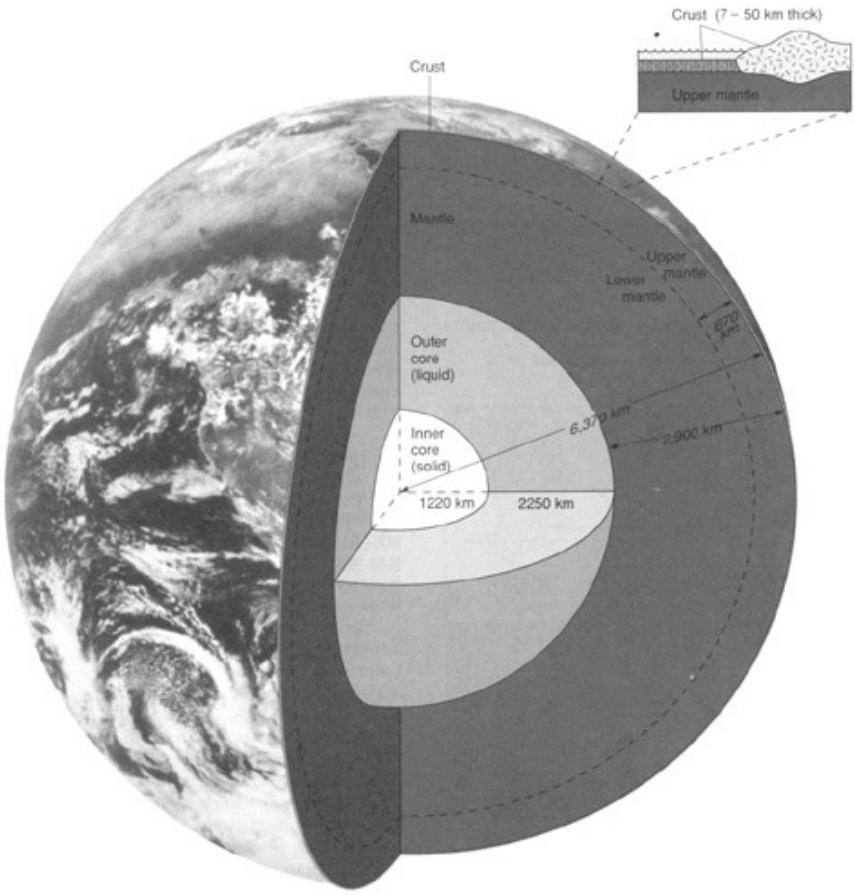

Figure 1.1: The standard model of the Earth's interior (McGeary and Plummer, 1998).

1.3 Wave propagation

Due to the lack of direct accessibility of the Earth's interior, seismologists use seismic wave propagation as a tool to extract, interpret, and understand inherent Earth processes and structural formation. Seismic waves are powerful for extending our knowledge of the Earth's interior. They propagate from the source point (earthquake or artificial explosion) to the Earth surface, where they are recorded by a seismic station. Therefore, seismic waves contain important information related not only to the wave nucleation process, but also to the physical properties of the medium the waves path traveled through from the source to the recording station.

The analysis of the recorded seismological information allows extensive interpretations which, at the seismic resolution, could not have been obtained by other techniques. The analysis of arrival times, amplitude, phase, and damping of seismic waves provides important information for geological and geophysical interpretations with respect to physical

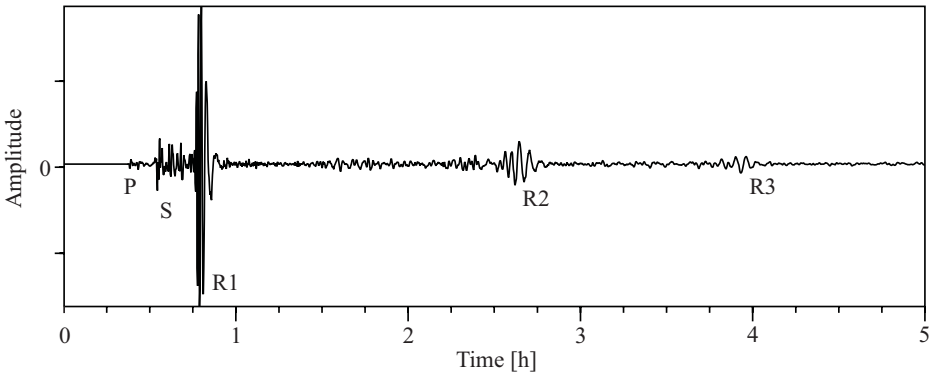

Figure 1.2: Vertical component of a seismogram recording from the PPT station (*Geoscope* network) in Tahiti on the 5^{th} March 1985. The epicentre of the earthquake causing the ground motion is in Valparaiso (Chile) at a depth of approximately $40Km$. The magnitude is $M_s = 7.8$. I plot the seismogram up to $5h$, though the complete recording lasts about $20h$. Clearly visible are different arrival times for wave-trains having different characteristic forms and amplitude. For example, I indicate the main body-waves, such as P- and S-waves, as well as several Raleigh wave-trains (R1, etc.).

rock-properties and dynamic processes in the Earth.

As an example, consider the earthquake recording plotted in Figure 1.2. Depending on the resolution chosen for the recording and analysis, we may distinguish between groups of wave-trains (for example **S** and **R2-3**), separate distinct arrivals (**P**), or even the characteristics of amplitude and phase of an arrival (**R1**). The question arises how the waves have been excited and modulated during the passage to the Earth surface, and what insights might be gained from that knowledge.

A typical processing sequence starts with recording the seismological data, then performing synthetic wave modelling in a pre-defined synthetic Earth model. The combined comparison of the synthetic wave simulation and the actual recorded data provides the basis of a geological study. The interpretation of seismological data requires trustworthy synthetic wave propagation modelling, in order to distinguish between different possible complex geological scenarios that may all fit the recorded data.

1.4 Forward modelling

One strategy to understand wave propagation phenomena is the numerical simulation of seismic wave propagation. The objective of wave propagation modelling is the study of wave phenomena in a synthetic Earth model under certain, more or less realistic conditions. In other words, wave modelling permits the construction of a seismogram that would be recorded for a given specific acquisition geometry, wave generation (source), and physical Earth model.

The interest in synthetic wave modelling arises from the fact that numerical wave

simulation is the main tool to provide accurate and trustworthy synthetic seismograms for strongly heterogeneous, i.e., close to realistic, Earth models. Over the years, very many different simulation techniques have been developed. All have specific advantages and areas of application, depending on the problem at hand.

Numerical forward modelling is widely used to understand complex wave propagation phenomena in complex heterogeneous structures, assuming linear or even non-linear physical rheology. Time-photographs of the wave propagation at a certain time, called snapshots, provide an imperative tool to understand the physics of the rather complex interaction of the waves. Other applications use forward modelling to compare synthetic and recorded seismograms. Then, precise conclusions on the accuracy of the pre-assumed synthetic Earth model, with respect to the unknown real model, can be drawn.

In recent years, wave propagation modelling has been used for the control and monitoring of waste sites, search for near-surface water aquifers, and the detection of buried materials having significantly contrasted physical parameters (e.g., density) with respect to the surrounding soil. Many applications include forward modelling of wave phenomena in order to find a representative Earth model that *fits* the collected data. The inversion process requires fast and efficient modelling algorithms so that synthetic and real data comparisons become feasible in a reasonable amount of time. Oil industry needs high resolution reproductions of the underground reservoirs in order to accurately control the extraction of the oil. Since boreholes are extremely expensive and only provide punctual information, oil industry acquires artificial multi-source seismic data. After signal processing, the seismic data provides a reservoir image, that helps devising reservoir exploitation strategies.

In order to avoid unrecoverable errors during seismic data acquisition, numerical forward modelling is largely applied to test acquisition parameters and different geometry setups. Then, the best adapted geometry and precise judgement of the expected outcomings of the survey can be determined before action is taken. Moreover, repeated seismic multi-source experiments, called $4D$ time-lapse seismic, combined with 3D forward wave-field simulations allow the tracking of changes in the reservoir and optimise oil extraction.

1.5 Motivation

As we have seen, synthetic wave propagation simulations are crucial for numerous seismological applications. Over the years, many different forward modelling algorithms and techniques have been developed by seismologists and other scientists (e.g., mathematicians, electrical engineers, etc.), that provide wave simulation approaches for more or less specific problematics.

With the extensive development of computational power, these days seismologists perform wave-field simulations in large-scale three-dimensional Earth models using fast supercomputer structures. Still, wave modelling that incorporates close-to-real rheology in large models is by-far not evident to perform, because of difficulties to construct optimised algorithms with respect to resolution, precision, CPU speed, and memory re-

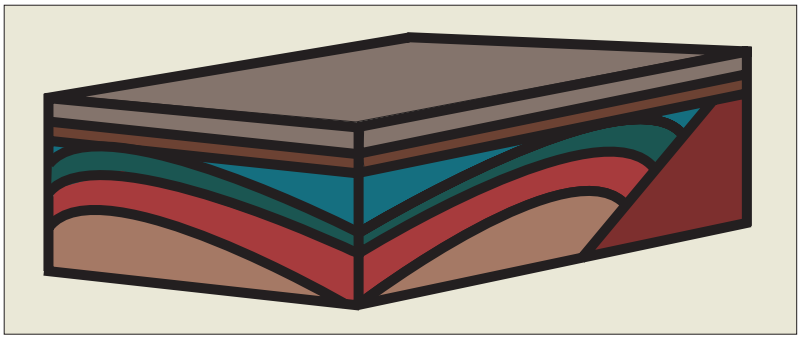

Figure 1.3: Typical 3D model with complex heterogeneous rheology for wave propagation simulations. The model dimensions are $30Km \times 30Km \times 10Km$ and ideally we would like to model accurately frequencies in a band from $0 - 10Hz$.

quirements. A typical 3D model with complex heterogeneous rheology may have spatial dimensions of about $30Km \times 30Km \times 10Km$ and a frequency band of $0 - 10Hz$ (see Figure 1.3). This is the kind of scenario I am targeting in this thesis.

Popular mathematical tools to obtain the desired optimisations of the numerical code are adapted representations of the wave propagation in hierarchical approximations. One of the numerical tools that naturally defines a hierarchy of resolution spaces is the wavelet transform. Many powerful and interesting applications of the wavelet transform, e.g., in the field of image processing, complex non-linear simulations of turbulent flows, etc., have been presented in recent years. Even though many of these developments did not replace existing standard techniques, in my opinion, it is still necessary to further investigate the application of the wavelet transform. Since it is an extension to other more standard hierarchical procedures it might provide additional, previously undetected or unseen informations.

In this thesis, I present a new wavelet-based forward modelling scheme for acoustic seismic wave simulations. The new scheme aims to overcome limits of current modelling approaches by rendering feasible large-scale simulations of complex 3D wave propagation phenomena in strongly heterogeneous media, for large frequency bandwidth data and numerous external source functions. On one hand, the new algorithm relies, on well-known, stable, and powerful strong formulations of the partial differential equations that are used for small and simple 3D problematics. On the other hand, the extension to handle more complex physical rheologies for large-scale Earth models is obtained through the coupling with a wavelet-based hierarchical decomposition.

Wavelets have been widely used for wave propagation modelling, though many applications only use the provided wavelet decomposition e.g., for defining the numerical grid, numerically computing derivatives, or numerical thresholding. The new modelling algorithm developed in this thesis is more ambitious: the desirable properties of standard space algorithms combined with the complete wavelet structure provide a powerful tool for wave propagation simulations.

Typical applications of this new approach are wave simulations for extensive multi-source experiments, such as carried out in oil exploration. Also, site-effect studies for natural disaster prevention in highly populated areas situated in e.g., large sedimentary basins with high seismic risk, become more and more important. These studies rely extensively on large-scale 3D seismic wave modelling in order to simulate possible ground motion scenarios.

1.6 Outline of the thesis

The thesis is subdivided into seven chapters. In Chapter 2, I discuss and illustrate the necessity to define a numerical approximation to the partial differential wave equation, that allows the desired wave propagation simulations. I give a brief review of existing discretization possibilities, together with handicaps and advantages of these methods with respect to large-scale wave simulations. This chapter deals with the spatial approximation of equations. Time discretizations of the wave equation are briefly commented at the end, since time dependencies play a minor role for the work presented here.

In Chapter 3, I present the state-of-the-art frequency domain finite-difference (FDFD) modelling approach. The standard FDFD grid-rotation formulation is compared to a FD discretization of the wave equation based on a staggered-grid geometry rather than grid-rotation. The 13-points cross stencil, that combines spatially staggered grids in the frequency domain, is examined with respect to numerical accuracy and computational efficiency in 2D homogeneous and heterogeneous media.

In order to overcome computational limits of the grid-rotation and staggered grid-combination strategies for FDFD wave simulations in 3D Earth models, in Chapter 4 I develop a new FDFD modelling algorithm that relies on a combination of multi-grid wave modelling techniques. Chapter 4 starts with a general review of grid optimisation techniques that have been developed for numerical simulations of partial differential equations. I discuss shortcomings and benefits of existing techniques that will lead to the conclusion that initially motivated my work. The new FDFD modelling scheme is based on a combination of coarse-grid and fine-grid wave-field solutions. I develop two different methods that rely on either a spatial or a wavelet-based grid combination, called Direct-Iterative-Space Solver (DISS) and Direct-Iterative-Wavelet Solver (DIWS). Both approaches are introduced for SH-wave propagation in 2D media and tested with respect to computational efficiency and accuracy in structurally complex heterogeneous model scenarios.

Chapter 5 provides further benchmark tests of the modelling scheme developed in Chapter 4 for homogeneous and heterogeneous media, as well as performance tests related to external software used in the implementation to guarantee trustworthy computational results.

In Chapter 6, the DISS and DIWS strategies are extended for wave simulations in acoustic 3D media. The 3D code is first tested for small 3D model scenarios using a sequential implementation. Moreover, I discuss in detail problems related to a parallel extension of the sequential code.

Chapter 7 summarises the work presented in the thesis and gives some concluding remarks concerning the results I have obtained. Finally, I close the discussion with my ideas about future developments and continuation of my work.

Chapter 2

From Continuum to Discretization

2.1 Résumé

Dans ce chapitre, je présente et discute plusieurs stratégies de discrétisation numérique d'une équation aux dérivés partielles (PDE) telle que l'équation d'onde. Idéalement, nous voudrions obtenir des solutions analytiques des PDEs. Malheureusement, même pour des modèles simples telles que des corps isotropes homogènes, le calcul de la solution de l'équation d'onde nécessite une analyse soignée des formulations fondamentales et est loin d'être trivial. Puisqu'il est difficile d'obtenir les solutions analytiques pour des milieux généralement non homogènes, les sismologues discrétisent les PDE, et calculent des solutions approchées du champ d'onde en résolvant les équations numériquement.

Beaucoup de techniques ont été développées pour représenter des PDEs sur des grilles numériques, telles que les méthodes des différences finis, des éléments finis, des volume finis, et des éléments spectraux. Toutes ces méthodes peuvent être replacées dans le contexte d'une formulation spécifique de la méthode des résidus pondérés ("*weighted residuals*" (WR)). En général, la méthode WR utilise des fonctions de base, également appelées fonctions d'interpolation, pour développer la solution de la PDE en série. L'approximation de la solution vient de la troncation de la série. Afin de garantir la précision de la solution, des fonctions d'essai sont utilisées pour réduire au minimum l'erreur résiduelle qui est obtenue quand la solution approchée est injectée dans la PDE. Les différents choix possibles des fonctions d'interpolation et des fonctions d'essai permettent de distinguer les différentes approches numériques mentionnées ci-dessus. Toutes les approches mentionnées ci-dessus permettent la simulation numérique des ondes dans des modèles bidimensionnels (2D) sur une simple station de travail. Quand les modèles deviennent structurellement complexes et/ou tridimensionnels (3D), les modélisations des ondes ne deviennent envisageables que sur des super calculateurs ou sur des architectures parallèles, ces dernières nécessitant l'implémentation de stratégies de parallélisation pouvant se révéler fort complexes (par exemple, décomposition de domaines).

Alors qu'il reste difficile de calculer des simulations tri-dimensionnelles dans des modèles de taille réaliste, l'acquisition de données sismiques 3D et les techniques de visualisation et d'interprétation de volumes 3D sont devenus des outils standard de l'industrie

pétrolière et de certains groupes de recherche sismologiques aux universités. Afin de venir autour de l'anomalie entre les données enregistrées et les outils de modeler, deux possibilités existent.

D'une part, on estime que des propriétés physiques du matériel d'ordinateur réel, mémoire disque c.-à-d., de noyau et vitesse informatique d'unité centrale de traitement doublent chaque 18 mois. D'autre part, la différence entre les besoins informatiques et les possibilités réelles est susceptible de rester ou même augmenter à l'avenir, puisque l'acquisition de données deviendra de plus en plus précise et spatialement dense. Alors des phénomènes de propagation des ondes devront être étudiés pour des données à bande haute fréquence (par exemple, $0 - 50Hz$ pour des études des effets de site détaillés), et l'incorporation des effets non linéaires de propagation des ondes aura un impact significatif pour résoudre complètement toute l'information actuelle dans les données. Afin d'effectuer ces simulations des ondes à grande échelle dans des milieux 3D, nous avons la possibilité d'attendre les ordinateurs pour devenir rapides et assez grands pour traiter le problématiques réel avec des techniques standard existantes. À mon avis c'est fallacieux, parce que, donné un niveau d'ordinateur et performance des logiciels, l'outil ayant la meilleure performance adaptée à les problèmes réels actuels seront employées par les sismologues.

Par conséquence, l'autre possibilité doit optimiser les codes existants de logiciel pour améliorer l'ajustement les problèmes actuels et/ou pour développer des nouveaux codes, celui, en général, ou pour des problèmes spécifiques seulement, fournissent les manières qui permettent la simulation exigée de propagation des ondes avec les ressources d'informatique courantes disponibles. C'est ce point de vue qui justifie l'effort entrepris durant ma thèse.

2.2 Introduction

Imagine a town where there are no streets. In order to go from one place to another you would have to pass through spaces left over between buildings and houses. In this case, finding the right way would probably be a difficult matter.

Therefore, towns are run through by numerous streets that allow easy and fast navigation to almost any desired place. Then, it is rather a question of *how well* or *easy* you find your way through, which again is controlled by the complexity of the streets and buildings in the town. In effect, the *how well* you find your way will probably depend, simplifying, on the town being built in America or Europe. American towns, in general, have a clear and simple structure since streets are lined up in a quadratic manner, which allows a rather *easy* navigation. In Europe, streets are not constructed following an obvious geometrical structure, and therefore navigation is more difficult.

However, imagine that you would just want to find the way to the cultural centre of the town. Although asking for the right way is probably the best choice, there is another characteristic in the town structure that may guide us in the right direction: the street size and density. When approaching the town centre, in general in both types of towns, American or European, the number of streets will increase while their size decreases.

Although most of us can relate to the significance of streets in towns, where is the

connection to numerical modelling in Geoscience? Well, the numerical grid designed on a computer lets the geophysicists find wave-field solutions to partial differential equations (PDE), just as the streets permit the navigation in a town.

In numerical modelling the desired exact analytic solution is computed without the help of a numerical grid. As for the town-without-streets example where navigation is manageable only when the town is simple and easily comprehensible, finding an analytic solution of a PDE is only possible for very simple model structures. When it comes to more complex models where physical parameters are distributed heterogeneously, the continuous PDEs can be projected in the discrete world with the help of a numerical grid. However, since we expand the PDE on a computer architecture, it is the computer basis (the numerical grid) that controls the accuracy and performance of the expansion. Therefore, the numerical grid is of great importance.

Many different types of grids and grid constructions exist, and it is a matter of debate which grid or grid structure is the best adapted for a given problem at hand. Coming back to the town-street example, I mentioned that common points of interest, such as the cultural town centre, are run through by an increased number of streets having smaller and smaller size. We also find this kind of refined-grid-structures in numerical modelling. Though the general need to refine the grid in regions having complex rheology is unquestionable, the way how the refinement from one grid to another is performed, is far from being obvious.

In this Chapter, I will discuss different techniques to form a numerical grid for seismic wave propagation simulations, where the aim is the best exploitation of the model structure using the least computational possible resources.

2.3 Computation on a grid

Seismic wave propagation is mathematically described by the wave equation:

$$\nabla^2 u = \frac{1}{c^2}\frac{\partial^2 u}{\partial t^2} \tag{2.1}$$

where u is the scalar wave potential and c the wave velocity.

Ideally, we would like to obtain analytical solutions to Equation 2.1 in the presence of external sources. Unfortunately, even for simple model structures such as homogeneous isotropic bodies, computation of the solution of the wave equation requires careful analysis of the underlying formulations and is by far not trivial (Morse and Feshbach, 1953). Since analytic solutions are difficult or impossible to obtain for general inhomogeneous media, seismologists discretize the PDE in Equation 2.1, and compute approximate wave-field solutions by solving the equations numerically.

Many different techniques have been developed to approximate PDEs on numerical grids, such as finite-differences, finite-elements, finite-volume, and spectral element techniques. All these methods may be viewed as specific formulations of the weighted residuals method. In general, the weighted residuals method employs basis expansion functions,

also called interpolating functions, for a truncated series expansion of the PDE solution. The approximation of the solution comes from the truncation of the series expansion. In order to guarantee accurate PDE solutions, in general, testing functions are used to minimise a residual error that is obtained when the approximate solution is substituted in the PDE. It is the combination of series expansions and testing functions that distinguishes between the above mentioned numerical approaches.

To illustrate the underlying framework of the residuals method, I consider the wave equation in the one-dimensional domain $\Omega \subset R$ with boundary Γ:

$$\begin{cases} \mathcal{L}u - f = 0 \ in \ \Omega \\ u = u_\Gamma \end{cases} \tag{2.2}$$

where $\mathcal{L}$ is a differential operator. I now define a set a of interpolating and testing functions, denoted by U and W, respectively, to fulfil:

$$\begin{aligned} U &= \{u \mid u \epsilon H^2(\Omega), u = u_\Gamma \ on \ \Gamma\} \\ W &= \{w \mid w \epsilon L^2(\Omega), w = 0 \ on \ \Gamma\} \end{aligned} \tag{2.3}$$

Then, I write the corresponding *strong formulation* of Equation 2.2:

$$\begin{aligned} &Find \ u \epsilon U \ such \ that: \\ &(\mathcal{L}u - f, w)_w = 0 \quad \forall w \epsilon W \end{aligned} \tag{2.4}$$

Moreover, I introduce a finite-dimensional subspace of the interpolating functions U^h with the corresponding basis functions ϕ_i, which gives the discrete strong formulation:

$$\begin{aligned} &Find \ u^h \epsilon U^h \ such \ that: \\ &(\mathcal{L}^h u^h - f, w^h)_w = 0 \quad \forall w^h \epsilon W^h \end{aligned} \tag{2.5}$$

In point collocation methods the testing functions, denoted by $\psi_j \epsilon W^h$ (where $W^h \subset W$ is a finite-dimensional subspace of W), are Dirac delta functions defined on discrete collocation points in Ω:

$$\psi_j(x) = \delta(x - x_j) \tag{2.6}$$

Popular point collocation methods are finite difference (FD) methods. FD methods only define the discrete differential operator $\mathcal{L}^h$ around the collocation points, which gives:

$$\begin{aligned} &Find \ u(x_j) \ such \ that: \\ &\mathcal{L}^h u \mid_{x=x_j} = f(x_j) \quad j = 0, ..., N \end{aligned} \tag{2.7}$$

Since FD methods use Dirac delta testing functions, they verify the wave equation exactly on discrete collocation grid points.

Finite-volume methods (FV) subdivide the initial domain Ω into a set of sub-domains Ω_j. The testing functions are then chosen with respect to the sub-domain:

$$\psi_j(x) = \begin{cases} 1 & \text{for } x \epsilon \Omega_j, \\ 0 & \text{for } x \notin \Omega_j. \end{cases} \tag{2.8}$$

and the residual formulation verifies surface integrals, where the sum of in- and outcoming flow has to be zero. This gives a surface integral formulation:

$$\begin{aligned} &Find\ u^h\ such\ that: \\ &\int_{\Gamma_j} (\mathcal{L}^h u^h - f) d\Gamma_j = 0 \quad j = 0, ..., N \end{aligned} \tag{2.9}$$

In my point of view, FV and FD methods are somehow similar in that both approaches rely on collocation points. While FD methods use Dirac interpolating functions, FV methods determine 'averages' over each sub-domain Ω_j (see Integral in Equation 2.9). The testing functions are chosen such that the flux over the surface Γ_j becomes zero. Therefore, FV discretizations are sub-domain collocation methods, and I denote them as *average formulations*.

The *weak formulation* of a PDE can be constructed through an integration by parts of the residual formulation given in Equation 2.4. In many cases, an equivalent bilinear form can be derived, such that the equation to be solved becomes:

$$\begin{aligned} &Find\ u \epsilon U\ such\ that: \\ &a(u, w)_w = (f, w)_w \quad \forall w \epsilon W \end{aligned} \tag{2.10}$$

The problem in Equation 2.10 has a unique solution when certain constraints of the bilinear form are verified. Often, the inner product $a(u, w)_w$ weakens the restriction on the solution of the PDE, which is why this approach is called the *weak formulation*. Another possibility to derive the *weak formulation* is via a variational formulation of the problem.

As for FV methods, the computational domain is divided into sub-domains and interpolating functions are defined in each element locally. Appearing volume or surface integrals in the formulation can be computed by different numerical integration techniques of varying accuracy, that rely on polynomial basis expansions of the solutions.

Numerical codes using the *weak formulation* are distinguished by the method used for numerical integration. Typical methods include finite-elements (FE) and spectral elements (SE) methods. The *weak formulation* is less ambitious compared to the *strong formulation* since equations are verified over elements, rather than discrete collocation points as in FD methods.

All the above mentioned approaches permit numerical wave simulation modelling in limited two-dimensional (2D) models on single desktop work stations. When it comes to structurally complex and/or three-dimensional (3D) models that require fine mesh discretizations, wave simulations can, if at all possible, only be performed using standard schemes when large computer resources are available.

In contrast to the actual limitations of wave simulation software, 3D seismic data acquisition and interpretation have become standard tools for the petroleum industry and seismological research groups at universities. In order to come around the discrepancy between recorded data and modelling tools, two possibilities exist.

On one hand, physical properties of actual computer hardware i.e., core- and disk memory and CPU speed are estimated to double each 18 months (Moore, 1965). On the other hand, the difference between computational needs and actual capabilities is likely to remain or even increase in the future, since data acquisition will become more and more accurate and spatially dense. Then wave propagation phenomena will have to be investigated for high frequency bandwidths data (e.g., $0 - 50Hz$ for detailed site effects studies), and the incorporation of non-linear wave propagation effects will have a significant impact to completely resolve all information present in the data. In order to run these large-scale wave simulations in 3D media, we have the possibility to wait for the computers to become fast and big enough to treat actual problematics with existing standard techniques. In my opinion this is misleading, because, given a level of computer hard- and software capabilities, the tool having the best adapted performance for the actual problems at hand will be used by the seismologists.

Therefore, the other possibility is to optimise the existing software codes to better fit the problems at hand and/or develop new codes, that, in general, or for specific problems only, provide ways that permit the required wave propagation simulation within the current computer resources available. It is this point of view that has given rise to the motivation of my work.

2.4 Strong formulations

Continuous PDEs can be approximated on a numerical grid using the FD approach. FD methods discretize the wave equation on a numerically equidistant grid where physical model parameters, such as density and velocity, and partial derivatives are defined and verified on discrete grid points, while between grid points no control of the wave-field-solution is provided. Since the PDEs are projected on the numerical grid, it is the grid parameters (e.g., number of grid points per shortest wavelength, grid spacing, etc.) and the order of numerical approximation of spatial derivative operators that define the accuracy and performance of the modelling code. Therefore, the definition or construction of the numerical grid is crucial for the accuracy of the modelling scheme.

Historically, standard FD methods have been projected on Cartesian grids (Kelly et al., 1976). They have been widely used for 2D wave simulations, since the FD approximation provides the complete wave-field response within predefined numerical precision limits. Moreover, the stability of the numerical scheme is easily controlled and the implementation stays rather simple. Various FD approximation techniques have been developed, where the interpolation based estimation of partial derivatives plays a crucial role. The classic FD scheme by Kelly et al. (1976) uses Taylor series expansions in the physical domain.

In order to obtain more accurate derivative estimations, other developments transform the derivative approximation from the physical space to the spectral space while the main differential equations are still verified in the physical domain. The above mentioned interpolating functions ϕ_i are used as basis functions for a truncated series expansion of

the solution $u(x)$, such that:

$$u^h = \sum_{i=0}^{N} c_i \phi_i \tag{2.11}$$

The coefficients c_i in the physical space depend on all values of $u(x)$ and are computed by numerical integration. Since this is not always possible for arbitrary functions $u(x)$, the set of coefficients $\hat{c}_i$ in the spectral space are derived using interpolating orthogonal polynomials. These methods, denoted by pseudo-spectral methods, replace the classic Taylor expansion by e.g., Fourier (Kosloff and Baysal, 1982), Laguerre (Mikhailenko, 2000), Chebyshev (Tessmer and Kosloff, 1994; Igel, 1999), or Wavelets (Operto et al., 2002; Hong and Kennett, 2002) formulations.

In contrast to pseudo-spectral methods, that profit from increased accuracy in the spectral domain to approximate spatial derivatives while equations are verified in the space domain, spectral methods perform a complete transformation of the underlying equations in the spectral domain. A classical example is the Fourier spectral method (Fuchs and Muller, 1971), that uses the set of functions

$$\phi_i(x) = e^{ikx} \tag{2.12}$$

The transformation in the spectral domain is performed because the complete wave simulation problem is thought to be easier to solve in the new space. Computations that are simple in the physical space, such as the product of spatial derivatives with medium parameters appearing in time domain finite differences (TDFD), become convolution type procedures in the spectral domain that, in general, are costly to compute:

$$g(x,y,z) \cdot \frac{\partial f(x,y,z,t)}{\partial x} \;\Rightarrow < g(x,y,z)\frac{\partial f(x,y,z,t)}{\partial x}, \Psi_i(x)\Psi_j(y)\Psi_k(z) > \tag{2.13}$$

where Ψ denotes basis functions of the transformed spectral space.

In order to avoid convolution type computations, locally smooth model parameters have to be assumed. Then, the model parameter function $g(x,y,z)$ of the spectral expansion in Equation 2.13 is a constant and can be left outside the inner product, which greatly simplifies computations. Such an approach was developed by Wu and McMechan (1998) for a wavelet-based FD seismic wave-field simulation strategy.

For strongly heterogenous media the homogeneity assumption breaks down and convolution type computations are unavoidable when the strictly spectral approach is used (Operto et al., 2002). However, computing the spatial derivatives-medium parameters product in the physical domain, while performing the simulations in the spectral domain, leads to a pseudo-spectral type formulation (Operto et al., 2002), where the performance is strongly dependent on forward and inverse transformation algorithms between the physical and the spectral domain.

When it comes to 3D models or complex 2D models, computer resources required for the modelling on an equidistant Cartesian grid forbid the wide-spread usage of standard

FD and pseudo-spectral methods. The most complex part in the model controls the spatial discretization for stable wave propagation modelling. Since only a unique spatial discretization step is defined, the obligatory fine stepping has to be applied to the whole model which in effect renders standard FD and pseudo-spectral methods inefficient, if not impossible to use.

Along with the optimisation of the derivative approximation, other techniques have been developed that enhance the computational performance by optimising implementations for single desktop work stations (Graves, 1996; Moczo et al., 1999). However, different constraints, such as the restriction to equidistant Cartesian FD-grids or expensive forward and inverse transformations necessary for pseudo-spectral methods, did not sufficiently enough improve the limits of standard simulation techniques. Therefore their usage is prohibited for larger and more complex heterogeneous Earth model simulations in a broader sense.

2.5 Space mesh optimisation

In order to overcome the computational limits caused by the restriction to use a unique Cartesian grid, FD schemes have been extended to allow computations on different grids of different resolution. The underlying idea is the distribution of corresponding computational power to the complexity and the physical significance of the regions in the model.

For example, the ground motion simulation for a sedimentary basin including shallow low-velocity layers, typically requires a fine discretization for the low-velocity zones while the deeper layers with faster velocities can be modelled with larger discretizations. However, standard FD schemes would require the fine discretization of the low-velocity zones for the whole model, therefore spending large computer resources for unnecessary detailed wave simulations in the fast-velocity regions. Another example would be a sedimentary model with a salt dome. While the undisturbed sedimentary layers are horizontally aligned and rather simple in structure, they are assigned a coarse spatial discretization step. The flanks of the salt dome are structurally complex and thus require a much finer discretization than the surrounding parts.

It is desirable, from a computational point of view, that structurally complex zones in the model are treated with a fine discretized grid, while large spatial discretization steps are applied to model regions where physical parameters change smoothly .

One popular approach to combine numerical grids of varying spatial resolution is the multi-grid technique (Hackbusch, 1978; Briggs, 1987). The procedure to refine or coarsen the numerical approximation grid and subsequent iterative computations of wave-field solutions is obtained through a series of approximation, correction, and interpolation steps, called V- and W-cycles (Hackbusch, 1978).

A typical full multi-grid method (FMG) starts the simulation procedure by computing approximative wave-field solution on the finest discretized grid by an iterative solver. Since iterative solvers, such as Gauss-Seidel or GMRES, easily suppress high frequency components while leaving low frequency components almost untouched, the

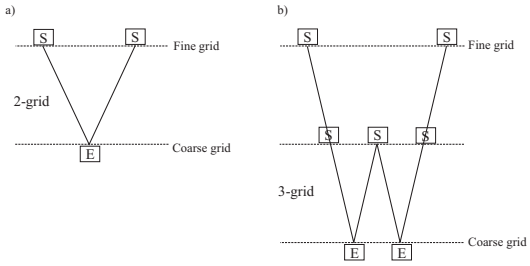

Figure 2.1: V- and W-cycles applied in a multi-grid approach. In (a) I show the *two-grid* situation, where iterative solutions are computed, projected and corrected on two grids having different spatial resolution. (b) shows a V- and W-cycle for a *three-grid* situation.

FMG methods projects the solution on a sequence of coarser discretized grids. This restriction procedure is called *Coarse Grid Correction* (CGC). On these grids, initially low frequency components at some coarse grid become local high frequency components, and can therefore easily be adapted by the iterative solver. Once a good coarse-grid solution is obtained, the standard FMG methods prolongates the coarse-grid solution on grids having finer discretizations until the desired fine-grid is reached. The solution prolongation may be effectively performed by simple bilinear interpolation and is called *Nested Iteration* (NI). On each fine grid, the interpolated solution needs to be corrected due to interpolating phase-shift errors. The procedure of going forth and back between different resolution grids is meant to eliminate the existing artefacts. An illustration of a typical two-grid and three-grid FMG setup is shown in Figure 2.1.

The multi-grid technique has been applied and further developed for numerous problems in physical sciences to solve PDEs (see Debicki, 1999; Pessel, 2000, for FD multi-grid modelling of Maxwell's equations). Its usage is supported by the fact that the definition of several Cartesian grids of varying resolution is straight-forward, easy to implement, and modelling accuracy is controlled just as for the single-grid approach.

Although multi-grids provide a nice and convenient way to couple numerical grids, the main drawback is that convergence to an approximately accurate solution can not be guaranteed, since local error estimates during the V- and W-cycles always depend on tolerance levels of underlying iterative solvers. It is the grid connections that should be investigated in more detail, in order to eliminate the ambiguity introduced by the difficult error estimates in multi-grid approaches.

2.5.1 Variable staggered grid sizes

Despite of the numerical method applied, the physical model dimensions need to be discretized on a numerical grid. The staggered-grid TDFD scheme, as introduced to seismology by Madariaga (1976); Virieux (1984), uses two spatially staggered grids that have a unique spatial discretization for each spatial dimension. Spatial staggering of grids reduces the computational cost (though it is small compared to what we are aiming) and

enhances the stability of the FD simulation since derivative approximations are always spatially centred with respect to the information used from neighbouring grid points (Virieux, 1984).

Pitarka (1999) extended the staggered grid geometry to allow the variation of the spatial grid size in the model. The order of the derivative discretization (and therefore its numerical accuracy) depends entirely on the number of grid points used in the FD approximations, but not on their spatial location. Therefore, the derivative operator coefficients were shifted to the corresponding grid nodes after discretization. Other approaches combined FD grids of different spatial resolution corresponding to the major complexities in the model (Moczo, 1980; Jastram and Behle, 1992). The approaches developed, either continuously varied the spatial grid size (Moczo, 1980), or changed the grid-node distance at a certain depth (grid size $\times 2$ or $\times 3$) corresponding to wave speed changes in the model (Jastram and Behle, 1992). However, these approaches require manual discretization changes from one grid step size to another by a passage through a transition zone where parameters are mapped between the different grids. Although, these grid changing techniques do enhance the computational performance of FD simulations, they are not sufficiently adequate, in terms of variability, for strongly complex heterogeneous model structures.

2.5.2 Curved discretization

One of the main difficulties of FD methods is the correct simulation of a free surface including topography i.e., the contact between the solid earth and air (Kristek et al., 2002). Standard FD schemes refine the numerical grid in the vicinity of the free surface and discretize the topography by fine sampled staircases (Robertsson, 1999). Even though this approach gives acceptable results, another possibility to adapt the computational grid to a complex model structure, such as the free surface with topography, is the expansion of the PDE on Curvilinear grids rather than Cartesian grids. Then, the numerical grid can be designed such that it perfectly *fits* the geometry of the surface model, and therefore eliminates artefacts due to artifical staircase approximations.

Hestholm and Ruud (1998) in seismology and Xie et al. (2002) for electric circuits formulated staggered FD methods on Curvilinear grids for arbitrary topographies without any grid refinement involved, though the surface variations are limited to smooth variations only. The exact verification of the free surface boundary conditions are obtained through a transformation of the standard rectangular grid to a curved grid, such that the vertical coordinate axis is locally normal to the surface. Then, the grid perfectly matches the topography of the free surface and no further grid refinement or staircases are needed to guarantee correct differencing near and on the surface. The results shown so far are promising, but still require a detailed verification and/or comparisons with already established analytic solutions.

2.5.3 Discussion

Although FD methods defined on several spatial grids significantly enhance the computational efficiency of a wave propagation simulation, the *manual* wave-field transfer from one grid to another is critical and rather complicated. Moreover, the user has to determine the regions where to refine the spatial stepping before the modelling starts. Ideally, we would desire a simple and accurate strong formulation, like the FD scheme, to verify the PDE on discrete grid points. The numerical scheme should automatically refine the spatial grid-stepping during wave propagation through the model, with respect to local model properties as well as the wave-field behaviour.

2.6 Weak formulations

The weak formulation of a PDE is often constructed using a variational argument of a minimisation problem, and is referred to as the *variational formulation* of the differential equation. I consider solutions to the linear hyperbolic wave problem:

$$\rho(x) \cdot u_{tt}(x,t) - \nabla \cdot [\mu(x) \nabla u(x,t)] = f(x,t) \quad in \quad \Omega \times (0,T) \tag{2.14}$$

and the following first-order absorbing boundary conditions:

$$\sqrt{\mu(x)\rho(x)} \cdot u_t(x,t) + \mu \nabla u(x,t) \cdot \boldsymbol{n} = 0 \quad on \quad \Gamma \times (0,T) \tag{2.15}$$

and initial conditions on displacements and velocities:

$$u(x,0) = u_0(x), \quad u_t(x,0) = u_1(x) \tag{2.16}$$

where Ω is the model domain with the boundary Γ, $(0,T)$ a time interval, ρ the medium density, μ the Shear modulus, f the source function, and $u(x,t)$ the unknown wave-field. Time derivatives are denoted by underscore u_t.

If I now assume V to be a space of functions over Ω, then I can multiply both sides of Equation 2.14 by a testing function $v \epsilon V$, and integrate over the domain Ω using Green's theorem to transform integrals. The variational formulation is then

$$\begin{aligned} &\int_\Omega \rho(x) u_{tt}(x,t) v(x) dx + \int_\Omega \mu(x) \nabla u(x,t) \nabla v(x) dx + \\ &\int_\Gamma \sigma u_t(\xi,t) v(\xi) d\xi = \int_\Omega f(x,t) v(x) dx \end{aligned} \tag{2.17}$$

where I simplified $\sigma = \sqrt{\mu(x)\rho(x)}$. Equation 2.17 is similar to Equation 2.14 in taking for $t > 0$ the variation with respect to all testing functions v of a given space. The wave equation is solved approximately by determining integrals over inspected sub-domains, which is less ambitious compared to strong formulations that exactly verify the equation on discrete grid nodes.

Typical weak formulations of PDEs are finite-elements (Zienkiewicz and Morgan, 1982) and spectral-elements (Patera, 1984) techniques. One of the main advantages over strong formulations is that the PDE is discretized over the inspected volume of interest through a sub-division in a number of elements of irregular size and location, such that the volume is sampled in an optimal way. Although the distribution and size of elements is free up to certain limits, the elements are based on one geometrical form (e.g., triangulars). Still, the possibility to perform computations on geometrically optimised numerical grids that perfectly match e.g., the free-surface with topography in seismology, is very powerful. Moreover, the weak formulation allows numerical errors to be restricted to local sub-domains, which in effect gives almost dispersion-free wave-field propagation simulations.

In an ideal wave-field simulation, the elements are constructed to perfectly match the complex structure of the model volume. The accuracy of the PDE expansion on the discrete FE-grid depends on constraints of the testing functions used in the variational formulation. In other words, a FE discretization is constructed for a specific accuracy requirement. Then, the numerical grid has to be constructed to guarantee that the numerical error stays in the pre-defined accuracy-bands during wave propagation. When the grid has been constructed correctly, the FE simulation gives exact modelling results up to a desired grid-accuracy.

Although FE modelling schemes have been used for a long time, it was only recently that Faccioli et al. (1996) and later Komatitsch and Vilotte (1998) and Komatitsch and Tromp (1999) developed a FE scheme for seismic wave propagation simulations. Their schemes allow exact propagation of surface waves with topography, fluid-solid interfaces, and anisotropy. Moreover, the spectral element approach presented, easily adapts to fast implementation schemes using domain decomposition on parallel computer structures. Komatitsch and Tromp (2001) recently even extended the SE approach to perform seismic wave propagation modellings in a complete Earth model up to a frequency of $f = 1Hz$.

Finite-element methods require the numerical grid to be constructed before the modelling starts. In general, this is not a simple task. The generation of an adequate mesh controls the accuracy of the weak formulation (Sambridge et al., 1995), and therefore becomes a key step of the modelling procedure. In case the mesh is not constructed correctly or includes small errors, it can not be resolved by the user during the modelling nor by analysing the results after the simulation has terminated. The problematic of constructing the best adapted grid for a wave propagation simulation is discussed further in the following.

2.7 Average formulations

The third group of possible PDE discretization schemes is denoted by *average formulations* or more popular finite-volume methods, because they incorporate well-known developments of both, strong- and weak-formulations of PDEs. In general, the model domain is sub-divided into finite volumes of sufficiently small size, such that wave-field and physical model parameter variations stay small in the local volume. Then, wave-field

solutions may be obtained by expressing volume integrals over sub-domains Ω_i as surface integrals, again using Green's theorem. The accuracy of the chosen average formulation depends then on the number of sub-domains and the accuracy of the numerical integration scheme applied. An elastic wave-field propagation simulation using a FV methods has been shown by Dormy and Tarantola (1995) and more recently using the, so called *grid-method* for 2D and 3D media by Jianfeng and Tielin (1999, 2002).

2.8 Time discretization

All of the above mentioned PDE formulations require, in addition to the spatial discretization step, a discrete time stepping in order to propagate the wave-field solution with respect to time. The exception are spectral methods where time-dependencies are eliminated by the transformation in the spectral domain.

Despite of the actual time evolution scheme applied, the time step is uniquely defined before the modelling starts, such that stable wave propagation is guaranteed. Clearly, a unique time stepping is the simplest approach. Ideally, we would like discrete time evolution steps to vary with respect to the local complexity in the model and the behaviour of the wave-field solution. For example, the unique temporal discretization of a TDFD wave propagation simulation in a model having a high-velocity contrast structure is governed by the high velocities in order to allow a stable simulation. This creates significant temporal oversampling in lower-velocity zones, which means CPU-time is wasted.

Following spatial connections of numerical grids, Falk et al. (1998) and later Tessmer (2000) introduced a FD time adaptive scheme that allows different time steps for different regions in the model. The change from one time step to another is performed by a passage through a transition zone that adapts the numerical scheme to the new time stepping. As for manual spatial grid combinations, the temporal adaption is static in that the user has to determine the regions of the model where to refine or coarse the time step, before the modelling starts. Moreover, this kind of time adaptivity can only be applied reasonably for nicely separated regions in the model, since the passage from one set of spatial and temporal grid parameters to another is costly and may alter the computed wave-field solution. Although manually changing the grid stepping is a clear step forward compared to a unique temporal step, strongly heterogeneous model structures still require more dynamic time stepping adaption.

Chapter 3

Frequency Domain Modelling through a Staggered Finite Difference Analysis

Bernhard Hustedt, Stephane Operto and Jean Virieux
UMR Geosciences Azur, CNRS-UNSA-UPMC 250, rue Albert Einstein - Sophia Antipolis, 06560 Valbonne, France
Manuscript submitted to Geophysical Journal International

3.1 Résumé

Dans ce chapitre, nous comparons une nouvelle approche de modélisation des ondes dans le domaine fréquence-espace 2D acoustique utilisant des schémas aux différences finies en quinconce avec une approche fréquentielle plus communément utilisée fondée sur la combinaison de schémas discrétisés suivant deux systèmes d'axe tournés de 45 degrés (schémas tournés). La comparaison des deux approches est fondée sur une analyse analytique de dispersion classique et sur des simulations numériques dans des milieux 2D homogènes et hétérogènes.

Pour des approximations des dérivées spatiales du quatrième ordre, les schémas en quinconce contiennent 13 coefficients non nuls. Ces schémas seront dénommés *croix 13-points* en raison de leur architecture en forme de croix dans l'espace spatial bidimensionnel. Le schéma obtenu par combinaison de deux systèmes d'axe tournés ne contient que 9 coefficients. Ces schémas sont dénommés *étoile 9-points* en raison de leur forme en étoile résultant de la discrétisation suivant un repère tourné de 45 degrés.

Le problème numérique associé à une modélisation dans le domaine fréquence-espace est la résolution d'un système matriciel de type $\mathbf{Ax}=\mathbf{b}$, ou $\mathbf{A}$ est la matrice d'impédance dont les coefficients dépendent de la fréquence et des paramètres physiques du milieu, $\mathbf{x}$ le champ d'onde pour une fréquence donnée, $\mathbf{b}$ et la source externe. La matrice $\mathbf{A}$ à coefficients complexes est bande diagonale avec 2 franges. Le champ d'onde exact est calculé sur une grille numérique donnée en appliquant une factorisation LU de la

matrice d'impédance. On utilise une approche de factorisation basée sur une méthode multi-frontale optimisée.

En terme de précision numérique, les deux schémas conduisent à des résultats équivalents. En terme de temps calcul et de stockage mémoire, l'approche sur des grilles en quinconce se révèle moins performante en raison du nombre plus élevé de coefficients non nuls dans le schéma et de la répartition moins compacte de ces coefficients dans la matrice d'impédance (distance entre la bande diagonale et une frange de la matrice).

J'en conclus que la discrétisation suivant des grilles tournées doit être utilisée pour des simulations 2D. Par ailleurs, cette analyse suggère que l'approche utilisant des grilles tournées devrait être explorée pour des modélisations par différences finies dans le domaine temps-espace.

Dans le cas 3D, le schéma tourné conduit à une étoile constituée de 27 coefficients. Par contre, le schéma utilisant une structure en quinconce contient seulement 19 coefficients. Néanmoins, la distance entre franges reste supérieure par rapport au cas du repère tourné. Par conséquence, je suggère que les performances, en termes de précision numérique et de stockage mémoire, des deux types de discrétisation doivent être examinées dans le futur.

3.2 Abstract

We compare a new finite-difference scheme for 2D acoustic frequency domain forward modelling based on a staggered grid geometry with the standard finite-difference frequency domain grid rotation approach. The deduced staggered cross stencil is examined for both the wavelength content and azimuthal variation. For fourth-order derivative approximations, the staggered grid geometry leads to a 13-points cross stencil. Comparisons to the 9-points star stencil that results from the grid rotation approach are shown for 2D homogeneous and heterogeneous media. Wave-field solutions are computed using a direct matrix solver based on an optimized multi-frontal method. Both stencils give similarly accurate results, though the 13-points stencil is less efficient in terms of memory- and CPU-time requirements, because of its enlarged spatial size and increased number of coefficients. Therefore, the grid rotation approach is superior for 2D modelling and its usage for time domain finite-difference modelling should be investigated. For 3D modelling the staggered grid geometry leads to a 19-points cross stencil while grid rotation gives a star incorporating 27-points. Therefore, the conclusions for 2D frequency domain finite-difference modelling might not be valid for 3D modelling.

3.3 Introduction

Modelling seismic wave propagation is essential to understand complex wave phenomena in realistic heterogeneous medium. Numerical results from finite-difference (FD) modelling are particularly useful since they provide the complete wave-field response.

Frequency domain forward modelling is of special interest for multi-source experiments because of its computational efficiency (Štekl and Pratt, 1998). Moreover, a realistic rheology is easily incorporated in the modelling scheme by introducing complex, frequency

dependent velocities. The key step in frequency domain finite-difference (FDFD) modelling that controls computational efficiency is the numerical inversion of a massive matrix equation.

In recent years, computational efficiency has been increased by enhancing the numerical accuracy of the modelling scheme. Pratt and Worthington (1990) applied second-order spatial derivative approximations in two dimensions using the so called '5-points' stencil. This scheme required 10 grid points per shortest wavelength in order to perform accurate FD modelling. Jo et al. (1996) reduced the number of grid points per shortest wavelength to about 4, by including additional surrounding grid points for the derivative approximations. They combined the 2^{nd}-order wave equation discretized on a Cartesian grid and a 45^o degree rotated grid. The two combined grids lead to a computational stencil that will be called the '9-points star stencil' in the following, because of its star geometry. The optimal coupling of the two grids is the crucial step in this approach and leads to significant improvements of matrix inversions and accurate wave-field constructions.

Following time domain finite-difference (TDFD) developments (Madariaga (1976), Virieux (1984)), we investigate effects of FD staggered grid stencils in the frequency domain instead of directly constructing star stencils through grid rotations. We consider a frequency-space FD scheme (1^{st}-order hyperbolic system) where derivatives are discretized using either second-order or fourth-order spatially staggered difference stencils. As for the grid rotation approach, staggered stencils combine neighboring points for derivative approximations, though now the combination of surrounding points comes automatically with the staggered stencil interpolation. No further ad-hoc optimization procedure is required in order to combine neighboring points in Cartesian and rotated grids, as is necessary in the star stencil strategy to reduce anisotropy of the numerical dispersion. Still, one may perform a differential operator optimization as suggested by Holberg (1987). The staggered stencil construction is the first point we want to analyze in this paper.

The complex matrix that appears in two-dimensional frequency domain modelling using the staggered stencil approach with PML absorbing boundary conditions (Perfectly Matched Layer (see Berenger, 1994)) contains $(nx \cdot nz)^2$ elements of which $13 \cdot nx \cdot nz$ are non zero in the case of fourth-order derivative approximations. We denote the model dimensions in number of grid points for a 2D medium by nx and nz. For second-order derivative approximations, the grid rotation strategy and the staggered stencil strategy, named cross stencil because of its shape, give equivalent results. That is, both discretization scheme result in the same 5-points stencil. Note, only for the staggered cross stencil approach, PML conditions can be implemented correctly. Wave-field solutions at each source position for each frequency component are computed by a direct multi-frontal solver technique developed by Davis and Duff (1997).

In this paper, we show the equivalence between the second-order FD staggered cross stencil and the standard 5-points star stencil. Further we formulate the FD staggered cross stencil strategy for fourth-order derivative approximations. We shall compare the deduced fourth-order staggered cross stencil with the usual 9-points star stencil. Numerical dispersion is investigated for both the wavelength content and azimuthal variation. We illustrate results on an example of frequency domain seismic wave propagation in

2D homogeneous and heterogeneous media. Finally, we briefly discuss implications of the staggered- and rotated-grid formulations for FDFD modelling in 3D heterogeneous media.

3.4 9-points star strategy

We give a brief summary of the 9-points star strategy for the two-dimensional, 2^{nd}-order acoustic wave equation (Equation (3.1)). Details can be found in Jo et al. (1996). We write the 2^{nd}-order acoustic wave equation as

$$\begin{aligned} &\frac{\partial}{\partial x}\{\frac{1}{\rho(x,z)}\ \frac{\partial}{\partial x}\ P(x,z,\omega)\}\ +\ \frac{\partial}{\partial z}\{\frac{1}{\rho(x,z)}\ \frac{\partial}{\partial z}\ P(x,z,\omega)\} \\ &-\ \frac{\omega^2}{K(x,z)}\ P(x,z,\omega)\ =\ S(x,z,\omega) \end{aligned} \tag{3.1}$$

where ρ is the density, K the Bulk modulus, ω the angular frequency, P the pressure wave-field, and S the external source.

Partial derivatives are discretized using the 5-points stencil strategy. That is, conventional second-order, centered, finite-differences are used throughout (Kelly et al., 1976). Numerical dispersion, quite important along bissectrices, is further suppressed by adding four additional points to the 5-points stencil (see Figure 3.1). The combination of derivative approximations on the 5-points stencil (Cartesian grid) and the four additional corner points (45^o degree rotated grid) leads to the 9-points star stencil. Averaging coefficients (a, b, c, and d) account for the coupling between the Cartesian (black dots) and the four additional points on the rotated grid (white dots). Moreover, the mass acceleration term $\omega^2/K(x,z)$ is approximated using a weighted average over the 9-points star stencil similar to the lumped mass approach in finite-element modelling (Zienkiewicz and Morgan, 1982). Numerical accurate results up to 4 points per shortest wavelength are guaranteed by an optimization technique that determines the averaging coefficients such that the velocity dispersion is minimized, as has also been done for the TDFD approach (Holberg, 1987). The Cartesian and rotated equations are numerically combined to

$$a \cdot A\ +\ (1-a) \cdot B\ +\ C = S \tag{3.2}$$

where A represents the derivative approximations on the 5-points stencil, B equivalent of A but on the rotated grid, C the mass acceleration term that depends on the averaging coefficients b, c, and d, and S the external source.

We discretize the 9-points star on the Cartesian and the rotated grid including artifical

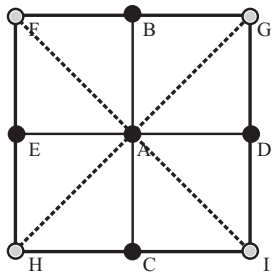

Figure 3.1: The 9-points star stencil consists of the standard FD 5-points stencil (black dots) and four corner points (grey dots on rotated grid). Derivatives are discretized on both the 5-points stencil and the additional points using second-order centered differences throughout. Optimal combination of the 5-points stencil and the additional surrounding points together with the a lumped mass procedure leads to the 9-points-star-stencil that assures numerical accuracy up to a minimum of 4 points per shortest wavelength.

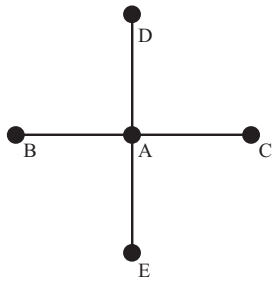

Figure 3.2: The 5-points cross stencil that results from second-order staggered differences discretization of the wave equation written as first-order hyperbolic system of equations.

PML absorbing boundary conditions in the medium.

$$\begin{aligned}\frac{-\omega^2}{K_{i,j}}P_{i,j} &= \frac{1}{\Delta x^2}\{\frac{1}{\xi_{x_i}}(\frac{1}{\xi_{x_{i+1/2}}\cdot\rho_{i+1/2,j}}(P_{i+1,j}-P_{i,j}) \\ &\quad -\frac{1}{\xi_{x_{i-1/2}}\cdot\rho_{i-1/2,j}}(P_{i,j}-P_{i-1,j}))\} \\ &+ \frac{1}{\Delta z^2}\{(\frac{1}{\xi_{z_j}}(\frac{1}{\xi_{z_{j+1/2}}\cdot\rho_{i,j+1/2}}(P_{i,j+1}-P_{i,j}) \\ &\quad -\frac{1}{\xi_{z_{j-1/2}}\cdot\rho_{i,j-1/2}}(P_{i,j}-P_{i,j-1}))\}+S_{i,j}\end{aligned} \tag{3.3}$$

where $\xi_i = 1 + i\gamma_i/\omega$ and $\xi_j = 1 + i\gamma_j/\omega$ denote the PML contributions that depend on one spatial dimension only. PML functions at intermediate grid node positions are computed by averaging over the neighboring points $\gamma_{x_{i+1/2}} = 1/2 \cdot (\gamma_{x_i} + \gamma_{x_{i+1}})$. Within

the PML layers only the 5-points stencil is used (see Figure 3.2):

$$\begin{aligned}
A = \frac{-\omega^2}{K_{i,j}} &- \frac{1}{\Delta x^2 \cdot \xi_i}\left(\frac{1}{\xi_{i+1/2} \cdot \rho_{i+1/2,j}} + \frac{1}{\xi_{i-1/2} \cdot \rho_{i-1/2,j}}\right) \\
&- \frac{1}{\Delta z^2 \cdot \xi_j}\left(\frac{1}{\xi_{j+1/2} \cdot \rho_{i,j+1/2}} + \frac{1}{\xi_{j-1/2} \cdot \rho_{i,j-1/2}}\right) \\
B = &- \frac{1}{\Delta z^2}\frac{1}{\xi_j}\frac{1}{\xi_{j-1/2} \cdot \rho_{i,j-1/2}} \\
C = &- \frac{1}{\Delta z^2}\frac{1}{\xi_j}\frac{1}{\xi_{j+1/2} \cdot \rho_{i,j+1/2}} \\
D = &- \frac{1}{\Delta x^2}\frac{1}{\xi_i}\frac{1}{\xi_{i+1/2} \cdot \rho_{i+1/2,j}} \\
E = &- \frac{1}{\Delta x^2}\frac{1}{\xi_i}\frac{1}{\xi_{i-1/2} \cdot \rho_{i-1/2,j}} \\
F = G &= H = I = 0
\end{aligned} \tag{3.4}$$

Equation (3.2) is recast into a matrix-type equation of the form $M \cdot P = S$, where M is the so called Impedance Matrix, P the pressure wave-field (desired solution), and S the source. The matrix M is complex valued and depends on the physical model parameters: the density ρ, the bulk modulus K, and the angular frequency ω. The full matrix contains $(nx \cdot nz)^2$ elements of which $9 \cdot nx \cdot nz$ are different from zero. The non-zero elements are distributed on the diagonal and two adjacent bands. The bandwidth (which is more or less full of zeros) is approximately $2 \cdot nz + 1$.

In standard FDFD modelling, the optimization coefficients a, b, c, and d are determined through fitting dispersion curves for a homogenous model before the forward modelling is started. Then the complex matrix can be constructed and is factorized into its LU-factors. Pressure wave-field solution for each source position and frequency component are computed separately. Clearly, the LU decomposition needs to be computed only once for each frequency component, making this approach very appealing especially for multi-source experiments (Pratt and Worthington, 1990). For example, the complex impedance matrix construction and subsequent LU-factorization for one frequency component f_j requires 98% CPU-time (10% matrix construction + 88% matrix factorization) while the solve phase ($(LU_{f_j}) \cdot x_{f_j} = b^i_{f_j}$) for one source position b^i only needs 2% CPU-time.

3.5 Staggered stencil strategy

3.5.1 Staggered versus star stencils

The grid rotation approach (we also call it the star-stencil-strategy) is the state-of-the-art tool applied in FDFD modelling to numerically represent derivative approximations

(Štekl and Pratt, 1998). In contrast to this approach, we investigate a staggered-cross-stencil strategy which has been developed up to the present mainly in the time domain. The leap-frog structure of the grid maintains accurate derivative estimations and good performance for numerical dispersion. The staggered grid formulation leads to simple FD discretizations of 1^{st}-order hyperbolic systems of equations. Moreover, this formulation provides guidelines for constructing FD discretizations of 2^{nd}-order hyperbolic systems when one requires high computer memory performance (Luo and Schuster, 1990).

We assume that first derivatives are discretized using conventional second-order, centered first difference stencils $(-0.5, 0, 0.5)$ on a non-staggered grid. Then, impulsive point source excitation automatically leads to two un-coupled staggered grids. One grid is associated with the source node point, while the other one is left unexcited by the stencil (see Figure 3.3a). This intrinsic feature of centered, second-order derivative approximations was the reason to cancel out the unexcited grid, which has led to the staggered grid geometry formulation in seismology (Madariaga (1976), Virieux (1984)).

In Figure 3.3b and 3.3c we show two frequency maps ($f = 10Hz$) computed in a homogeneous two-dimensional media with PML absorbing boundary conditions on all edges of the model. Figure 3.3b approximates spatial derivatives using the stencil represented in Figure 3.3a on a non-staggered grid. Clearly visible are the grey spaces that correspond to the non-excited second grid. Figure 3.3c is the same wave propagation example but now using the staggered derivative operator. The unexcited grid is cancelled out. When considering fourth-order derivative approximations, the centered FD-stencil $(1/12, -2/3, 0, 2/3, -1/12)$ on a non-staggered grid does not automatically lead to un-coupled staggered grids (see Figure 3.3d). The extension from second-order to fourth-order approximations, namely the additional coefficient $\pm 1/12$ in the stencil, weakly couples the two existing grids and creates expected numerical dispersion. This weak coupling is cancelled out when considering the star stencil approach. One may consider only centered stencils, such as the fourth-order staggered grid stencil $(1/24, 0, -9/8, 0, 9/8, 0, -1/24)$. If this stencil is applied to a full non-staggered grid, only the ad-hoc staggered grid is correctly excited (see Figure 3.3e). The second sub-grid is left untouched, giving the desired staggered grid feature in this FD approximation. The complete staggered stencil in two dimensions for the velocity-stress FD scheme is shown in Figure 3.3f.

Again, let us mention that the full grid formulation of the fourth-order system requires the star stencil geometry for both time and frequency approaches, although the star stencil has been developed for the frequency domain formulation and the staggered stencil for the time domain formulation.

3.5.2 Second-order staggered cross stencil construction

We develop the staggered cross stencil for second-order derivative approximations. We formulate the wave equation as a 1^{st}-order hyperbolic system of equations. This system is discretized using strict centering of FD derivatives throughout.

We write the 1^{st}-order hyperbolic system of equations with PML absorbing boundary conditions as:

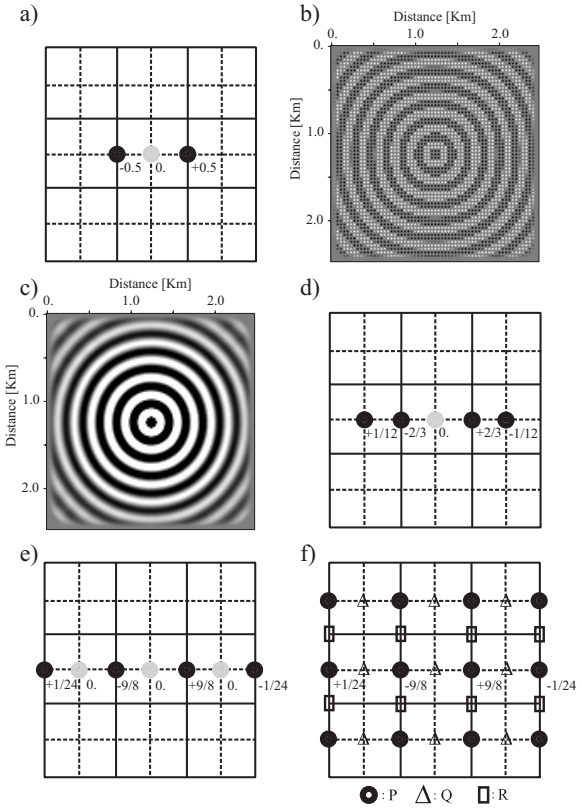

Figure 3.3: (a) Second-order centered difference stencil (-0.5,0,0.5) on a non staggered grid. Impulsive punctual source excitation automatically leads to two un-coupled staggered grids. One grid is associated with the source node point (dashed line), while the other grid is left unexcited by the stencil (continuous line). (b) We show a frequency map (f=10Hz) computed in a homogeneous two-dimensional media with PML absorbing boundary conditions on all edges of the model where spatial derivatives are approximated using the stencil represented in Figure 3.3a on a non-staggered grid. Clearly visible are the grey spaces that correspond to the non-excited grid. (c) is the same wave propagation example as (b) but now using the corresponding staggered derivative operator. (d) Standard fourth-order centered difference stencil (1/12,-2/3,0,2/3,-1/12). The stencil weakly couples the two existing grids and therefore creates spurious noise. (e) Fourth-order staggered difference stencil (1/24,0,-9/8,0,9/8,0,-1/24) which correctly excites one grid only while leaving the second grid untouched. (f) Fourth-order staggered difference stencil for the first-order hyperbolic acoustic wave equation.

$$
\begin{aligned}
\frac{\partial P_x(x,z,t)}{\partial t} + \gamma_x(x) P_x(x,z,t) &= K(x,z) \cdot \frac{\partial Q(x,z,t)}{\partial x} + S(x,z,t) \\
\frac{\partial P_z(x,z,t)}{\partial t} + \gamma_z(z) P_z(x,z,t) &= K(x,z) \cdot \frac{\partial R(x,z,t)}{\partial z} \\
\frac{\partial Q(x,z,t)}{\partial t} + \gamma_x(x) Q(x,z,t) &= b(x,z)\left(\frac{\partial P_x(x,z,t)}{\partial x} + \frac{\partial P_z(x,z,t)}{\partial x}\right) \\
\frac{\partial R(x,z,t)}{\partial t} + \gamma_z(z) R(x,z,t) &= b(x,z)\left(\frac{\partial P_x(x,z,t)}{\partial z} + \frac{\partial P_z(x,z,t)}{\partial z}\right)
\end{aligned}
\tag{3.5}
$$

where we introduced two wave-fields P_x and P_z to account for the PML absorbing boundary conditions (see Operto et al., 2002). The damping functions are denoted by γ_x and γ_z. We note that the new wave-fields can be combined into the physical P wave-field through simple addition $P(x,z,t) = P_x(x,z,t) + P_z(x,z,t)$. We transform the system of equations in the Fourier domain and introduce the new variables $\xi_x(x) = 1 + i\gamma_x(x)/\omega$ and $\xi_z(z) = 1 + i\gamma_z(z)/\omega$.

$$\begin{aligned}
\frac{-i\omega\xi_x(x)}{K(x,z)}P_x(x,z,\omega) &= \frac{\partial Q(x,z,\omega)}{\partial x} + S(x,z,\omega) \\
\frac{-i\omega\xi_z(z)}{K(x,z)}P_z(x,z,\omega) &= \frac{\partial R(x,z,\omega)}{\partial z} \\
-i\omega Q(x,z,\omega) &= \frac{1}{\xi_x(x)\rho(x,z)}\frac{\partial P(x,z,\omega)}{\partial x} \\
-i\omega R(x,z,\omega) &= \frac{1}{\xi_z(z)\rho(x,z)}\frac{\partial P(x,z,\omega)}{\partial z}
\end{aligned} \tag{3.6}$$

We discretize the system of equations using a second-order, spatially staggered stencil (see Virieux, 1984) and introduce effective medium parameters for the density and the Bulk modulus (see Graves, 1996). This and the following algebraic computations are shown in Appendix A. After discretizing the system of equations (see Equations (A. 2) and (A. 3)), parsimonious elimination of equations depending on Q and R (Luo and Schuster, 1990) leads to two equations that depend on P_x and P_z only (see Equation (A. 4)). We then re-combine P_x and P_z and get the staggered grid finite difference equation with PML absorbing boundary conditions for the pressure field P (see Equation (3.7) and Equation (A. 5)).

$$\begin{aligned}
\frac{-\omega^2}{K_{i,j}}P_{i,j} = \quad & \tfrac{1}{\xi_{xi}} \cdot \frac{1}{\Delta x^2}\Big[\frac{1}{\xi_{xi+1/2}\cdot\rho_{i+1/2,j}}\cdot(P_{i+1,j} - P_{i,j}) \\
& - \frac{1}{\xi_{xi-1/2}\cdot\rho_{i-1/2,j}}\cdot(P_{i,j} - P_{i-1,j})\Big] \\
+ \quad & \tfrac{1}{\xi_{zj}} \cdot \frac{1}{\Delta z^2}\Big[\frac{1}{\xi_{zj+1/2}\cdot\rho_{i,j+1/2}}\cdot(P_{i,j+1} - P_{i,j}) \\
& - \frac{1}{\xi_{zj-1/2}\cdot\rho_{i,j-1/2}}\cdot(P_{i,j} - P_{i,j-1})\Big] \\
+ \quad & S_{i,j}
\end{aligned} \tag{3.7}$$

We compare our new 5-points staggered cross stencil with the standard 5-points stencil used by Pratt and Worthington (1990, pp. 306). They discretized the 2^{nd}-order hyperbolic wave equation using standard centered differences given by Kelly et al. (1976). The 5-points stencil and the new 5-points staggered cross stencil give similar density weightings for the points used in the stencil. Therefore, both 5-points stencils are equivalent, though the staggered one was obtained through strict centered differencing throughout.

3.5.3 Fourth-order staggered cross stencil construction

Exactly in the same way as we constructed the 5-points staggered cross stencil for second-order derivative approximations, we introduce the 13-points staggered cross stencil that propagates wave-field solutions with fourth-order accuracy (details are given in Appendix B).

We apply the same procedure as before and obtain for the P-wave-field:

$$
\begin{aligned}
\frac{-\omega^2}{K_{i,j}}P_{i,j} \quad = \quad & \frac{1}{\Delta x^2 \cdot \xi_i}\{ \\
& \frac{9}{8}\{\frac{1}{\xi_{xi+1/2} \cdot \rho_{i+1/2,j}}\{\frac{9}{8}(P_{i+1,j} - P_{i,j}) - \frac{1}{24}(P_{i+2,j} - P_{i-1,j})\} - \\
& (\frac{1}{\xi_{xi-1/2} \cdot \rho_{i-1/2,j}}\{\frac{9}{8}(P_{i,j} - P_{i-1,j}) - \frac{1}{24}(P_{i+1,j} - P_{i-2,j})\}\} - \\
& \frac{1}{24}\{\frac{1}{\xi_{xi+3/2} \cdot \rho_{i+3/2,j}}\{\frac{9}{8}(P_{i+2,j} - P_{i+1,j}) - \frac{1}{24}(P_{i+3,j} - P_{i,j})\} - \\
& (\frac{1}{\xi_{xi-3/2} \cdot \rho_{i-3/2,j}}\{\frac{9}{8}(P_{i-1,j} - P_{i-2,j}) - \frac{1}{24}(P_{i,j} - P_{i-3,j})\}\} \\
& + \frac{1}{\Delta z^2 \cdot \xi_j}\{ \\
& \frac{9}{8}(\frac{1}{\xi_{zj+1/2} \cdot \rho_{i,j+1/2}}\{\frac{9}{8}(P_{i,j+1} - P_{i,j}) - \frac{1}{24}(P_{i,j+2} - P_{i,j-1})\} - \\
& (\frac{1}{\xi_{zj-1/2} \cdot \rho_{i,j-1/2}}\{\frac{9}{8}(P_{i,j} - P_{i,j-1}) - \frac{1}{24}(P_{i,j+1} - P_{i,j-2})\}\} - \\
& \frac{1}{24}\{\frac{1}{\xi_{zj+3/2} \cdot \rho_{i,j+3/2}}\{\frac{9}{8}(P_{i,j+2} - P_{i,j+1}) - \frac{1}{24}(P_{i,j+3} - P_{i,j})\} - \\
& (\frac{1}{\xi_{zj-3/2} \cdot \rho_{i,j-3/2}}\{\frac{9}{8}(P_{i,j-1} - P_{i,j-2}) - \frac{1}{24}(P_{i,j} - P_{i,j-3})\})\} \\
& + S_{i,j}
\end{aligned}
\tag{3.8}
$$

We find that the staggered fourth-order derivative approximation requires 13 points in the FD stencil (see Figure 3.4). The system of equations (3.6) is still the 1^{st}-order hyperbolic staggered system, while the equation (3.7) is the corresponding 2^{nd}-order staggered equation that can be compared to the 2^{nd}-order star equation (see Equation (3.3)) as noted by Luo and Schuster (1990).

3.6 Solutions for the matrix equation

We compute wave-field solutions for each source position and each frequency component by solving the corresponding matrix equation through an optimized minimum order scheme developed by Davis and Duff (1997). In case of fourth-order derivative approximations, the 13-points staggered cross stencil gives a matrix M that contains $(nx \cdot nz)^2$

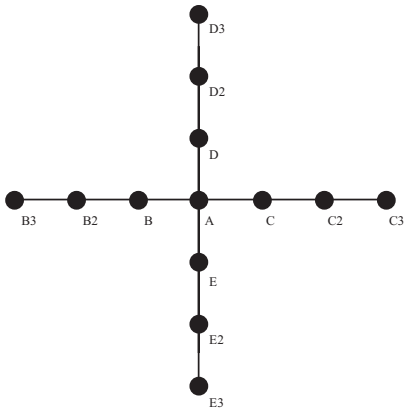

Figure 3.4: The 13-points cross stencil that results from fourth-order staggered differences discretization of the wave equation written as first-order hyperbolic system of equations.

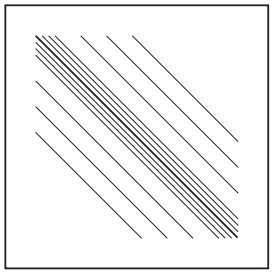

Figure 3.5: Structure of the complex impedance matrix that results from fourth-order staggered cross stencil discretization of the parsimonious second-order hyperbolic acoustic wave equation. The matrix contains $(nx \times nz)^2$ elements from which $13 \times nx \times nz$ are non-zero. The elements are distributed along the diagonal, 6 bands close to the main diagonal (z-derivatives), and 6 parallel adjacent bands further away from the diagonal (x-derivatives). The overall bandwidth of the matrix is approximately $6 \times nz$.

elements from which $13 \cdot nx \cdot nz$ are non-zero. The elements are distributed along the main diagonal (7 coefficients) and 6 adjacent parallel bands. The structure of the matrix is shown in Figure 3.5. The bandwidth of the matrix is $6 \cdot nz$, which is approximately 3 times larger than the matrix-bandwidth resulting from the grid rotation approach. The matrix appearing in the 1^{st}-order PML formulation increases the number of non-zero coefficients for the same model configuration, since 13 points instead of 9 points are used for derivative approximations. Therefore, increasing the matrix bandwidth and number of non-zero coefficients results in higher memory demands for the matrix ordering scheme.

For 3D modelling the situation is a different one. The corresponding computational star that results from grid rotation in 3D medium incorporates 27 points (see Janod, 1999), while the staggered cross stencil is constructed using 19 points only. Neverthe-

less, the matrix bandwidth resulting from cross stencil discretizations exceeds the matrix bandwidth of the star stencil formulation. Despite of 2D or 3D media, this is always true since the staggered cross stencil is less compact than the star stencil. As was noted before, the main features controlling the performance of a matrix factorization are the number of non-zero coefficients and their spatial distribution in the matrix. Therefore, we might expect different memory and computational CPU time requirements for the matrix factorization for 3D FDFD modelling. Note, there exists a model size from which on the star stencil formulation does not allow the construction of the impedance matrix anymore because of limited memory resources available. In this case, the staggered cross stencil might still be able to handle the problem since significantly less coefficients have to be stored. This is subject to future investigations.

3.7 Grid dispersion analysis

The numerical precision of the fourth-order 13-points cross stencil was investigated for both the wavelength content and azimuthal variation. In Figures 3.6 and 3.7, we show dispersion curves for relative phase and group velocity for both the 9-points star strategy and the 13-points cross strategy for plane wave propagation angles ranging from 0^o to 90^o degrees. We used non-optimized fourth-order staggered grid derivative approximations for the cross stencil (Levander, 1988). From Figures 3.6 and 3.7 we find that the 9-points star stencil permits less dispersive wave propagation modelling for the same number of grid nodes per shortest wavelength compared to the 13-points cross stencil. This is true for phase and group velocity dispersion curves. In Appendix C we demonstrate that the staggered cross stencil strategy exactly determines relative phase velocity v_{ph}/v and group velocity equal to 1 ($v_{ph}/v = v_{gr}/v = 1$) for an infinitely fine medium discretization ($1/G \Rightarrow 0$). The grid rotation approach obtains similar results for numerical phase and group velocity, though only approximately. Combining the rotated grids and subsequently optimizing numerical dispersion shifts the dispersion curves. Indeed, dispersion curves are better aligned to the ideal relative medium velocity for higher $1/G$ -ratios (coarser discretization) while at the same time the accuracy for lower $1/G$-ratios is altered. This is observed from relative velocity values at $1/G \rightarrow 0$ for the standard staggered and optimized operators (see Figure 3.7).

A partly similar optimization strategy, first introduced for TDFD modelling by Holberg (1987) can be applied for the staggered cross stencil approach (Arntsen et al., 1998). In their approach, coefficients describing classic staggered derivative operator coefficients are replaced by optimized operator coefficients that are obtained through a dispersion relation minimization technique. An example of the staggered cross dispersion curve optimization is shown in Figure 3.8. As for the grid rotation approach, dispersion curves are shifted to better fit the desired numerical medium velocity at coarse grid discretizations while decreasing accuracy at fine discretizations. In this example the fourth-order staggered grid operator coefficients ($\alpha_1 = 9/8$ and $\alpha_2 = 1/24$) were replaced by $\alpha_1 = 1.13824281853071e^{+00}$ and $\alpha_2 = 4.64142728435701e^{-02}$ which incorporates a final error of $2.53067e^{-06}$. While wave propagation accuracy of both numerical phase

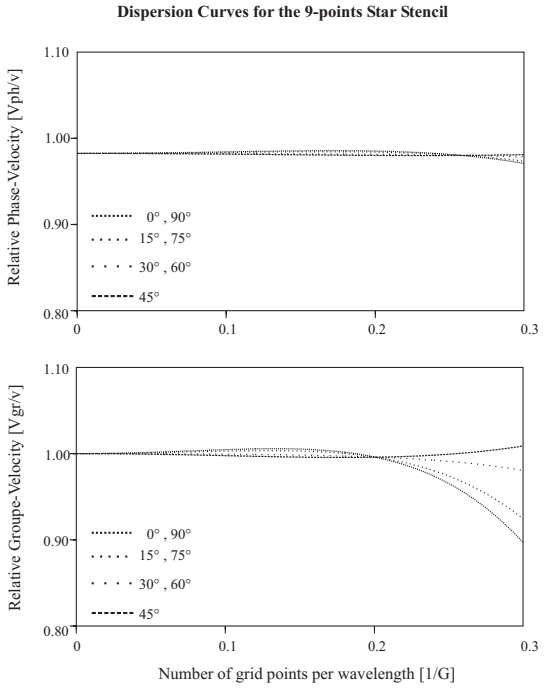

Figure 3.6: Relative phase v_{ph} and group v_{gr} velocity curves for the 9-points star stencil formulation. We used the following optimization coefficients a = 0.5461, c = 0.6248, $d = 0.9381e^{-1}$ and $e = 0.25 * (1 - 4 \times d - c)$. Propagation angles from the vertical are denoted by different types of dashed lines.

and group velocity is increased for coarse grid discretizations, compared to the 9-points star stencil no significant improvements are observed. Note, that any dispersion curve optimization to enhance the numerical accuracy of the modelling scheme is completely optional for the staggered cross stencil approach. In contrast, the grid rotation approach does always require grid coupling, i.e. some kind of optimization strategy in order to provide superior results (Jo et al., 1996).

Altogether, we observe increased numerical distortion due to discretizations for the 13-points cross stencil compared to the 9-points star stencil. This is understandable, since the star stencil not only optimizes the grid coupling but also distributes the algebraic term over the neighboring grid points. As was shown by Jo et al. (1996) the star stencil optimization only results in enhanced dispersion curves when the grid rotation strategy is combined with the lumped mass strategy. Only one of the two procedures decreases numerical accuracy. This star stencil feature, which is the first step to finite-elements, suppresses additional numerical noise and no analogous was developed for the staggered cross stencil approach. Remarkable is the fact that the 9-points star stencil preserves the very compact star geometry while including the maximum amount of existing information in the surroundings of the center point - a clear advantage for numerical FD modelling.

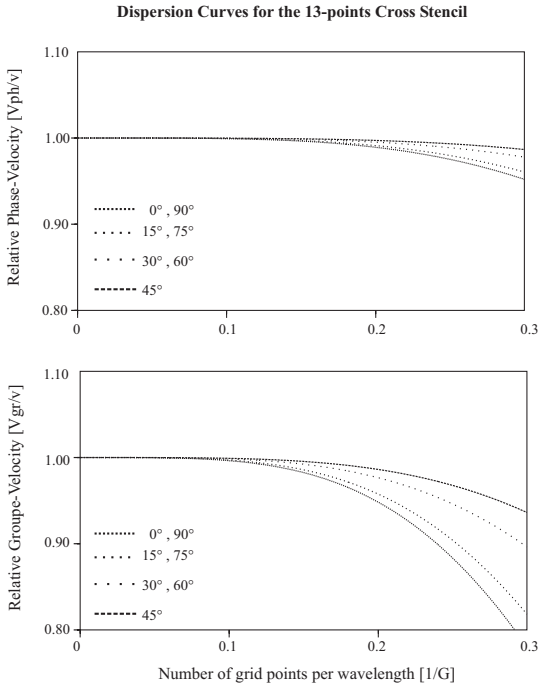

Figure 3.7: Relative phase v_{ph} and group v_{gr} velocity curves for the 13-points cross stencil formulation using standard fourth-order staggered stencils ($\alpha_1 = \frac{9}{8}$ and $\alpha_2 = \frac{1}{24}$). Propagation angles from the vertical are denoted by different types of dashed lines.

3.8 Comparison of the 9-points star stencil and the 13-points cross stencil

3.8.1 The homogeneous half-space model

We first compare the 9-points star stencil with the 13-points staggered cross stencil for a two-dimensional homogeneous media. The velocity is $4000m/sec$ and the density $2500kg/m^3$. The dimension of the model is $4000m$ x $4000m$. The spatial sampling was $40m$, which corresponds to 10 points per shortest wavelength. The source is a smoothed point source located at ($500m$,$1000m$). We used a Gaussian derivative $S(t) = -2\alpha(t - t_0)e^{-\alpha(t-t_0)^2}$ with $\alpha = 200$, $t_0 = 0.31sec$ and a maximum frequency of $10Hz$.

We computed frequency domain solutions for 52 frequency components spanning a range from $0Hz$ - $10Hz$. For both the 9-points star stencil and the 13-points cross stencil, PML absorbing boundary conditions were set on all edges of the model using the same damping conditions throughout. In Figure 3.9(a) we show seismograms for the 9-points star stencil (continuous line) and the 13-points cross stencil (dashed line). The overall agreement is excellent. In Figure 3.9(b),(c),(d) and (e) we extracted two traces (5 and 40) from the seismogram shown in (a) and compared them to the analytic solution computed

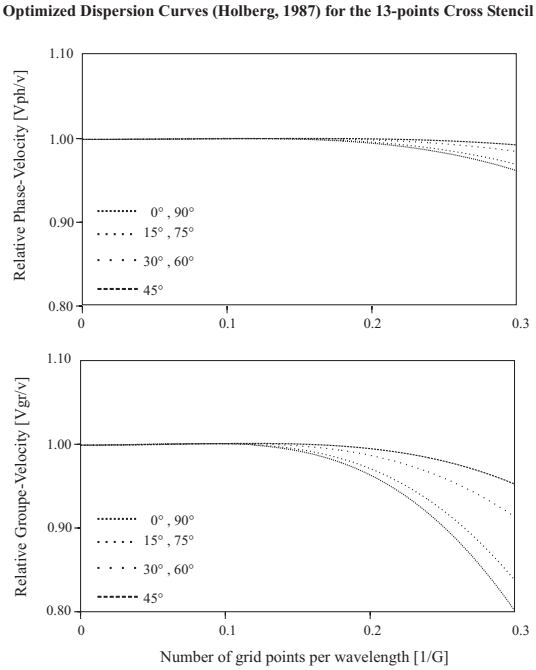

Figure 3.8: Relative phase v_{ph} and group v_{gr} velocity curves for the optimized 13-points cross stencil. The operator coefficients used for numerical differentiation are $\alpha_1 = 1.13824281853071e^{+00}$ and $\alpha_2 = 4.64142728435701e^{-02}$ which gives a final error of $2.53067e^{-06}$. Propagation angles from the vertical are denoted by different types of dashed lines.

for the same model parameters. Figure 3.9(b) and (c) show the comparison for trace number 5 for the 9-points star and the 13-points cross respectively. Figure 3.9(d) and (e) show the results for trace number 40.

To our knowledge the star-stencil strategy does not allow a combination of the PML conditions together with the grid rotation approach for partial derivative approximation. The PML absorbing boundary condition requires that the partial derivatives are computed with respect to the Cartesian spatial coordinate system that is parallel to the edges of the model. Therefore the star strategy implies a reduction to second-order accuracy inside the absorbing PML layer and we treat waves inside the PML medium with the 5-points stencil only.

3.8.2 The corner edge model

The corner edge model combines two homogeneous media separated by a horizontal and a vertical interface making a corner (see Figure 3.10). The velocity and density in the two spaces are $2000m/sec$, $8000m/sec$ and $2000kg/m^3$, $2500kg/m^3$ respectively. The dimension of the model is $6400m$ x $6400m$ and was discretized with a mesh spacing of

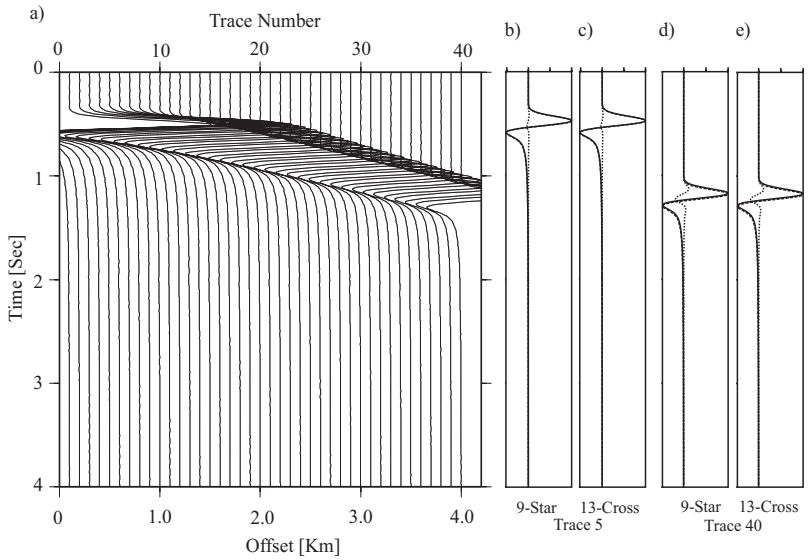

Figure 3.9: Comparison of the 9-points star stencil (continuous line) and 13-points cross stencil (dashed line) for a two-dimensional homogeneous model surrounded by PML absorbing boundary conditions. The medium velocity is 4000m/sec, the density $2500kg/m^3$, and the source a derivative of a Gaussian. Frequency domain solutions were computed for 52 frequency components from 0Hz to 10Hz. (a) shows the time seismogram recorded at 40 receivers at 200m depth. The source was localized at (500m,1000m). In (b), (c), (d) and (e) we extracted two traces (5 and 40) from the seismogram shown in (a) and compared them to the corresponding analytic solution. (b) and (c) show the comparison for trace number 5 for the 9-points star and the 13-points cross respectively while (d) and (e) give the results for trace number 40. The analytic solution is plotted as continuous line and the 9-points star and 13-points cross solutions as dashed lines. The dotted line is the residual.

$40m$ (equal to 5 points per shortest wavelength). All four edges of the model are treated with PML absorbing boundary conditions where the layer size was set to 20 grid points. The overall grid therefore has 200x200 grid points.

In Figures 3.11 and 3.12 we show time seismograms recorded at 80 receiver positions horizontally lined up over the whole model at a depth of $150m$ for the 9-points star and the 13-points cross stencil respectively. The receiver spacing was approximately $80m$. The source position is at $(250m, 4000m)$. Note, we used the same source as for the homogeneous model comparison. Both solutions are compared to a TDFD solution (continuous line). The overall agreement of the three solutions is good. In Figure 3.11(b),(c),(d) we show three traces $(10, 50, 75)$ extracted from the seismogram in Figure 3.11(a), though now we replaced the TDFD solution by an analytic solution computed for an homogeneous media having the physical properties of the upper medium of the Corner Edge model ($v = 2000m/sec, \rho = 2000kg/m^3$). Figure 3.12(a),(b),(c) and (d) give results ob-

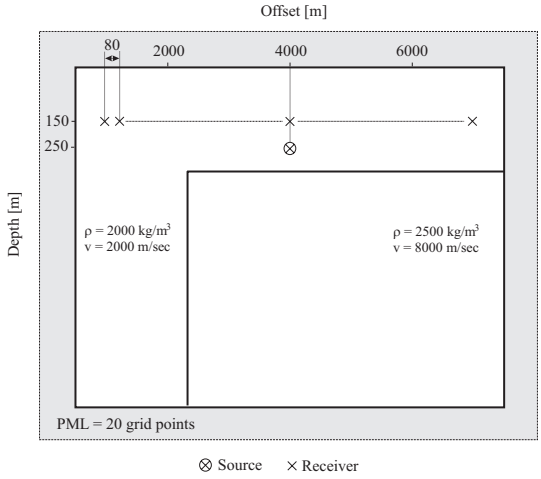

Figure 3.10: The two-dimensional corner edge model that consists of two homogeneous media separated by a horizontal and a vertical line building a corner edge. The model grid size is 200 × 200 grid points of which 20 grid points on each edge of the model correspond to the PML damping layer. The medium velocity and density are 2000m/sec, $2000kg/m^3$ in the upper and 8000m/sec, $2500kg/m^3$ in the lower half space respectively.

tained for the 13-points cross stencil. The velocity and density distribution generates a sharp reflection (second event) and a diffracted wave with strongly reduced amplitude (third event), at the interface of the two media. We note excellent agreement for the direct wave for both 9-points star and 13-points cross stencil. At the far offset trace 5 we recognize a small amount of wave dispersion that behaves slightly differently for the two computational stencils. The reflection from the corner edge shows a small phase shift between the 9-points star and 13-points cross stencil (see difference of second pulse in Figures 3.11 and 3.12(b),(c),(d)). From Figure 3.11(a) we note that it is the 9-points star solution that is shifted from the 13-points FDFD and TDFD solutions. In Figure 3.13 we extracted a time-trace window (Time window: $t_1 = 2.5sec - t_2 = 4.5sec$, Traces: $40 - 80$) from Figures 3.11(a) and 3.12(a) in order to evaluate the performance of the PML absorbing boundary conditions in strongly contrasted medium. Figures 3.13(a) and 3.13(b) show the solution for the 9-points star and the 13-points cross respectively. Both seismograms where amplified by a factor several times larger than the maximum amplitude in Figures 3.11 and 3.12 in order to recognize any spurious noise. While the PML condition for the 13-points cross (b) perfectly absorbs the incoming waves, the reduction to second-order accuracy (5-points stencil) for the 9-points star creates very weak but noticeable spurious reflections.

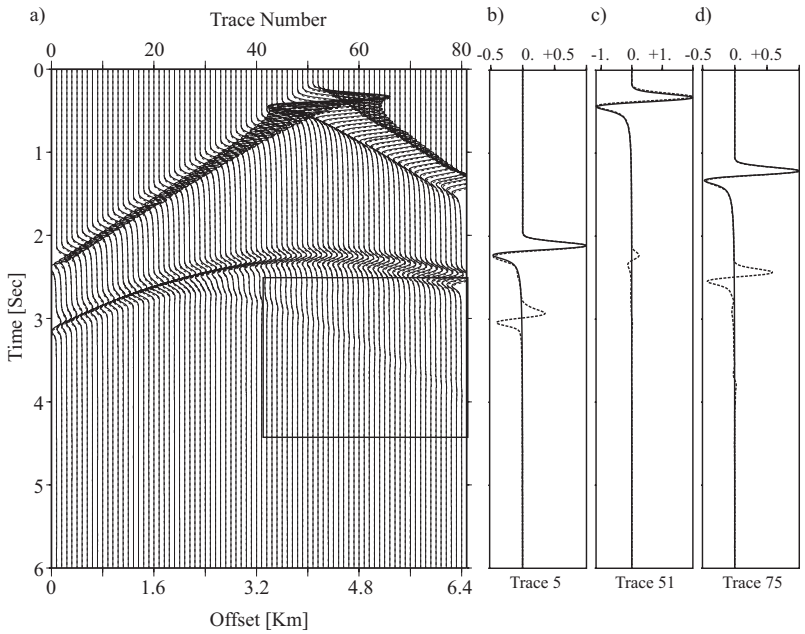

Figure 3.11: Comparison of a TDFD solution (continuous line) and the 9-points star stencil (dashed line) for the two-dimensional corner edge. The medium velocity is 2000m/sec in the upper and 8000m/sec in the lower half space respectively. We set the density to $2000kg/m^3$ and $2500kg/m^3$. We used a spatial sampling in x- and z-direction of $\Delta x = \Delta z = 40m$. The model is surrounded by PML absorbing boundary conditions (20 grid points). The source is similar to the one used for the homogeneous model. Frequency domain solutions were computed for 103 frequency components from 0Hz to 10Hz. In (a) we show a time seismogram for a source at (250m,4000m) and 80 receiver positions at a depth of 100m. The receiver spacing is 80 m. In (b), (c), and (d) we show extracted traces from the time seismogram for receiver positions 5, 51, and 75 respectively. Instead of the TDFD solution we plotted an analytic solution (continuous line) for a homogeneous half space where the physical medium pr perties have been set equal to the upper part of the Corner Edge model ($\rho = 2000kg/m^3$ and v=2000m/sec). Note, wave propagation dispersion becomes visible on the far offset trace in (b) for the direct wave.

3.9 Perspectives and conclusion

We have presented a staggered cross stencil strategy for FDFD acoustic wave propagation modelling in 2D media. The staggered grid approach discretizes the wave equation written as a 1^{st}-order hyperbolic system of equations including PML absorbing boundary conditions. Parsimonious elimination followed by re-injection leads to a 2^{nd}-order hyperbolic equation which defines the cross stencil geometry.
We have shown that the staggered cross stencil for second-order derivative approximations is exactly similar to the 5-points stencil strategy. Fourth-order staggered derivative ap-

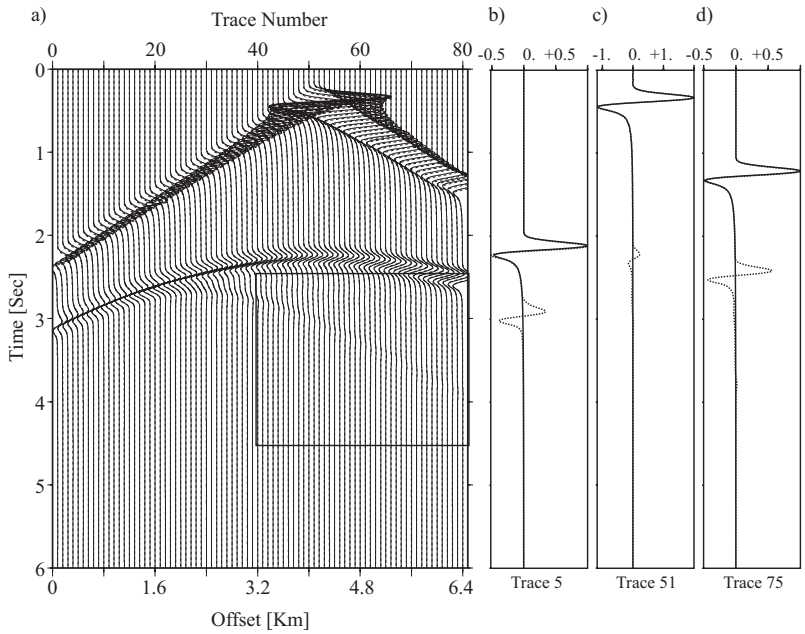

Figure 3.12: Comparison of a TDFD solution (continuous line) and the 13-points cross stencil (dotted line) for the two-dimensional corner edge. All model and acquisition parameters are similar to the ones described in the legend of Figure 3.11. In (b), (c), and (d) we show extracted traces from the time seismogram for receiver positions 5, 51, and 75 respectively. Instead of the TDFD solution we plotted an analytic solution (continuous line) for a homogeneous half space where the physical medium properties have been set equal to the upper part of the Corner Edge model ($\rho = 2000 kg/m^3$ and v=2000m/sec).

proximations result in the 13-points cross stencil. We have compared the 13-points stencil with the 9-points star stencil that is obtained by grid rotation and subsequent optimized grid combination. Since the cross stencil for fourth-order approximations incorporates 12 surrounding points instead of 8 for the 9-points star stencil, memory requirements and CPU-floating point operations for matrix factorizations are increased. This is true in the two-dimensional case. In case of 3D media this result might not hold since the staggered grid strategy leads to a 19-points cross stencil while the grid rotation approach gives a 27-points star stencil. Further investigations concerning the 3D problematic are still under development.
Numerical dispersion was investigated for both the 9-points star and the 13-points cross. Compared to the 13-points cross both phase and group velocity for the 9-points star show less numerical dispersion. Since the combination of the rotated grids for the star stencil approach requires some dispersion relation optimization technique, we applied analogous dispersion curve optimizations to the 13-points cross stencil. Though numerical dispersion was decreased, compared to the standard fourth-order staggered grid approximation, it still was not found to be competitive to the star geometry. The better performance

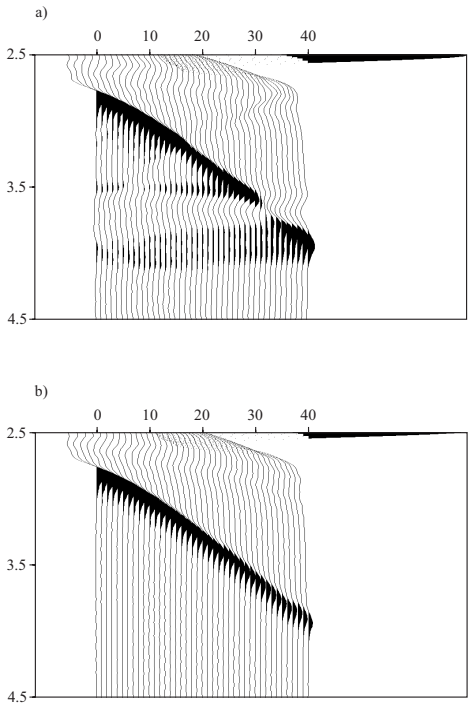

Figure 3.13: Plot showing the performance of the PML absorbing boundary conditions in a contrasted medium for the 9-points star and the 13-points cross. (a) Rectangle extracted from Figure 3.11(a) showing the traces 40 up to 80 for the times $t_1 = 2.5sec$ to $t_2 = 4.5sec$ for the 9-points star solution. (b) The same rectangular is extracted from the 13-points cross solution (see Figure 3.12(a)). Both (a) and (b) show the end of the reflection event on the top of the extracted time window. The event crossing from top left to bottom right is the diffraction from the corner edge. In (a) we see noise generated by the absorbing PML layers, while in (b) the PML perfectly absorbs any spurious reflection. Note, the noise in (a) only becomes visible for strongly heterogeneous models (such as the Corner Edge) and is recognized when the amplitude is increased by several tens of the maximum amplitude (see amplitude of reflection event in (a) and (b) compared to e.g. Figure 3.11(a)) We explain the spurious noise in (a) by the fact that the 9-point star only allows the usage of the second-order approximations in the PML layers (5-points stencil), compared to the fourth-order stencil used throughout in (b).

of the 9-points star in terms of numerical dispersion can be explained by the additional optimization through lumped mass distribution applied to the algebraic term. The CPU-efficiency of the two approaches is controlled by the matrix factorization scheme and therefore by the compactness of the star geometry. Fewer surrounding points involved in the stencil construction are therefore favorable.
Altogether, the grid rotation strategy shows clearly superior results in terms of memory requirements and CPU efficiency for 2D FDFD modelling. In view of the performance

of the grid rotation approach the question arises why in TDFD modelling the staggered grid approach predominates, while in FDFD modelling the star geometry is preferred? In TDFD modelling the compactness of the star plays a less important role since no matrix factorization has to be computed. Nevertheless, the numerical dispersion analysis indicates clearly superior performance of the star geometry over the staggered geometry. The combination of grid rotation and staggered grids was already addressed by Saenger et al. (2000), though in their approach only derivative approximations were described on rotated axis while the wave equation was left untouched. They obtained superior results for a crack propagation problem, but did not address a more general grid rotation scheme in order to enhance the numerical performance of their TDFD scheme. Therefore, we propose that the compact and optimized star geometry should be investigated for TDFD modelling for 2D and 3D heterogeneous media.
Also, the cross stencil geometry will be extended to 3D media and then compared to the grid rotation approach in a more formal investigation. This work is under way.

3.10 Acknowledgments

We are thankful to D. Rodrigues for providing us with the fourth-order staggered cross stencil optimization coefficients. We would like to thank P. Amestoy for assistance with the optimized minimum degree ordering scheme. Support from IDRIS (Institut du Développement et des Ressources en Informatique Scientifique) through project 21560 is acknowledged. The research leading to this paper was partly founded by DASE/CEA through the PROSIS3D group. This paper is Contribution No. XXX from UMR Geosciences Azur - CNRS, FRANCE.

3.11 Appendix A - Second-order discretization of the wave equation

We show the discretization scheme of the 1^{st} order hyperbolic system of equations using a second-order, spatially staggered stencil. The 5-points staggered cross stencil is exactly similar to the 5-points stencil that was used by Pratt and Worthington (1990).

The 1^{st} order hyperbolic system of equations for FDFD scheme is

$$\begin{aligned}
\frac{-i\omega\xi_x(x)}{K(x,z)}P_x(x,z,\omega) &= \frac{\partial Q(x,z,\omega)}{\partial x} + S(x,z,\omega) \\
\frac{-i\omega\xi_z(z)}{K(x,z)}P_z(x,z,\omega) &= \frac{\partial R(x,z,\omega)}{\partial z} \\
-i\omega Q(x,z,\omega) &= \frac{1}{\xi_x(x)\rho(x,z)}\frac{\partial P(x,z,\omega)}{\partial x} \\
-i\omega R(x,z,\omega) &= \frac{1}{\xi_z(z)\rho(x,z)}\frac{\partial P(x,z,\omega)}{\partial z}
\end{aligned} \tag{A. 1}$$

We discretize equation (A. 1) using second-order staggered stencils (Virieux, 1984)

$$\begin{aligned}
\frac{\partial Q}{\partial x} &\approx \frac{1}{\Delta x}(Q_{i+1/2,j} - Q_{i-1/2,j}) \\
\frac{\partial R}{\partial z} &\approx \frac{1}{\Delta z}(R_{i,j+1/2} - R_{i,j-1/2}) \\
\frac{\partial P}{\partial x} &\approx \frac{1}{\Delta x}(P_{i+1,j} - P_{i,j}) \\
\frac{\partial P}{\partial z} &\approx \frac{1}{\Delta z}(P_{i,j+1} - P_{i,j})
\end{aligned} \tag{A. 2}$$

and obtain the following equations

$$\begin{aligned}
\frac{-i\omega\xi_x}{K_{i,j}} P^x_{i,j} &= \frac{1}{\Delta x}(Q_{i+1/2,j} - Q_{i-1/2,j}) + S_{i,j} \\
\frac{-i\omega\xi_z}{K_{i,j}} P^z_{i,j} &= \frac{1}{\Delta z}(R_{i,j+1/2} - R_{i,j-1/2}) \\
-i\omega Q_{i+1/2} &= \frac{1}{\xi_{xi+1/2,j}\rho_{i+1/2,j}} \cdot \frac{1}{\Delta x}(P_{i+1,j} - P_{i,j}) \\
-i\omega R_{j+1/2} &= \frac{1}{\xi_{zi,j+1/2}\rho_{i,j+1/2}} \cdot \frac{1}{\Delta z}(P_{i,j+1} - P_{i,j}) \\
-i\omega Q_{i-1/2} &= \frac{1}{\xi_{xi-1/2,j}\rho_{i-1/2,j}} \cdot \frac{1}{\Delta x}(P_{i,j} - P_{i-1,j}) \\
-i\omega R_{j-1/2} &= \frac{1}{\xi_{zi,j-1/2}\rho_{i,j-1/2}} \cdot \frac{1}{\Delta z}(P_{i,j} - P_{i,j-1})
\end{aligned} \tag{A. 3}$$

where we considered the averaging coefficients $\frac{1}{\rho_{i+1/2,j}} = \frac{1}{2}(\frac{1}{\rho_{i+1,j}} + \frac{1}{\rho_{i,j}})$, $K_{i,j} = \{\frac{1}{4}(\frac{1}{K_{i,j}} + \frac{1}{K_{i+1,j}} + \frac{1}{K_{i,j+1}} + \frac{1}{K_{i+1,j+1}})\}^{-1}$, and the PML function $\xi_{i+1/2}$. These averaging coefficients were used by Graves (1996) for fourth-order staggered grid TDFD simulations in 3D media.

We eliminate the additional equations depending on Q and R by re-injecting them into the first two equations that depend on P_x and P_z only and obtain

$$\begin{aligned}
\frac{-i\omega\xi_{xi}}{K_{i,j}} P^x_{i,j} = \frac{1}{\Delta x}[\quad & (\quad -\frac{1}{i\omega} \cdot \frac{1}{\xi_{xi+1/2} \cdot \rho_{i+1/2,j}} \cdot \frac{1}{\Delta x}(P_{i+1,j} - P_{i,j}) - \\
& (\quad -\frac{1}{i\omega} \cdot \frac{1}{\xi_{xi-1/2} \cdot \rho_{i-1/2,j}} \cdot \frac{1}{\Delta x}(P_{i,j} - P_{i-1,j})] + S_{i,j} \\
\frac{-i\omega\xi_{zi}}{K_{i,j}} P^z_{i,j} = \frac{1}{\Delta z}[\quad & (\quad -\frac{1}{i\omega} \cdot \frac{1}{\xi_{zj+1/2} \cdot \rho_{i,j+1/2}} \cdot \frac{1}{\Delta z}(P_{i,j+1} - P_{i,j}) - \\
& (\quad -\frac{1}{i\omega} \cdot \frac{1}{\xi_{zi-1/2} \cdot \rho_{i,j-1/2}} \cdot \frac{1}{\Delta z}(P_{i,j} - P_{i,j-1})]
\end{aligned} \tag{A. 4}$$

We add the two wave-fields P_x and P_z and get the 2^{nd}-order staggered cross FD equation with PML absorbing boundary conditions for the P wave-field

$$\begin{aligned}\frac{-\omega^2}{K_{i,j}}P_{i,j} = \quad & \tfrac{1}{\xi_{xi}} \cdot\frac{1}{\Delta x^2}[(\frac{1}{\xi_{xi+1/2}\cdot\rho_{i+1/2,j}}\cdot(P_{i+1,j}-P_{i,j}) \\ & -(\frac{1}{\xi_{xi-1/2}\cdot\rho_{i-1/2,j}}\cdot(P_{i,j}-P_{i-1,j})] \\ + \quad & \tfrac{1}{\xi_{zj}} \cdot\frac{1}{\Delta z^2}[(\frac{1}{\xi_{zj+1/2}\cdot\rho_{i,j+1/2}}\cdot(P_{i,j+1}-P_{i,j}) \\ & -(\frac{1}{\xi_{zj-1/2}\cdot\rho_{i,j-1/2}}\cdot(P_{i,j}-P_{i,j-1})] \\ + \quad & S_{i,j}\end{aligned} \tag{A. 5}$$

From equation (A. 5) we extract the coefficients that correspond to the 5-points cross stencil (see Figure 3.2)

$$\begin{aligned}A = \frac{-\omega^2}{K_{i,j}} \quad & - \quad \frac{1}{\xi_{xi}\cdot\Delta x^2}[\frac{1}{\xi_{xi+1/2}\cdot\rho_{i+1/2,j}}+\frac{1}{\xi_{xi-1/2}\cdot\rho_{i-1/2,j}}] \\ & - \quad \frac{1}{\xi_{zj}\cdot\Delta z^2}[\frac{1}{\xi_{zj+1/2}\cdot\rho_{i,j+1/2}}+\frac{1}{\xi_{zj-1/2}\cdot\rho_{i,j-1/2}}] \\ B = \quad & \frac{1}{\xi_{xi}\cdot\Delta x^2}[\frac{1}{\xi_{xi-1/2}\cdot\rho_{i-1/2,j}}] \\ C = \quad & \frac{1}{\xi_{xi}\cdot\Delta x^2}[\frac{1}{\xi_{xi+1/2}\cdot\rho_{i+1/2,j}}] \\ D = \quad & \frac{1}{\xi_{zj}\cdot\Delta z^2}[\frac{1}{\xi_{zj-1/2}\cdot\rho_{i,j-1/2}}] \\ E = \quad & \frac{1}{\xi_{zj}\cdot\Delta z^2}[\frac{1}{\xi_{zj+1/2}\cdot\rho_{i,j+1/2}}] \\ F = \quad G \quad & = H = I = 0\end{aligned} \tag{A. 6}$$

3.12 Appendix B - Fourth-order discretization of the wave equation

We show the discretization procedure of the 1^{st} order hyperbolic system of equation using the fourth-order, spatially staggered stencil. The procedure is in complete analogy to the developments carried out for the 5-points cross stencil, which then leads to the 13-points cross stencil that propagates pressure wave-field solutions with fourth-order accuracy.
We discretize equation (3.6) using fourth-order staggered stencils (see Equation (B. 1))

developed by Levander (1988):

$$\begin{aligned}
\frac{\partial Q}{\partial x} &\approx \frac{1}{\Delta x}[\frac{9}{8}(Q_{i+1/2,j} - Q_{i-1/2,j}) - \frac{1}{24}(Q_{i+3/2,j} - Q_{i-3/2,j})] \\
\frac{\partial R}{\partial x} &\approx \frac{1}{\Delta Z}[\frac{9}{8}(R_{i,j+1/2} - R_{i,j-1/2}) - \frac{1}{24}(R_{i,j+3/2} - R_{i,j-3/2})] \\
\frac{\partial P}{\partial x} &\approx \frac{1}{\Delta x}[\frac{9}{8}(P_{i+1,j} - P_{i,j}) - \frac{1}{24}(P_{i+2,j} - P_{i-1,j})] \\
\frac{\partial P}{\partial z} &\approx \frac{1}{\Delta z}[\frac{9}{8}(P_{i,j+1} - P_{i,j}) - \frac{1}{24}(P_{i,j+2} - P_{i,j-1})]
\end{aligned} \tag{B. 1}$$

We obtain the following relations

$$\begin{aligned}
\frac{-i\omega\xi_{xi}}{K_{i,j}} P_{xi,j} &= \frac{1}{\Delta x}\{\frac{9}{8}(Q_{i+1/2,j} - Q_{i-1/2,j}) - \frac{1}{24}(Q_{i+3/2,j} - Q_{i-3/2,j})\} + S_{i,j} \\
\frac{-i\omega\xi_{zi}}{K_{i,j}} P_{zi,j} &= \frac{1}{\Delta z}\{\frac{9}{8}(R_{i+1/2,j} - R_{i-1/2,j}) - \frac{1}{24}(R_{i+3/2,j} - R_{i-3/2,j})\} \\
Q_{i+1/2,j} &= -\frac{1}{i\omega\xi_{i+1/2}\cdot\rho_{i+1/2,j}}\frac{1}{\Delta x}\{\frac{9}{8}(P_{i+1,j} - P_{i,j}) - \frac{1}{24}(P_{i+2,j} - P_{i-1,j})\} \\
Q_{i-1/2,j} &= -\frac{1}{i\omega\xi_{i-1/2}\cdot\rho_{i-1/2,j}}\frac{1}{\Delta x}\{\frac{9}{8}(P_{i,j} - P_{i-1,j}) - \frac{1}{24}(P_{i+1,j} - P_{i-2,j})\} \\
Q_{i+3/2,j} &= -\frac{1}{i\omega\xi_{i+3/2}\cdot\rho_{i+3/2,j}}\frac{1}{\Delta x}\{\frac{9}{8}(P_{i+2,j} - P_{i+1,j}) - \frac{1}{24}(P_{i+3,j} - P_{i,j})\} \\
Q_{i-3/2,j} &= -\frac{1}{i\omega\xi_{i-3/2}\cdot\rho_{i-3/2,j}}\frac{1}{\Delta x}\{\frac{9}{8}(P_{i-1,j} - P_{i-2,j}) - \frac{1}{24}(P_{i,j} - P_{i-3,j})\} \\
R_{i,j+1/2} &= -\frac{1}{i\omega\xi_{j+1/2}\cdot\rho_{i,j+1/2}}\frac{1}{\Delta z}\{\frac{9}{8}(P_{i,j+1} - P_{i,j}) - \frac{1}{24}(P_{i,j+2} - P_{i,j-1})\} \\
R_{i,j-1/2} &= -\frac{1}{i\omega\xi_{j-1/2}\cdot\rho_{i,j-1/2}}\frac{1}{\Delta z}\{\frac{9}{8}(P_{i,j} - P_{i,j-1}) - \frac{1}{24}(P_{i,j+1} - P_{i,j-2})\} \\
R_{i,j+3/2} &= -\frac{1}{i\omega\xi_{j+3/2}\cdot\rho_{i,j+3/2}}\frac{1}{\Delta z}\{\frac{9}{8}(P_{i,j+2} - P_{i,j+1}) - \frac{1}{24}(P_{i,j+3} - P_{i,j})\} \\
R_{i,j-3/2} &= -\frac{1}{i\omega\xi_{j-3/2}\cdot\rho_{i,j-3/2}}\frac{1}{\Delta z}\{\frac{9}{8}(P_{i,j-1} - P_{i,j-2}) - \frac{1}{24}(P_{i,j} - P_{i,j-3})\}
\end{aligned} \tag{B. 2}$$

where we used effective medium parameters and PML boundary conditions as before. We combine the equations and obtain for the P-wave-field:

$$
\begin{aligned}
\frac{-\omega^2}{K_{i,j}} P_{i,j} \quad = \quad & \frac{1}{\Delta x^2 \cdot \xi_i} \{ \\
& \frac{9}{8} \{ \frac{1}{\xi_{xi+1/2} \cdot \rho_{i+1/2,j}} \{ \frac{9}{8} (P_{i+1,j} - P_{i,j}) - \frac{1}{24} (P_{i+2,j} - P_{i-1,j}) \} - \\
& \frac{1}{\xi_{xi-1/2} \cdot \rho_{i-1/2,j}} \{ \frac{9}{8} (P_{i,j} - P_{i-1,j}) - \frac{1}{24} (P_{i+1,j} - P_{i-2,j}) \} \} - \\
& \frac{1}{24} \{ \frac{1}{\xi_{xi+3/2} \cdot \rho_{i+3/2,j}} \{ \frac{9}{8} (P_{i+2,j} - P_{i+1,j}) - \frac{1}{24} (P_{i+3,j} - P_{i,j}) \} - \\
& \frac{1}{\xi_{xi-3/2} \cdot \rho_{i-3/2,j}} \{ \frac{9}{8} (P_{i-1,j} - P_{i-2,j}) - \frac{1}{24} (P_{i,j} - P_{i-3,j}) \} \} \} \\
+ \quad & \frac{1}{\Delta z^2 \cdot \xi_j} \{ \\
& \frac{9}{8} \{ \frac{1}{\xi_{zj+1/2} \cdot \rho_{i,j+1/2}} \{ \frac{9}{8} (P_{i,j+1} - P_{i,j}) - \frac{1}{24} (P_{i,j+2} - P_{i,j-1}) \} - \\
& \frac{1}{\xi_{zj-1/2} \cdot \rho_{i,j-1/2}} \{ \frac{9}{8} (P_{i,j} - P_{i,j-1}) - \frac{1}{24} (P_{i,j+1} - P_{i,j-2}) \} \} - \\
& \frac{1}{24} \{ \frac{1}{\xi_{zj+3/2} \cdot \rho_{i,j+3/2}} \{ \frac{9}{8} (P_{i,j+2} - P_{i,j+1}) - \frac{1}{24} (P_{i,j+3} - P_{i,j}) \} - \\
& \frac{1}{\xi_{zj-3/2} \cdot \rho_{i,j-3/2}} \{ \frac{9}{8} (P_{i,j-1} - P_{i,j-2}) - \frac{1}{24} (P_{i,j} - P_{i,j-3}) \} \} \} \\
+ \quad & S_{i,j}
\end{aligned}
\tag{B. 3}
$$

Finally, we write grid point contributions of the new staggered cross stencil for fourth-order derivative approximations that are valid for the whole media including PML absorbing boundary conditions. We note that the staggered grid approach results in a stencil that incorporates 12 grid nodes surrounding the center point (see Figure 3.4). Therefore

we denote the new stencil as the 13-points staggered cross stencil.

$$
\begin{aligned}
A = \frac{\omega^2}{K_{i,j}} \quad & -\tfrac{1}{\Delta x^2 \cdot \xi_i}\{ \quad \frac{9\cdot 9}{8\cdot 8}\Big(\frac{1}{\xi_{i+1/2}\cdot\rho_{i+1/2,j}} + \frac{1}{\xi_{i-1/2}\cdot\rho_{i-1/2,j}}\Big) \\
& \qquad + \frac{1\cdot 1}{24\cdot 24}\Big(\frac{1}{\xi_{i+3/2}\cdot\rho_{i+3/2,j}} + \frac{1}{\xi_{i-3/2}\cdot\rho_{i-3/2,j}}\Big)\} \\
& -\tfrac{1}{\Delta z^2 \cdot \xi_j}\{ \quad \frac{9\cdot 9}{8\cdot 8}\Big(\frac{1}{\xi_{j+1/2}\cdot\rho_{i,j+1/2}} + \frac{1}{\xi_{j-1/2}\cdot\rho_{i,j-1/2}}\Big) \\
& \qquad + \frac{1\cdot 1}{24\cdot 24}\Big(\frac{1}{\xi_{j+3/2}\cdot\rho_{i,j+3/2}} + \frac{1}{\xi_{j-3/2}\cdot\rho_{i,j-3/2}}\Big)\} \\
B = \quad & +\tfrac{1}{\Delta x^2}\tfrac{1}{\xi_i}\{ \quad \frac{9\cdot 9}{8\cdot 8}\frac{1}{\xi_{i-1/2}\cdot\rho_{i-1/2,j}} + \frac{9\cdot 1}{8\cdot 24}\frac{1}{\xi_{i+1/2}\cdot\rho_{i+1/2,j}} \\
& \qquad + \frac{1\cdot 9}{24\cdot 8}\frac{1}{\xi_{i-3/2}\cdot\rho_{i-3/2,j}}\} \\
B2 = \quad & -\tfrac{1}{\Delta x^2}\tfrac{1}{\xi_i}\{ \quad \frac{9\cdot 1}{8\cdot 24}\frac{1}{\xi_{i-1/2}\cdot\rho_{i-1/2,j}} + \frac{1\cdot 9}{24\cdot 8}\frac{1}{\xi_{i-3/2}\cdot\rho_{i-3/2,j}}\} \\
B3 = \quad & +\tfrac{1}{\Delta x^2}\tfrac{1}{\xi_i}\{ \quad \frac{1\cdot 1}{24\cdot 24}\frac{1}{\xi_{i-3/2}\cdot\rho_{i-3/2,j}}\} \\
C = \quad & +\tfrac{1}{\Delta x^2}\tfrac{1}{\xi_i}\{ \quad \frac{9\cdot 9}{8\cdot 8}\frac{1}{\xi_{i+1/2}\cdot\rho_{i+1/2,j}} + \frac{9\cdot 1}{8\cdot 24}\frac{1}{\xi_{i-1/2}\cdot\rho_{i-1/2,j}} \\
& \qquad + \frac{1\cdot 9}{24\cdot 8}\frac{1}{\xi_{i+3/2}\cdot\rho_{i+3/2,j}}\} \\
C2 = \quad & -\tfrac{1}{\Delta x^2}\tfrac{1}{\xi_i}\{ \quad \frac{9\cdot 1}{8\cdot 24}\frac{1}{\xi_{i+1/2}\cdot\rho_{i+1/2,j}} + \frac{1\cdot 9}{24\cdot 8}\frac{1}{\xi_{i+3/2}\cdot\rho_{i+3/2,j}}\} \\
C3 = \quad & +\tfrac{1}{\Delta x^2}\tfrac{1}{\xi_i}\{ \quad \frac{1\cdot 1}{24\cdot 24}\frac{1}{\xi_{i+3/2}\cdot\rho_{i+3/2,j}}\} \\
D = \quad & +\tfrac{1}{\Delta z^2}\tfrac{1}{\xi_j}\{ \quad \frac{9\cdot 9}{8\cdot 8}\frac{1}{\xi_{j-1/2}\cdot\rho_{i,j-1/2}} + \frac{9\cdot 1}{8\cdot 24}\frac{1}{\xi_{j+1/2}\cdot\rho_{i,j+1/2}} \\
& \qquad + \frac{1\cdot 9}{24\cdot 8}\frac{1}{\xi_{j-3/2}\cdot\rho_{i,j-3/2}}\} \\
D2 = \quad & -\tfrac{1}{\Delta z^2}\tfrac{1}{\xi_j}\{ \quad \frac{9\cdot 1}{8\cdot 24}\frac{1}{\xi_{j-1/2}\cdot\rho_{i,j-1/2}} + \frac{1\cdot 9}{24\cdot 8}\frac{1}{\xi_{j-3/2}\cdot\rho_{i,j-3/2}}\} \\
D3 = \quad & +\tfrac{1}{\Delta z^2}\tfrac{1}{\xi_j}\{ \quad \frac{1\cdot 1}{24\cdot 24}\frac{1}{\xi_{j-3/2}\cdot\rho_{i,j-3/2}}\} \\
E = \quad & +\tfrac{1}{\Delta z^2}\tfrac{1}{\xi_j}\{ \quad \frac{9\cdot 9}{8\cdot 8}\frac{1}{\xi_{j+1/2}\cdot\rho_{i,j+1/2}} + \frac{9\cdot 1}{8\cdot 24}\frac{1}{\xi_{j-1/2}\cdot\rho_{i,j-1/2}} \\
& \qquad + \frac{1\cdot 9}{24\cdot 8}\frac{1}{\xi_{j+3/2}\cdot\rho_{i,j+3/2}}\} \\
E2 = \quad & -\tfrac{1}{\Delta z^2}\tfrac{1}{\xi_j}\{ \quad \frac{9\cdot 1}{8\cdot 24}\frac{1}{\xi_{j+1/2}\cdot\rho_{i,j+1/2}} + \frac{1\cdot 9}{24\cdot 8}\frac{1}{\xi_{j+3/2}\cdot\rho_{i,j+3/2}}\} \\
E3 = \quad & +\tfrac{1}{\Delta z^2}\tfrac{1}{\xi_j}\{ \quad \frac{1\cdot 1}{24\cdot 24}\frac{1}{\xi_{j+3/2}\cdot\rho_{i,j+3/2}}\}
\end{aligned}
\tag{B. 4}
$$

3.13 Appendix C - Dispersion analysis

We substitute a plane wave solution of the form $P = P_0 \cdot e^{-i(k_x \cdot \Delta x \, + \, k_z \cdot \Delta z)}$ into equation (3.8) for the fourth-order staggered cross stencil. We further assume $\Delta x = \Delta z = \Delta$ to be the uniform grid spacing in x- and z-direction. The propagation angle from the z-axis is denoted by θ, the spatial wave-number by k, and the operator coefficients for the staggered derivative approximation by α_1 and α_2. The dispersion equation may then be formulated as

$$\begin{aligned} \omega^2(k) = \frac{v^2}{\Delta^2} \quad \{ \quad & 4\alpha_1\alpha_1 - 2\alpha_1\alpha_1 cos(k\Delta sin\theta) - 4\alpha_1\alpha_2 cos(k\Delta sin\theta) \\ + \quad & 4\alpha_1\alpha_2 cos(2k\Delta sin\theta) - 2\alpha_2\alpha_2 cos(3k\Delta sin\theta) \\ + \quad & 4\alpha_2\alpha_2 - 2\alpha_1\alpha_1 cos(k\Delta cos\theta) - 4\alpha_1\alpha_2 cos(k\Delta cos\theta) \\ + \quad & 4\alpha_1\alpha_2 cos(2k\Delta cos\theta) - 2\alpha_2\alpha_2 cos(3k\Delta cos\theta)\} \end{aligned} \tag{C. 1}$$

We define the numerical phase and group velocities as $v_{ph} = \frac{\omega}{k}$ and $v_{gr} = \frac{\partial\omega}{\partial k}$. From equation C. 1 we get the relative numerical phase and group velocities

$$\begin{aligned} \frac{v_{ph}^2}{v^2} = \frac{G^2}{4\pi^2} \quad \{ \quad & 4\alpha_1\alpha_1 sin^2(\frac{\pi}{G} sin\theta) + 8\alpha_1\alpha_2 sin^2(\frac{\pi}{G} sin\theta) - 8\alpha_1\alpha_2 sin^2(2\frac{\pi}{G} sin\theta) \\ & + 4\alpha_2\alpha_2 sin^2(3\frac{\pi}{G} sin\theta) \\ + \quad & 4\alpha_1\alpha_1 sin^2(\frac{\pi}{G} cos\theta) + 8\alpha_1\alpha_2 sin^2(\frac{\pi}{G} cos\theta) - 8\alpha_1\alpha_2 sin^2(2\frac{\pi}{G} cos\theta) \\ & + 4\alpha_2\alpha_2 sin^2(3\frac{\pi}{G} cos\theta) \end{aligned} \tag{C. 2}$$

$$\begin{aligned} \frac{\partial\omega}{\partial k} = \frac{1}{2} \quad \{ \quad & 2\alpha_1\alpha_1(sin\theta \cdot sin(k\Delta sin\theta) + cos\theta \cdot sin(k\Delta cos\theta)) \\ + \quad & 4\alpha_1\alpha_2(sin\theta \cdot sin(k\Delta sin\theta) + cos\theta \cdot sin(k\Delta cos\theta)) \\ - \quad & 8\alpha_1\alpha_2(sin\theta \cdot sin(2k\Delta sin\theta) + cos\theta \cdot sin(2k\Delta cos\theta)) \\ + \quad & 6\alpha_2\alpha_2(sin\theta \cdot sin(3k\Delta sin\theta) + cos\theta \cdot sin(3k\Delta cos\theta))\} \cdot B^{-\frac{1}{2}} \end{aligned} \tag{C. 3}$$

where B is

$$\begin{aligned} B = \quad & - \quad 2\alpha_1\alpha_1(cos(k\Delta sin\theta) + cos(k\Delta cos\theta)) \\ & - \quad 4\alpha_1\alpha_2(cos(k\Delta sin\theta) + cos(k\Delta cos\theta)) \\ & + \quad 4\alpha_1\alpha_2(cos(2k\Delta sin\theta) + cos(2k\Delta cos\theta)) \\ & - \quad 2\alpha_2\alpha_2(cos(3k\Delta sin\theta) + cos(3k\Delta cos\theta)) \\ & + \quad 4\alpha_1\alpha_1 + 4\alpha_2\alpha_2 \end{aligned} \tag{C. 4}$$

In order to illustrate the determination of accurate wave velocities by the staggered cross stencil approach we assume $sin\theta \approx \theta$ for small angles θ and simplify the phase velocity dispersion relations to (C. 1 and C. 3)

$$\begin{aligned} \frac{v_{ph}}{v} &= \alpha_1 - 3 \cdot \alpha_2 \\ \frac{v_{gr}}{v} &= \sqrt{\alpha_1\alpha_1 - 6 \cdot \alpha_1\alpha_2 + 9 \cdot \alpha_2\alpha_2} \end{aligned} \qquad \text{(C. 5)}$$

Using fourth-order staggered operator coefficients $\alpha_1 = \frac{9}{8}$ and $\alpha_2 = \frac{1}{24}$ (Levander (1988)) we deduce for both phase and group velocity exactly 1. Therefore, in the ideal case (no dispersion) the numerical velocity does not diverge from the true medium velocity.

Chapter 4

Mesh Generation by a wavelet formulation

4.1 Résumé

Dans le chapitre précédent, j'ai présenté une méthode de modélisation des ondes par différences finies dans le domaine fréquence-espace (FDFD). Indépendamment de l'approche choisie pour discrétiser le système d'équation (étoile 9-points ou croix 13-points), la performance de l'algorithme est limitée par l'utilisation exclusive d'une méthode directe. Par conséquent, les modélisations par FDFD ne sont appliquées qu'à des problèmes 2D et d'autres approches doivent être envisagées pour rendre accessibles des simulations 3D à grande échelle.

Dans ce chapitre, je présente tout d'abord différentes techniques de discrétisation spatiale optimisée d'une PDE qui ont pour dénominateur commun l'idée d'adapter dynamiquement la grille numérique à la complexité du milieu et les caractéristiques des ondes au cours de leur propagation dans le milieu.

Les approches de discrétisation d'équation d'onde par des formulations faibles et moyennes utilisent par définition des méthodes de raffinement automatique ("*MRM: Mesh Refinement Method*"). Fondées sur une telle discrétisation par MRM, les approches par éléments finis (FE) ou éléments spectraux (SE) fournissent des algorithmes précis et, à ma connaissance, les plus performants actuellement. L'inconvénient principal de ces approches est l'incertitude introduite par la création de la grille par MRM dont la précision est difficile à évaluer.

Les performances des méthodes fondées sur une discrétisation par formulation forte (méthodes par différences finies) peuvent être optimisées en combinant les calculs sur plusieurs grilles de résolution différente. Les approches dans le domaine espace-fréquence, fondées sur une approche multigrille complète "*Full Multi-Grid methods*" (FMG), utilisent des méthodes itératives qui sont appliquées sur différentes grilles d'approximation suivant un parcours entre grilles formant des cycles en V et W ("*V- and W-cycles*"). Ces transferts de grille sont utilisés dans le but d'accélérer la convergence des méthodes itératives, le chemin de parcours entre grilles étant défini de manière plus ou moins empirique.

Une alternative pour décomposer les calculs sur un ensemble des grilles numériques est d'utiliser l'analyse multirésolution fournie par la transformée en ondelettes (WT). Les propriétés importantes de la WT dans le contexte d'un problème de modélisation numérique de la propagation d'onde sont présentées en détail.

Suite à l'introduction sur la construction d'une grille adaptative, je présente une nouvelle approche mixte multi-échelles combinant une méthode directe et itérative de résolution du système matriciel associé à l'approche FDFD de modélisation de la propagation d'onde. Cette nouvelle approche, qui est considérée comme une extension des approches classiques de modélisations par FDFD (voir Chapitre 3), permet d'effectuer des modélisations des ondes acoustiques dans des milieux 3D complexes et et de rhéologie hétérogène.

Dans un premier temps, le champ d'onde exact est calculé par une factorisation LU de la matrice d'impédance sur une grille de résolution grossière, dont le pas de grille est déterminé par la capacité maximale de mémoire disponible pour traiter le problème. Deuxièmement, ce champ d'onde exact est prolongé sur une grille numérique de résolution fine pour fournir un estimé initial à l'algorithme de résolution itérative. J'ai développé deux approches différentes qui sont fondées respectivement sur une prolongation du champ d'onde grossier sur la grille fine par une interpolation spatiale bilinéaire, appelée méthode "*Direct-Iterative-Space Solver*" (DISS), et sur une décomposition multi-échelles obtenue par projection sur une base d'ondelettes, appelée méthode "*Direct-Iterative-Wavelet Solver*" (DIWS). Les performances respectives, en terme de temps-CPU et de stockage mémoire, de ces deux méthodes de modélisation des ondes dans des milieux 2D complexes et hétérogènes sont comparées. L'algorithme de la méthode DISS, qui ressemble à une approche FMG en raison de la méthode d'interpolation utilisée, permet la construction rapide du système matriciel. La performance de l'algorithme itératif dépend fortement de sa capacité à éliminer des artefacts numériques associés à des phénomènes de déphasage. L'importance de ces artefacts dépend de la précision de la solution initiale et de la discrétisation numérique du champ modélisé dans l'algorithme itératif. Un nombre important d'itérations ou l'utilisation des cycles en V et W sont nécessaires pour supprimer ces phénomènes de déphasage. Dans la méthode DIWS, une représentation multi résolution du système matriciel est développée par projection sur une base d'ondelettes Daubechies-4. Malgré le coût induit pour transformer le système dans le domaine spectral, la représentation multi résolution fournit un outil numérique de préconditionnement permettant de stabiliser et d'accélérer significativement la performance de l'algorithme itératif. L'accélération est attribuée à la représentation du système d'équation sur plusieurs grilles numériques de résolution différente dont les interactions sont prises en compte automatiquement au cours des itérations. Par ailleurs, la formulation en ondelettes ouvre des perspectives d'optimisation sous forme d'adaptation spatiale du maillage en fonction des propriétés locales du milieu et du champ propagé.

Plusieurs exemples de simulations d'onde dans des milieux 2D de complexité variable sont présentés pour illustrer les performances respectives des méthodes DISS et DIWS.

4.2 Mesh generation

Meshing describes the procedure of breaking up a physical domain into a number of sub-domains. Each sub-domain is characterised through its inherent grid, which, by definition, has a different resolution than the surrounding domains. The subdivision of the initial model aims to facilitate the computation of a numerical solution of a partial differential equation (PDE), since local model structures, such as high-velocity intrusions in low-velocity surroundings, can be treated using the best adapted grid for the required numerical accuracy. This construction procedure is called mesh refinement method (MRM).

As was noted in Chapter 2, strong formulations of the wave equation verify the PDE on discrete Cartesian grid points. Even though numerical schemes based on a strong formulation have been extended to manually combinations of numerical grids, the constructed grids are still Cartesian and mainly vary the equidistant spatial stepping. MRM is a different approach in that only one computational grid is constructed that dynamically adapts to guarantee the desired accuracy of the simulation.

In contrast, weak and average formulations of PDEs, by definition, require the construction of non-Cartesian numerical grids, based on some pre-defined geometrical form, such as triangulars. Then, MRM may be applied to enhance the computational performance of the numerical scheme. Exactly the same solution can be computed when the finest spatial discretization is applied in the whole model without distinguishing between sub-domains of different complexity in the model.

In the past years, MRM schemes have mainly been developed for FE and SE modelling schemes (LeVeque, 1997; Berger and LeVeque, 1998; Komatitsch and Tromp, 1999). Many different types of mesh forms and construction techniques exist, and it has long been a debate which basic element shape might produce the most accurate modelling results. For example, surfaces might be subdivided by regular sub-grids, triangles or quadrilateral shapes, while volumes could be made up of tetrahedra or hexahedra shapes. Which of these elementary shapes best combines with the pre-defined accuracy of a weak formulation of a PDE problem, depends on the problem at hand and, to my knowledge, no general unique best element shape exists.

4.2.1 Automatic mesh refinement

Automatic mesh refinement (AMR) denotes a MRM, where the numerical grid is not constructed before the simulation starts but during the simulation procedure, such that the grid adapts to the complexity of the model structure and the behaviour of the numerical solution. In general, solutions for PDEs are computed on a principal coarse grid that incorporates patches of fine discretized grids, where the structure of the model and or external constraints require higher accuracy. Ideally, we would like the mesh refinement to be carried out during execution of the simulation in such a way that the meshing identifies regions requiring more resolution with respect to:

- local structure in the model
- behaviour of the numerical solution during simulation

Numerical solution of PDEs approximate the exact solution of a mathematically posed problem. Especially, the error in a weak formulation decreases as the element-size of the sub-division gets smaller or the order of the polynomial in the interpolating functions increases. AMR is therefore controlled by error estimates that characterise the accuracy of the wave-field solution. Two basic principles that control errors may be distinguished:

- a posteriori error estimates in a given finite element
- mesh refinement to achieve a desired accuracy economically

In general, the error control will be an adaptive mixture of the two. Typical grid refinement can be obtained through the introduction of new elements of the already used type (e.g. triangulars) but of smaller size, or keeping the element definition and increase the order of the polynomials by adding new grid nodes placed in already existing elements.

The actual error that defines refinement requirements can be measured by various *norms*, that represent integral scalar quantities. A typical measure of the error is the *energy norm* or for wave propagation applications the L^2-*norm* for displacement or stress errors (Zienkiewicz and Morgan, 1982). The error evaluation can be applied over the whole computational domain Ω, sub-domains Ω_i, or even individual elements in the grid.

In order to perform the dynamic adaption, AMR techniques continuously inspect the calculated solution on all grid nodes during propagation. In case the solution is found to be *critical*, which means that the local error exceeds pre-defined error *norms*, the grid position is flagged. In a second step, another procedure checks on the neighbouring points next to the flagged grid nodes, and based on their location defines an area where grid refinement needs to be applied. Finally, all flagged regions are refined by the next finer level grid and the whole procedure is repeated in order to see if an even increased precision in a certain region is required.

In exactly the same way as regions at some point (in space and time) need refinement, they also might be judged to be sufficiently accurate on a coarser grid (for example, after a complex zone has been passed by the wave-front) and therefore the refinement will be cancelled. Although AMR is of great interest in many numerical simulation algorithms, it is especially important for modellings where the solution tends to produce singular shock behaviour, as it is the case for seismic rupture propagation, for example.

Many different AMR techniques have been developed in the past years following different strategies of how grid-elements are formed and placed, where the truncation error can be controlled by some physical parameter (see Owen, 1998, for a detailed discussion). Since the numerical grid controls the accuracy of the modelling solution and AMR becomes rather difficult and computational intensive for large and more complex models, research in this field has become extremely important. Berger and Oliger (1984); LeVeque (1997) and Berger and LeVeque (1998) developed an AMR technique for 3D wave propagation problems. Moreover, AMR has been extended to run on large parallel computer structure environments, which makes it very appealing for large-scale wave modellings.

4.2.2 Discussion

The (automatic) mesh design problematic is that of attempting to construct or define a set of grid-nodes, using a basic geometrical form, in order to best describe a spatial physical domain while guaranteeing pre-defined accuracy requirements. MRM and AMR techniques are of great interest especially for sudden shock-like behaviours, since the numerical mesh is adapted and refined to perfectly match the structure of the model and the behaviour of the solution. Still, the ambiguity introduced by the automatic mesh generation is not easily controllable. If, for example, the meshing creates errors during the refinement, these are completely hidden from the user and the numerical pollution in the obtained solution is undetectable.

MRM and AMR combine principal features that are important for precise and computationally optimised algorithms for PDE simulations. These features are:

- sampling
- resolution

The first feature, *sampling*, is provided by the weak formulation of the wave equation. The introduction of interpolating- and testing-functions up to a desired accuracy provides stable and precise discretization schemes. Then, the necessary *resolution* of the wave simulation is guaranteed by adaptive refinement performed by an AMR approach.

Even though these two principal features are illustrated here for the framework of weak formulations and AMR, similar properties can be defined for wavelet orthonormal bases. The wavelet notation provides a natural framework to handle efficient operator and function approximations, with respect to their propagation (*sampling*) and scaling (*resolution*) behaviour (Beylkin, 1998). Equations formulated with the help of the multi-resolution framework of the orthogonal wavelet transform are interesting, because contributions from numerical grids having varying spatial resolution are naturally combined. Then, coarse scales can be interpreted as *homogenized* representations, which, in effect, gives the desired spatial frequency decomposition of a standard Full Multi-Grid technique and is therefore investigated in greater detail in the following.

4.3 Wavelet discretization

The refinement of a computational grid by dividing the model in sub-domains and *manually* combining grids of different spatial resolution, both permit wave propagation simulations with increased computational efficiency compared to standard schemes. Ideally, we would like the numerical grid to interact with respect to the behaviour of the wave-field solution computed at a time or space location. The numerical grid should automatically detect local grid-parameters required to perform precise wave propagation simulations within pre-defined error bars. Clearly, we further demand the grid structure to adapt to the detected local accuracy requirements. Then, variable grid-parameters guarantee optimised and efficient calculations, which in effect renders numerical modelling of complex wave propagation phenomena feasible.

Although many strategies for either strong or weak formulations have been developed and applied to fulfil that aim, all methods have significant shortcomings. While methods based on weak formulations depend on correct meshing algorithms, strong formulations lead to numerical schemes that suffer from rather brutal grid combinations that are not dynamic during wave propagation.

Another way to achieve a multi-grid representation of a signal is the expansion on a wavelet basis. The wavelet basis automatically provides the desired multi-scale structure, where grid combinations and interactions are accounted naturally by the multi-resolution framework. Therefore, wavelets give a convenient formulation for a decomposition of a wave-field on different grids of various resolution. The wavelet coefficients computed during an orthogonal wavelet transformation (OWT) encode the wave-field information corresponding to each resolution grid separately. The inverse OWT allows the re-combination of all grid contributions to form the initial wave-field solution. Both forward and inverse OWT are performed through a cascaded down- and up-sampling procedure, called multi-resolution analysis (MRA).

The MRA provides a tool with which a signal can be analysed on approximation spaces having variable resolution. It uses a scaling function, which forms a basis functions on each resolution scale. The decomposition algorithm typically starts from a fine-discretized signal and then subsequently finds coarser and coarser grid-representations of the initial fine-grid signal. The scaling function therefore acts as a low-pass filter. Although the MRA already provides the desired multi-scale representation, it is not sufficient to build a formal basis.

The introduction of a corresponding wavelet function and combination with the scaling properties of the MRA, gives the desired wavelet transform. The discrete wavelet transform (DWT) is computed by a step-wise decomposition algorithm. At each step of the cascaded decomposition, the application of a convolution-type algorithm allows the projection from a fine to a coarse discretized signal approximation. The wavelet algorithm is repeated until a desired final decomposition is obtained. Since the WT is a linear transformation, perfect reconstruction is possible by simply inverting the initial decomposition scheme.

One of the main interests of wavelets in numerical analysis and image processing is the fact that the user may interfere at each step of the wavelet decomposition, in order to alter or adapt the current signal in a desired manner. For example, in signal processing images may be compressed by eliminating at each step of the decomposition, wavelet coefficients having an amplitude inferior to some pre-defined tolerance limit. Similar ideas have been implemented for simulating time evolution problematics, such as turbulent flows, etc.. Many of these approaches use wavelets in a Galerkin-type method, where the wavelet space provides interpolating and testing functions for the weak formulation of the PDEs. A review of wavelet-based methods for acoustic and electromagnetic modelling is given by Wells (1994). Note that in the above introduced notation, a method is called Galerkin if the spaces U^h and W^h of interpolating and testing functions are the same, and a weak formulation is chosen as discretization scheme.

Strong formulations combined with a wavelet framework for wave propagation problematics have been investigated by many authors in the last years: Maday et al. (1991);

Joly et al. (1994); Charton (1996); Jameson and Miyama (1999). The motivation in using wavelets was driven by the possibility to define local adaptivity parameters on each sub-resolution level during a wavelet decomposition. In practice, the adaption of the solution is obtained through a thresholding procedure of wavelet coefficients with respect to the behaviour of some physical parameter that characterises the local solution. Different strategies have been developed to define these thresholding parameters, as well as their physical meaning and rules for their application.

Other developments use the wavelet transform in a strong formulation as a pseudo-spectral approach. A rather classic scheme was recently illustrated by Hong and Kennett (2002). They applied the wavelet basis as a tool to perform accurate derivative estimations in the spectral wavelet space. Other wavelet-based pseudo-spectral methods are more ambitious in that more intrinsic wavelet properties, such as adaptivity, are incorporated in the numerical scheme (Operto et al., 2002).

In order to avoid difficulties encountered in complete wavelet-spectral formulations, Jameson and Miyama (1999) proposed a FD modelling scheme that applies the wavelet transform as a meshing-tool only to construct an adaptive numerical grid. Their scheme shows nice results for 2D problematics, even though interesting and desirable wavelet features are not considered. Despite of numerous developments of wavelet-based formulations for the solution of PDEs, significantly superior results over other modelling techniques, such as weak formulations combined with AMR, have only been demonstrated for simulations based on non-linear PDEs (Beylkin, 1998).

The expansion of a signal on a wavelet basis brings key advantages over representations in the physical domain, such as the signal decomposition with respect to scale and spatial location. Although these characteristics are of great importance, since a wave propagating in a complex heterogeneous media has contributions from a variety of scales and frequencies, others such as the verification of physical boundary conditions might become extremely complicated and by far not obvious. To my knowledge, the WT has been shown to be competitive for simulations of non-linear wave phenomena where computations on a large number scales (e.g., $J = 20$ resolution scales) clearly out-performed standard multi-grid techniques (Chiavassa, 1997).

In the case of linear PDEs, as investigated in this thesis, I do not expect a large number of scales necessary to perform wave-field simulations (e.g. $J < 5$ resolution scales), and it is questionable whether wavelets provide a powerful tool as for the non-linear case. This is not surprising since the existing weak, average, and strong formulations have been developed over a long period of time by many researchers, while current wavelet-based formulations have been re-discovered only recently by Mallat (1989); Meyer (1992). Therefore, we might find that wavelets are interesting for non-linear wave propagation only, while the existing modelling techniques out-perform wavelets for linear PDEs in terms of computational efficiency for a given computer resources standard. However, this eventuality should not stop us from continuing research on interesting applications of the wavelet transform for numerical modelling, since the wavelet transform provides a powerful tool to obtain a multi-scale decomposition with respect to exact mathematical basis formulations.

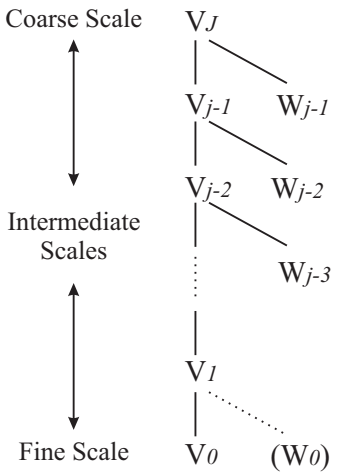

Figure 4.1: Resolution approximation spaces in a wavelet decomposition. The finest resolution is denoted by V_0. The wavelet transform finds subsequently coarser approximation spaces $V_{j=0,\ldots,J}$ until a final coarsest resolution is reached. The coarsest resolution is denoted by V_J.

4.3.1 Orthogonal wavelet transform

The orthogonal wavelet transform permits the decomposition of a signal on a hierarchy of sub-grids of different resolution (Daubechies, 1988; Mallat, 1989). The OWT initially projects the signal on the finest discretized grid, denoted V_0-space, which, in general, is determined preliminarily by computer limitations. The WT subsequently projects the signal on coarser discretized grids ($V_{j=1,\ldots,J}$-spaces) until, in practice, a fixed coarsest resolution level in practice is reached.

Each sub-grid encodes the information that is *filtered out* when going from a finer to a coarser grid, in the so called *wavelet* or *detail* coefficients. The corresponding approximation space of the filtered signal components is denoted by W_j-space. When the coarsest grid is reached, the WT additionally stores the remaining signal components in the *scaling* or *average* coefficients (V_J-space). The different wavelet resolution spaces are illustrated in Figure 4.1.

As was noted before, the MRA defines a basis for each resolution approximation space. The intuitive idea that a signal approximation on a resolution level V_j is also included in the next finer resolution level V_{j-1} is true for the MRA. Therefore, the scaling functions do not form a standard basis of all approximation spaces. Only the MRA extension by the wavelet functions provides the desired formal non-redundant (orthogonal) basis transformation properties.

Starting from an initial fine discretized signal, on each step of the WT-cascade, the

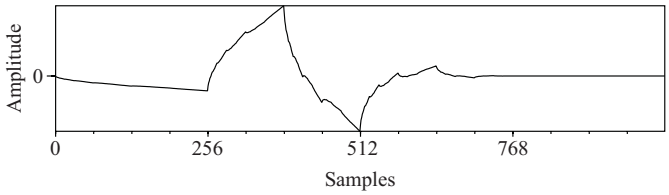

Figure 4.2: Illustration of a Daubechies-4 wavelet basis vector.

signal is projected on a next coarser resolution grid. Then, the filtered out data is encoded in the wavelet space, and the procedure repeated for the next resolution pair. One step of the WT algorithm is:

- signal discretized on grid V_j
- compute projection on next coarser grid V_{j+1} (down-sampling)
- store signal difference in W_{j+1} ($V_j = V_{j+1} \bigoplus W_{j+1}$)
- store signal discretized on V_{j+1} and restart

The algorithm may be inverted by restarting the procedure from the signal representation on the coarsest grid. Then, MRA re-constructs grid by grid, finer and finer signal representations through adding wavelet coefficients, until the initial signal is obtained.

The combination of the scaling and wavelet functions led Daubechies (1992) to construct an orthogonal wavelet basis, where the wavelet basis functions have compact support. The different Daubechies wavelets are labeled Daub2, Daub4,..., Daub2M where 2M indicates twice the number of vanishing moments of the specific wavelet basis. For example, Daub4 wavelets have two *vanishing moments*. In Figure 4.2, as an example, I plot one basis vector of the Daub4 wavelet basis. The developments presented in this thesis were performed using the Daub4 wavelet basis throughout.

In Appendix A, I give a rather limited mathematical introduction to the WT. For a detailed review of the theory of wavelets, I refer to the works of Daubechies (1992) and Mallat (1999). In practice, the discrete wavelet transform (DWT) is computed by a convolution-type procedure that uses a set of *quadrature mirror filters*. The forward wavelet transform operator for Daub4 wavelets is illustrated in Figure 4.3. The operator entries represent the *quadrature mirror filters* coefficients. Operator coefficients $c_0, ..., c_3$ perform a low-pass filtering, while coefficients $c_3, -c_2, c_1, -c_0$ are rather a high-pass filtering process because of the minus sign involved.

In the case of Daubechies wavelets, the number of *vanishing moments* of the wavelet basis is related to the number of *quadrature mirror filter* coefficients. In order to guarantee fast wavelet transform algorithms it is therefore interesting to keep the number of *quadrature mirror filter* coefficients low, since convolution-type computations can then be computed in a fast and efficient way. On the other hand, the number of *vanishing moments* of a given wavelet basis also defines the accuracy of the wavelet approximation,

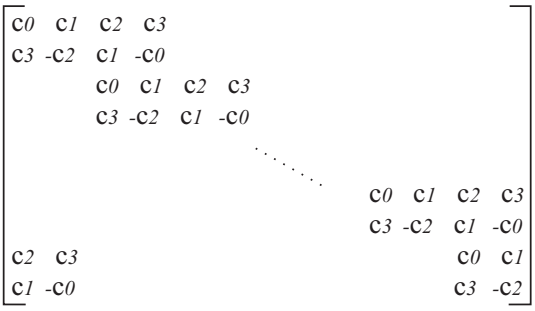

Figure 4.3: Illustration of the forward wavelet transform operator. The coefficients in the operator perform two different convolution-type procedures. While the odd rows compute a smoothed average (low-pass filter), the even rows can be interpreted as high-pass filters.

and a good equilibrium between efficient algorithms and accurate computations has to be found for a given problem at hand.

The WT has proven to be of great value for different problematics in science, because not only it gives a decomposition with respect to the frequency content of a signal, such as the Fourier Transform (FT), but it also gives a spatial indicator where the frequency components are located. Several key features of the WT motivated my work and, therefore, will be discussed in more detail here. These are:

- decomposition → Frequency and location
- scaling → Coarse- and fine-grid contributions
- uniqueness → Expansion on an orthogonal basis

In Figure 4.4(a) and Figure 4.4(b), I show the wavelet transform of an initially dense and sparse signal, respectively. The wavelet decomposition is shown for $J = 3$ projection steps separately. From the top to the bottom, I plot the projection of the signal on the scaling and wavelet spaces for each of the three resolution levels. The dense signal in Figure 4.4(a) has an overall smooth behaviour with a single jump in amplitude at the sample number $ns = 256$. Through the decomposition procedure, we see that the localisation of the jump (high frequency content), though smeared out because of MRA sub-sampling, is encoded in all approximation spaces (W_j-spaces) at the right spatial location. The smooth part, which is mainly made up of low frequency components, does not contribute with any wavelet coefficients for the fine grids ($W_{j=1,2,3}$). The scaling spaces ($V_{j=1,2,3}$) hold coarse-grid versions of the initial signal discretized on the $V_{j=0}$ space. Similar observations can be made for the wavelet expansion of the initially sparse signal in Figure 4.4(b). Wavelet spaces store the filtered-out high-frequency data, while scaling spaces hold averaged versions of the initially Dirac-like signal.

In Table 4.1, I give the required samples necessary to store the signals in Figure 4.4(a) and (b) on $J = 6$ resolution spaces. The dense signal with the shock-like jump is stored in $ns = 512$ samples in the physical domain. Then, wavelet expansion on several resolution

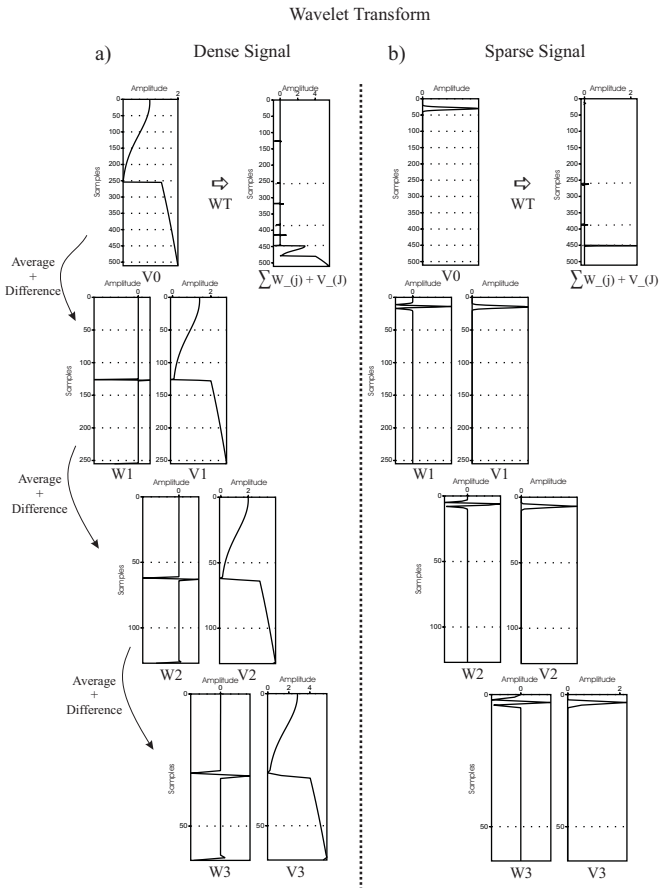

Figure 4.4: A dense and a sparse signal are projected on the orthogonal Daubechies-4 wavelet basis. In (a) and (b), I show the averaging and differencing steps of the MRA for a dense and a sparse signal, respectively, that are necessary to decompose the signals on $J = 3$ resolution scales. At each step the signal discretized on the V_j-space is decomposed (filtering+sub-sampling) into a coarser discretized signal V_{j+1} plus the the data that has been filtered out (W_{j+1}) to obtain the next coarser signal. The filtered data is stored in the wavelet transformed vector, while the average data is used for the next step of the MRA. When the coarsest approximation space ($J = 3$) is reached the average space is stored as well. Note that a former dense signal ($ns = 512$ samples) is suppressed to $ns = 193$ samples, while the initially sparse signal ($ns = 31$ samples) requires $ns = 35$ storage samples after projection on the wavelet basis.

scales allows a data compression of up to 25% for $J = 6$ scales, compared to the storage on the finest grid only. Note that the projection on only one scale already provides a data compression of about 40%.

In contrast to the good compression results for the dense signal, the initially sparse signal in Figure 4.4(b) is not compressed under wavelet expansion. In the physical domain,

Resolution Scale	Nr. of Samples Dense Function	Nr. of Samples Sparse Function
$V_{J=0}$	512	31
$W_{j=1} + V_{J=1}$	296	30
$\sum_{j=1}^{2} W_j + V_{J=2}$	222	32
$\sum_{j=1}^{3} W_j + V_{J=3}$	193	35
$\sum_{j=1}^{4} W_j + V_{J=4}$	163	37
$\sum_{j=1}^{5} W_j + V_{J=5}$	148	41
$\sum_{j=1}^{6} W_j + V_{J=6}$	131	43

Table 4.1: Number of non-zero coefficients necessary to store the projection of a sparse and a dense signal (see Figure 4.4) on $J = 1, ..., 6$ resolution approximation spaces using Daubechies-4 wavelets.

the signal requires $ns = 31$ samples to store the Dirac-like function, while on $J = 6$ resolution scales, $ns = 43$ non-zero coefficients are necessary to hold all the information.

This little test shows that one of the main advantages of wavelet representations compared to the physical domain is relative. Only if the initial function is dense, can wavelets significantly compress the required storage amount. In case a sparse signal is projected, an even increased number of coefficients is required to hold all the necessary information in a number of resolution approximation scales.

Until now, I presented two important characteristics of the projection on a wavelet basis: these are signal decomposition with respect to *scale* and *location*. However, the most important wavelet feature has not yet been addressed explicitly. As I already mentioned, the combination of scaling and wavelet functions constructs a formal transformation on the wavelet basis.

The decomposition on a multi-scale representation is obtained through the MRA, which itself provides a basis for each sub-scale, though not for the complete decomposition. Briggs and Henson (1993) and later Beylkin (1998) stated that multi-resolution wavelet decomposition is equivalent to a multi-grid method without V- and W-cycles. The reason for the absence of V- and W-cycles derives from the fact that the OWT constructs orthogonal projections of the true solution simultaneously on each of the resolution approximation spaces, during the decomposition. No further interpolating phase-shift corrections are needed, since all necessary information is currently encoded in the combination of scaling, wavelet, and scale-interaction coefficients.

For illustration, we note that the coarsest representation of the signals in Figure 4.4(a)

and (b) are stored on $ns = 64$ samples, which corresponds to $J = 3$ decomposition steps (see the $V_{J=3}$ space). Assuming we perform one step of the inverse OWT, that is combining W_3 and V_3, we obtain the next finer representation in the V_2 space. In a multi-grid method the same step would require the application of an interpolation scheme, which might introduce phase-shifts. This is not the case for wavelets since the missing information necessary to go to the next finer scale is stored in the wavelet sub-space. Thus, we find the correct signal representation in V_2, that again is spanned by the scaling functions for this resolution space. This crucial advantage of wavelet-based methods over multi-grid methods is what I am aiming for.

4.3.2 FD operator in wavelet basis

One of the principal aspects of a wavelet-based PDE solver is the representation of derivative operators in the wavelet domain. Despite that for a general wavelet transform no direct statements may be provided, here I briefly review the remarkable close relation between the differential operator in the Daub4 wavelet basis and the centred finite-difference approximation of the differential operator in the physical domain (Beylkin et al., 1991; Jameson, 1993).

In general, two possibilities exist to construct the derivative operator in the wavelet domain. The first approach relies directly on the properties of scaling and wavelet interpolating functions and was developed by Beylkin et al. (1991). They explicitly determined wavelet derivative coefficients using Daubechies wavelets, where the derivative properties are uniquely introduced via wavelet basis approximation properties.

Alternatively, one can define a discrete derivative operator in the physical space, such as the standard centred FD operator, without considering any wavelet or scaling function properties (Wu and McMechan, 1998). Then, standard wavelet projection procedures may be applied to the operator, which gives the desired derivative approximation transformed in the wavelet domain.

Note that in the latter approach the discrete operator in the wavelet domain is assumed to be equivalent to the derivative operator on the finest resolution scale V_0 of a wavelet expansion. This assumption is called the *wavelet crime* (see Strang and Nguyen, 1996, for details). Beylkin et al. (1991) and Jameson (1993) showed that for the Daub4 wavelet basis the two procedures are equivalent, if the differential operator in the physical space is the fourth-order centred FD derivative operator.

Jameson (1993) showed a more general connection between the FD differential operator in physical space and the wavelet space. He concluded that the expansion of the FD differential operator in a Daubechies wavelet basis with M *vanishing moments* has approximatively similar properties as a FD Taylor series expansion of the differential operator of order $2M$. Moreover, Beylkin et al. (1991) and Jameson (1993) illustrated that the wavelet transformed derivative operator defines local FD operators on each resolution scale. I emphasise that the close relationship of the standard FD operator in the physical space and its expansion in the Daub4 basis has been illustrated for non-staggered grids only (see Operto et al., 2002, for a detailed discussion).

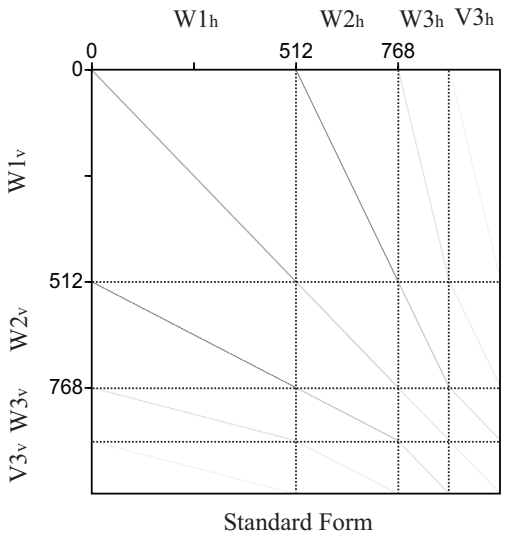

Figure 4.5: The fourth-order FD operator is projected on an orthogonal wavelet basis having $J = 3$ resolution approximation spaces. Coefficients different from zero are plotted in black. On each sub-grid the Daub4 wavelet basis constructs scaled versions of the initial FD operator. The FD operator is constructed in the denominated Standard Form (Beylkin, 1992), that results from a wavelet transformation procedure similar to the one described earlier for a one-dimensional signal. Note the finger-band structure of the operator in the wavelet basis. Additional coefficients located in the off-diagonal blocks encode interaction coefficients that are necessary to interchange information between different resolution grids.

The standard form

The FD modelling scheme developed by Operto et al. (2002) constructs spatial FD operators on the orthogonal Daub4 wavelet basis using the Standard Form (STF) representation (Beylkin et al., 1991). The STF of an operator in the wavelet domain can be computed by applying one-dimensional (1D) WTs to each dimension of the operator (see Figure 4.4 and Operto et al. (2002)) or through a more complicated procedure, introduced by Beylkin et al. (1991) that relies on scaling and wavelet functions properties.

The transformation of an operator on the wavelet basis not only encodes scaled versions of the initially discretized operator (local FD operators), but also intermediate coefficients that control the interaction between the different approximation scales. The STF of the fourth-order FD operator projected on $J = 3$ resolution scales is shown in Figure 4.5. Just as for the 1D signal shown earlier (see Figure 4.4), the operator is first discretized on the finest scale V_0 and then coarser approximations are subsequently computed through the application of a step of the wavelet transformation. The procedure stops once the pre-defined coarsest discretization is reached.

Finite difference operator coefficients in the physical domain are situated in bands

around the main diagonal, where the bandwidth depends on the order of the differentiation used. In the wavelet domain, we observe from Figure 4.5 that the projection on the Daub4 wavelet basis creates additional coefficients situated in a finger-band structure around the main diagonal. The diagonal blocks ($W_j^h \times W_j^v$) represent the previously mentioned scaled versions of the FD operator. Coefficients situated in the finger-bands define the interaction between different approximations spaces. For example, the space $W_1^h \times W_3^v$ encodes the interaction between the wavelet space W_1 and the scaling space V_2, i.e. $W_1 \rightarrow V_2$. The intuitive idea that the further approximation spaces are apart, the less their interaction will be, can be observed from the diminution of operator coefficients away from the diagonal (see Figure 4.5).

Sparsity of the FD operator in the wavelet domain depends, up to a certain degree, on the wavelet basis chosen. Each non-zero coefficient of the FD stencil in the physical domain is transformed on the wavelet basis, where the number of non-zero wavelet coefficients depends on the number of filter coefficients that define the wavelet basis. As I demonstrated for a 1D signal (see Figure 4.4), a sparse function in the physical domain is not compressed in the wavelet domain. Similar phenomena apply for the FD operator. The number of non-zero coefficients is significantly increased because the wavelet expansion holds contributions of the operator on each wavelet projection space plus additional interaction coefficients (see Figure 4.5).

Sparsity of the derivative operator is one of the primary concerns for TDFD schemes, since time evolution is performed through operator wave-field products at each time step (Virieux, 1984). Despite of the problematics related to heterogeneous media properties, from a simple sparsity point of view, the wavelet expansion of the FD operator rather decreases the performance of the modelling algorithm. However, the great advantage of the wavelet projection is the multi-scale representation of the FD method. On each resolution scale, the Daub4 wavelet basis provides a local FD operator that perfectly matches accuracy requirements for the corresponding scale. In that sense, the WT automatically provides a multi-grid FD scheme.

In order to render the wavelet based FD scheme competitive, Operto et al. (2002) implemented a space adaptive scheme in the wavelet domain. Two different approaches were proposed to render the code more efficient: thresholding and *a priori* masks. Thresholding eliminates wavelet coefficients whose amplitude is inferior to some pre-defined scale-dependent physical parameter. The idea is that the wave propagation is performed on several resolution grids simultaneously with the help of a wavelet representation. Then, in model regions where physical parameters change only smoothly, fine-grid wavelet coefficients will be small and therefore might be suppressed by thresholding.

Although there exist powerful applications for thresholding, numerical tests performed by Operto et al. (2002) for seismic wave propagation in strongly heterogeneous media did not show significant compression. Therefore, they manually defined areas in the physical model before the modelling starts, called masks, where the corresponding wavelet coefficients are set to zero since their contribution to the wave propagation simulation is estimated to be insignificant. A typical application of masks in a FD-wavelet method is in the vicinity of the free surface, where high precision and fine griding is required in order to obtain acceptable results.

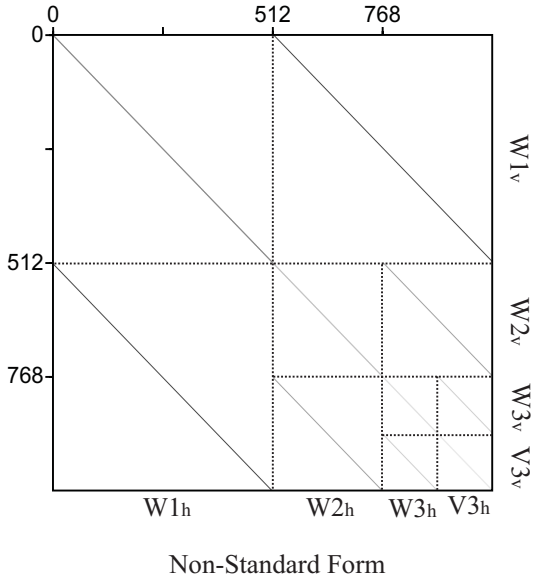

Figure 4.6: The fourth-order FD operator is projected on a NSF wavelet basis having $J = 3$ resolution approximation spaces. Coefficients different from zero are plotted in black. On each sub-grid the Daub4 wavelet basis constructs scaled versions of the initial FD operator (diagonal blocks). The FD operator is constructed in the so called Non-Standard Form (Beylkin, 1992), that results from an expansion of the operator in a telescopic series. Note that coefficients distributed in parallel bands around the diagonal encode interaction coefficients, that are necessary to interchange information between different resolution grids.

The non-standard form

Another operator representation in a wavelet-type expansion was introduced by Beylkin (1992). In contrast to the STF, the so called Non-Standard Form (NSF) of an operator results from a combination of wavelet projections and the expansion in a telescopic series. The resulting spectral domain is not the standard wavelet space, but a space that holds contributions from both, scaling and wavelet information, on each resolution scale (see Appendix A for further details).

An illustration of an operator projected in NSF is shown in Figure 4.6. As for the STF, diagonal blocks hold scaled versions of the initial operator projected in the V_0-space. Additional coefficients are aligned in parallel bands around the diagonal, that describe interactions between a given approximation scale with all the coarser scales.

The expansion in a telescopic series results in an *apparent* decoupling of resolution scales in the NSF, since, for example, a standard matrix-vector product $A_j \times x_j$ is applied on each resolution scale independently from other scales (Beylkin, 1992). The resultant vector (b_j) holds scaling (s_j) and wavelet (d_j) contributions from each resolution scale j $(b_j = (d_j, s_j))$. In order to obtain a standard wavelet expansion $(\sum_{j=1,J}^{J} d_j + s_J)$ from

the NSF representation, additional wavelet projections are applied on each resolution scale. These additional projections cannot be decoupled and are controlled by the finest resolution space. Beylkin and Keiser (1995) applied the NSF to solve non-linear PDEs, such as Burger's or Navier-Stokes equations, and provided performance and stability analysis.

4.3.3 Time domain FD approaches

Over the last years different strategies have been developed that try to couple the favourable multi-resolution wavelet formulation with standard forward modelling schemes for strong formulations of linear PDEs (Bacry et al., 1992; Lazaar et al., 1994; Joly et al., 1994; Wu and McMechan, 1998; Jameson and Miyama, 1999; Operto et al., 2002). Joly et al. (1994, 1995) showed seismic wave simulations using a projection on an orthogonal wavelet bases, though their attempt was limited to rather simple model configurations. Following a similar approach, Wu and McMechan (1998) investigated a FD-wavelet formulation for more complex heterogeneous models using the first-order hyperbolic wave equation. Unfortunately, the model complexity is significantly reduced, since they applied a local homogeneity assumption to render computations more efficient.

A nice application of a wavelet-based PDE solver for time evolution problems was proposed by Bacry et al. (1992). Following ideas of Liandrat and Tchamitchian (1990) and Perrier and Basdevant (1988), they noted that each resolution approximation space in a wavelet decomposition is related to a characteristic spatial FD discretization and time extrapolation scheme. If the spatial resolution is refined through a space-adaptive procedure, then the time step should also be refined in order to maintain the stability and accuracy of the numerical scheme. They implemented space adaptivity using an approach proposed by Perrier and Basdevant (1988), added a time-adaptive component, and applied their scheme to linear and non-linear PDEs.

More recently, Operto et al. (2002) developed TDFD modelling schemes for seismic wave propagation simulations in structurally complex models. They formulated the 2D velocity-stress FD method of Virieux (1984) in the time-space-wavelet domain using Daub4 wavelets. The first-order hyperbolic wave equation is discretized in the physical domain and then projected in the wavelet space using the Daub4 wavelet basis. Spatial wave-field coordinates and spatial differential operators are decomposed on the wavelet basis following Beylkin et al. (1991).

In contrast to Wu and McMechan (1998), they developed two TDFD schemes for arbitrary heterogeneous media where the local homogeneity condition is eliminated. The first scheme is a pure spectral approach where wave-field simulations are entirely performed in the wavelet domain. Even though computations have been optimised by the introduction of two different space-adaptivity strategies, the computation of convolution-type derivative-medium parameter products significantly limited the computational performance of their approach. Therefore, Operto et al. (2002) developed a second strategy that uses well-known ideas from pseudo-spectral methods. The pseudo-wavelet TDFD approach avoids the computation of the convolution-procedure in the wavelet domain through inverse transformation in the physical domain. At each time step, their scheme

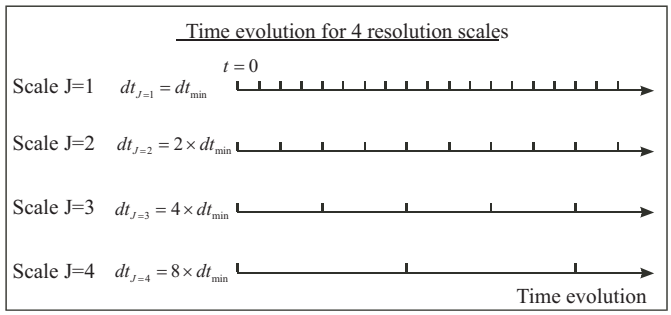

Figure 4.7: Cartoon showing time adaptivity for a wavelet decomposition on $J = 4$ resolution scales. The finest approximation space ($j = 1$) is assigned the finest time step, denoted by dt. Then, subsequently coarser scales have time-steps that double when going to the next coarser scale. In this example we assumed Daub4 wavelets that double the spatial discretization under resolution scale changes (from finer to coarser).

requires an inverse and a forward wavelet transform in order to compute the derivative-medium parameter product in the physical domain.

Time adaptivity, as described by Bacry et al. (1992) for the advection-diffusion equation, has not been implemented in both of their approaches. The main reason that prevented an adaptive time-stepping, was the interaction between resolution scales, which is expressed in the finger-band structure of the FD operator in the wavelet basis in Figure 4.5. Ideally, we would like to construct a wavelet expansion were different resolution scales are sufficiently decoupled. Then, we would be able to assign an appropriate time-step for each scale level (see Figure 4.7). As is shown in Appendix A, the wavelet expansion algorithm is controlled by the finest discretization applied in the V_0 space. Since wavelet resolution scales are coupled through interaction coefficients, an obvious time adaptivity implementation, as shown in Figure 4.7, is not easy to implement.

4.3.4 Frequency domain FD approaches

One possibility to eliminate problems related to the time discretization in a FD strong formulation, is the transformation of the equations in the temporal Fourier domain. Since in the frequency domain no temporal sampling is required, one of the main handicaps of wavelet-based FD schemes in the time-domain is eliminated.

Frequency domain finite-difference modelling (FDFD) denotes a strong formulation of the PDEs, where the hyperbolic wave equation is initially developed in the time domain and then projected on the Fourier basis. Since time evolution is eliminated, FD wave propagation simulations are carried out for a set of discrete frequency components, that ideally represent the Fourier spectrum of the wave simulation under inspection. In practice, the hyperbolic wave equation in the Fourier space is recast into a matrix-type

formulation:

$$\nabla^2 u = \frac{1}{c^2}\omega^2 u + b \quad \Rightarrow \quad A \times u = b \tag{4.1}$$

where b denotes the external source function, also called right-hand side (RHS), u the unknown wave-field solution, and A the complex impedance matrix.

While in TDFD modelling, at each time-step, matrix-vector products are computed in order to obtain an update of the wave-field solution, in FDFD modelling the complex impedance matrix A needs to be constructed for each frequency component f_i. Then wave-field solutions can be computed by either *inverting*, or estimating an effective *inverse* of the matrix A, for each frequency component separately.

One important feature that allows the formal inversion of the matrix A, in order to compute separate frequency domain solutions, is the introduction of absorbing boundary conditions to simulate infinite model dimensions. The matrix A in the continuous Equation 4.1 is formally inverted without any difficulties. The procedure becomes critical when passing over to a discrete numerical grid, in this case a Cartesian FD grid, since normal frequency modes corresponding to the characteristic length of the grid will cause strong wave-reflections on the boundaries. In general, this problem can be avoided by adding a complex frequency component to the normally real-valued discrete frequency, that acts as a damping term in the complex space. The alteration of the solution due to the artificial complex component is, in general, eliminated through an un-damping procedure in the time-domain. Unfortunately, it can only be applied correctly, when a large number, i.e. theoretically an infinitesimal number, of frequency components has been computed in the frequency domain and inverse-transformed in the time domain.

One of the great advantages of frequency domain modelling is the possibility to compute single frequency responses instead of complete wave-field time seismograms. The single frequency response is of great interest for seismic risk analysis of e.g., engineering structures. Therefore, I added PML (Perfectly Matched Layers, see Berenger, 1994, for details) absorbing boundary conditions to the Equation 4.1. Exact computation of the inverse matrix A^{-1} is not considered because of the extremely large computational resources required to perform the inversion and to store the matrix in RAM or disk memory afterwards (Rewienski, 1999). However, an effective inverse can be computed through factorizing the matrix A into a lower- and an upper-triangular matrix.

Matrix factorization schemes are also called *direct solvers*, since the LU-factors permit the computation of an exact direct wave-field solution. With the help of the LU-factors the initial matrix equation in Equation 4.1 becomes,

$$(L \cdot U) \times u = b \quad with \quad L \cdot U = A \tag{4.2}$$

which easily solves the matrix equation, without computing the inverse A^{-1}, in a two

step procedure:

$$\begin{aligned} L \cdot w &= b \\ U \cdot u &= w \end{aligned} \tag{4.3}$$

The performance of a matrix factorization scheme depends mainly on the number of non-zero coefficients and their location in the matrix. In FDFD forward modelling, the structure of the matrix is controlled by the discretization scheme applied to the wave equation (Rewienski, 1999). In general, FD discretizations lead to an overall sparse matrix, where matrix coefficients are more-or-less distributed in bands around the main diagonal. During LU factorization additional numerical fill-in coefficients have to be stored, in order to properly separate A into a lower- and an upper-triangular matrix (Golub and van Loan, 1996).

The numerical fill-in significantly limits the application of direct matrix equation solvers since, in addition to the large impedance matrix A, numerical fill-in needs to be stored. Moreover, the fill-in is difficult to estimate before the modelling starts. Matrix solvers based on a direct LU factorizations are not appropriate for frequency domain seismic wave propagation simulations in 3D media, since available computer resources are largely exceeded during the factorization process (Mulder and Plessix, 2002).

Another possibility to solve the matrix equation is through the application of an iterative solver scheme. Iterative solvers require the construction of the matrix A, an initial wave-field solution u_0 and the RHS vector. Then approximated wave-field solution are computed by an iteration process, that during each loop of the iteration refines the solution $u_0 \Rightarrow u_i$. The iterative loop stops if either the solution approximation for a given iteration count converges to the desired solution (u) within some pre-defined error norm $\|u - u_i\| < tol$, or the iteration count reached a pre-defined maximum amount of permitted iterations $n_{it} > n_{it}^{max}$.

Ideally, the initial solution u_0 closely approximates the final desired solution u, such that fast convergence of the iterative loop is guaranteed. The update of the approximated solution u_i during the iterative loops is performed through matrix-vector and dot-products, as well as left- and right-preconditioning to influence the convergence of the scheme. Therefore, the number of non-zero coefficients has a direct influence on the performance of an iterative scheme, even though the number of coefficients, once constructed, are not as-far-as crucial as for direct solvers.

The main handicap of *iterative solvers* compared to *direct solvers* is that numerical convergence of the iterative scheme can not be guaranteed and, in general, depends strongly on a good initial solution. Moreover, the obtained solution is only an approximation that resembles the exact *direct* solution up to a pre-defined tolerance level. Unfortunately, a good initial solution that closely approximates the desired solution is not easy to estimate. A popular approach therefore investigates how the matrix structure and the absolute numerical values in the matrix and RHS may be modulated in order to allow fast and stable convergence, even if the initial solution is far from close to the desired solution. This procedure, called *matrix preconditioning* (Golub and van Loan, 1996), has

become increasingly important and often the success of a numerical solver based on an iterative scheme entirely depends on a good preconditionning.

Iterative solvers are often applied in FMG methods to either compute a preliminary solution on a coarse discretized grid that is further refined by a multi-grid procedure, or to correct the solutions on different resolution levels during the passage of a multi-grid V- and W-cycle (Debicki, 1999). In order to overcome the ambiguity and computational effort necessary to perform a sequence of multi-grid V- and W-cycles, Gines et al. (1999) developed a wavelet-based FMG method that relies on a multi-resolution LU matrix factorization. They profit from the multi-scale representation in the wavelet basis, where grid interactions between different resolution approximations spaces are accounted for automatically. Their approach defines a multi-resolution LU factorization with the help of a NSF matrix representation on a wavelet basis. The matrix A, that corresponds to the specific matrix-equation at hand, is first constructed in the wavelet basis and projected in the NSF space. The multi-resolution LU factorization computes a standard LU decomposition of the homogenized matrix A in the $V \times V$-space of the wavelet expansion, and then finds subsequently finer LU-factor contributions through a NSF-wavelet projection procedure. Numerical fill-in, that can not be suppressed by the wavelet formulation, is significantly reduced by an efficient thresholding procedure applied to the wavelet coefficients.

Gines et al. (1999) applied the new approach to dense matrices, that result from electro-magnetic simulations based on an integral equation method. They obtained significantly speed-up for the factorization procedure in the wavelet space, compared to standard LU schemes in the physical domain. Although their results look promising, one important initial requirement that entirely controls the efficient application of the wavelet-based LU direct solver is not fulfilled for FDFD discretizations of wave propagation problems.

Gines et al. (1999) applied the wavelet solver to matrices that are dense in the physical space. Then, already the transformation in the wavelet space reduces the number of non-zero coefficients in the projection and, moreover, efficient numerical thresholding is supported by the wavelet formulation. In contrast, FDFD discretizations of the wave equation lead to an extremely sparse impedance matrix.

As was illustrated for a 1D-signal in Table 4.1, the projection of a sparse signal in the wavelet domain rather increases the number of non-zero coefficients as a function of the resolution scales used. We therefore expect a similar increases of matrix coefficients after wavelet expansion. Moreover, *wavelet fill-in* caused by the factorization procedure will even increase the already larger number of non-zero coefficients. One of the main interests of the multi-resolution LU solver is data compression through wavelet formulation. Unfortunately, this is not the case for the FDFD wave equation and can not be compensated i.e., becomes even worse due to matrix fill-in during the matrix factorization.

4.3.5 Discussion

Numerical wave propagation simulations are necessary when the wave-field response for complex heterogeneous media is required. The wave equation can be discretized by using

a weak-, average- or strong-formulation of the PDEs, where the main difference comes from the construction of the corresponding numerical grid and how the corresponding equations are verified on the grid. Weak- and average-formulations provide powerful modelling schemes, where equations are verified approximately over elements or volumes making up the grid. Their overall performance, in terms of accuracy and computational speed, depends mainly on the grid construction technique applied. Very popular are mesh refinement techniques, that automatically adapt the numerical grid with respect to local complexities in the model and the behaviour of the wave-field solution during propagation.

In contrast, strong formulations of the wave equations obtain exact solutions on a naturally Cartesian grid, using FD type discretization techniques in the physical domain or spectral spaces. In order to release restrictions due to Cartesian grids, FD methods have been extended to allow wave simulations on manually combined grids of irregular size.

Another approach that performs computations on a set of numerical grids of different resolution is provided by the multi-grid framework. Multi-grids are applied as preconditioners for iterative solvers of matrix-type PDEs. They decompose computations with respect to the frequency content through sequences of V- and W-cycles, in order to calculate resolution adapted iterative wave-field contributions. The grid combination is performed manually with respect to error measurements during the computations, which may prohibit fast and efficient convergence.

Wavelets provide a natural multi-scale representation, and therefore have widely been used for numerical modelling of wave propagation phenomena. Unfortunately, TDFD modelling is handicapped by shortcomings in the implementation of time adaptivity and numerous computational expensive wavelet expansions, while multi-resolution LU factorization for wave simulations in the temporal Fourier space (FDFD) requires an initially dense impedance matrix to render the approach efficient. Standard FDFD modelling is limited because of either significant amount of computer resources required to perform a direct matrix factorization, or by a large amount of iteration steps to converge to an approximate iterative solution. Moreover, the convergence of the iterative scheme cannot, in general, be guaranteed.

In view of the present shortcomings in TDFD and FDFD wave simulation schemes, it seems reasonable to combine the direct solver with the iterative solver technique, in order to allow FDFD wave-field simulations for strongly heterogeneous media in three spatial dimensions. Since an automatic multi-grid formulation is provided through a wavelet expansion, I investigate the impact of space and wavelet-based numerical preconditioning in an iterative matrix solver scheme.

4.4 A Multi-Level Direct-Iterative Solver for seismic wave propagation modelling: Space and wavelet approaches

Bernhard Hustedt, Stephane Operto and Jean Virieux

UMR Geosciences Azur, CNRS-UNSA-UPMC 250, rue Albert Einstein - Sophia Antipolis, 06560 Valbonne, France

Manuscript submitted to Geophysical Journal International

4.5 Abstract

We present a new numerical modelling approach for frequency domain finite-difference (FDFD) wave simulations. The new approach is developed as an extension to standard FDFD modelling schemes, when wave propagation simulations are performed in large-scale two-dimensional or three-dimensional models with complex heterogeneous rheology. Partial differential equations are presented in matrix-type form. Wave-field solutions are computed on different coarse- and fine-discretized numerical grids by a combination of a direct solver with an iterative solver. Two different connection strategies are designed. Both compute a coarse-grid wave-field solution using a direct matrix solver. The obtained solution is projected on a fine-discretized grid, which is used as an initial solution for an iterative solver to compute the desired fine-grid solution. The wave-field projection that combines coarse- and fine-grids, is either based on a space interpolation scheme, called the Direct-Iterative-Space Solver (DISS), or on a multi-scale wavelet expansion, called Direct-Iterative-Wavelet Solver (DIWS). The DISS scheme mimics a nested iteration scheme of a Full Multi-Grid (FMG) method, since numerical grids are prolonged by a simple bilinear interpolation scheme. The simple grid combination leads to wave-field solutions that are affected by spatial phase-shift artefacts (aliasing), which may be suppressed by a large amount of iteration steps or a standard V- and W-cycles sequence between grids. The actual DIWS matrix construction implementation is computationally more expensive, though the wavelet iteration scheme guarantees fast and stable iterative convergence. Coarse-grid wave-field solutions are combined with fine-grid solutions through the multi-resolution scaling property of a standard orthogonal wavelet expansion. Since the wavelet transformation accounts for grid interactions, phase-shift artefacts are greatly reduced and significantly less iteration steps are required for convergence. We demonstrate the performance and accuracy of the DISS and DIWS strategies for two complex two-dimensional heterogeneous wave simulation examples.

4.6 Introduction

Seismic wave propagation modelling is a useful tool to study the response of complex geological structures under excitation of earthquake waves. Moreover, synthetic seismograms that result from efficient forward modelling schemes are necessary to invert e.g., multi-source-receiver seismic exploration data. Unfortunately, synthetic wave propagation simulations either allow fast and accurate computations but are incomplete, or they provide the required precision for the complete wave-field solution but then traditional schemes based on Cartesian coordinate systems are slow and dispersive, therefore demand unrealistic high computer memory and CPU-time resources. Very many different

approaches have tried to resolve this discrepancy in order to make highly accurate numerical modelling feasible.

In recent years, the choice of a forward modelling method best adapted for simulating large scale geological models was dominated by asymptotic methods, such as the ray-tracing approach (Červený et al., 1977). Their main interest is high computational efficiency to allow the geological interpretation of large data volumes on a standard basis. Despite of many advantages, these methods are based on a high frequency approximation of the wave equation, and therefore provide incomplete results. In the vicinity of complex rheology models the high frequency approximation is not valid anymore and standard asymptotic methods do not provide desired solutions.

Nowadays 3D and 4D time-lapse data acquisition in seismic exploration and/or the instrumentation of sedimentary basins and foothills by large seismic arrays have become standard tools in seismology. In order to profit to a maximum of these enhanced data acquisition techniques, geoscientists need to simulate large frequency bandwidth data with increased numerical precision for increasingly larger complex models.

Full-waveform methods such as finite-difference (FD) techniques on regular grids provide complete solutions to the wave equation. Due to developments of massive parallel computers structures their usage became feasible. As a consequence, FD modelling schemes enjoy great popularity for 2D problems since they provide accurate waveform results for complex rheology structures, while, at the same time, their implementation stays rather simple (Virieux, 1984, 1986). Even though FD methods are also applied to realistic 3D modellings (Graves, 1996; Olsen and Archuleta, 1996) with a rather low frequency content ($< 0.5Hz$), their widespread application is mainly limited by the huge computer memory and CPU time requirements. Simulations for large multi-source experiments stay an exception and are far from being a standard procedure (Mulder and Plessix, 2002).

Over years, advances in numerical wave propagation modelling were mainly aimed to either enhance the performance of standard FD modelling schemes or to investigate new numerical approaches in order to handle the problematic related to the simulation of large data volumes with sufficiently high accuracy. Graves (1996) and Moczo et al. (1999) developed memory optimization techniques that permit 3D FD modellings on a single-processor desktop workstation. Other FD optimization techniques vary the spatial and temporal discretization of the simulation parameters. The common idea behind these techniques is the distribution of computational power to model regions corresponding to the local model complexity. For example, zones with complex structure need small grid spacing and time stepping, while zones with smooth parameter variations can be modelled with a relatively coarse spatial and temporal discretizations. Varying the spatial grid size in the model (Pitarka, 1999), combining FD grids with different spatial (Moczo, 1980; Jastram and Behle, 1992) and temporal (Falk et al., 1998; Tessmer, 2000) discretizations enhance the numerical performance of the modelling. Unfortunately, the wave-field transfer from one grid to the next is critical and rather complicated. Moreover, the accuracy of proposed implementations for strongly heterogeneous complex models is questionable. In order to prevent problematics caused by manual grid changes, Operto et al. (2002) used the wavelet transform to introduce a time domain FD (TDFD) modelling scheme on grids

of different resolution. In their approach, grids of different spatial resolution and their interactions were introduced by the wavelet transform. Although space-adaptivity was incorporated in their approach, grid coupling in the wavelet domain and convolution type projection procedures resulted in rather heavy computational cost compared to standard FD techniques.

Hestholm and Ruud (1998) and Xie et al. (2002) among others formulated FD modelling schemes on curvilinear grids. Since free-surface boundary conditions for arbitrary topographies are implemented exactly, no further grid-refinement as necessary for FD modellings on regular grids is needed, which increases the efficiency of the FD scheme.

Pseudo-Spectral methods enhance computational efficiency and accuracy by computing spatial derivatives in one domain while the principal equations are solved in another domain (see Fuchs and Muller, 1971, for example). Moreover, they address problems related to the correct free-surface representation (Tessmer and Kosloff, 1994; Igel, 1999) which is a main drawback of FD methods defined on rectangular Cartesian grids. Unfortunately, pseudo-spectral methods are restricted to smooth surface variations only.

In recent years, other techniques that rely on mesh generation have dominated developments of forward modelling schemes. Faccioli et al. (1996) and later Komatitsch and Vilotte (1998); Komatitsch and Tromp (1999) developed a scheme for wave propagation modelling for seismology, called spectral elements, that is based on finite-element (FE) discretizations (Zienkiewicz and Morgan, 1982). The main advantages are exact propagation of surface waves in the presence of topography and fast implementation schemes (Domain Decomposition using parallel computations). Fluid-solid interfaces and anisotropy have been included. More recently, their approach has been extended to mixed spectral elements (Cohen and Fauqueux, 2000), that provide even higher computational efficiency and flexibility than the spectral elements approach.

Finite-element techniques require the computational grid to be constructed before the modelling starts. Therefore mesh generation is a key step of FE approaches that controls the accuracy of the scheme (Sambridge et al., 1995). Inaccuracies may occur when the mesh is not constructed correctly. They will cause errors in the final wave-field solution which are not detectable by the user. Therefore, LeVeque (1997) formulated a FE modelling scheme for hyperbolic systems of equations based on standard Cartesian grids that dynamically applies grid-refinements in both space and time. Still, if repeated wave propagation simulations have to be performed because small model parts changed due to new acquired information e.g., for 4D time lapse simulations, the complete mesh generation and wave propagation simulation have to be recomputed each time the model changes.

Another group of methods, called multi-grid approaches (Hackbusch, 1978), perform simulations using direct and iterative matrix equation solvers on a set of numerical grids having different spatial resolution. The elimination of low-frequency (smooth) wave-field components on a given (fine-discretized) grid are difficult to eliminate by an iterative solver. Therefore, multi-grid techniques introduce a sequence of grids having different resolution, in order to treat the components of the approximative solution with respect to their characteristic frequency content on the best adapted discrete numerical grid.

Ideally on each resolution grid, the grid spacing is chosen such that the represented

solution component (e.g., that may be a rather low frequency component on the finest discretized grid) becomes a high frequency one with respect to the local grid spacing. Then iterative solvers may be applied effectively. Numerical grids are combined by numerous passages through so called V- and W-cycles, where the combination of V- and W-structures depend on the behaviour of the solution during iteration steps. A nice introduction to the multi-grid philosophy was given by Briggs (1987).

In this article, we propose a new FD scheme that addresses the problematic of large scale wave propagation simulations in complex media for multi-source experiments carried out on a standard basis. A typical example would be the exploration for hydrocarbons but also the instrumentation of a zone with high seismic risk such as e.g., Mexico City (Sanchez-Sesma, 1983). Even though today spectral elements are superior over FD methods in terms of CPU-time requirements and accuracy of the solution (free surface), the ambiguity caused by the mesh generation and necessary complete recalculations for small model changes which are not required for FD modellings (Robertsson and Chapman, 2000), motivates a deeper investigation of FD methods.

To our knowledge, 3D wave propagation simulations are mainly carried out by the TDFD rather than by frequency domain finite-differences (FDFD), because of higher computational efficiency (Mulder and Plessix, 2002) and easy extension to distributed memory computer structures (Olsen et al., 1995). For multi-source experiments in the framework of waveform inversions, the method of choice has been the FDFD technique, because solutions for multiple right-hand sides (RHS) are computed at minimal additional cost (Pratt, 1990), and non-linear rheology, such as attenuation, is easily incorporated in the scheme. The main step in FDFD is the inversion of a massive matrix equation, and therefore FDFD schemes are limited by the performance of either direct matrix factorization or iterative solver schemes. Despite of their advantages, both solver approaches (direct and iterative) have only been competitive for rather limited 2D models (Mulder and Plessix, 2002).

In order to benefit from the classic advantages of FDFD over TDFD modelling for large 2D and 3D media and extended frequency ranges ($f = 0 - 10Hz$), we propose the combination of a direct and an iterative solver scheme in a multi-grid framework. The direct solver is mainly limited by the computer memory available. Therefore, the new Direct-Iterative Solver (DIS) will be used to compute an approximate FDFD solution for a coarse-grid model, that results from smoothing the fine-discretized model and accordingly adapting the spatial sampling to allow the run of the direct solver scheme. Then the iterative scheme is used to fill the gap between the coarse-grid solution and the desired fine-grid solution. Since the performance of an iterative solver scheme strongly depends on a stable preconditioned matrix and the initial solution provided, we will use the exact reduced-model solution to approximate the desired fine solution. This strategy is similar to a *nested iteration* procedure in multi-grid methods (Briggs, 1987). This then permits accelerated convergence of the iterative part with respect to a zero initial solution. The critical point in our approach will be the combination of the two solver schemes, such that the iterative solver takes maximum advantage of the multi-grid framework.

In this paper, we first present a new FDFD modelling scheme that is based on a first-order hyperbolic formulation of the 2D SH-wave equation. By means of this formulation

we discuss the general problematic of FDFD modelling. Then we introduce the general idea of a combination of a direct and an iterative solver scheme to overcome the limits of separate usage of one of the schemes only. Moreover, we present two different DIS multi-level approaches; the first one, called Direct-Iterative-Space Solver (DISS), is similar to a *nested iteration* scheme and is based on space linear interpolation when moving from one grid to the other one. The second one, called Direct-Iterative-Wavelet Solver (DIWS), uses an intrinsic feature of an orthogonal wavelet transform and can be directly compared to a *Full Multi-Grid method* (FMG). Both schemes will be discussed in detail and their performances are tested on two heterogenous 2D models. Although we show wave-field solutions for 2D media only, the underlying aim of our developments are FDFD modellings of realistic complex 3D media. Since developments carried out for 2D models set important directions leading to the actual DIS approach, we present it here.

4.7 Frequency domain forward modelling

Frequency domain forward modelling in two-dimensional media for SH-wave propagation may be formulated using a velocity-stress finite-difference scheme that automatically leads to the staggered grid geometry developed in TDFD modelling (Virieux, 1984). We write the SH-wave equation as a first-order system and construct the corresponding complex impedance matrix in the frequency domain.

We introduce the elastodynamic equations combined with Hooke's law for SH-wave propagation in the y-direction (Virieux, 1984):

$$\begin{aligned} \rho(x,z)\frac{\partial v_y(x,z,t)}{\partial t} &= \frac{\partial \sigma_{xy}(x,z,t)}{\partial x} + \frac{\partial \sigma_{zy}(x,z,t)}{\partial z} + S(x,z,t) \\ \frac{1}{\mu(x,z)}\frac{\partial \sigma_{xy}(x,z,t)}{\partial t} &= \frac{\partial v_y(x,z,t)}{\partial x} \\ \frac{1}{\mu(x,z)}\frac{\partial \sigma_{zy}(x,z,t)}{\partial t} &= \frac{\partial v_y(x,z,t)}{\partial z} \end{aligned} \tag{4.4}$$

where $v_y(x,z,t)$ is the velocity field in the time domain, $\rho(x,z)$ the density, $\mu(x,z)$ the shear modulus, $\sigma_{xy}(x,z,t)$ and $\sigma_{zy}(x,z,t)$ shear stresses, and $S(x,z,t)$ the external source. With a slight abuse of notation we assume the shear stress and velocity components to be normalized (e.g., $\sigma_{xy} = \sigma_0 \cdot \sigma_{xy}^{'}$ and $v_y = v_0 \cdot v_y^{'}$, where $\sigma_{xy}^{'}$ and $v_y^{'}$ are the un-normalized wave-field components). The normalisation becomes necessary in order to stabilise subsequent matrix computations. Following TDFD developments for electromagnetic waves, we add PML absorbing boundary conditions (Berenger, 1994) to simulate infinite media boundaries. We separate spatial derivatives appearing in the first equation for the x- and z-direction and add a damping function term (γ) for each spatial component that only takes effect in the absorbing layer (see Operto et al., 2002, for details):

$$
\begin{aligned}
\rho(x,z)(\frac{\partial v_{yx}(x,z,t)}{\partial t} + \gamma_x(x) \cdot v_{yx}(x,z,t)) &= \frac{\partial \sigma_{xy}(x,z,t)}{\partial x} + S(x,z,t) \\
\rho(x,z)(\frac{\partial v_{zy}(x,z,t)}{\partial t} + \gamma_z(z) \cdot v_{zy}(x,z,t)) &= \frac{\partial \sigma_{zy}(x,z,t)}{\partial z} \\
\frac{1}{\mu(x,z)}(\frac{\partial \sigma_{xy}(x,z,t)}{\partial t} + \gamma_x(x) \cdot \sigma_{xy}(x,z,t)) &= \frac{\partial v_{yx}(x,z,t)}{\partial x} + \frac{\partial v_{zy}(x,z,t)}{\partial x} \\
\frac{1}{\mu(x,z)}(\frac{\partial \sigma_{zy}(x,z,t)}{\partial t} + \gamma_z(z) \cdot \sigma_{zy}(x,z,t)) &= \frac{\partial v_{yx}(x,z,t)}{\partial z} + \frac{\partial v_{zy}(x,z,t)}{\partial z}
\end{aligned}
\tag{4.5}
$$

The two velocity wave-fields v_{yx} and v_{zy} can be combined to the physical v_y-wave-field through simple addition $v_y = v_{yx} + v_{zy}$. We transform the system of equations in the Fourier domain and introduce the new variables $\xi_x(x,\omega) = 1 + i\gamma_x(x)/\omega$ and $\xi_z(z,\omega) = 1 + i\gamma_z(z)/\omega$ to simplify the equations:

$$
\begin{aligned}
i\omega\xi_x(x,\omega)\rho(x,z) \cdot v_{yx}(x,z,\omega) + \frac{\partial \sigma_{xy}(x,z,\omega)}{\partial x} &= -S(x,z,\omega) \\
i\omega\xi_z(z,\omega)\rho(x,z) \cdot v_{yz}(x,z,\omega) + \frac{\partial \sigma_{zy}(x,z,\omega)}{\partial z} &= 0 \\
i\omega\xi_x(x,\omega)\frac{1}{\mu(x,z)} \cdot \sigma_{xy}(x,z,\omega) + \frac{\partial v_{yx}(x,z,\omega)}{\partial x} + \frac{\partial v_{yz}(x,z,\omega)}{\partial x} &= 0 \\
i\omega\xi_z(z,\omega)\frac{1}{\mu(x,z)} \cdot \sigma_{zy}(x,z,\omega) + \frac{\partial v_{yx}(x,z,\omega)}{\partial z} + \frac{\partial v_{yz}(x,z,\omega)}{\partial z} &= 0
\end{aligned}
\tag{4.6}
$$

The resulting system of Equation 4.6 is solved for each angular frequency component ω_i separately.

4.7.1 Matrix construction

The system of Equation 4.6 is discretized using a staggered grid geometry (Virieux, 1984; Levander, 1988) and recast into matrix-type form ($\mathbf{A} \times x = b$). In the case of the velocity-stress formulation of the first-order hyperbolic wave equation, mainly two different matrix construction techniques are possible. We may follow standard TDFD modelling approaches (Graves, 1996) and multiply medium parameters, such as density $\rho(x,z)$ and shear modulus $\mu(x,z)$, angular frequency ω and the PML function $\xi_(,\omega)$ with the partial derivatives of the wave-field components. We follow another strategy that combines all model and PML contributions on the diagonal matrix entries, because it allows the development of rather simple and computationally fast algorithms. Then the matrix-type equation that is equivalent to the system of Equations 4.6 writes:

$$
\begin{pmatrix}
i\omega\xi_x\rho & 0 & \partial/\partial x & 0 \\
0 & i\omega\xi_z\rho & 0 & \partial/\partial z \\
\partial/\partial x & \partial/\partial x & i\omega\xi_x\frac{1}{\mu} & 0 \\
\partial/\partial z & \partial/\partial z & 0 & i\omega\xi_z\frac{1}{\mu}
\end{pmatrix}
\begin{pmatrix} v_{yx} \\ v_{yz} \\ \sigma_{xy} \\ \sigma_{zy} \end{pmatrix}
=
\begin{pmatrix} -S \\ 0 \\ 0 \\ 0 \end{pmatrix}
\tag{4.7}
$$

The elements of the impedance matrix **A** are complex valued and depend on the media properties $\rho(x, z)$ and $\mu(x, z)$ and on the angular frequency ω. Since each point on the FD grid is coupled to its nearest neighbours only, the matrix **A** is sparse. The full matrix contains $(4 \cdot nx \cdot nz)^2$ elements from which, in the case of second-order staggered grid FD derivative approximations, $6 \cdot nx^2 + 6 \cdot nz^2 + 4 \cdot nx \cdot nz$ are different from zero. Only diagonal matrix-blocks depend on the physical model parameters and on the frequency. The off-diagonal blocks i.e., spatial derivative operators, are constructed only once for all frequency components ω_i before the modelling starts. Moreover, the non-zero frequency-dependent coefficients are all distributed on the diagonal. Therefore, constructing the complex impedance matrix for several angular frequency components can easily be performed by simply replacing diagonal matrix coefficients. In the current implementation, the matrix is constructed in sparse CSR (Compact Sparse Row) or HB (Harwell-Boeing) format, that allows fast matrix computations, such as matrix-vector products.

4.7.2 The Direct-Iterative-Solver approach

The bottle neck in any frequency domain modelling scheme is the factorization of the complex impedance matrix (Štekl and Pratt, 1998). In general, the desirable matrix inversion is not performed, since the sparse matrix structure will result in a rather dense inverse matrix, and therefore the number of non-zero coefficients to compute or even to hold the inverse matrix in memory is too large to be acceptable. To avoid the computation of the inverse matrix, typically two different solution strategies are applied.

An effective decomposition might be obtained by computing the LU factorization of the impedance matrix. In this case, which is called the direct solver approach, the system $\mathbf{A} \cdot x = b$ is converted into two triangular systems using Gaussian elimination, which then permits fast computations of solutions (Golub and van Loan, 1996). The algorithm divides the matrix **A** into a lower triangular (**L**-factor) and an upper triangular (**U**-factor) part of the form $\mathbf{L} \cdot \mathbf{U} = \mathbf{A}$. The fill-in that is created during the separation procedure (number of non-zero coefficients exceeding the number of non-zero coefficients of the initial matrix), is significantly reduced compared to the computation of the true inverse, and highly optimised preconditioners and scaling techniques make this procedure fast and convenient (Štekl and Pratt, 1998). Once the **LU** factors have been computed for each frequency component separately, they can be stored and wave-field solutions for multiple RHSs are obtained at low computational cost (Pratt, 1990). The direct solver approach is only limited by the computational fill-in to compute and store the **LU** factors.

The second approach provides an approximated matrix equation solution by an iterative scheme. The direct solver approach might be impractical because the **LU**-factors need to be constructed and additional matrix fill-in occurs during the factorization that may significantly increase memory requirements. In contrast, iterative methods generate a sequence of approximate solutions x^i, that are supposed to converge to the true solutions for some fixed tolerance error. Update of solutions is mainly performed through matrix-vector multiplications and dot-product computations and therefore, fast optimised computer structures can be exploited to the maximum. Moreover, significantly larger

model sizes may be treated, because numerical fill-in does not occur. The drawback is the finding of a good initial solution that closely resembles the desired true solution and an adapted iterative framework (e.g., multi-grids), such that fast iterative convergence can be guaranteed. In general, this is not at all a trivial task and modelling approaches exist that start iterations from a zero initial solution (Janod, 1999). Moreover, for each RHS the iteration procedure has to be repeated and one of the main advantageous features of frequency domain modelling is lost, if convergence of the iterative scheme is not fast enough.

4.8 The Direct-Iterative-Space Solver

Suppose we want to perform FDFD simulations for huge 2D models, large number of RHSs and frequency ranges where, for example, the corresponding real data could result from a marine seismic experiment. Even though for one RHS (source), TDFD would be the best adapted method for the simulation, the number of repeated computations for the numerous RHSs renders the TDFD approach inefficient. If we further assume that FDFD modelling using a direct solver technique is excluded because of the size to hold or factorise the complex impedance matrix, the only possibility to perform a FDFD simulation would be via an iterative procedure. Such a scenario, which becomes even more true for 3D modelling, underlines the need for a FDFD modelling scheme that is capable of treating large volume data. Nevertheless, FDFD modellings using an iterative approach suffer from similar restrictions as encountered for TDFD modellings for multi-source experiments, since iterations have to be computed for each RHS. The new scheme should profit to a maximum from the performance and uniqueness of wave-field solutions obtained by a direct solver, while at the same time it shall have the capabilities to treat large Earth models for high frequency ranges at an acceptable computational cost for multiple RHSs.

In view of this demand and the limits and strengths of the two existing solver techniques (direct and iterative solver) we propose their combination in a multi-grid formulation to form the Direct-Iterative Solver (DIS) approach. The key point in this combination will be the connection of the two solver schemes i.e., how a good initial iterative solution may be obtained and how the iterative convergence may be accelerated significantly.

4.8.1 Combination of two solver schemes

We combine the direct solver with the iterative solver by a *nested iteration* formulation. Typically, *nested iteration* is applied in a V-cycle of a *Full Multi-Grid* (FMG) approach. Two-dimensional (2D) SH-wave-field solutions (u^{2h}) are computed for a restricted coarse discretized model (V^{2h}) by the direct solver ($\mathbf{A}^{2h}u^{2h} = b^{2h}$), where h is the fine-grid spatial discretization step. Coarse, in the sense used here, implies that a finer model (V^h) FD discretization would be desirable but is computationally too expensive to be computed by the direct solver approach. We use a highly optimised multi-frontal technique to compute the **LU** matrix factorization, called MUMPS (Amestoy et al., 2001).

The next step involves the combination of the coarse grid solution with an iterative solver scheme in order to obtain the desired solution for a fine model discretization (u^h). Following the *nested iteration* approach, we prolongate the exact coarse-grid solution (u^{2h}) on a fine discretized grid using a simple bilinear interpolation scheme ($V^{2h} \Rightarrow V^h$). The prolongation operator is denoted by $\mathbf{I}_{2h}^h$. The prolongation result will then serve as an initial solution (v^h) for a GMRES iterative solver scheme developed by Frayssé et al. (1997).

$$\mathbf{I}_{2h}^h u^{2h} = v^h \tag{4.8}$$

We denote this approach the Direct-Iterative-Space Solver (DISS). The DISS approach is similar to the *nested iteration* part of multi-grid V-cycle, since the prolonged coarse-grid solution provides an acceptable initial solution for the GMRES iterative solver. Note that a complete FMG scheme using V- and W-cycles would first require the restriction of an approximative fine-grid solution on the coarse grid, which is called *Coarse Grid Correction* (CGC). A typical FMG V-cycle sequence is (f^h is the RHS vector):

1. Initial Iteration $v^h \leftarrow f^h - \mathbf{A}^h u^h$
2. `CGC` $f^{2h} \leftarrow \mathbf{I}_h^{2h}(f^h - \mathbf{A}^h v^h)$
   Approximate Solution $\Rightarrow v^{2h}$
3. Correct $v^h \leftarrow v^h + \mathbf{I}_{2h}^h v^{2h}$

(4.9)

We compared the convergence of the iterative scheme using the prolonged coarse-grid wave-field solution and a zero solution as a first initial approximation for the iterative scheme. Even though in both cases the iterative scheme converged in the given tolerance limits, the simulation using the *nested iteration* formulation required 50% less CPU-time.

For both direct and iterative solver schemes, we construct the complex impedance $\mathbf{A}$ directly for the corresponding grid discretization. In case the number of non-zero elements of the matrix for the fine-grid iterative part exceeds the actual free memory available, the construction *on the fly*, though costly, is possible. This is to say, that the iterative scheme does not necessarily need the matrix available in core memory at a given iteration step. In contrast, the matrix only contributes to the iteration through matrix-vector multiplications, dot-products and matrix preconditionings. Therefore matrix coefficients contributing to the actual computations may be constructed when needed (Pessel, 2000). The complete DISS procedure is shown in Figure 4.8 and Figure 4.9.

4.9 The Direct-Iterative-Wavelet Solver

We present a second DIS strategy that instead of space grid prolongations, relies on a rather natural multi-level formulation through orthogonal wavelet expansions. The

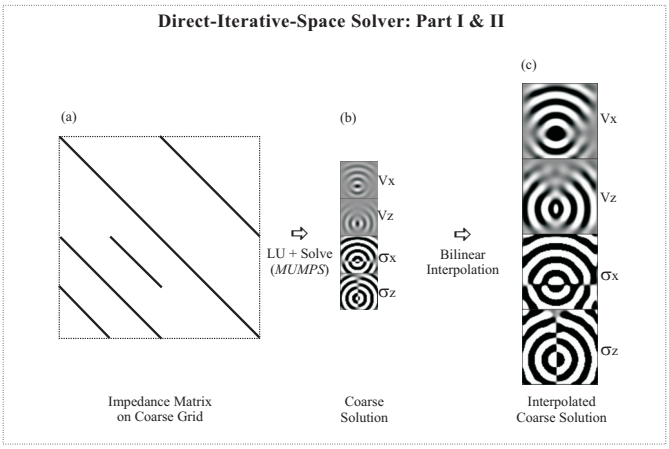

Figure 4.8: Flowchart showing the Direct-Iterative Solver approach: Part I and II. (a) We construct the complex impedance matrix for a coarse model discretization and compute its **LU** factorization using the MUMPS direct solver. (b) We compute coarse grid solutions for each source position and frequency component. (c) Coarse solutions are interpolated on a fine discretized grid using a simple bilinear interpolation procedure.

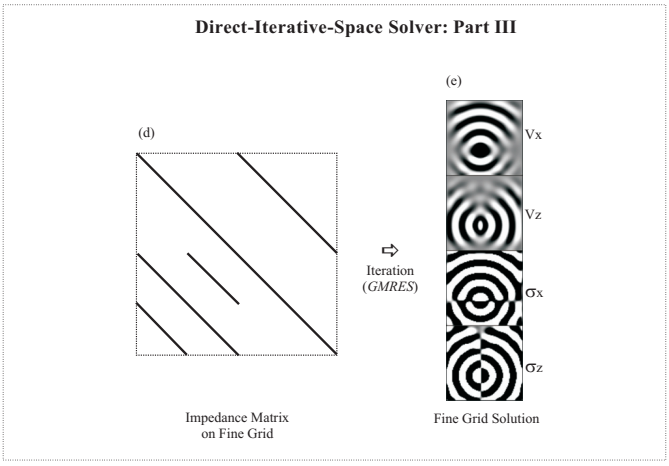

Figure 4.9: Flowchart showing the Direct-Iterative Solver approach: Part III. (d) We construct the complex impedance matrix for the fine discretized grid. The interpolated coarse solution in Figure 4.8(c) approximates the desired fine grid solution. Therefore, we use it as initial solution in a GMRES iterative solver scheme (e) which gives the final frequency map solution.

approach is denoted by Direct-Iterative-Wavelet Solver (DIWS). The wavelet transform permits us the direct construction of wavelet projected fine grid wave-field solutions, where contributions from all spatial frequency components and resolution approximation

grids are incorporated in the desired adapted way (Briggs and Henson, 1993; Beylkin, 1998). The wavelet based DIWS approach is directly comparable to a Full Multi-Grid (FMG) method, where iterations are performed simultaneously on a sequence of adapted resolution grids without the necessity to perform artifical V- and W-cycles. In the following, we demonstrate the enhanced iterative convergence of the DIWS scheme. For completeness, we use Daubechies wavelets with four vanishing moments throughout. The problem how to find the best adapted wavelet basis for the DIWS scheme is not addressed here.

4.9.1 The $V_J \times V_J$-space in a wavelet expansion

Without reviewing the theory of the discrete wavelet transform (DWT) we introduce some of its features that are especially important for our study. For a basic review of the why and how of the wavelet transform (WT), we refer to Mallat (1989) or Daubechies (1992) for further readings. In Appendix A, we give a short introduction to the wavelet theory which is mainly provided to set notations right and give a little understanding of the wavelet features used here.

The DWT decomposes a signal on a sequence of nested finite difference grids ($V_0 \supset V_1 \supset V_2 ... \supset V_j \supset V_{j+1} ... \supset V_J$) of decreasing resolution ($V_0 \Rightarrow V_J$). The finest resolution grid is denoted by V_0, the coarsest by V_J. The basis for each resolution approximation space V_j is constructed through dilations and translations of the so called *scaling function*. The signal decomposition on scaling spaces of varying resolution is the basis of the multiresolution analysis (MRA). The scaling-spaces are complemented by the wavelet spaces W_j. The wavelet spaces are constructed by the *wavelet function*. The wavelet space encodes the information that is necessary to interchange between different resolution scaling spaces ($V_j \oplus W_j = V_{j-1}$). Together, the *scaling* and *wavelet* functions build an orthogonal non-redundant wavelet transform.

With a slight abuse of notation, we set the $V_0 \times V_0$ space equal to the initial signal discretized with the finest spatial discretization step. This assumes equality of discretized function values and scaling function coefficients $s_{0,k} = f_k = f(x_0 + k \cdot \Delta)$, where the finest approximation is set to $j_0 = 0$ and Δ is the spatial sampling, which obviously is not right. For Daubechies wavelets, the so-called *wavelet crime* is permitted, because the Daubechies scaling function approximatively verifies an *interpolating* property of the form $s_{0,k} = \delta_{0,k} \cdot f$. For details we refer to the discussions by Strang and Nguyen (1996).

For example, we suppose a signal being projected on an orthogonal Daubechies wavelet basis consisting of $J = 3$ resolution scales.

$$P_0 f = \sum_{k \epsilon Z} s_{1,k} \phi_{1,k} + \sum_{j=1}^{J=3} \sum_{k \epsilon Z} d_{j,k} \psi_{j,k} \tag{4.10}$$

where f_k are discrete function samples, k the spatial position parameter, and s_k and d_k the corresponding discrete scaling and wavelet functions samples.

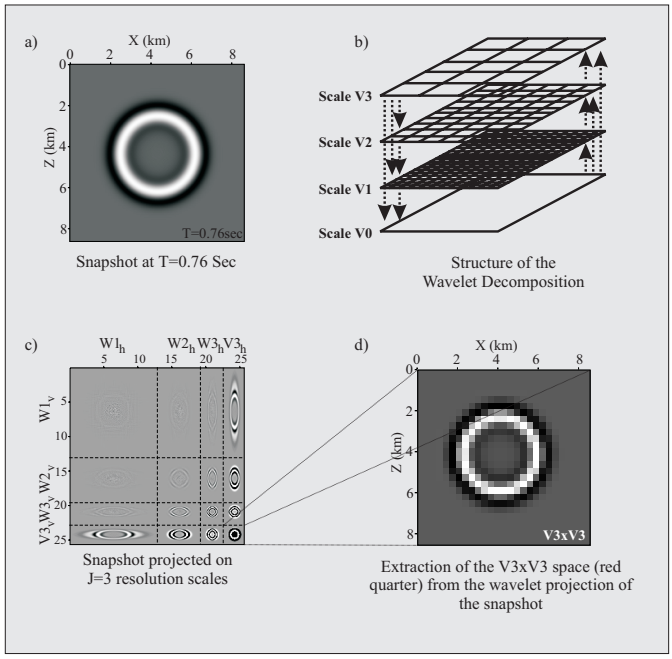

Figure 4.10: A two-dimensional signal is projected on an orthogonal wavelet basis with $J = 3$ resolution scales. (a) Time-Snapshot of wave propagation in a homogeneous medium after $T = 0.76s$. (b) Structure of the wavelet transform on $J = 3$ resolution scales. The initial signal is decomposed on three subsequently coarser grids ($V_{i=0,...,3} \times V_{i=0,...,3}$-spaces) while the coarsest representation of the initial signal is also stored in the final $V_3 \times V_3$-space. Arrows denote interaction between different resolution scales. (c) The initial signal decomposed on $J = 3$ resolution scales. The $W_{i=1,...,3} \times W_{i=1,...,3}$-spaces store the coefficients that are needed to change from one to the next resolution scale. The $V_3 \times V_3$-space is the coarsest discretized representation of the initial signal. All other contributions in spaces $V_{i=1,...,3} \times W_{i=1,...,3}$ and $W_{i=1,...,3} \times V_{i=1,...,3}$ control the interaction between different resolution grids. The wavelet transform stores a low frequency representation in the $V_3 \times V_3$-space and subsequently higher frequency contributions in the $W_{i=1,...,3} \times W_{i=1,...,3}$-spaces. When the $V_{i=1,...,3} \times V_{i=1,...,3}$-spaces are summed up with the $W_{i=1,...,3} \times W_{i=1,...,3}$-spaces and including interactions ($W_{i=1,...,3} \times V_{i=1,...,3}$ and $V_{i=1,...,3} \times W_{i=1,...,3}$) spaces we obtain the initial signal projection in the $V_0 \times V_0$-space. (d) We extract the $V_3 \times V_3$-space from the wavelet transform in (c). This signal is a low frequency (coarse discretized) version of the initial signal shown in (a).

In Figure 4.10a we show a time snapshot of a wave-field propagating in a two-dimensional homogeneous media and in Figure 4.10c the corresponding projection on an orthogonal wavelet basis. In the wavelet terminology, $J = 3$ resolution scales means that the signal is distributed corresponding to its frequency content on three different

grids of decreasing resolution, where each subspace $W_j \times W_j$ encodes the information that is lost when going from a fine to the next coarser scale $V_j \Rightarrow V_{j+1}$. The spatial discretization of the signal is doubled while changing to the next coarser grid. Additionally, the DWT is accompanied by the $V_J \times V_J$ space, which represents an average of the signal initially discretized on the $V_0 \times V_0$ space (see Figure 4.10d). The projection of the signal on different resolution grids is shown schematically in Figure 4.10b.

The orthogonal wavelet expansion of a signal provides the following important features.

- We find the signal being decomposed on several grids of decreasing resolution up to a pre-defined coarsest representation of the initial signal (scaling coefficients).
- The wavelet and interaction spaces ($W_j \times W_j$, $W_j \times V_j$, and $V_j \times W_j$) control the information transfer between the coarsest V_J and the finest resolution V_0 level grid. Therefore, spatial aliasing that typically occurs in CGC-FMG schemes is avoided.
- As was pointed out by Briggs and Henson (1993) and Beylkin (1998), the wavelet transform therefore provides a tool to suppress V- and W-cycles in FMG techniques, since grids of decreasing resolution and the corresponding grid interactions are treated simultaneously.
- The wavelet expansion provides an adapted signal decomposition where frequency components are automatically represented in the best suited resolution grid, with respect to the spatial discretization. Misinterpretation of spatial frequency components may be significantly reduced.

4.9.2 The DIWS algorithm

The DIWS algorithm, in general, resembles the one from the DISS, though now the iterative scheme will be applied to the wavelet expansion coefficients rather than to the prolonged coarse-grid solution in the physical space. We propose the application of the wavelet transform to construct fine grid solutions instead of manual prolongation by bilinear interpolation. Then, the DIWS approach resembles a wavelet-based FMG method, where V- and W-cycles become obsolete. Since spatial frequency components are automatically decomposed on the corresponding wavelet resolution spaces optimal iteration may be performed and therefore the computational efficiency may be increased significantly. We compute coarse-grid wave-field solutions for each frequency component ω_i and right-hand side (RHS) using the MUMPS direct solver (see Figure 4.11a and b). The obtained coarse-grid solutions are recast in a wavelet expansion of the desired fine-grid solution, where all wavelet coefficients are initially zero: $W_1 \times W_1 = V_1 \times W_1 = W_1 \times V_1 = 0$ (see Figure 4.11c). In contrast, the scaling coefficients $V_1 \times V_1$, are approximated by the coarse-grid solution (see Figure 4.11c). The impedance matrix on the coarse grid is constructed through a wavelet-projection procedure. Initially, we define the physical model parameters, such as the density, on the desired fine discretized grid, e.g., the density model ρ^{h_0}, where h_0 is the fine-grid discretization step. In order to obtain a coarse-grid model representation ρ^{h_J} (J denotes the coarse grid), we transform the fine-grid models

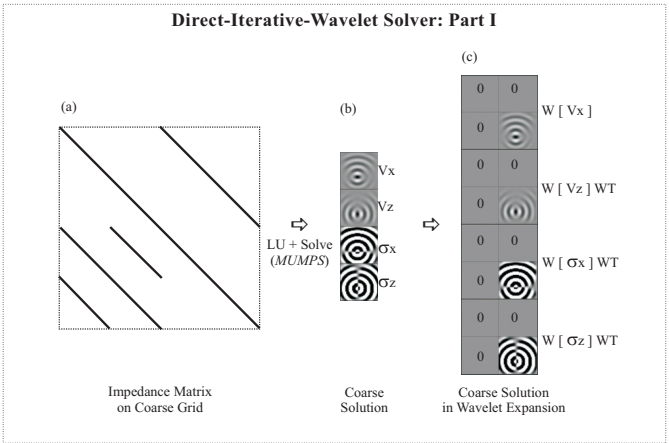

Figure 4.11: The Direct-Iterative-Wavelet Solver (DIWS): Part I. (a) The complex impedance matrix is constructed for a coarse-grid discretization in the physical space. The matrix is factorized into its **LU**-factors by the MUMPS direct solver and a wave-field solution for one frequency component is obtained by solving the resulting system of equations (b). In (c) the calculated coarse-grid wave-field solution is then recast into the scaling coefficients of the wavelet expansion of the desired fine-grid solution ($V_1 \times V_1$-space), where all wavelet and interaction coefficients are initially zero ($W_1 \times W_1 = V_1 \times W_1 = W_1 \times V_1 = 0$).

on the same wavelet basis as the one used later for the iterative scheme. From the wavelet expansion we extract the coarse-grid model contribution in the scaling space and use it as a physical parameter input model for the coarse-grid matrix construction. For example, the fine-grid density model ρ^{h_0} is projected on J resolution scales:

$$P_0(\rho) = \sum_{k \epsilon Z} s_{J,k} \phi_{J,k} + \sum_{j=1}^{J} \sum_{k \epsilon Z} d_{j,k} \psi_{j,k}$$

$$\text{where} \quad \rho^{h_J} = s_J \; \epsilon \; V_J \times V_J \tag{4.11}$$

The scaling-space $V_J \times V_J$ provides the coarse-grid density model ρ^{h_J}. The model construction process is illustrated in Figure 4.13. The RHS-model is obtained in the same way. Note that the amplitude of the coarse-grid solution is scaled with respect to the wavelet projection on a scaling resolution approximation space.

In this wavelet construction, all wavelet and interaction coefficients are not known and need to be added somehow. We apply the iterative solver scheme to construct the missing fine-grid wavelet coefficients, while the initial coarse-scale solution may be updated if necessary (see Figure 4.12d and e). The complex impedance matrix is directly constructed in the wavelet domain (see Figure 4.11d).

The application of the iterative solver on the wavelet basis brings some significant advantages compared to the application in the physical domain. As was discussed before,

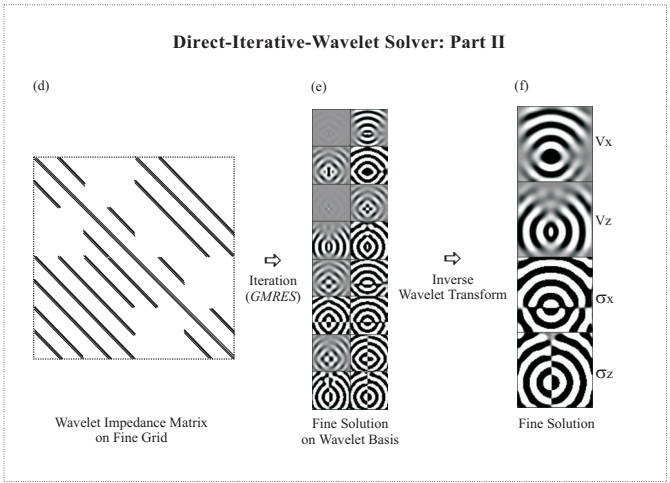

Figure 4.12: The Direct-Iterative-Wavelet Solver (DIWS): Part II. (d) We construct the complex impedance matrix for the fine-grid discretization on the orthogonal Daubechies-4 wavelet basis. Wave-field solutions are computed by a GMRES iterative solver, where the initial solution is the coarse-grid solution expanded in the wavelet basis (see Figure 4.11(c)). The iterative solver constructs all missing wavelet and interaction coefficients (e). No additional V- and W-cycles are necessary to correct for spatial aliasing and interpolation phase-shifts. The wave-field in the physical space domain is obtained by an inverse wavelet transform (f).

the missing wavelet coefficients represent the projection of the true solution on different resolution scales incorporating all interactions between the scales. A priori, we construct wavelet coefficients simultaneously on all wavelet resolution scales. The wavelet expansion provides a natural decomposition with respect to the frequency content of the signal on a sequence of scales of decreasing resolution. We may drive the DIWS projection scheme, such that local wavelet coefficients on a given resolution scale become relatively high frequency, even though they are low frequency components when discretized on the initial fine grid. Then, the iterative solver effectively prolongates the numerical solution on the fine grid and, as a consequence, V- and W-cycles become obsolete. The simultaneous iteration on all resolution scales may then significantly accelerate the iterative convergence. Finally, the desired fine grid solution in the physical space can be obtained by applying the inverse wavelet transform (see Figure 4.12f).

4.9.3 First-order formulation

Initially, we compute a coarse-grid wave-field solution using the direct solver scheme for the largest possible model configuration that can be handled by the presently available computer resources. We then construct the complex impedance matrix in the wavelet domain. This is explained in detail in the following.

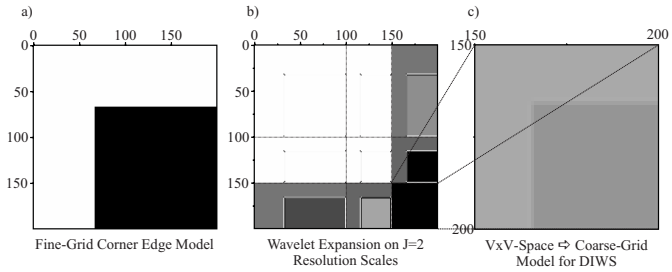

Figure 4.13: Illustration of the procedure to define a physical parameter model used for the coarse-grid impedance matrix construction of the DIWS modelling scheme. The Corner Edge model is initially defined for the fine-grid DIWS configuration. Note that in this illustration we plotted the density model, that is $\rho = 2000kg/m^3$ in the upper and $\rho = 2500kg/m^3$ in the lower medium. In (a) the fine-grid model consists of 200×200 grid-nodes. The model is projected on the Daubechies-4 wavelet basis with $J = 2$ resolution scales (b). From the expansion we extract the $V_1 \times V_1$-scaling space. This coarse-scale representation of the initial fine-grid Corner Edge model is used for the coarse-grid impedance matrix construction (c). A similar coarse-grid model construction is applied for the source function.

We formulate the SH-wave equation as a first-order hyperbolic system of equations with PML absorbing boundary conditions in the frequency domain (see Equation 4.6). In order to construct the complex impedance matrix in the wavelet domain, we project the system of Equation 4.6 on a 2D orthogonal wavelet basis with respect to the spatial coordinates x and z:

$$\begin{aligned}
\mathbf{W}[i\omega\xi_x\rho \cdot v_{yx}]\mathbf{W}^T + \mathbf{W}[\frac{\partial \sigma_{xy}}{\partial x}]\mathbf{W}^T &= \mathbf{W}[-S]\mathbf{W}^T \\
\mathbf{W}[i\omega\xi_z\rho \cdot v_{yz}]\mathbf{W}^T + \mathbf{W}[\frac{\partial \sigma_{zy}}{\partial z}]\mathbf{W}^T &= 0 \\
\mathbf{W}[i\omega\xi_x\frac{1}{\mu} \cdot \sigma_{xy}]\mathbf{W}^T + \mathbf{W}[\frac{\partial v_{yx}}{\partial x}]\mathbf{W}^T + \mathbf{W}[\frac{\partial v_{yz}}{\partial x}]\mathbf{W}^T &= 0 \\
\mathbf{W}[i\omega\xi_z\frac{1}{\mu} \cdot \sigma_{zy}]\mathbf{W}^T + \mathbf{W}[\frac{\partial v_{yx}}{\partial z}]\mathbf{W}^T + \mathbf{W}[\frac{\partial v_{yz}}{\partial z}]\mathbf{W}^T &= 0
\end{aligned} \tag{4.12}$$

where $\mathbf{W}$ and $\mathbf{W}^T$ denote direct and inverse wavelet transform operators, respectively. In the system of Equation 4.12 three different kinds of terms need to be projected on the wavelet basis. The first term is the product of medium parameters ρ and μ with the wavefield components e.g., v_{yx}, etc. The second and third terms are spatial derivative operators $\partial/\partial x$ and $\partial/\partial z$ in x- and z-direction, respectively. We will discuss the projection on the orthogonal wavelet basis for each term separately. The complete wavelet transformation

is provided in Appendix B. The equations in matrix-type form are:

$$\begin{pmatrix} \mathbf{W}[i\omega\xi_x\rho]\mathbf{W}^T & 0 & \mathbf{W}[\frac{\partial}{\partial x}\sigma_{xy}]\mathbf{W}^T & 0 \\ 0 & \mathbf{W}[i\omega\xi_z\rho]\mathbf{W}^T & 0 & \mathbf{W}[\frac{\partial}{\partial z}\sigma_{zy}]\mathbf{W}^T \\ \mathbf{W}[\frac{\partial v_{xy}}{\partial x}]\mathbf{W}^T & \mathbf{W}[\frac{\partial v_{zy}}{\partial x}]\mathbf{W}^T & \mathbf{W}[i\omega\xi_x\frac{1}{\mu}]\mathbf{W}^T & 0 \\ \mathbf{W}[\frac{\partial v_{xy}}{\partial z}]\mathbf{W}^T & \mathbf{W}[\frac{\partial v_{zy}}{\partial z}]\mathbf{W}^T & 0 & \mathbf{W}[i\omega\xi_z\frac{1}{\mu}]\mathbf{W}^T \end{pmatrix}$$

$$\cdot \begin{pmatrix} \mathbf{W}[v_{yx}]\mathbf{W}^T \\ \mathbf{W}[v_{yz}]\mathbf{W}^T \\ \mathbf{W}[\sigma_{xy}]\mathbf{W}^T \\ \mathbf{W}[\sigma_{zy}]\mathbf{W}^T \end{pmatrix} = \begin{pmatrix} \mathbf{W}[-S]\mathbf{W}^T \\ 0 \\ 0 \\ 0 \end{pmatrix} \tag{4.13}$$

The products of physical medium parameters with the wave-field components are situated around the diagonal in the complex matrix. The wavelet projection of these products requires the computation of a convolution-type system:

$$\mathbf{W}[i\omega\xi_x(x,\omega)\rho(x,z)v_{yx}(x,z,,\omega)]\mathbf{W}^T = \sum_{\alpha,\beta}\sum_{i,j} < v_{yx}(x,z,\omega),\psi_j\psi_\beta >< \psi_j\psi_\beta, i\omega\xi_x(x,\omega)\rho(x,z)\psi_i\psi_\alpha > \psi_i\psi_\alpha \tag{4.14}$$

where $\psi_{i,j}$ and $\psi_{\alpha,\beta}$ denote wavelet and scaling basis functions in the x- and z-direction, respectively. The combined inner products form a term-to-term product of the wavelet expansions of medium parameters $i\omega\xi_x\rho$ and wave-field components v_{yx}. The wavelet projection of the diagonal terms (Equation 4.13) plays a key role for the CPU-time requirements of the complex impedance matrix construction on an orthogonal wavelet basis. A similar computational procedure was encountered by Operto et al. (2002), who performed wavelet-based FD modelling in the time-domain. The DIWS requires convolution projections (Equation 4.13) to be computed only once before the modelling starts.

However, computational inefficiency related to costly convolution projections are likely to become obsolete or, simplifying, the standard situation. The incorporation of increasingly complex wave phenomena in modelling schemes, in the end will lead to non-linear wave propagation simulations. In this context, the rather simple linear PDE used here, is replaced by a non-linear one, that by definition will require the computation of products as encountered in Equation 4.13. While standard techniques at this point will struggle, the wavelet-based DIWS will not require more computational power than before.

We have preferred the development of the DIWS scheme using a first-order hyperbolic formulation instead of the second-order standard FDFD formulation. The reason becomes clear when estimating the computational effort necessary to construct the complex impedance matrix in the wavelet domain. In case of the first-order formulation, the construction of one coefficient $c_{i\alpha} = \mathbf{W}[i\omega\xi_i\rho_{i\alpha}]\mathbf{W}^T$ in the matrix (Equation 4.13) requires the multiplication of medium parameters with the wavelet basis functions ψ_j and ψ_β. The term-to-term product is then computed via the matrix-vector product through

corresponding storage of transformed terms in the matrix. We are interested in fast computations of the diagonal terms in order to keep the computational cost of the DIWS scheme as low as possible. The Daubechies-4 quadrature mirror filters that define the wavelet expansion consist of 4 coefficients only and therefore lead to fast convolution projection algorithms.

In order to evaluate the computational cost for one coefficient $\mathbf{W}[i\omega\xi_x\rho \cdot v_{yx}]\mathbf{W}^T$ we assume dense basis functions. Then the convolution computation for the first-order hyperbolic system is proportional to N^4 floating point operations, where N denotes the spatial model dimensions $nx = nz = N$.

We compare the first-order hyperbolic matrix to the standard second-order FDFD formulation combined with a similar projection on an orthogonal wavelet basis (see Appendix B for details). The coupled spatial derivatives applied to the product of medium parameters and wave-field components is projected on the wavelet basis. This gives:

$$\mathbf{W}[\frac{\partial}{\partial x}(\rho(x,z)\frac{\partial}{\partial x}\xi_x(x,\omega))v_{yx}(x,z,\omega)]\mathbf{W}^T = \sum_{\alpha,\beta}\sum_{i,j,k,l} < v_{yx}(x,z,\omega), \psi_l\psi_\beta >$$
$$< \frac{\partial}{\partial x}\psi_k, \psi_l >< \frac{\partial}{\partial x}\psi_i, \psi_j >< \psi_k\psi_\beta, \xi_x(x,\omega)\rho(x,z)\psi_j\psi_\alpha > \psi_i\psi_\alpha \tag{4.15}$$

The construction of the second-order analogues of the complex impedance matrix requires the computation of two term-to-term products plus the product of medium parameters and wavelet basis functions. As before, we assume dense basis functions to evaluate the computational cost, and obtain N^6.

Since the second-order hyperbolic wave equation combined with the wavelet transformation is proportional to N^6 floating point operations compared to N^4 for the first-order hyperbolic formulation, we developed the DISS and DIWS solver schemes using the latter approach. Moreover, the first-order hyperbolic velocity-stress formulation of the wave equation allows the introduction of more complex rheological laws (non-linear elasticity) at almost no additional cost.

4.9.4 Derivative projection on wavelet basis

To complete the wavelet expansion of terms appearing in the complex impedance matrix we discuss the projection of spatially staggered derivative operators on an orthogonal Daubechies wavelet basis. The entire development is shown in Appendix B.

We apply the orthogonal wavelet transform to the product of spatial derivatives in x- and z-direction and wave-fields v_{yx}, v_{yz}, σ_{xy} and σ_{zy}. As an example, we give the results for the velocity wave-field components v_{yx} and v_{yz}:

$$\mathbf{W}[\frac{\partial}{\partial x}v_{yx}(x,z,\omega)]\mathbf{W}^T = -\sum_{\alpha}\sum_{i,j} < \frac{\partial}{\partial x}\psi_i, \psi_j >< v_{yx}(x,z,\omega), \psi_i\psi_\alpha > \psi_i\psi_\alpha \tag{4.16}$$

$$\mathbf{W}[\frac{\partial}{\partial z} v_{yz}(x,z,\omega)]\mathbf{W}^T = -\sum_{\alpha,\beta}\sum_{i} < \frac{\partial}{\partial z}\psi_\alpha, \psi_\beta >< v_{yz}(x,z,\omega), \psi_i\psi_\beta > \psi_i\psi_\alpha \tag{4.17}$$

In practice, the derivative operator may be constructed in the wavelet domain following two different approaches. The first one was developed by Beylkin et al. (1991) and Jameson (1993). They directly derived the operator coefficients for FD derivatives from the definition of scaling and wavelet interpolating functions of several different orthogonal Daubechies wavelet bases.

In contrast, Wu and McMechan (1998) discretized the spatial FD operator in the physical domain (which approximately corresponds to the FD operator in the V_0-space) and then computed its projection in the wavelet domain. Their approach is independent of the properties of scaling and wavelet functions, as long as they form an orthogonal basis.

In case of the Daubechies-4 wavelet basis, both approaches lead to the same operator coefficients in the wavelet basis, if the standard FD operator in the V_0-space is the non-staggered centered difference stencil $(-1/12, +2/3, 0, -2/3, +1/12)$. Moreover, Jameson (1993) showed that the projection of this FD operator on a Daubechies-4 orthogonal wavelet basis results in a local FD operator on each resolution scale together with interaction spaces that relate different FD approximations on different resolution scales.

For simplicity, we follow the latter approach by Wu and McMechan (1998) and construct discrete staggered derivative operators in the physical space and transform then in the wavelet space.

4.10 Numerical Examples

We show two SH-wave propagation simulations in strongly heterogeneous media. Both examples have been computed for the DISS and DIWS using similar physical model parameters and source and receiver setup in order to allow relative comparisons of the two approaches. Even though we show 2D examples only, we would like to remind that the DISS and DIWS approaches were developed in view of large-scale wave-field simulations in complex 3D media. However, at this stage we address a verification of the code together with first insights to the convergence performance of the space bilinear interpolation and wavelet-based preconditioning of the complex impedance matrix. The wave propagation simulations are currently run on a single desktop computer in sequential mode. This significantly limits the actual model size treated, though first wave simulations and proofs of the method are not negatively influenced by the 2D simulation. The passage from 2D to 3D necessarily includes the transformation of the sequential code to run on large state-of-the-art super-computers (e.g., PC-Clusters) using an MPI (Message Passing Interface Forum, 1994) based parallelization of the matrix construction and the direct and iterative solver. Provided the outcome of the 2D numerical tests, we will develop strategies for the desired real-case 3D simulations that may be compared to other

highly optimised modelling schemes, such as a spectral-element code.

We used the same source configuration for all model simulations. The source is spatially set on one grid-node without smoothing over neighbouring points,

$$S(x,z,t) \quad = \quad S(t)\delta(x-x_s)\delta(z-z_s) \tag{4.18}$$

The time signature is the derivative of a Gaussian,

$$S(t) \quad = \quad -2\alpha(t-t_0)e^{-\alpha(t-t_0)^2} \tag{4.19}$$

with $\alpha = 200$, $t_0 = 0.31sec$ and a maximum frequency of $10Hz$. In order to simulate infinite model dimensions, we added PML absorbing boundary layers on all four edges of the model. Problems related to the free-surface implementation are not addressed at this stage. The PML attenuating function, denoted by γ in Equation 4.5 ($\xi = 1 + i\gamma/\omega$), smoothly rises from 0 at the interior model-PML boundary up to some empirically estimated value at the outer PML boundary (Operto et al., 2002).

4.10.1 The Corner Edge model

The first wave simulation is performed for the Corner Edge model for two different direct-iterative grid combinations. The Corner Edge model consists of two homogeneous spaces, that are separated by horizontal and vertical interfaces that build a corner. The medium surrounding the corner edge has a wave velocity of $v = 2000m/sec$ and density $\rho = 2000kg/m^3$, while the medium inside the corner has a wave velocity of $v = 8000m/sec$ and a density of $\rho = 2500kg/m^3$. The significant physical parameter contrast between the two spaces creates a strong reflection from the interface and a diffraction from the corner point. The physical model size is $6400m \times 6400m$ with an additional PML layer of $800m$ thickness on all four edges of the model. All wave simulations were carried out using fourth-order derivative approximations. Frequency maps are calculated separately for 103 frequency components that equidistantly sample a frequency band from $0Hz$ to $10Hz$. This corresponds to a time sampling of $dt = 0.01sec$ and an overall time-length of the seismogram of $6sec$.

Simulation 1: Two-step case

The first numerical Corner Edge simulation for the DISS/DIWS schemes was set up for a so-called *two-step* geometry, that is equivalent to a two-grid multi-grid scenario. The coarse-grid wave-field solution is calculated on a numerical grid having a spatial discretization of at least 2.5 points per shortest wavelength for the slowest velocity present in the model. We then halfed the discretization step and computed the fine-grid contributions by the iterative solver part. The name *two-step* denotes the fact that the spatial discretization for the direct and iterative computations of the DISS scheme changes by a factor of *two*, which is similar to a DIWS-projection on *two* resolution scales ($J = 1$).

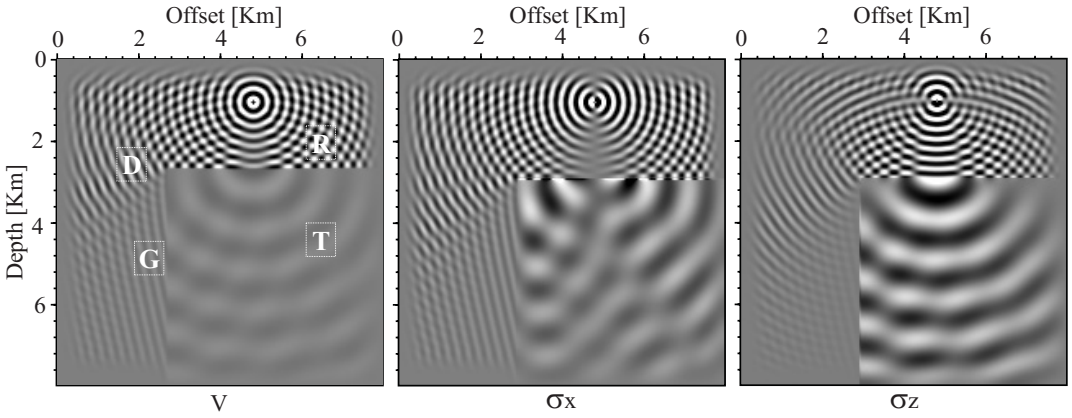

Figure 4.14: Wave-field solution for a fine-grid Corner Edge simulation. Frequency maps are computed by the DISS for the frequency $f \approx 8Hz$. From left to right, we plot frequency maps for the three wave-field solutions v_y, σ_{xy} and σ_{zy} for the first-order hyperbolic system of equations in Equation 4.7. Note that the velocity wave-field is recombined from its PML components ($v_y = v_{yx} + v_{yz}$). Clearly visible are strong reflections (**R**) as well as guided (**G**) and transmitted (**T**) waves from the horizontal interface. Diffraction phenomena from the corner point where the wave speed and model density change significantly from one grid point to the next are indicated by (**D**). On all four edges of the model we note wave-attenuation in the PML absorbing layers.

Both solver approaches compute coarse-grid wave-field solutions using the direct solver *MUMPS* in sequential mode. The coarse-grid spatial sampling was set to $dx = dz = 80m$, which gives a numerical grid of 100×100 grid-nodes including 10 nodes for the PML layers on each side of the model. The coarse-grid discretization leads to 2.5 grid-nodes per shortest wavelength. Fine-grid solutions are calculated on a grid having double size i.e., 200×200 grid-nodes including 20 nodes for the PML. The fine-grid spatial discretization is reduced from $80m$ to $40m$. The source is located at the position $(250m, 4000m)$.

Wave-field solutions are computed for a fixed number of iteration steps of $n_{it} = 1500$. In Figure 4.14, we show an example of a fine-grid wave-field solution computed by the DISS for the frequency $f \approx 8Hz$. From left to right, we plot the frequency maps for the wave-field solutions v_y, σ_{xy} and σ_{zy} (see Equation 4.7). Note that the velocity wave-field has been re-combined from its PML components $v_y = v_{yx} + v_{yz}$. Clearly visible are wave-field reflections (**R**), guided (**G**) and transmitted (**T**) waves, and diffractions (**D**) from the horizontal interface and the corner point where physical model parameters change significantly from one grid-node to the next. In Figure 4.15 and Figure 4.16, we show DISS seismograms computed from the coarse-grid direct solutions (Figure 4.15) and the results from the fine-grid iterative solver (Figure 4.16). Eighty receivers were lined out over the whole physical model (without PML boundaries) with a spacing of $80m$. In addition to the complete seismograms we also include three extracted traces, namely trace number 10, 50, and 75. The extracted traces are compared to an analytical solution

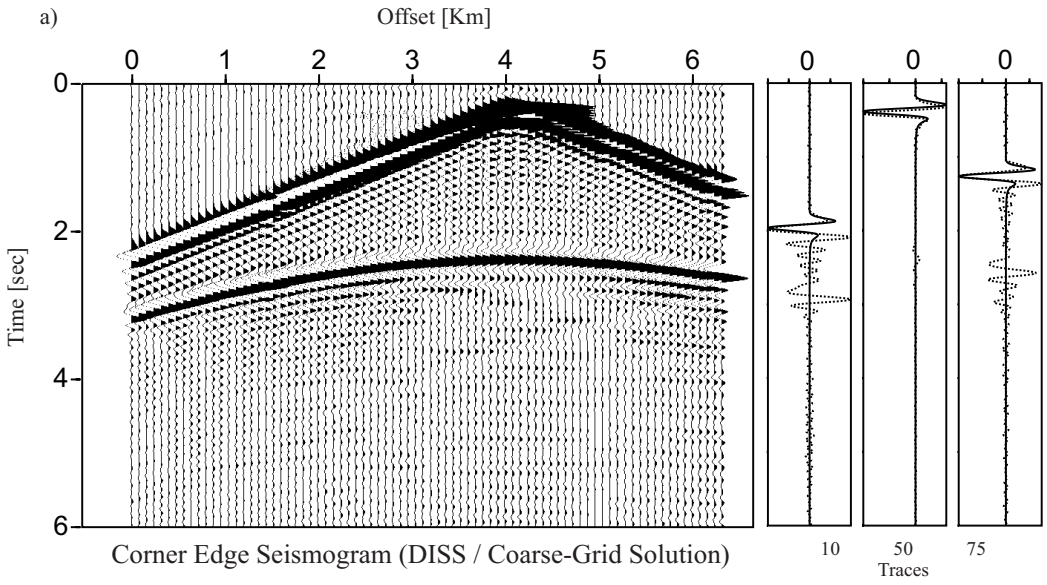

Figure 4.15: Seismogram for the Corner Edge model computed from the coarse-grid direct solution of the DISS. The seismogram includes arrivals from 80 receiver stations equally separated over the whole model (receiver spacing: $80m$; receiver depth: $150m$). We also plotted three extracted traces (trace-number: 10, 50, 75) together with an analytic solution for the upper model full-space, which allows the verification of the direct wave only. We used 2.5 grid points per shortest wavelength to fix the coarse discretization step. Therefore, the time-seismogram shows significant amount of noise due to wave dispersion.

that was computed for a homogeneous media having the physical specifications of the upper full-space in the Corner Edge model. The analytic solution is added to verify the correct simulation of the direct wave, and moreover to demonstrate possible numerical dispersion on far offset traces.

The seismogram in Figure 4.15 is affected by a significant amount of noise, because numerical dispersion limits for FDFD modelling in strongly contrasted media are not respected properly. Still, the direct first arrival and the reflection of the interface between the two media are clearly visible. The interpolated coarse-grid frequency maps serve as initial solution for the iterative scheme. From Figure 4.16, we observe that halfing the spatial discretization step by a factor of 2 and applying an iterative solver, produces a dispersion-free wave-field simulation. We detect direct and reflected (**R**) arrivals and note the presence of a weak diffraction event (**D**), that is excited by the corner edge.

In general, the PML absorbing boundary conditions work well for the Corner Edge model, though in Figure 4.16 we clearly remark a spurious reflection (**N**) at Trace 75 and $t = 3sec$, that propagates from left to right in the seismogram. Numerical tests performed to evaluate the performance and accuracy of wave absorption using PML worked well for structurally simple models. For more complex models, such as the Corner Edge,

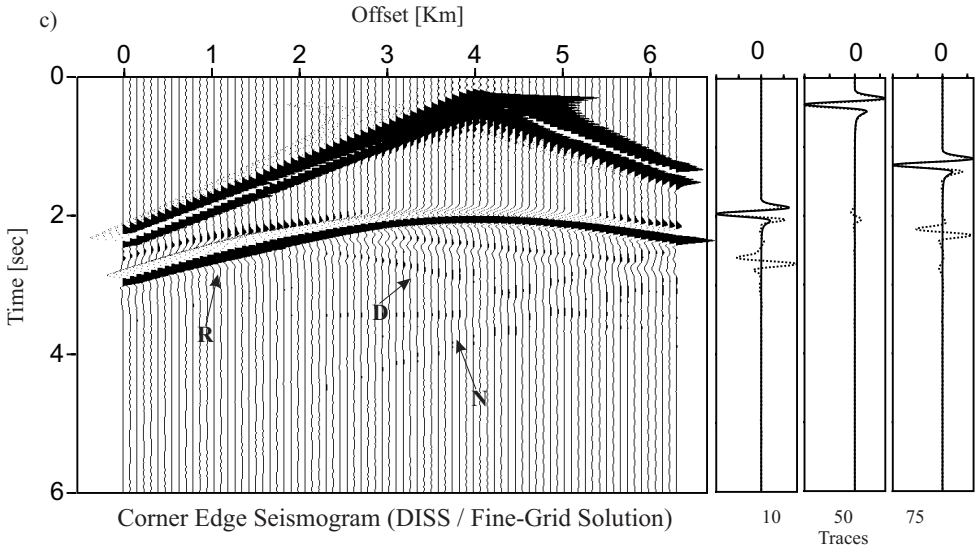

Figure 4.16: Seismogram for the Corner Edge model computed from the fine-grid iterative solution of the DISS. We clearly distinguish between wave-field reflections (R) and diffractions (D) from the horizontal interface and the corner point, where physical model parameters change significantly from one grid-node to the next. We observe good attenuation of the wave amplitude for all four PML absorbing layers surrounding the model. Note the spurious reflection that travels from right (trace 75, $t = 3sec$) to the left (N). This noise is caused by improper treatment of the PML absorbing boundary conditions. Its amplitude, though largely enhanced here, is approximately similar to the rather weak diffraction event from the corner edge located in the middle of the seismogram.

our rather empirical PML study did not reveal a simple and sufficiently accurate PML attenuating function and needs to be investigated in greater detail. In this article, we are mainly interested in the comparison of the DISS and DIWS method with respect to the performance and accuracy of the iterative scheme, and therefore leave the PML problematic aside.

In Figure 4.17, we show the DIWS Corner Edge seismogram that is computed using similar modelling parameters as the ones used for the DISS simulation for a *two-scale* geometry. In wavelet language, *two-scale* geometry corresponds to a projection of the wave-field on two resolution scales ($J = 1$).

The initial solution for the iterative solver in the wavelet domain consists of the coarse-grid solution recast in the $V_1 \times V_1$-space, where fine-grid and interaction coefficients in spaces $W_1 \times W_1$, $W_1 \times V_1$ and $V_1 \times W_1$ are initially zero. Then, the *GMRES* iterative solver constructs the missing wavelet coefficients on all resolution scales $W_j \times W_j$ simultaneously and the grid-interaction-coefficients in spaces $W_1 \times V_1$ and $V_1 \times W_1$. More important is that the iterative solver also modifies the coarse-grid scaling space coefficients, such that the low-frequency components are adapted on the fine-grid automatically with respect to the

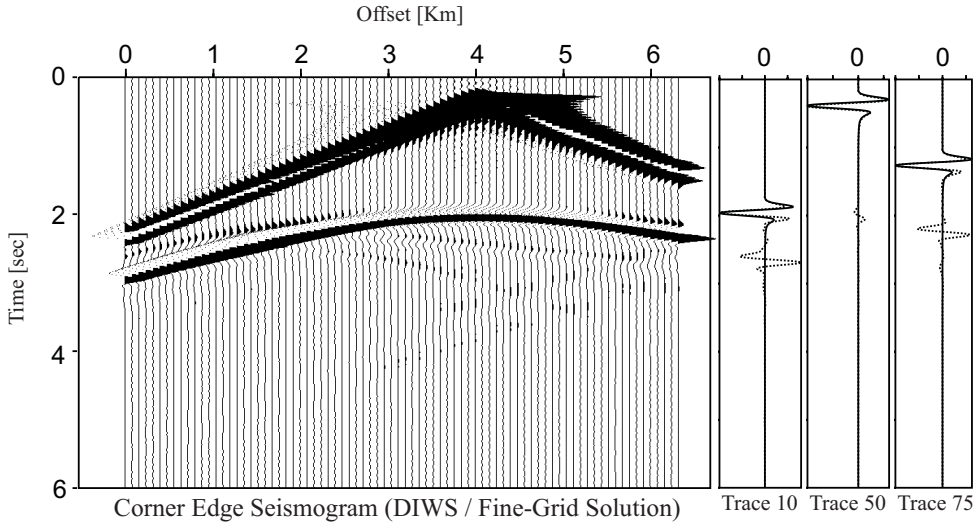

Figure 4.17: Seismogram for the Corner Edge model computed from the fine-grid iterative solution of the DIWS. Wave arrivals have been computed for 80 receiver stations having a horizontal distance of $80m$ and depth of $150m$. We plot three extracted traces (trace-number: 10, 50, 75) together with an analytic solution for the upper model full-space, which allows the verification of the direct wave only.

fine-grid high-frequency content. The modification of the scaling space is similar to the *Coarse-Grid Correction* scheme of a *Full Multi-Grid* method, while the wavelet coefficient construction corresponds to a *relaxation* process on the fine-grid. The wavelet scale interactions may be interpreted as the *interpolation* and *restriction* procedures in a V- and W-cycle. DIWS-wavelet iteration performs complete multi-grid cycles simultaneously at each iteration step, and therefore may provide superior iterative convergence rates.

In Figure 4.18, we plot a final frequency map ($f \approx 8Hz$) in the wavelet basis iteration (from left to right, we plot v_y, σ_{xy} and σ_{zy}). Each wave-field in the wavelet domain consists of the $V_1 \times V_1$-space, the $W_1 \times W_1$-space, and two interaction spaces $V_1 \times W_1$ and $W_1 \times V_1$. We note that coefficients having strong amplitude are constructed in the wavelet and interaction spaces for the upper medium, while the corner edge medium is encoded by coefficients with weak amplitude throughout. Moreover, the wavelet decomposition clearly identifies the strong velocity contrast at the interface between the two Corner Edge spaces. The heterogeneous distribution of coefficients with varying amplitude illustrates the strong influence of the wavelength change ($v = \lambda \times f$) due to the change in physical parameters between the two media of the Corner Edge model.

The distribution of wavelet coefficients with respect to the complexity of the model structure and the inherent frequency content in a wavelet expansion formulation allows the definition of space adaptivity through the introduction of numerical masks (Operto et al., 2002). We may define model regions where wavelet coefficients do not contribute to the wave-field simulation in certain resolution approximation spaces. Adaption to a

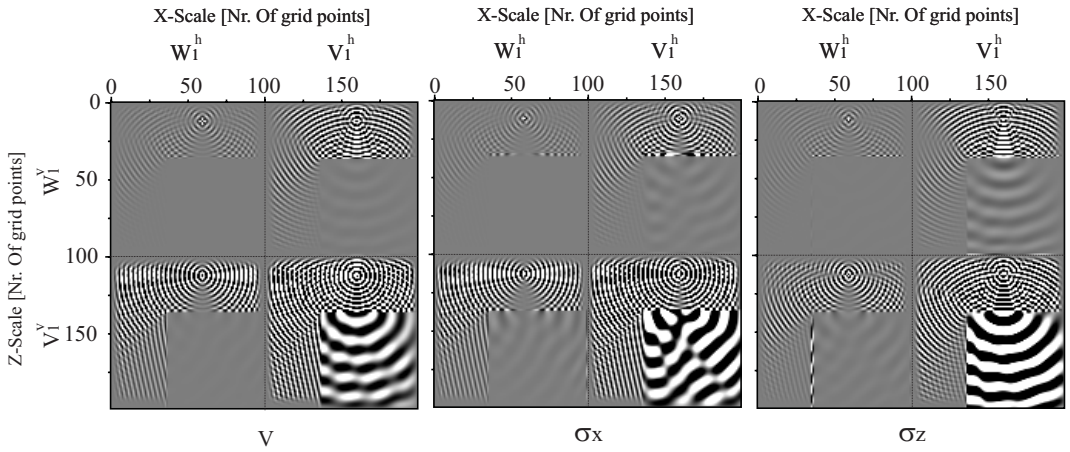

Figure 4.18: Wave-field solution for the DIWS fine-grid Corner Edge simulation. Frequency maps are computed by the DIWS for the frequency $f \approx 8Hz$. From left to right, we plot frequency maps for all wave-field solutions v_y, σ_{xy} and σ_{zy} on two wavelet resolution scales ($J = 1$) using the Daub4 wavelet basis. The upper left block is the wavelet space ($W_1 \times W_1$), upper right and lower left blocks interaction spaces ($V_1 \times W_1$ and $W_1 \times V_1$) and the lower right block the scaling space ($V_1 \times V_1$). Clearly visible are strong reflections from the horizontal interface and diffraction phenomena from the corner point where the wave speed and model density change significantly from one grid point to the next. On all four edges of the model we also note the wave-attenuation in the PML absorbing layers.

local physical parameter that characterises the behaviour of the wave-field solution may be obtained by inspecting the smoothness of the model structure. A typical region to apply a mask would be the corner edge space on the fine-grid approximation scales in Figure 4.18, where wavelet coefficients are small and therefore do not provide significant contributions to the wave-field propagation at this frequency component. Although we expect great CPU-time savings from the definition of masks, at this initial stage of the DISS-DIWS comparison we did not address its implementation in the DIWS algorithm.

We compare the DISS and DIWS wave-field solutions to a time-seismogram that was computed using a standard fourth-order staggered TDFD modelling scheme. The DISS, DIWS and TDFD seismograms are shown in Figure 4.19. The overall *fit* of the three solutions is good. We observe slight phase shifts between the TDFD and the FDFD solutions for the reflection event from the corner edge interface. This illustrates the approximative character of the iterative wave-field solutions computed by the DISS and DIWS. An increase of *GMRES* iteration steps eliminates these artefacts.

Differences in CPU-time between the two DIS methods are related to the iterative part of the algorithm, since both use the MUMPS solver for the coarse-grid computations. Moreover, the DISS and DIWS prolongation of the coarse-grid solution is negligible from a computational point of view. Therefore, we compare the DISS and DIWS performance

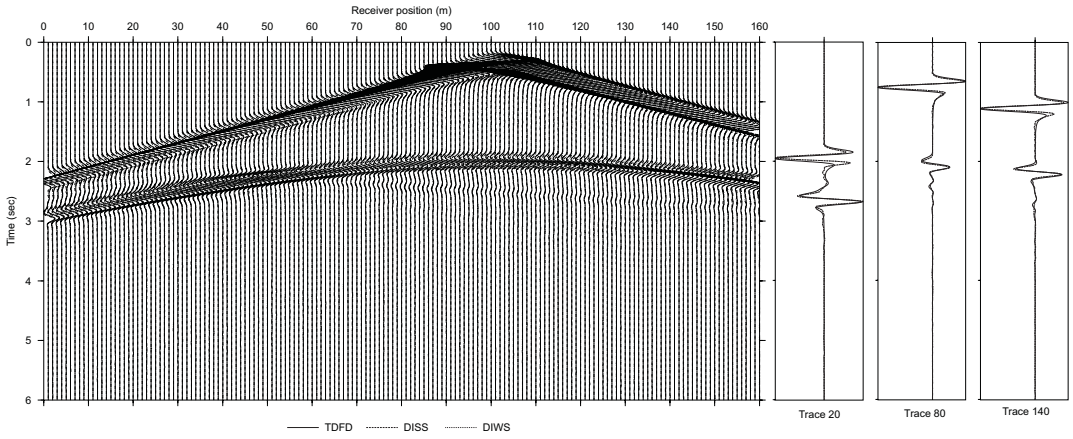

Figure 4.19: Comparison of time-seismograms for the Corner Edge model computed by the DISS, DIWS and a TDFD modelling schemes. The continuous, dotted and dashed lines show the TDFD, DIWS and DISS solutions, respectively. The overall fit is good. We observe phase shifts between the TDFD and FDFD solutions for the reflection event from the corner edge interface.

for the matrix construction and convergence of the iterative scheme. At this stage, we are mainly interested in the comparison of the DISS and DIWS iterative convergence behaviour under spatial and wavelet-based preconditioning by an initial coarse-grid solution (nested iteration).

The DIWS impedance matrix needs to be constructed analytically in the wavelet domain by projecting matrix sub-blocks in the wavelet space (see Equation 4.13). Spatial derivative operator expansions and convolution-type wavelet projections for diagonal matrix blocks (see Equation 4.13) are performed only once before the modelling starts. For each frequency component, the DIWS-matrix is then easily constructed by combining pre-computed terms with the complex angular frequency ω_i. In the current implementation, we did not seek to optimise the sequential convolution computations which results in large DIWS matrix construction times. For example, the construction of all diagonal matrix blocks in Equation 4.13 for the DIWS Corner Edge simulation on $J = 1$ resolution scales, requires $t_{A_{DIWS}} \approx 70min$. In contrast, the DISS fine-grid impedance matrix construction in the space-frequency domain for the same Corner Edge model is done at practically no computational cost ($t_{A_{DISS}} \approx 1sec$). Note that all computations are carried out on a stand-alone Linux-PC with $1GByte$ of RAM and $1GHz$ speed.

The *GMRES* iterative solver is set to perform a fixed number of iterations $n_{iter}^{max} = 1500$ with a tolerance (backward error) of $tol = 1.e^{-7}$. Note that the case where the tolerance is fixed and the number of iterations required for convergence is investigated, is not addressed at this initial stage. The DISS and DIWS CPU-time for $n_{iter}^{max} = 1500$ iterative steps for a single frequency simulation on the 200×200 fine-grid is ranging from $t_{f_{\approx 1Hz}} \approx 11/10min$ to $t_{f_{\approx 10Hz}} \approx 12/11min$, respectively.

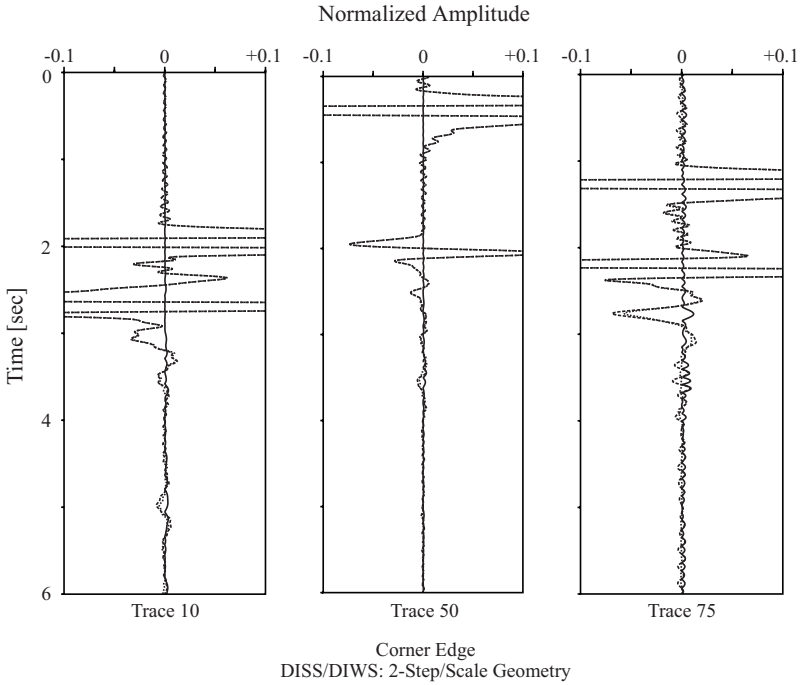

Figure 4.20: Comparison of three traces that are extracted from the DISS- and DIWS-seismograms of the Corner Edge model. Fine-grid solutions are obtained after $n_{it} = 1500$ iteration loops. The dotted line is the DISS, the dashed line the DIWS solution. The continuous line is the difference between DISS and DIWS solutions. In order to visualise any differences we limited the amplitude to 10% of the maximum amplitude. Only on trace 75 slight differences can be observed, while the overall fit is practically perfect.

For the DISS *two-step* and DIWS *two-scale* simulations, no significant difference in CPU-time is observed, even though the number of non-zero coefficients in the DIWS-matrix compared to the DISS-matrix is significantly larger. Normally we would expect an increased number of matrix-coefficients to be accompanied by an increase of CPU-time to perform the fixed number of iterations. This is not confirmed by our simulations and gives a first indication of an accelerated convergence rate for the wavelet preconditioning.

In Figure 4.20, we show the DISS and DIWS comparison of the fine-grid Corner Edge solution for three extracted traces (trace-number 10, 50 and 75). Note that the traces amplitude is cut-off at 10% of the maximum amplitude. The ringing on the traces, for example, on trace 10 for $0sec < t < 1.8sec$, is due to the wave-field solution being computed by an iterative solver in the frequency domain with a limited number of iteration steps. Increasing the number of iterations may suppress ringing completely. The overall fit for the first arrival and reflection is good. More interesting is the difference of the DISS and DIWS solutions that we observe on trace 75 for times $0sec < t < 1sec$ and $3sec < t < 4sec$. The DISS solution (dashed line) shows stronger ringing compared to

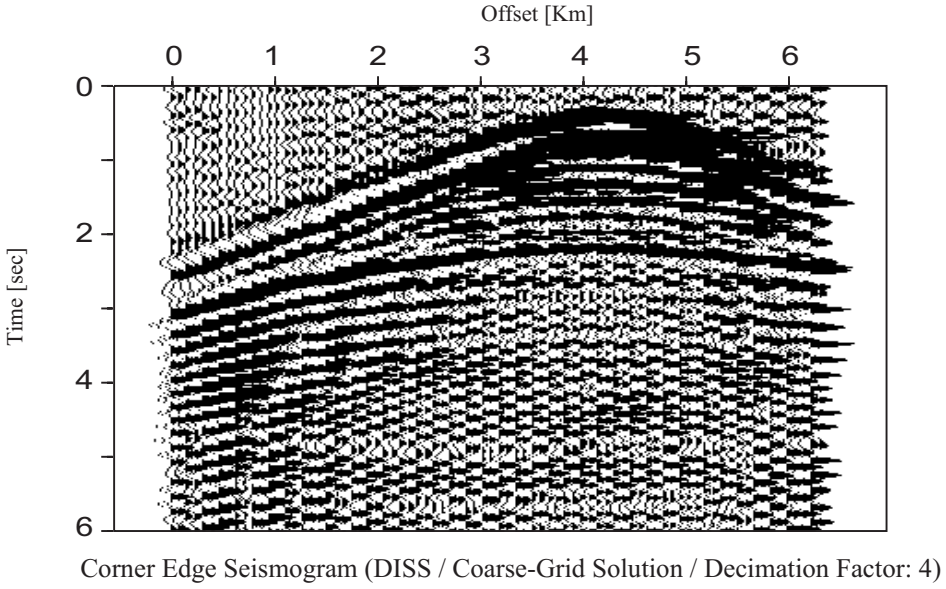

Figure 4.21: Seismogram for the Corner Edge model computed from the DISS coarse-grid solution. The spatial discretization step was set to $\Delta x = \Delta z = 160m$, which corresponds to 1.25 grid points per shortest wavelength. Because of the large under-sampling of wavelength components strong wave dispersion dominates the seismogram.

the DIWS solution (dotted line).

Simulation 2: Four-step case

We performed a second wave simulation for the Corner Edge model using the same model-, source- and receiver-geometry as before. In contrast to the first simulation, we now compute wave-field solutions on a coarse-grid that has half the size of the previous one. The prolongation of the DISS and DIWS coarse-grid frequency solutions is performed on the same fine-grid used for the two-step scenario (200×200). This is similar to a two-grid situation, where the spatial discretization of the coarse-grid is divided by a factor of 4 for the fine-grid simulation. For the DIWS scheme, this implies a wavelet decomposition on $J = 2$ resolution approximation scales. The grid-combination set-up is therefore denoted by *four-step/three-scales* geometry. The coarse-grid has a size of 50×50 grid nodes, of which 5 nodes on each side of the model are PML absorbing layers. The spatial discretization on the coarse-grid is $dx = dz = 160m$, which corresponds to 1.25 grid points per shortest wavelength. Applying the decimation factor 4 then gives a spatial discretization for the fine-grid of $dx = dz = 40m$.

In Figure 4.21, we show the seismogram obtained by the coarse-grid wave simulation. Because of the large spatial discretization step with respect to the highest frequency modelled, we observe strong wave dispersion that significantly pollutes wave-arrivals in the seismogram. As for the two-step case, the DISS scheme required $t_f \approx 11/12min$

CPU-time to perform the fixed number of iteration steps ($n_{iter}^{max} = 1500$), since despite of a modified phase-error of the initial iterative solution, the physical dimensions of the fine-grid stayed unchanged (number of non-zero coefficients in the DISS fine-grid matrix similar for *two-step* and *four-step* geometry). In contrast, the CPU-time necessary to construct the DIWS fine-grid matrix increases to 80 minutes, due to an increased number of non-zero coefficients in the wavelet decomposition on three scales. Moreover, this increase automatically leads to less efficient matrix-vector and dot-products during the iteration steps, i.e., $t_f \approx 20/21 min$ CPU-time for $n_{iter}^{max} = 1500$ DIWS iteration steps.

In Figure 4.22, we plot the comparison of the DISS and DIWS fine-grid solutions for the *four-step* geometry. The DISS solution significantly improved when compared to the previous *two-step/two-scales* simulation example, and now fits much better to the DIWS solution. This is due to the DISS solution being less ringing than for the *two-step* case. The improvement is related to the DISS low-frequency components being better represented by the interpolated coarse-grid solution with respect to the convergence of the GMRES iterative solver. This behaviour is not surprising, since standard multi-grid V- and W-cycles, and especially Coarse Grid Correction (CGC), descend from a fine to sets of coarser grids in order to obtain favourable iterative convergence conditions for the fine-grid low frequency components.

In order to better quantify differences between the *two-* and *four-step* simulation examples, we plot separately the direct comparison of the two DISS and DIWS solutions in Figure 4.23 and Figure 4.24, respectively. Moreover, in both Figures 4.23 and 4.24 we add the approximate *exact* solution that is obtained by the DISS scheme using $n_{it} = 5000$ iteration steps. As before, we observe an overall good agreement for both DISS and DIWS comparisons for traces 10 and 50. In contrast, trace 75, that is sensitive to the strong reflection from the horizontal corner edge interface shows remarkable differences for the DISS solutions. We find the *four-step* DISS solution (dotted line) significantly less ringing than the *two-step* solution (dashed line), which is related to the better representation of fine-grid low-frequency components on the four-step rather than the two-step coarse-grid. Nevertheless, increasing the number of DISS iteration steps (up to $n_{it} = 5000$) provides a *ringing-free* seismogram (continuous line solution in Figure 4.23), but also increases significantly the CPU-time from $t_{1500} \approx 10 min$ to $t_{5000} \approx 20 min$.

The DIWS wave simulations for the *two/three-scales* setups do not suffer from similar artefacts. Both simulation results fit well and practically no differences in amplitude are observed. Note that wiggles on trace 10 at $t \approx 5 sec$ and trace 75 at $t \approx 3.5 sec$ are artificial noise due to the model-PML reflection. The multi-scale formulation effectively combines numerical grids of varying resolution where grid interactions are accounted for automatically. Therefore, the performance of DIWS iterations on the wavelet coefficients is significantly less dependent on the number of iteration steps performed, since DIWS is comparable to a Full Multi-Grid (FMG) method where resolutions grids are treated simultaneously.

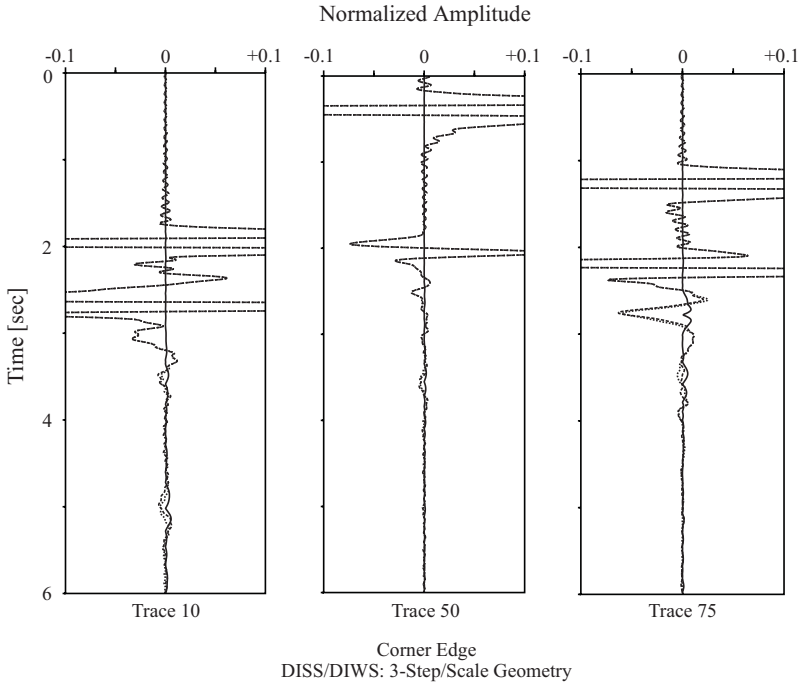

Figure 4.22: Comparison of three traces, that are extracted from the DISS- and DIWS-seismograms of the Corner Edge model for the *four-step* geometry after $n_{it} = 1500$ iteration loops. The dotted line is the DISS, the dashed line the DIWS solution. The continuous line is the DISS solution after $n_{it} = 5000$, which serves as the exact final solution. The amplitude is limited to 10% of the maximum amplitude in order to visualise any differences. Practically no difference between the two solutions can be observed.

4.10.2 The Marmousi model

We perform a second wave simulation example for a windowed part of the Marmousi model (Bourgeois et al., 1991). This case-study illustrates the iterative performance of the DIS approach for a wave simulation in a structurally complex heterogeneous media. DISS and DIWS wave-field simulations have been performed for a *two-step* situation. We applied PML absorbing boundary conditions on all four edges of the model (10, 20 grid nodes of the coarse-grid and fine-grid). The velocity in the model ranges from $1500m/sec$ up to $4500m/sec$ and the density from $1000kg/m^3$ to $2500kg/m^3$. We use a spatial stepping of $dx = dz = 16m$ and $8m$ for the coarse- and the fine-grid simulations, respectively. This corresponds to approximately 10 and 20 grid-nodes per shortest wavelength, respectively. The source, located at ($dz_s = 50m$,$dx_s = 720m$), is the derivative of a Gaussian having similar properties as the one used for the Corner Edge simulations.

Wave-field solutions are computed for 52 frequency components distributed over a range of frequencies from $f_{min} \approx 0Hz$ to $f_{max} = 10Hz$. Receivers are spread out over

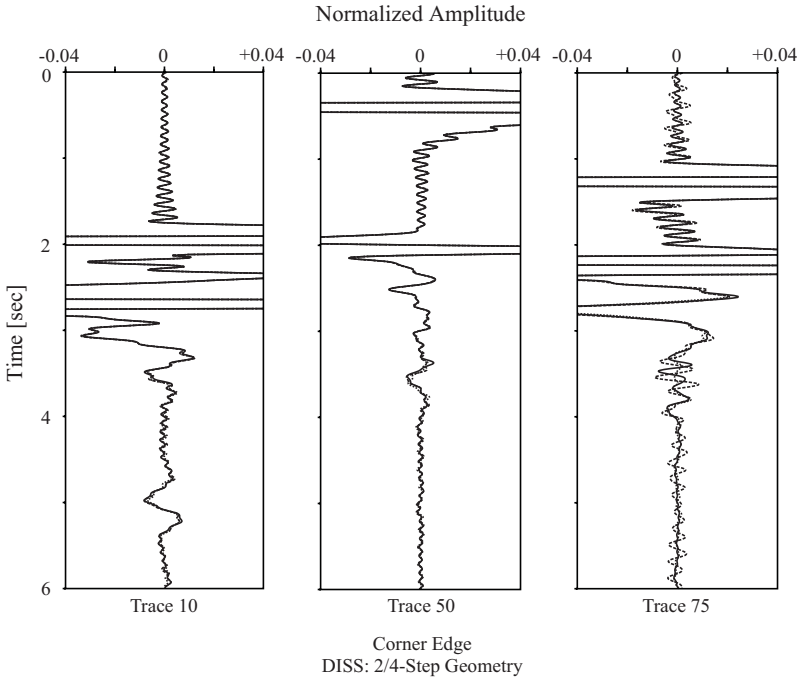

Figure 4.23: Comparison of the two-step and four-step wave-field solution computed by the DISS. The dotted line is the fine-grid solution for the *two-step setup* setup and the dashed line for the *four-step setup* simulation. The continuous line is the DISS solution after $n_{it} = 5000$, which serves as the exact final solution. Only a slight difference can be observed on trace 75.

the whole model at a depth of $100m$ and spacing of $12.5m$. An example of a frequency map ($f \approx 9.5Hz$) for the v_y-velocity component ($v_y = v_{yx} + v_{yz}$) is shown in Figure 4.25. In (a), we plot the wave-field solution after $n_{it} = 3000$ fixed *GMRES* iteration steps on $J = 1$ resolution scales. In the bottom right block of (a), we see the wave-field projection on the $V_1 \times V_1$ scaling approximation space. The upper left block is the fine-grid contribution to the v_y-wave-field ($W_1 \times W_1$) with respect to the initial $V_0 \times V_0$ wave-field approximation. Note the high frequency contribution on the fine wavelet scale in the surroundings of the source excitation location. The other two blocks illustrate the coupling between the two wave-field approximations spaces. Figure 4.25b is the same wave-field inverse wavelet transformed in the physical space.

Wave-field simulations are performed for different grid-model dimensions and number of fixed *GMRES* iterations (*GMRES* tolerance: $tol = 1.e-7$). We find the number of DISS iteration steps required to provide dispersion-free wave simulations strongly increased. In contrast, the DIWS simulations shows stable iteration rates that are independent of grid size and number of resolution-grids used.

For example, we perform a DISS and DIWS wave simulation using a coarse-grid and

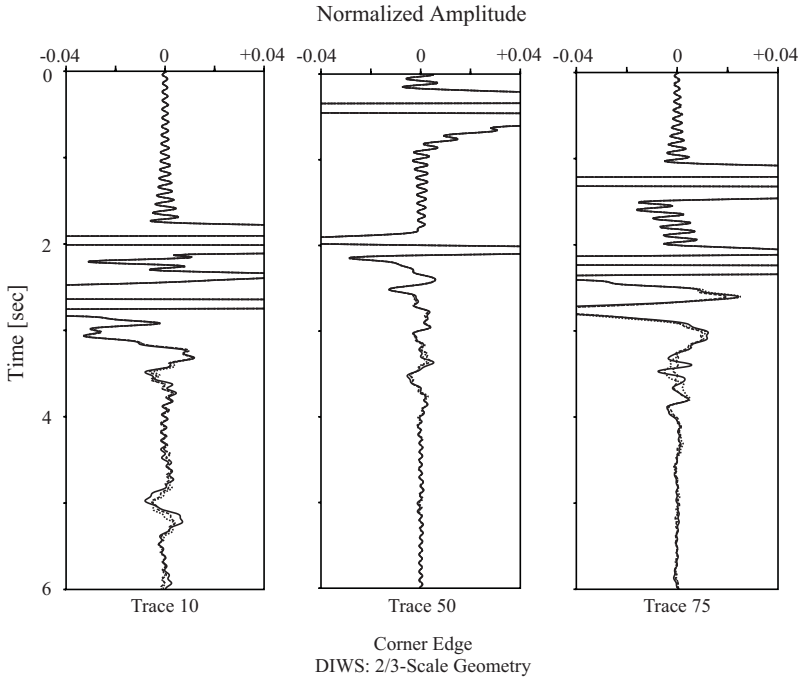

Figure 4.24: Comparison of the *two-scales* and *three-scales* wave-field solution computed by the DIWS. The dotted and dashed lines denote fine-grid wave-field solutions for the *two-* and *three-scales* simulation, respectively. The difference between the two is plotted as continuous line.

fine-grid of size 105×110 and 210×220, respectively. The DISS and DIWS seismograms for $n_{it} = 3000$ number of iterations are plotted in Figure 4.26 and Figure 4.27. The DISS seismogram contains strong vertically vibrating noise that hides interesting wave propagation events. In contrast, the DIWS simulation provides a dispersion-free seismogram. We extract three traces from each of the seismograms and plot the direct DISS-DIWS comparison in Figure 4.28. On all traces, we observe ringing of the DISS solution. Far offset traces, with respect to the source position, show stronger ringing artefacts.

We increase the maximum number of iterations from $n_{it} = 3000$ to $n_{it} = 5000$ and re-compute DISS iterative wave-field solutions. Moreover, we compute the exact seismogram using the direct solver for the fine-grid model setup. In Figure 4.29, we show the comparison of three traces obtained by the exact direct solver and the DISS after $n_{it} = 3000$ and $n_{it} = 5000$ iteration steps. The increase of iteration steps significantly reduces the previously detected ringing, and the DISS solution perfectly fits the exact wave-field solution.

As for the DISS, we compare extracted traces for the DIWS simulation with the exact Marmousi seismogram. In Figure 4.30, we plot the exact solution and two DIWS iterative solution approximations after $n_{it} = 1500$ and $n_{it} = 3000$ iteration steps. Even though

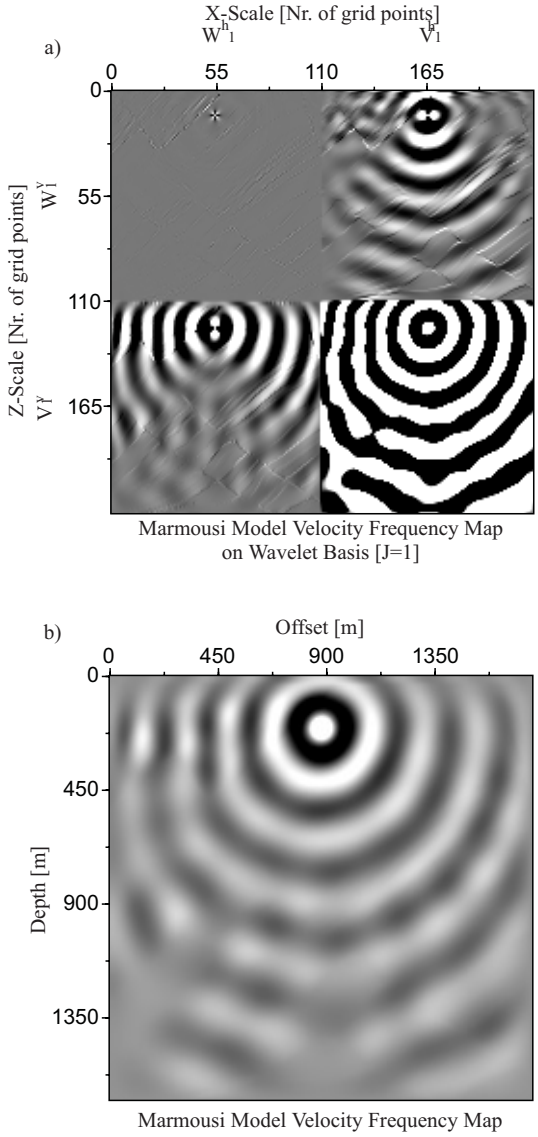

Figure 4.25: Frequency map ($f \approx 9.5Hz$) computed by the DIWS scheme for the windowed Marmousi Model. In (a) we show the frequency distribution of the wave-field velocity component ($v_y = v_{yx} + v_{yz}$) on the wavelet basis with $J = 1$ resolution scales. Note that we only plotted the real part of complex valued wave-field. The gain in (a) is significantly increased in order to enhance the interaction coefficients that appear on the boundaries of different layers in the model with varying physical parameters. Application of the inverse wavelet transform gives the velocity wave-field component in the physical domain in (b).

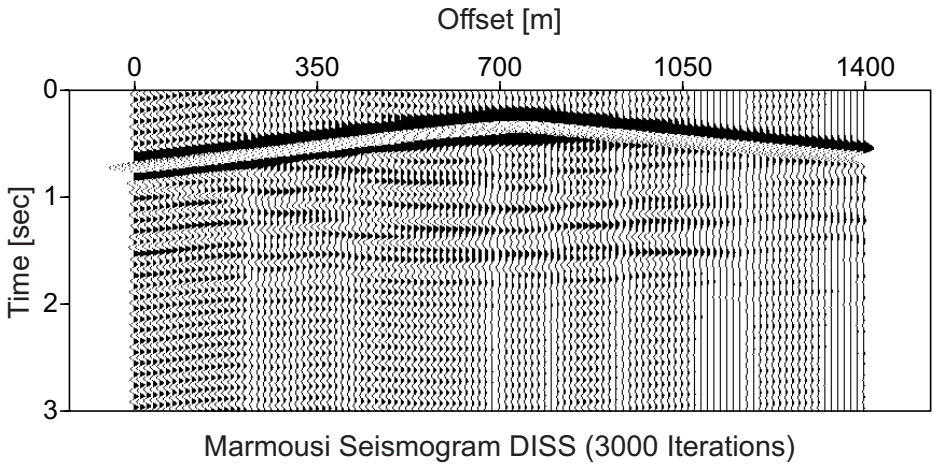

Figure 4.26: Time seismogram for the Marmousi model. The coarse-grid solution is extrapolated from 105×110 nodes ($dx = dz = 16m$) to the fine-grid 210×220 ($dx = dz = 8m$) by a bilinear interpolation. The seismogram is computed after $n_{it} = 3000$ iteration steps in the frequency domain.

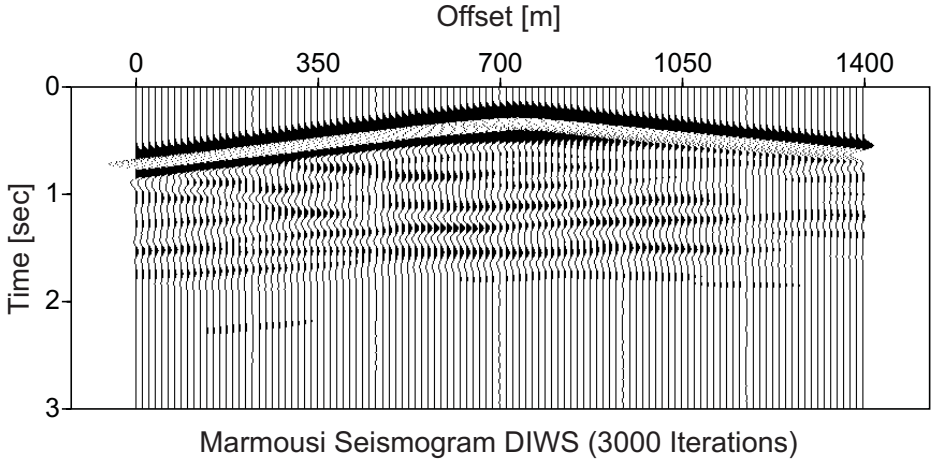

Figure 4.27: Time seismogram for Marmousi model computed by the DIWS scheme. We use $J = 1$ wavelet resolution spaces (coarse grid: $105 \times 110/dx = dz = 16m$, fine grid $210 \times 220/dx = dz = 8m$). The maximum number of iteration steps is set to 3000.

the DIWS iterative wave-field solution after $n_{it} = 1500$ still has deficiencies, at this *early* stage (in terms of number of iterations) it already reproduces the main structure of the final seismogram. After $n_{it} = 3000$ iteration steps the DIWS provides a seismogram that fits the exact solution very well.

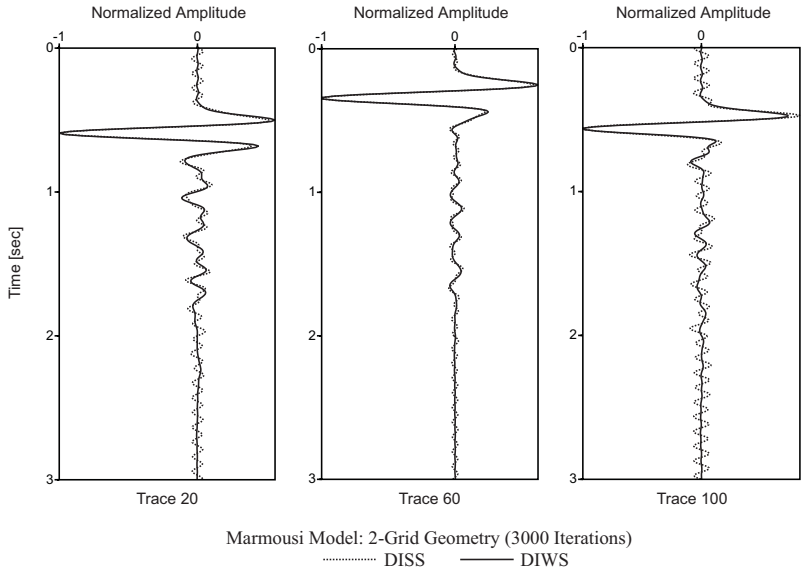

Figure 4.28: Comparison of three traces that are extracted from the Marmousi model DISS- and DIWS-seismograms. The dotted and continuous lines are the DISS and DIWS fine-grid solution after $n_{it} = 3000$ iteration steps, respectively.

Computation times for different number of DISS and DIWS iteration steps are given in Table 4.2. For a fixed number of iterations $n_{it} = 1500$, the DISS requires $\approx 40\%$ less computation time than the DIWS, though the obtained DISS wave-field solution is strongly distorted by noise. In order to obtain a qualitatively dispersion-free wave-field solution, the DISS scheme needs $\approx 30\%$ more computation time than the DIWS scheme. The increase in iterative computation time is significant if one has to perform iterations for many RHSs.

4.10.3 Discussion

The DISS and DIWS are tested for two complex modelling scenarios. Wave-field simulations in the Corner Edge model are performed for a *two-step* and *four-step* setup, where spatial discretization steps change by a factor of 2 and 4 between the coarse- and fine-grid. The second wave propagation simulation for the Marmousi model is performed using a *two-step* combination.

The spatial DISS approach permits fast and efficient matrix constructions. In general, the computation time related to the DIWS matrix construction is greatly increased, because of convolution-type projections in the wavelet space. Although expensive, the convolution calculations are carried out only once before the modelling starts.

The DISS matrix is sparse and therefore provides efficient computations of *GMRES* iteration steps. In contrast, the number of non-zero coefficients in the DIWS-matrix

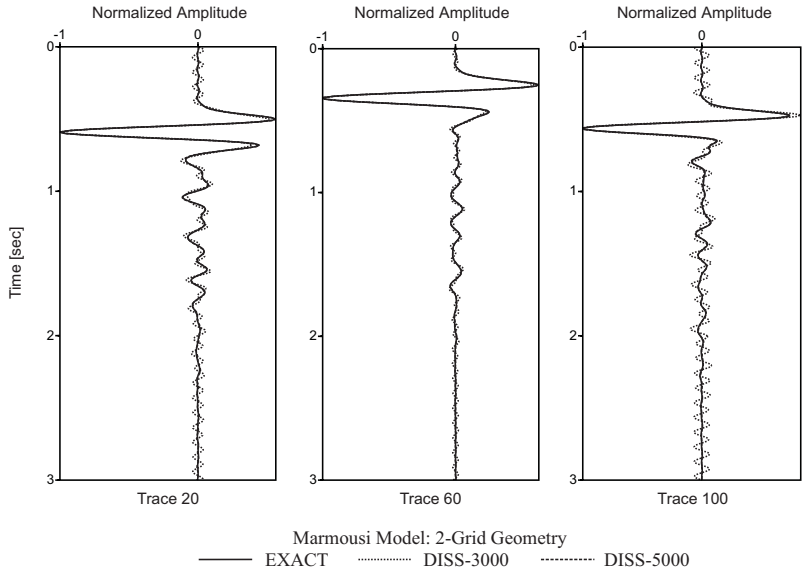

Figure 4.29: Comparison of three traces that are extracted from the Marmousi model exact seismogram and the DISS-seismograms after $n_{it} = 3000$ and $n_{it} = 5000$ iteration steps. The continuous line is the exact wave-field solution, the dotted and dashed lines the DISS solutions for $n_{it} = 3000$ and $n_{it} = 5000$ iterations, respectively.

increases with respect to the number of wavelet resolution scales used. Therefore, iterative matrix-vector and dot-product computations are slowed down, when compared to similar products in the physical space. We did not address any space adaptivity implementation at this stage of the development, although the wavelet formulation naturally supports the definition of spatial masks that significantly increase the computational performance.

Nevertheless, the multi-scale formulation through wavelet-based iterations provides a Full Multi-Grid environment, where intermediate iterative solutions on all resolution scales are directed versus the correct final solution in a desirable automatic manner. Already a relatively small number of iteration steps provide a useful *homogenized* version of the final solution. With increasing iterations the wavelet and scaling coefficients are modified to finally construct the fine-grid wave-field solution.

The iteration on the wavelet basis is favourable, because interactions of the fine-grid and coarse-grid approximations are accounted for automatically. Even though the DIWS matrix construction is expensive, it is only performed once. More important is the reduction of necessary iteration steps required to compute a dispersion-free wave-field solution, if one simulates large-scale multi-source experiments. The CPU-time performance may be increased in the future through the invention of space adaptivity and optimised parallel wavelet transform algorithms.

In contrast, the DISS matrix construction is performed at practically no computational cost. The matrix sparsity is guaranteed by the staggered finite-difference stencil

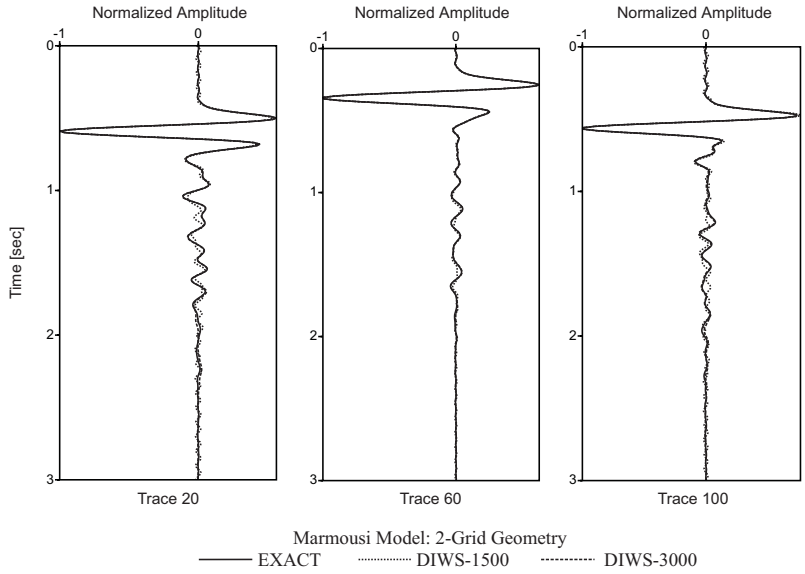

Figure 4.30: Comparison of three traces that are extracted from the Marmousi model exact seismogram and the DIWS-seismograms after $n_{it} = 1500$ and $n_{it} = 3000$ iteration steps. The continuous line is the exact wave-field solution, the dotted and dashed lines the DIWS solutions for $n_{it} = 1500$ and $n_{it} = 3000$ iterations, respectively.

applied in the physical domain. Therefore, fast and efficient matrix-vector and dot-products may be implemented. The main drawback of the DISS approach is related to the simple-grid formulation that can only treat coarse- or fine-grid errors at a time. Dispersion-free wave simulations are strongly dependent on the number of iteration steps performed. Even though phase-corrected frequency-maps may be obtained when large amounts of iteration steps are performed, the ambiguity for choosing the right amount of iterations is rather cumbersome.

One possibility to introduce more variability in the DISS scheme to suppress interpolation related phase-shifts and the convergence of low-frequency components on the fine-grid, is the extension of the current DISS *nested iteration* approach to a (space) FMG method through loops over sequences of V- and W-cycles.

The role of wavelet resolution scale interactions is illustrated in Figure 4.31a and b for a single frequency-map $f = 9.5Hz$ of the Marmousi simulation. In Figure 4.31a from left to right, we show the coarse-grid solution recast as initial iterative solution on $J = 1$ resolution scales, the result from the iteration process, and the difference between the initial and the final solution on the wavelet basis. Figure 4.31b is the same sequence, though now after inverse wavelet transformation in the physical space.

Interesting to note is the fact that the DIWS modified the coarse-grid solution in the $V_1 \times V_1$ space. This indicates the necessity of coarse grid corrections in the iterative scheme to suppress fine-scale low-frequency components that otherwise may cause

Solver	Nr. of Iterations	CPU-time / frequency $[min]$
DISS	1500	6
DISS	2500	12
DISS	3500	17
DISS	5000	23
DIWS	1500	16

Table 4.2: Computation times for the complex Marmousi Model for the DISS and DIWS schemes. DISS wave-field solutions have been computed for four increasing number of iteration steps ($n_{it}^{max} = 1500, 2500, 3500, 5000$) while the DIWS simulation was performed using $n_{it}^{max} = 1500$ iteration steps only.

severe difficulties in the iteration process. Even though fine-grid wavelet and interaction contributions are less strong, they still influence the iteration process at each iteration step. The wavelet multi-scale formulation naturally incorporates these effects, while the DISS nested iteration requires excessive CPU-time or *manual* corrections through V- and W-cycles that are difficult to perform.

4.11 Conclusion and Perspectives

We perform wave propagation simulations in structurally complex media with strong velocity contrasts. Wave-field solutions are computed using the DISS and DIWS schemes for a set of frequency components. The space- and wavelet-based solvers are compared with respect to CPU-time performance and accuracy of the solution.

The combination of a direct with an iterative solver (DIS) allows wave-field simulations in synthetic models of larger size, compared to applications of a single direct solver. The performance of the DIS approach depends mainly on the formulation of the iterative solution scheme.

We found that space linear grid-combinations lead to fast and efficient matrix constructions, matrix-vector, and dot-product algorithms. The DISS approach is similar to the nested iteration part of a standard multi-grid method. The phase-shifts introduced by simple bilinear interpolation require large numbers of iteration steps in order to provide dispersion-free wave simulation results.

The second DIS approach uses the multi-scale formulation of a standard orthogonal Daubechies-4 wavelet transform (DIWS). The analytic construction of the principal matrix terms in the spectral wavelet space, though performed only once before the modelling starts, requires the calculation of expensive convolution-type projection algorithms and leads to less efficient matrix computations than in the physical space.

The main advantage of the wavelet-based preconditioning is the simultaneous iteration on all wavelet resolution grids, where interaction between scales are accounted for automatically. In a way, the DIWS scheme therefore performs FMG V-cycles at each iteration step The wavelet-iteration was found to be largely independent of the number of

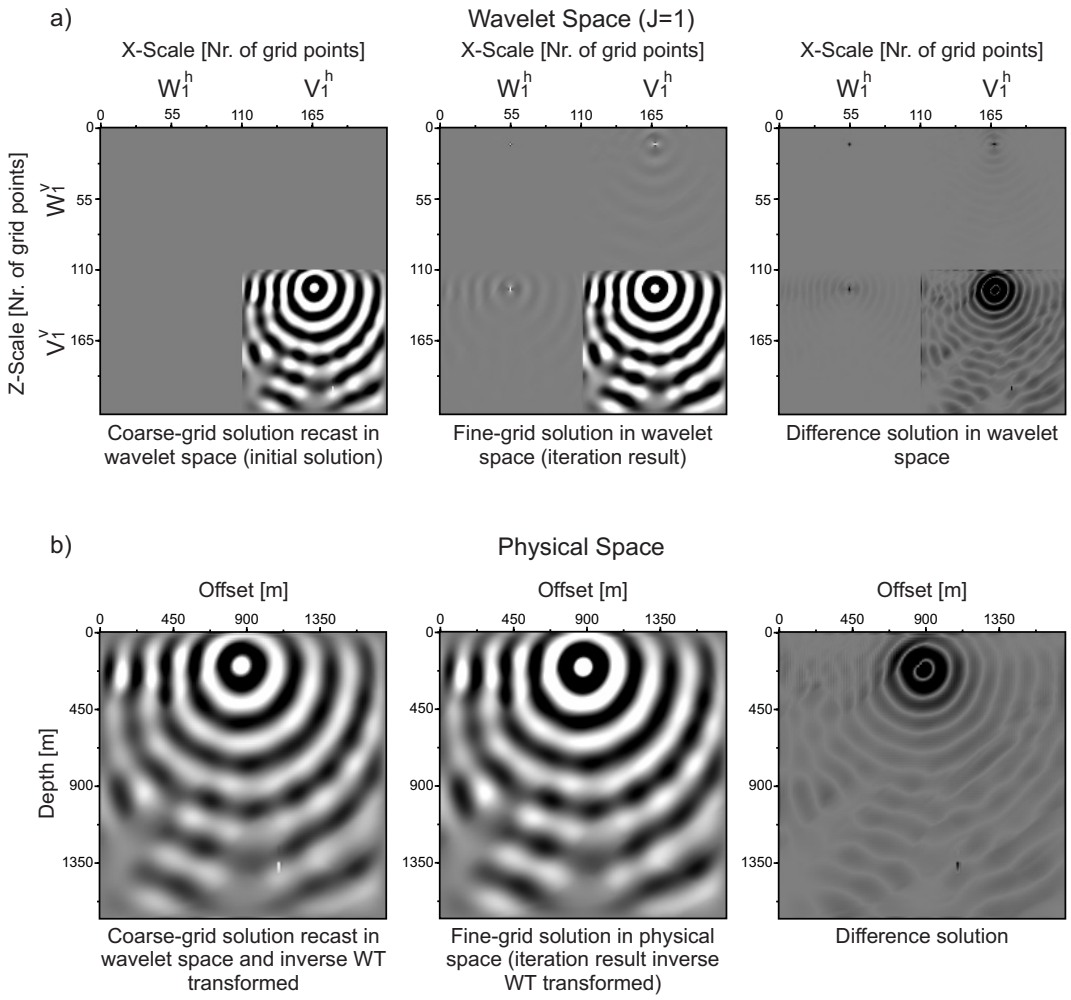

Figure 4.31: Illustration of grid interactions occurring during the iteration process on a wavelet expansion for the DIWS scheme. The example is shown for a frequency map ($f = 9.5Hz$) computed by the DIWS on $J = 1$ resolution scales for the Marmousi model. In (a) we plot the coarse-grid wave-field solution recast in the wavelet expansion, where all wavelet coefficients are initially zero. The middle panel shows the output of the *GMRES* iterative solver after $n_{it} = 3000$ iteration steps. The right panel is the difference of the initial and final wave-field solution. Part (b) is similar to (a), though now the velocity wave-field solutions have been inverse transformed in the physical domain. Interesting to note is that the iterative solver modified the $V_1 \times V_1$-space in the wavelet expansion. This signifies that the fine-grid wavelet coefficients interact and alter the coarse-grid representation of the wave-field solution.

iterations steps performed. Already a small number of iteration steps provided quantita-

tive dispersion-free seismograms where principal wave phenomena may be distinguished.

We illustrated the accuracy and performance of DISS and DIWS approaches for the Corner Edge model and the Marmousi model with respect to varying grid sizes and number of iteration steps.

The numerical tests clearly indicate superior iteration behaviour for the DIWS multi-scale formulation rather than for the DISS nested iteration approach. The combination of the wavelet multi-grid construction with an iterative solver eliminates the ambiguity of manual grid combinations of standard nested iteration techniques.

The computational cost for matrix constructions in the spectral wavelet space may be reduced when space adaptivity strategies are implemented. Moreover, significant speed-up is obtained by the extension of the DISS and DIWS sequential codes to run on parallel computer structures.

Nevertheless, large 2D and 3D wave propagation simulations require significantly increased memory and computational power, such that the passage of the existing sequential code to a parallel version seems unavoidable. Although it was not considered in this study, standard numerical preconditioning is expected to provide another important speed-up for the iterative scheme.

Altogether, the DIWS approach provides a powerful tool to investigate wave propagation phenomena for discrete frequency components or complete sets of frequencies for multiple RHSs in media having complex heterogeneous rheology. Typical applications are site effect studies, where the response to single frequencies is of great interest. Moreover, wave-field simulations of discrete frequency components provide powerful information for full waveform inversion schemes. Other applications include standard forward modelling of large-scale marine multi-source experiments for high frequency bands.

The next development step of the DIS strategy investigates the iterative convergence for a fixed tolerance level that was not addressed here. Furthermore, the numerical code will be parallelized together with an extension to 3D modelling for elastic wave propagation. This work is under way and will be presented in a separate article.

4.12 Acknowledgments

We are very grateful to Patrick Amestoy (ENSEEIHT-IRIT), Luc Giraud (CERFACS) and Jean-Yves Excellent (UMR CNRS-ENS Lyon-INRIA) for providing us with the multi-frontal matrix ordering software MUMPS, the iterative solver GMRES and some fruitful discussions regarding the direct-iterative strategy for wave simulations. We thank Stéphane Lanteri and INRIA Sophia Antipolis for the access to their PC-Cluster environment. We further acknowledge the usage of the IDRIS PC-Cluster. The research leading to this paper was partly founded by DASE/CEA through the PROSIS3D group. This paper is Contribution No. XXX from UMR Geosciences Azur - CNRS, FRANCE.

4.13 Appendix A - Basic wavelet theory

We introduce some important features of the orthogonal wavelet transform using Daubechies wavelets without reviewing the mathematical principals that led to the development of the wavelet theory. This appendix is rather limited in content and explications are mainly provided to set right the terminology used in the article. For further readings concerning wavelet theory, we refer to works of Mallat (1989), Daubechies (1992) and Beylkin (1998).

The orthogonal wavelet transform developed by Daubechies (1992) is defined by two functions: $\phi(x)$ is the scaling function and $\psi(x)$ the wavelet function. In order to see how these functions build the basis of the wavelet transform we first introduce the multi-resolution analysis (MRA). The MRA can be compared to a microscope with which we are able to analyse a function with any desired resolution. The MRA is a way to approximate a function, which is done by the above mentioned scaling function. In order to approximate an L^2-function, we try to represent it by a linear combination of a family of scaling functions, where family here denotes translations of scaling functions. We have:

$$P_{V_j}(f) \approx \sum_{k \epsilon Z} u_{j,k} \phi_{j,k} \tag{A. 1}$$

where $\phi_{j,k}$ are dilations (j) and translations (k) of the function ϕ:

$$\phi_{j,k}(t) := 2^{-\frac{j}{2}} \phi(2^{-j}t - k) \tag{A. 2}$$

If we now assume that the scaling functions $\phi_{j,k}(k \epsilon Z)$ build an orthonormal family at a given approximation, we can then write the coefficients $u_{j,k}$ as:

$$u_{j,k} =< \phi_{j,k}, f >= \int_{-\infty}^{+\infty} \phi_{j,k}(t) f(t) dt \tag{A. 3}$$

We note that the coefficients $u_{j,k}$ define a weighted average of the function f in the surroundings of the location $k2^j$. The smaller j gets, the smaller will be the approximation region and therefore the approximation of the discretized function f by the coefficients $u_{j,k}$.

In other words, the approximation of the initial function f is performed by an analysis with dilated and translated versions of the scaling function. The scaling function adapts to spatially local features in f that correspond to the actual resolution approximation. This gives the desired multi-resolution decomposition property.

With the definition of the scaling function, we have found a way to represent a function on any desired approximation space V_j, while the initial scaling function ϕ itself lies in V_0. We assume V_0 to be the finest discretization space. Clearly, several approximations of a function on different resolution scales (levels of j) are connected to each other. Intuitively

we would require that an exact approximation of a function f on a resolution scale V_j would imply an exact approximation on any finer resolution scale V_p, if $p < j$. In other words, the MRA defines a chain of approximation subspaces:

$$... \subset V_1 \subset V_0 \subset V_{-1} \subset V_{-2} \subset ... \tag{A. 4}$$

Without giving further evidence, it can also be shown that the scaling functions are connected by filter coefficients $h_k(k \epsilon Z)$ such that

$$\phi_{j,k} = \sum_{k \epsilon Z} h_{k-2n} \phi_{m-1,k} \tag{A. 5}$$

As a consequence the scaling function ϕ can be integrated and we get:

$$\int_{-\infty}^{+\infty} \phi(t) dt = 1 \tag{A. 6}$$

The MRA provides a tool to decompose a function on approximation spaces V_j of different resolution using scaling functions. In order to construct a complete orthonormal basis of L^2 on the basis of the MRA, we have to add some missing information. The scaling functions $\phi_{j,k}$ do not build a basis for two reasons. First, we did not require the functions $\phi_{j,k}$ of different resolutions spaces V_j to be orthogonal. And second, scaling functions of coarse subspaces can be constructed from linear combination of the scaling function from finer subspaces (Equation A. 5). Scaling functions $\phi_{j,k}$ only form an orthonormal basis for fixed subspaces V_j.

At this point the wavelet functions $\psi_{j,k}$ come into play. Since we have already constructed basis functions on each subspace V_j, it would be logic to just extend the existing bases in order to form a basis for the next coarser scale with respect to the underlying fine scale, and so forth.

Following this idea leads to the construction of the wavelet functions that again is defined through dilations and translations of one function (compare with the scaling function in Equation A. 2):

$$\psi_{j,k}(t) := 2^{-\frac{j}{2}} \psi(2^{-j} t - k) \tag{A. 7}$$

The scaling and wavelet functions are then related through:

$$\begin{aligned} \psi_{j,k} &= \sum_{n \epsilon Z} g_{n-2k} \phi_{j-1,n} \\ \psi(t) &= \sqrt{2} \sum_{n \epsilon Z} (-1)^n h_{l-n} \phi(2t - k) \end{aligned} \tag{A. 8}$$

with $g_k := (-1)^k h_{l-k}$.

It is possible to show that the shifted and translated wavelet functions $\psi_{0,k}$ (ϵV_0) do complete the scaling functions $\phi_{0,k}$ (ϵV_0) to an orthonormal basis of the subspace V_{-1}. Moreover, this procedure can be extended to any other subspace and it can further be shown that for any L^2function the following relation holds:

$$f = \sum_{j \epsilon Z} \sum_{k \epsilon Z} \nu_{j,k} \psi_{j,k} \tag{A. 9}$$

with $\nu_{j,k} =< \psi_{j,k}, f >$.

Since the wavelet functions do encode just the extension to complete the passage from one approximation subspace to the next coarser one, the resulting wavelet coefficients are also called 'details', and in the same logic the scaling coefficients 'averages'.

We are therefore able to replace a signal in the physical domain e.g., a time snapshot of a wave propagating in a homogeneous medium (see Figure 4.10a) by its projection on a number of subspaces that are spanned by the scaling and wavelet functions. They can be combined to form a cascaded algorithm where the initial signal is decomposed on a series of wavelet approximation spaces (W_j-spaces) and one scaling space (V_J-space). This representation is cascaded in the sense that we reconstruct the initial signal subspace by adding 'detail'-information to the scaling space ($V_j + W_j = V_{j-1}$):

$$A_{j_0} f = \sum_{k \epsilon Z} u_{j_1,k} \phi_{j_1,k} + \sum_{j=j_0+1}^{j_1} \sum_{k \epsilon Z} \nu_{j,k} \psi_{j,k} \tag{A. 10}$$

where we assumed $j_0 < j_1$.

$A_J f = \sum_{k \epsilon Z} u_{j,k} \phi_{j,k}$ is the approximation of f on the resolution scale m and $u_{j,k} =< \phi_{j,k}, f >$ and $\nu_{j,k} =< \psi_{j,k}, f >$ the corresponding projection coefficients.

At each step of the cascade, the combination of the corresponding V- and W-space forms the next finer approximation space and the re-construction can be continued until the initial representation. In Figure 4.10c we show the projection on 3 resolution scales. The $W_{1,\ldots,3} \times W_{1,\ldots,3}$ spaces encode the 'details' and the $V_{J=3} \times V_{J=3}$ is the coarsest 'average' space (see Figure 4.10d).

4.14 Appendix B - Matrix projection in orthogonal wavelet basis

4.14.1 Projection of physical medium parameters (diagonal blocks)

We first derive Equation 4.13, that is the product of medium properties with wave-field components projected on an orthogonal wavelet basis. Note that wave-field projections on the wavelet basis in x-direction are denoted by indices i, j, k, l and for the z-direction by α, β.

We start the wavelet transformation by expanding the expression $i\omega\xi(x,\omega)\rho(x,z) \cdot v_{yx}(x,z)$ first on an orthogonal wavelet basis with respect to the x-direction:

$$\sum_i < i\omega\xi_x\rho(x,z)v_{yx}(x,z), \psi_i > \psi_i \tag{B. 1}$$

We separate the wave-field component v_{yx} and the density term $i\omega\xi_x\rho(x,z)$ through permutation and subsequent application of a second wavelet expansion to the wave-field component v_{yx}. The new basis which is also a projection in x-direction, is denoted by ψ_j. We obtain the double sum:

$$\sum_{i,j} \quad < v_{yx}(x,z), \psi_j >< \psi_j, i\omega\xi_x\rho(x,z)\psi_i > \psi_i \tag{B. 2}$$

We are now ready to project Equation B. 2 on a wavelet basis in z-direction, denoted by ψ_α. This gives:

$$\sum_\alpha \sum_{i,j} << v_{yx}(x,z), \psi_j >< \psi_j, i\omega\xi_x\rho(x,z)\psi_i >, \psi_\alpha > \psi_i\psi_\alpha \tag{B. 3}$$

Again, we need to separate terms depending on z and therefore apply a second wavelet projection following the same procedure as before, but now in the z-direction (ψ_β):

$$\sum_{\alpha,\beta} \sum_{i,j} < v_{yx}(x,z), \psi_j\psi_\beta >< \psi_j\psi_\beta, i\omega\xi_x\rho(x,z)\psi_i\psi_\alpha > \psi_i\psi_\alpha \tag{B. 4}$$

The inner products in Equation B. 4 form a term-to-term product which has to be recast to verify the matrix equation $A \cdot x = b$, with x being the desired solution constructed by the GMRES iterative solver. In order to compute the necessary terms, we first need to construct the wavelet basis functions ψ_i and ψ_α. For each pair (i,α) we compute the product of medium parameters $i\omega\rho(x,z)$ with the wavelet basis functions ψ_i and ψ_α and then expand the resulting term on the wavelet basis through subsequent projections in the x- and z-directions. The term-to-term product will then be verified through correct storage of the corresponding term $< \psi_j\psi_\beta, i\omega\xi_x\rho(x,z)\psi_i\psi_\alpha >$ in the impedance matrix A and $< v_{yx}(x,z), \psi_j\psi_\beta >$ in the desired solution x to give a standard matrix-vector product.

4.14.2 Projection of differential operators

We compute the projection of staggered grid derivative operators on an orthogonal wavelet basis. For simplicity, we show the development for the x-derivative operator only, since replacing x by z and following a similar procedure, leads to the z-derivative operator:

We project the derivative operator on an initial basis ψ_i in x-direction and obtain

$$\sum_i < \frac{\partial}{\partial x} v_{yx}, \psi_i > \psi_i \tag{B. 5}$$

As before, we need to separate contributions depending on the x-direction, namely the operator $\partial/\partial x$ and the wave-field $v_{yx}(x,z)$. We go back to the definition of the inner product and apply an integration by parts which gives:

$$\begin{aligned} \sum_i < \frac{\partial}{\partial x} v_{yx}, \psi_i > \psi_i &= \int_{-\infty}^{+\infty} \frac{\partial v_{yx}(x,z)}{\partial x} \cdot \psi(x) dx \\ &= [\psi(x) \cdot u_{xy}(x,z)]_{-\infty}^{+\infty} - \int_{-\infty}^{+\infty} \frac{\partial \psi(x)}{\partial x} \cdot v_{yx}(x,z) dx \end{aligned} \tag{B. 6}$$

Because of the local support of the Daubechies wavelets, the first term in Equation B. 6 is zero. We therefore obtain,

$$\sum_i < \frac{\partial}{\partial x} v_{yx}, \psi_i > \psi_i = -\sum_i < \frac{\partial \psi_i}{\partial x}, v_{yx}(x,z) > \psi_i \tag{B. 7}$$

We separate the remaining expression by projecting the derivative term $\frac{\partial}{\partial x}\psi_i$ onto a new wavelet basis ψ_j, and obtain:

$$-\sum_{i,j} < \frac{\partial}{\partial x} \psi_i, \psi_j >< \psi_j, v_{yx} > \psi_i \tag{B. 8}$$

Finally, we perform the wavelet expansion in the z-direction. Since the derivative operator depends on the x-component only, no further projections have to be performed and we get the final wavelet expansion of the x-derivative operator on a two-dimensional orthogonal wavelet basis:

$$-\sum_{\alpha} \sum_{i,j} < \frac{\partial}{\partial x} \psi_i, \psi_j >< v_{yx}, \psi_j \psi_\alpha > \psi_i \psi_\alpha \tag{B. 9}$$

Chapter 5

Wave-field simulations: 2D benchmark tests

5.1 Résumé

Dans ce chapitre, les performances des méthodes DISS et DIWS développées au chapitre 4 sont évaluées à l'aide de plusieurs tests numériques calculés dans des modèles 2D homogènes et hétérogènes. Les algorithmes des méthodes directe et itérative de résolution de système d'équations linéaires sont évalués en détail.

Dans un premier temps, je présente une comparaison des méthodes de résolution numérique directs UMFPACK et MUMPS pour des modélisations calculées par l'approche DISS dans des modèles homogènes de taille différente et pour 3 fréquences de la bande $0 - 10Hz$. Les deux logiciels UMFPACK et MUMPS de factorisation LU d'une matrice sont basés sur une méthode de rangement "*frontal*" de la matrice. Les tests démontrent les performances supérieures du solver MUMPS par rapport à UMFPACK en termes de taille maximale des modèles pouvant être traités ainsi qu'un temps CPU indépendant de la fréquence modélisée.

Le solver itératif commun aux approches DISS et DIWS est fondé sur une approche de type *Krylov*. Ces méthodes permettent de calculer la solution d'un système matriciel dont la matrice associée est à coefficients complexes et non symétrique. Pour cela, j'utilise le logiciel GMRES développé au CERFACS. L'implémentation de GMRES au sein du code de modélisation est facile et laisse toute latitude à l'utilisateur pour l'optimisation du stockage et du calcul des produits matrice-vecteur.

Plusieurs résultats de modélisation du champ d'onde dans des milieux 2D dans le domaine des fréquences (cartes en fréquences) et du temps (sismogrammes) calculés par les approches DISS et DIWS sont présentés et comparés avec ceux obtenus avec des codes par différences finies classiques en temps (TDFD) et des solutions analytiques.

5.2 Introduction

In addition to wave-field simulations presented in the previous Chapter 4, I show benchmark tests for 2D homogeneous and heterogeneous media. All wave propagation simulations have been performed using the DISS and DIWS approaches for similar model geometries and physical parameter setups.

5.3 Direct and iterative solver

The implementation of the DISS and DIWS strategy uses external software to perform the direct matrix factorization and iterative procedure for the computation of coarse-grid and fine-grid wave-field solutions. I did not address the implementation of the solver schemes, because I am mainly interested in studying complex wave propagation phenomena rather than developing a numerical tool. For example, the estimated development time for an optimised direct matrix factorization solver is in the range of years (Amestoy and Giraud, 2002), and therefore was not considered here. Moreover, many different highly optimised solver software has become accessible without any difficulties, and it is rather a question which method and implementation scheme for a given problem at hand may provide the best numerical performance in terms of numerical stability and CPU-time and memory requirements.

5.3.1 Direct solver software

For the computation of the direct matrix factorization, I tested two different LU decomposition schemes that are both based on minimum matrix ordering approaches (Duff et al., 1997). The first software implemented in the DIS algorithm is the *UMFPACK* package developed by Davis and Duff (1997). *UMFPACK* is written in Fortran F77 and therefore is easily incorporated in the DISS and DIWS approach. The *UMFPACK* code combines two pivot strategies, namely uni-frontal and multi-frontal methods, in order to reduce matrix fill-in during the matrix factorization. The second software incorporated in the DISS and DIWS codes was directly provided by Amestoy et al. (2001). Their matrix factorization algorithm, called *MUMPS*, is based on a strict multi-frontal ordering method. Even though *MUMPS* was developed especially for direct matrix factorizations performed on parallel distributed computer environments, I used the existing sequential version to compare with the *UMFPACK* software. Both factorization schemes can treat un-symmetric complex-valued matrices in sparse format.

I tested the *UMFPACK* and *MUMPS* solvers for a DISS wave propagation simulation in the Corner Edge model of varying grid sizes. Moreover, I examined the performance of the two factorization schemes with respect to the frequency modelled. Performance variations of the matrix factorization depend strongly on the absolute numerical value of the coefficients in the matrix. As I noted in the previous Chapter 4, I equalised matrix entries by applying a simple normalisation strategy to the hyperbolic wave equation. The normalisation is necessary, since otherwise diagonal matrix entries for the DISS and DIWS scheme range from $1.e^{\pm 3}$ to $1.e^{\pm 11}$ depending on the physical medium parameters for

density ρ and the shear modulus μ. Although the physical normalisation may be applied specifically for each model scenario, I used a constant set of normalisation coefficients throughout all wave simulations. The deduced values are $\sigma^0 = 1.e^{+10}$ and $v^0 = 1.e^{+3}$.

The wave simulation test for the *UMFPACK* versus *MUMPS* performance comparison are performed on a stand-alone Linux PC with $1GByte$ of RAM and processor speed of $1MHz$. Table 5.1 summarises the parameters used for the performance comparison

Model	Matrix Size	Frequency	MUMPS		UMFPACK	
$nz \times nx$	NOZ	$[Hz]$	Factorize	Solve	Factorize	Solve
50×80	$16e^3 \times 16e^3$	0.1	100	< 1	330	< 1
	110440	4.5	95	< 1	59	< 1
		9.8	97	< 1	66	< 1
60×100	$24e^3 \times 24e^3$	0.1	238	< 1	1168	1
	166080	4.5	228	< 1	130	< 1
		9.8	228	< 1	227	1
80×120	$38.4e^3 \times 38.4e^3$	0.1	659	< 1	3146	3
	266400	4.5	660	2	676	1
		9.8	639	1	449	1
100×160	$64e^3 \times 64e^3$	0.1	2978	2	–	–
	444880	4.5	2785	3	–	–
		9.8	2908	3	–	–
140×200	$112e^3 \times 112e^3$	0.1	8356	6	–	–
	779920	4.5	7414	6	–	–
		9.8	7445	6	–	–

Table 5.1: Comparison of matrix factorization performed using *UMFPACK* and *MUMPS* for the Corner Edge model of varying size. All computations are computed by the DISS scheme on a stand-alone Linux PC with $1GByte$ of RAM memory and a processor speed of $1MHz$. Computation times are given in $[sec]$.

as well as the CPU time results for the matrix factorizations and the solving of the equations, separately. Note that the solve-phase computation time is interesting since it demonstrates the efficiency of FDFD direct approaches for wave propagation simulations with numerous RHSs.

In Figure 5.2 and Figure 5.3, I show the complex impedance matrix for the DISS and DIWS scheme for a *two-step/two scales* modelling scenario. All non-zero coefficients are plotted as black dots. The DIWS matrix holds wavelet and scaling coefficients from the spaces $W_1 \times W_1$, $V_1 \times W_1$, $W_1 \times V_1$ and $V_1 \times V_1$. I underline the increase of non-zero coefficients in the DIWS-matrix as a function of number resolution scales that is due to the expansion in the wavelet domain.

In Figure 5.1, I illustrate the results of the performance test for the complex DISS matrix graphically. The multi-frontal scheme *MUMPS* performs matrix factorizations up to a model size of about 150×200 grid-nodes, while the *UMFPACK* software already

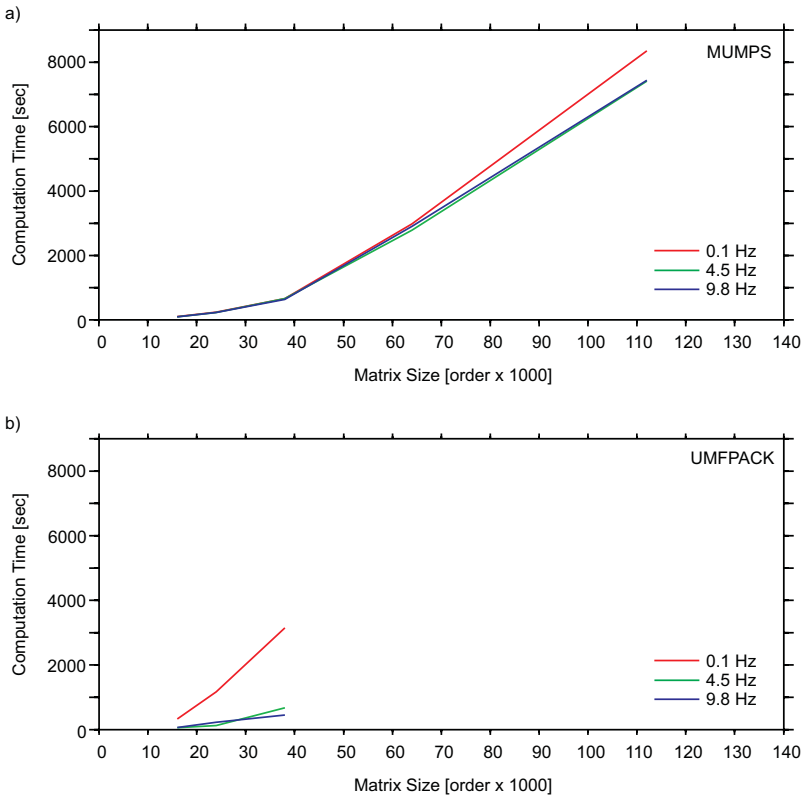

Figure 5.1: Comparison of matrix factorization software: *UMFPACK* versus *MUMPS*. The x-axis corresponds to the order $\times 1.e^3$ of the matrix that is factorized into its LU-factors. The y-axis indicates the computation time needed in [*sec*]. Tests are performed for three frequency components. The red line denotes $f = 0.1Hz$, the green line $f = 4.5Hz$ and the blue line $f = 9.8Hz$. (a) gives the numerical results for *MUMPS* and (b) for *UMFPACK*.

breaks down for model sizes of 80×120 grid-nodes. Note, *break down* signifies that not sufficiently RAM memory is available to perform the desired matrix factorization. Moreover, *MUMPS* matrix factorizations have been found to give stable computation times despite of the frequency used. In contrast, *UMFPACK* factorizations may vary significantly, or even break down depending on the frequency modelled.

I decided to use the *MUMPS* software for the DISS and DIWS direct matrix factorization, because of the possibility to simulate wave propagation in larger earth models independent from the frequency modelled. Moreover, since *MUMPS* is developed to run on parallel distributed computer structures by a combination of MPI and Fortran F90, a parallelization of the direct matrix factorization in the DISS and DIWS approaches is reduced to the construction or distribution of the impedance matrix with respect to the parallel environment.

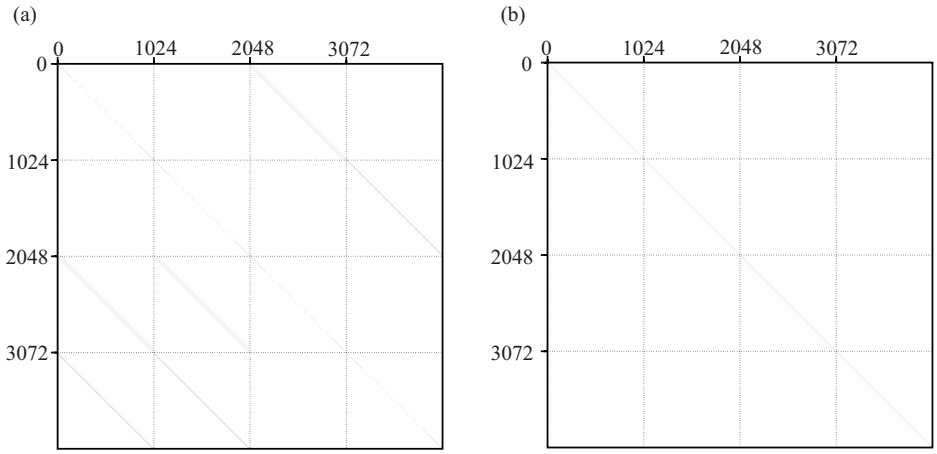

Figure 5.2: The FDFD matrix used in the DISS approach to compute coarse-grid and fine-grid solution of the first-order hyperbolic wave equation. In this plot the matrix is constructed using second-order staggered grid discretizations. The matrix contains $(4 \cdot nx \cdot nz)^2$ elements from which approximately $6 \cdot nx^2 + 6 \cdot nz^2 + 4 \cdot nx \cdot nz$ elements are different from zero. (a) shows the real part and (b) the imaginary part of complex DISS matrix. Non-zero coefficients are represented as black dots. All white coefficients are zero.

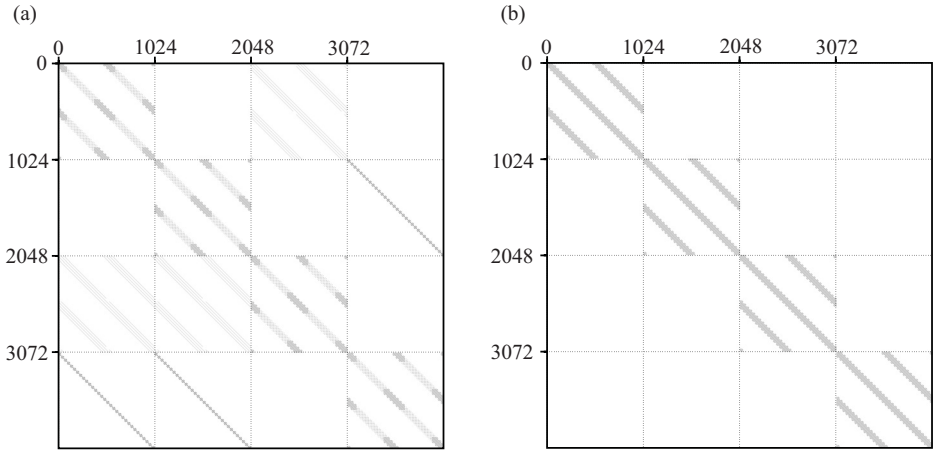

Figure 5.3: The FDFD matrix used in the DIWS approach to compute fine-grid solutions of the first-order hyperbolic wave equation projected on two resolution scales ($J = 1$). The matrix is constructed using second-order staggered grid discretizations. (a) shows the real part and (b) the imaginary part of complex DIWS matrix. Non-zero coefficients are represented as black dots. All white coefficients are zero.

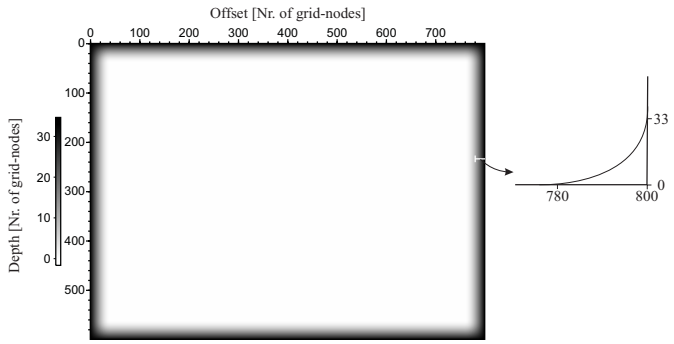

Figure 5.4: PML absorbing boundary function applied on all four edges of the two-dimensional homogeneous half space model. The PML layer size is 20 grid points.

5.3.2 Iterative solver software

The iterative solver method chosen needs to be applied to the complex-valued, unsymmetric impedance matrix. The constraints entered by the characteristics of the impedance matrix automatically lead an iterative method based on a Krylov formulation. A widely distributed iterative method of this group of approaches is the *GMRES* iterative solver developed by Saad and Schultz (1996). *GMRES* fulfils all above mentioned requirements. One of the key points of a practical *GMRES* implementation is an efficient restart strategy that avoids excessive amounts of computations and memory communication during iteration steps. Moreover, the overall iterative convergence of *GMRES* methods may be significantly increased by appropriate preconditioning through e.g., a parallel domain decomposition strategy.

I use a *GMRES* implementation that was provided by L. Giraud (Frayssé et al., 1997). Their algorithm essentially involves the impedance matrix A during iterations only through matrix-vector and dot-products. The routines to perform these operations are entirely written by the user. Therefore, sparse iterative computations in both, sequential and parallel mode are easily implemented and even the construction of the impedance matrix *on the fly* may be performed. Although the matrix construction *on the fly* is possible and has been implemented by e.g., Pessel (2000), I do not consider it a first choice alternative since matrix constructions become extremely expensive with respect to the necessary CPU-time.

5.4 2D homogeneous media

The first benchmark test is computed for a simple 2D model with homogeneous velocity and density distribution. I use a *two-step/two-scales* scenario, where the coarse-grid consists of $nz = 60 \times nx = 80$ grid-nodes including 10 grid-nodes on each edge of the model for PML absorbing boundary conditions. The fine-grid solution is computed on a grid of size $nz = 120 \times nx = 160$ with 20 PML-grid-nodes. In order to illustrate the

PML absorbing boundary conditions used for all wave simulation examples, I combined absorbing functions γ_x and γ_z in Equation 4.5 to a 2D-function and plotted the result for the fine-grid model setup in Figure 5.4. The PML absorbing layers are applied on all four edges of the numerical models. The implementation of a stable free-surface boundary condition has not been investigated at this stage.

5.4.1 Frequency maps

I show a set of frequency maps computed by the DISS and DIWS scheme for the homogeneous model and a frequency component of $f = 9.5Hz$. I use the derivative of a Gaussian as introduced in Chapter 4 as source function. The source is located near the upper model-PML boundary at $(nz = 160m, nx = 2400m)$. The coarse discretization step is $dx = dz = 80m$, which corresponds to 5 grid-points per shortest wavelength. The homogeneous wave speed and density are $v = 4000m/sec$ and $\rho = 2500kg/m^3$, respectively. This gives a shear modulus of $\mu = \rho \cdot v^2 = 4e^{10}$. I compute frequency domain solutions for 52 discrete frequencies ranging from $f_{min} \approx 0Hz$ to $f_{max} \approx 10Hz$. The frequency sampling corresponds to time seismograms of length $4sec$ and a time sampling of $nt = 0.01sec$. The direct coarse-grid solution for the DISS approach is shown in the left column of Figure 5.5 for all three wave-field components separately (v_y, σ_{xy} and σ_{zy}). The middle column is the coarse-grid solution expanded on the fine grid by the simple bilinear interpolation scheme. The discretization step on the fine-grid is half the coarse step size, i.e. $dx = dz = 40m$. In the right column, I present the final wave-field solution after 2000 iteration steps. Note that the *GMRES* backward error tolerance level was set to $tol = 1.e^{-7}$ which did not allow the DISS nor the DIWS scheme to converge in the tolerance limits. Therefore modelling computations stopped when the maximum number of iteration steps are performed. In the homogeneous model example, I set the limit to $n_{it}^{max} = 2000$ steps. In Figure 5.6, I show the DIWS frequency maps for the coarse-grid (left column) and the fine-grid (middle and right column) solutions. The middle column is the fine-grid solution after 2000 iteration steps computed on $J = 1$ resolution scales (*two-scales* scenario). The right column is obtained from the wavelet-domain solution by inverse wavelet transform.

The large difference in amplitde between the coarse-grid and fine-grid wave-field solution is caused by the normalisation of the hyperbolic wave equation. The coarse-grid solution is normalized, since it is subsequently used as initial solution for the iterative scheme that is based on the normalized equation discretized for the fine-grid model. The final frequency map has been corrected for the applied normalisation and therefore represents real amplitude values.

Fine-grid wavelet coefficients in the upper right $W_1 \times W_1$ approximation space are low in amplitude, therefore difficult to visualize. I note the interaction coefficients in spaces $W_1 \times V_1$ and $V_1 \times W_1$ between the wavelet and scaling approximation spaces.

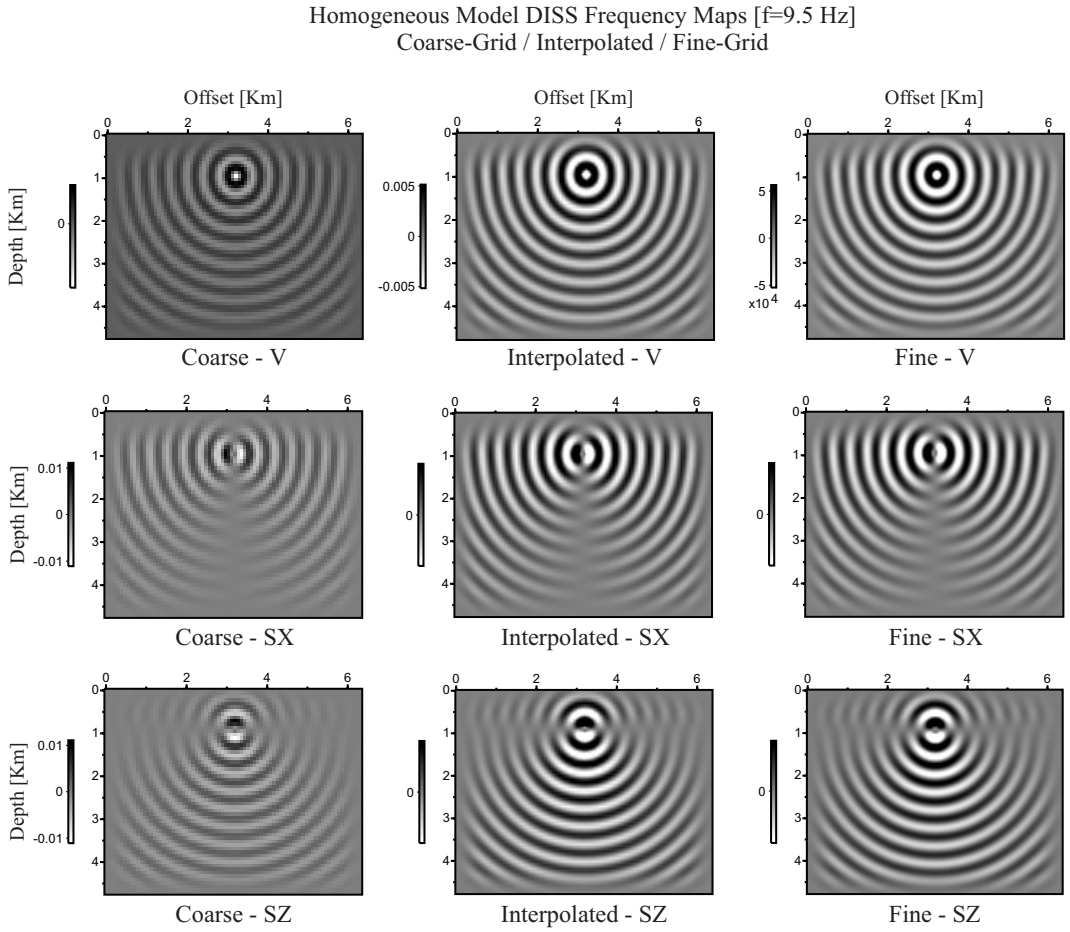

Figure 5.5: DISS Frequency solution maps for the *Homogeneous Model* for $f = 9.5Hz$.

5.4.2 Seismograms

In Figure 5.7, I illustrate the time seismogram that has been computed from the DISS and DIWS frequency domain wave-field solutions by inverse Fourier transform. Moreover, I add a time domain FD (TDFD) solution in order to verify correct modelling results. In general, the overall match of the DISS and DIWS solution is perfect. The wave arrival for near offset traces fits perfectly for all three modelling solutions. With increasing distance from the source point, differences in amplitude between the TDFD and the FDFD approaches become visible. This is shown in greater detail in Figure 5.8, on three extracted traces from the time seismogram. In order to better quantify the frequency domain solution, I compare the DISS and DIWS coarse-grid and fine-grid solutions to an analytic solution. Figure 5.9 and Figure 5.10 show the DISS and DIWS time seismogram solutions from Figure 5.8, though now I add the time solutions computed from the coarse-grid frequency maps. Moreover, I replace the TDFD solution by an analytic solution.

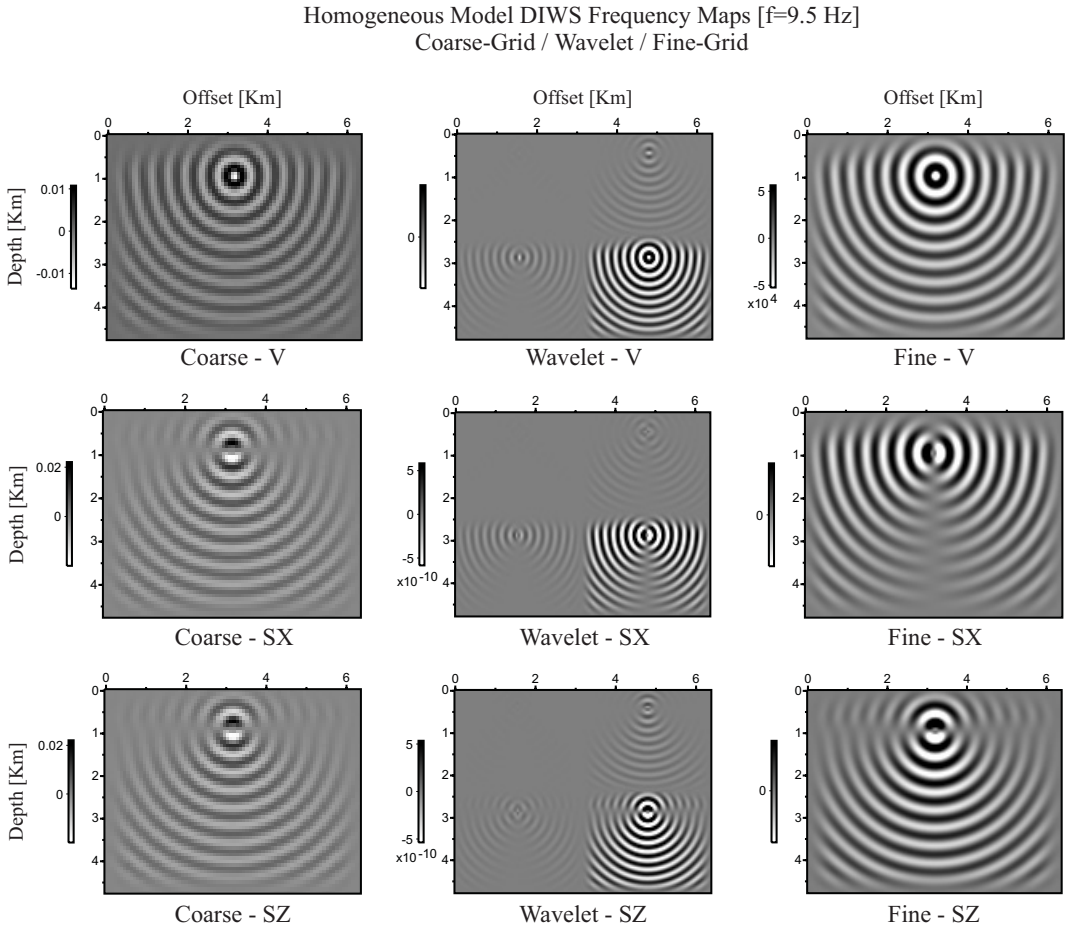

Figure 5.6: DIWS Frequency solution maps for the *Homogeneous Model* for $f = 9.5Hz$.

The comparison demonstrates that the DISS and DIWS solutions with increasing distance from the source develop increasing dispersion. The deviation of the frequency domain solutions from TDFD and analytic solutions is due to a coarse-grid discretization step that incorporates 5 grid-points per shortest wavelength only. Moreover, I limit the maximum number of iteration steps to 2000 which did not allow the DISS and DIWS scheme to converge in the pre-defined tolerance limits. Despite of the difference in the main arrival, I note a small signal on the far offset traces (Offsets $0.4Km$ and $4.4Km$) at a propagation time of about $2.2sec$. This event is due to an artifical reflection from the model-PML boundary.

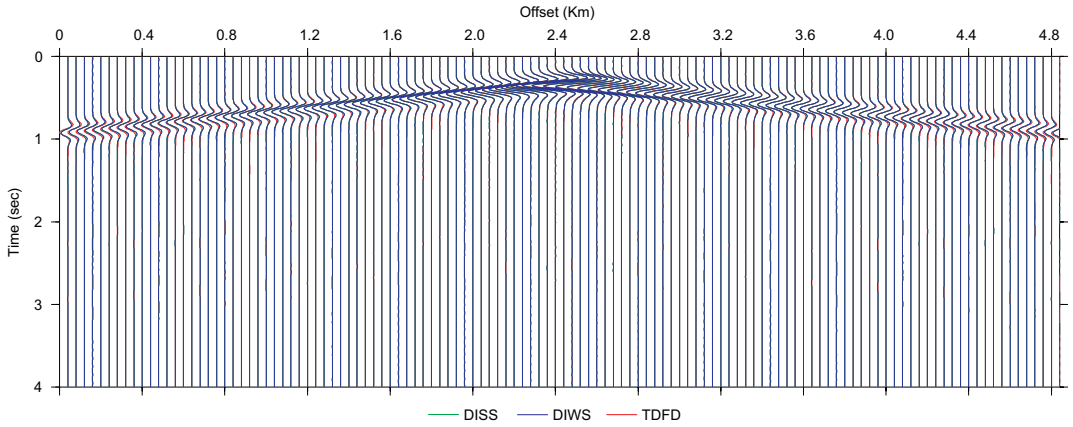

Figure 5.7: Seismograms for the *Homogeneous Model* simulation computed by the DISS, DIWS and a standard TDFD scheme. In red, I plot the TDFD solution. Green and blue are the DISS and DIWS modelling results, respectively.

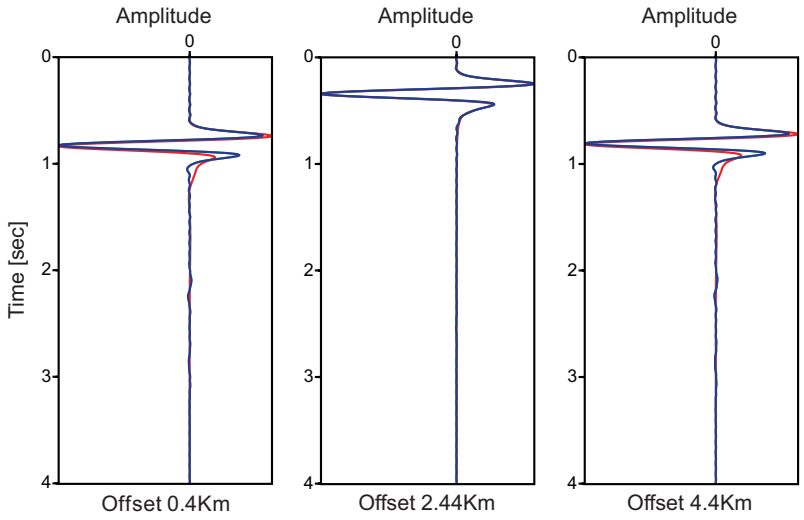

Figure 5.8: The plot shows three extracted traces (Offsets $0.4Km$, $2.44Km$ and $4.4Km$) from the *Homogeneous Model* time seismogram shown in Figure 5.7. Red is the TDFD, green the DISS and blue the DIWS solution. We note significant differences of the TDFD and FDFD solutions on the far offset traces.

5.5 Two-Layer model

I investigate the DISS and DIWS approaches for a simple heterogeneous media, denoted by *TwoLayer Model*, that consists of two homogeneous spaces separated by a horizontal interface. The upper medium has a velocity of $v = 2000m/sec$ and density of $2000kg/m^3$,

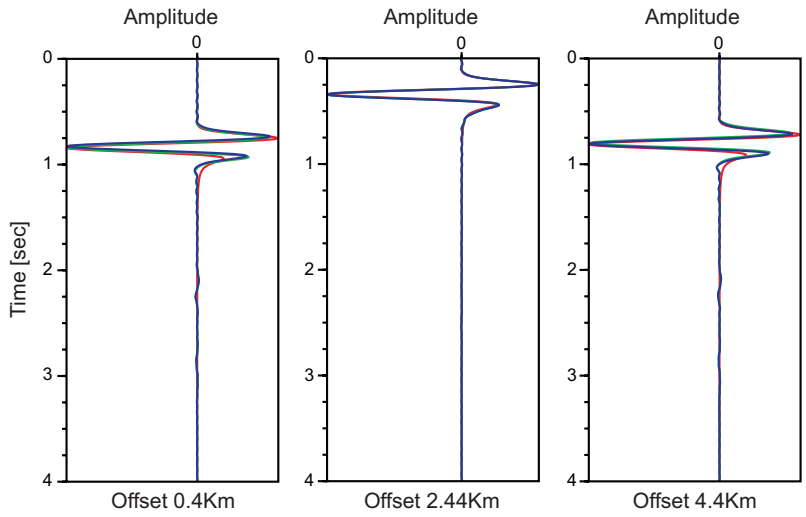

Figure 5.9: I compare the DISS wave-field solutions for the coarse-grid and the fine-grid simulation with an analytic solution computed for the homogeneous model. The plot shows traces from time seismogram in Figure 5.7 (Offsets $0.4Km$, $2.44Km$ and $4.4Km$). Red denotes the analytic response, green the coarse-grid and blue the fine-grid DISS solution.

and the lower medium $v = 5000m/sec$ and $2500kg/m^3$, respectively. The *TwoLayer Model* is illustrated in Figure 5.11. The numerical grid has a size of $nz = 60 \times nx = 120$ grid-nodes for the coarse-grid and $nz = 120 \times nx = 240$ grid-nodes for the fine-grid. The coarse- and fine-discretization steps are $dx = dz = 40m$ and $dx = dz = 20m$, respectively. The source is a derivative of a Gaussian also used for the Corner Edge model simulation. PML absorbing boundary conditions are applied on all four sides of the model. The PML layer thickness is $400m$ which is equivalent to 20 grid-nodes for the fine-grid scenario. The source is located at $(nx = 2400m, nz = 200m)$. Receivers are spread over the whole model at a depth of $100m$. This gives 84 receiver stations with a spacing of $48m$. I compute wave-field solutions for 52 frequency components spanning a frequency band from $0Hz$ to $10Hz$.

5.5.1 Frequency maps

I demonstrate results from the DISS and DIWS simulation for two frequency components. The first set in Figure 5.12, shows the DISS and DIWS frequency map solutions for a frequency of $f = 1.8Hz$. In the first column, I plot from top to bottom the corresponding wave-fields v, σ_{xy} and σ_{zy} for the DISS simulation. The second column to the right is the DIWS solution for the same wave-fields. The third column is the difference of the DISS and DIWS solution, where the size of the error is indicated by the legend on the left. For example, differences between the velocity wave-field solutions (v) at the

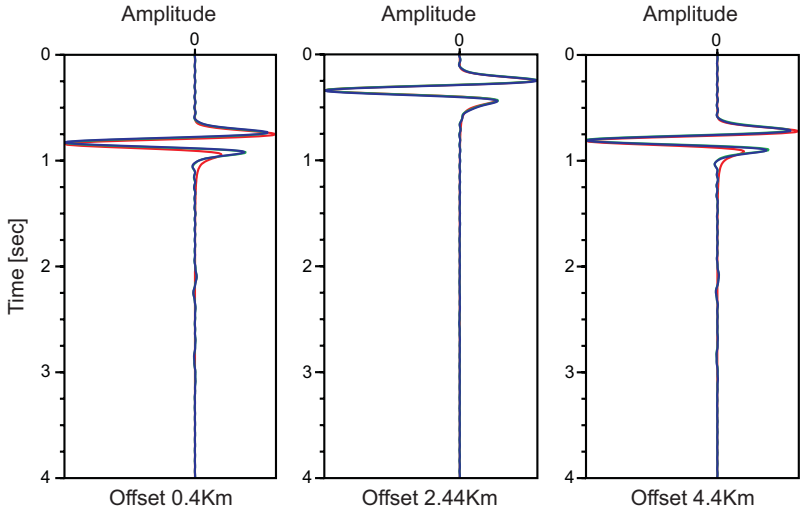

Figure 5.10: I compare the DIWS wave-field solutions for the coarse-grid and the fine-grid simulation with an analytic solution computed for the homogeneous model. The plot shows traces from time seismogram in Figure 5.7 (Offsets $0.4Km$, $2.44Km$ and $4.4Km$). Red denotes the analytic response, green the coarse-grid and blue the fine-grid DIWS solution.

frequency $f = 1.8Hz$ for the DISS and DIWS schemes are shown in the top right panel in Figure 5.12. The difference plot holds values in a range from 0 to 3 that have to be multiplied by $\times 10^{-2}$ to get the corresponding error amplitude value related to the DISS and DIWS wave-field plots. Note, the velocity wave-field has been re-combined from the PML-components $v_y = v_{yx} + v_{yz}$. Figure 5.13 shows the same setup, though now for a frequency of $f = 9.5Hz$. The overall fit of the DISS and DIWS wave-field solutions in the frequency domain is good. I note that the difference between the solutions is larger for the low frequency component $f = 1.8Hz$ with respect to the higher frequency comparison $f = 9.5Hz$. Moreover, differences in the frequency domain solutions close to the horizontal interface in e.g., Figure 5.13 are caused by the artifical interaction of the waves when hitting the model-PML boundary.

5.5.2 Seismograms

The 52 wave-field solutions in the frequency domain where combined and inverse Fourier transformed. The resulting seismogram has a time-length of $4sec$. In Figure 5.14, I show the seismograms for the *TwoLayer Model* for the DISS and DIWS simulations. The top and bottom panels are the DISS and DIWS solutions, respectively. On the right, I compare three traces extracted from the DISS and DIWS seismograms. I plot in red and green the DISS and DIWS solution, respectively. As I expect from the study of frequency map errors, both modelling approaches give almost identical results. In Figure 5.14,

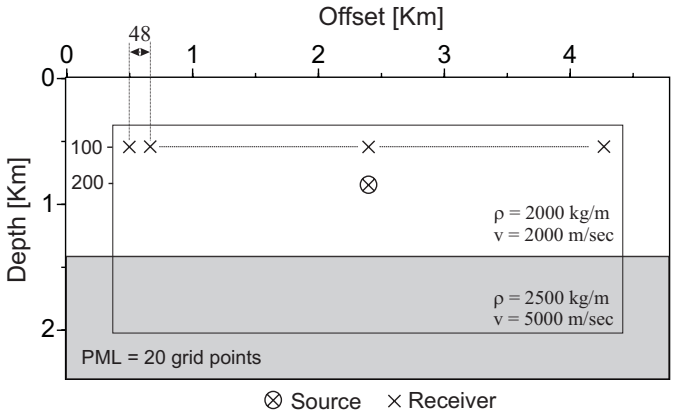

Figure 5.11: The *TwoLayer Model* consists of two homogeneous spaces separated by a horizontal interface. The upper medium has a velocity of $v = 2000m/sec$ and density of $2000kg/m^3$, and the lower medium $v = 5000m/sec$ and $2500kg/m^3$, respectively. The grid has a size of $nz = 60 \times nx = 120$ for the coarse-grid part and $nz = 120 \times nx = 240$ for the fine-grid part. The coarse and fine discretization steps are $dx = dz = 40m$ and $dx = dz = 20m$, respectively. The source is a derivative of a Gaussian also used for the Corner Edge model simulation. PML absorbing boundary conditions are applied on all four sides of the model. The PML layer thickness is $400m$ which is equivalent to 20 grid-nodes for the fine-grid scenario. The source is located at $(nx = 2400m; nz = 200m)$. Receivers are spread over the whole model at a depth of $100m$. This gives 84 receiver stations with a spacing of $48m$.

the first arrival and reflection from the interface that separates the two homogeneous sub-spaces are clearly visible.

I detect the creation of spurious noise when the reflection from the interface event hits the model-PML boundary. The PML function used inside the damping layer is (see also Figure 5.4),

$$\gamma_x(x) = a \; cos(\frac{x}{x_{pml}} \; \frac{\pi}{2}) \tag{B. 1}$$

where x_{pml} denotes the PML layer thickness, x the spatial position, and a an empirically estimated value that is a function of the PML layer thickness.

The damping function is illustrated in Figure 5.15. In the example shown in Figure 5.4, the value for a was set to $a = 33$. In order to eliminate the spurious reflection from the model-PML boundary, I tested the wave damping behaviour for different PML-layer thicknesses with varying coefficients a. The rather limited empirical study did not deliver a simple PML configuration that allows wave simulations without spurious noise reflections from the media-PML interface. Since the PML problematic was not one of my primary concerns, I continue the DISS and DIWS development, though I like to under-

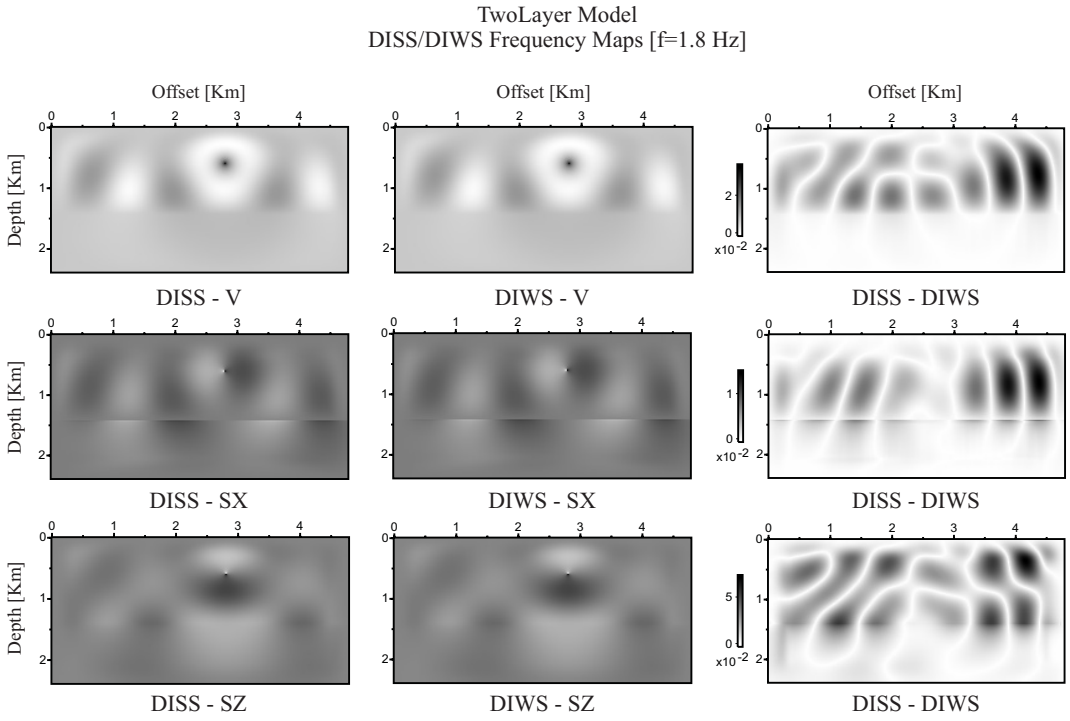

Figure 5.12: Frequency solution maps for the *TwoLayer Model* for $f = 1.8Hz$. In the first column, I plot the DISS solution separated for each wave-field solution from top to bottom: v_y, σ_{yx} and σ_{yz}. The second column contains the DIWS solutions for the same wave-fields. The third column is the difference of the two solutions.

line that the PML conditions for the frequency domain hyperbolic system of equations requires a more detailed investigation to suppress unwanted numerical noise.

5.6 Marmousi model

I present additional modelling result for the Marmousi model simulation discussed in the previous Chapter 4. The windowed part of the Marmousi model is illustrated in Figure 5.16, for e.g., the Shear modulus distribution. On the right and left, I plot the coarse-grid and fine-grid DISS input models, respectively. The colour scheme indicates strong heterogeneous variations of the physical medium parameters. The dotted line indicates the model-PML boundary.

5.6.1 Frequency maps

In the following, I show additional wave-field simulation results for the Marmousi simulation in the frequency domain. Even though in Chapter 4, the results were discussed by

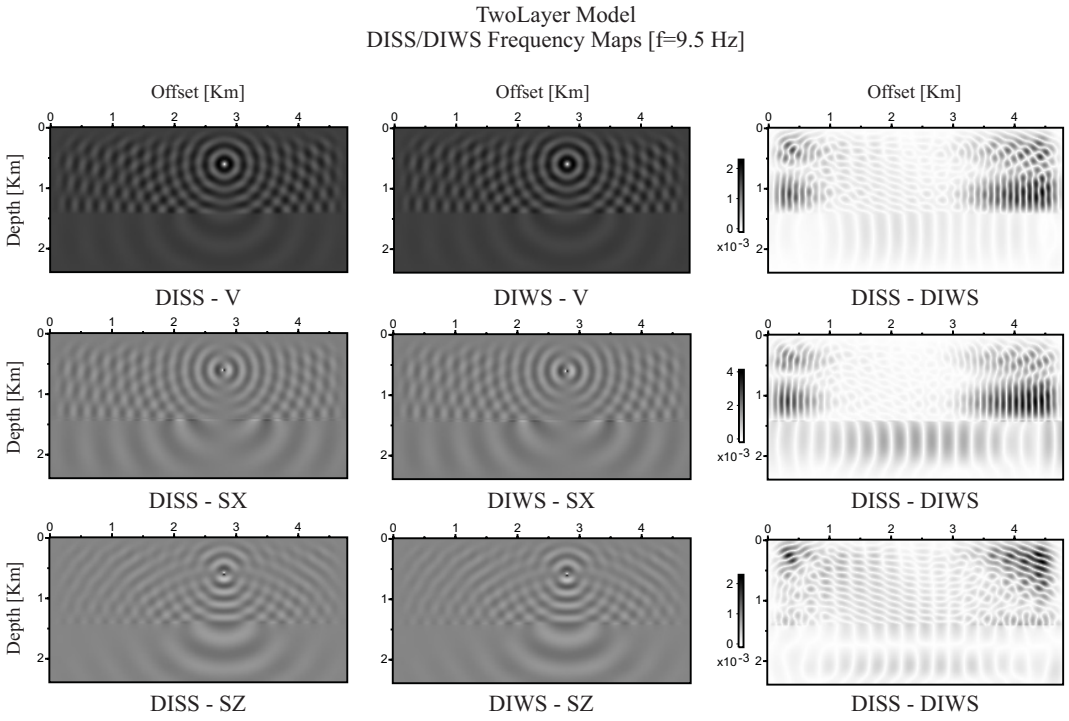

Figure 5.13: Frequency solution maps for the *TwoLayer Model* for $f = 9.5Hz$. In the first column, I plot the DISS solution separated for each wave-field solution from top to bottom: v_y, σ_{yx} and σ_{yz}. The second column contains the DIWS solutions for the same wave-fields. The third column is the difference of the two solutions.

studying time seismograms, here I present the primary output of the frequency domain DISS and DIWS wave simulation code. Each Figure contains three columns (from left to right) that represent the DISS and DIWS solutions plus the difference between them (DISS-DIWS) for the wave-field components v_y, σ_{yx} and σ_{yz}. Note that the velocity wave-field has been recombined from the PML wave-field components $v_y = v_{yx} + v_{yz}$. I plot the frequency response for a low and a high frequency $f_{low} = 1.8Hz$ and $f_{high} = 9.5Hz$, respectively. Figures 5.17 and 5.18 show wave-field solutions for the coarse-grid simulations (direct matrix solver), while Figures 5.19 and 5.20 are the solutions from the iterative scheme on the fine-grid. Coarse-grid solutions for the DISS and DIWS show strong differences, since the physical input models for the space-DISS and wavelet-DIWS simulations are not identical. The overall fit of the fine-grid solutions is good, though differences may be observed. Since the Marmousi model is structurally rather complicated, a more detailed study for several frequency components directly on computer screen allows further interpretations of the existing differences.

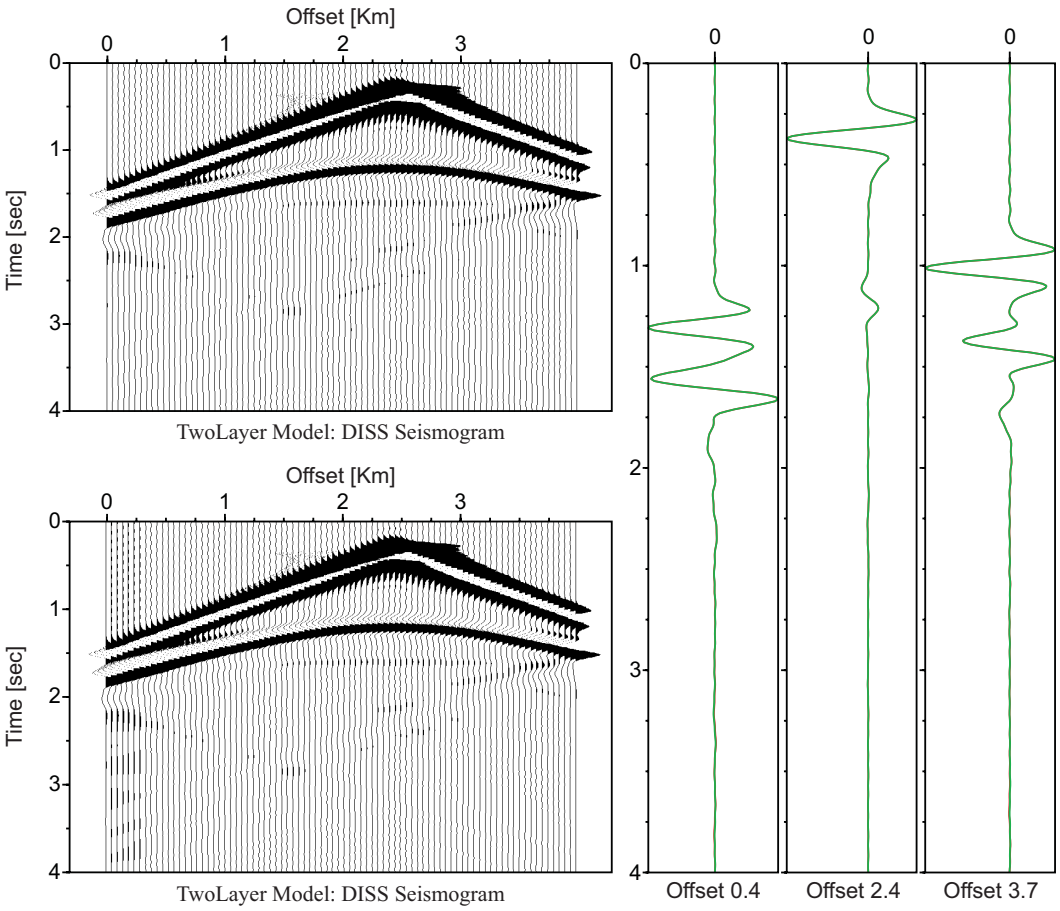

Figure 5.14: Seismograms for the *TwoLayer Model* for DISS and DIWS simulations. The top and bottom panels are the DISS and DIWS solution, respectively. On the right, I compare three traces extracted from the DISS and DIWS seismograms. I plot in red and green the DISS and DIWS solution, respectively.

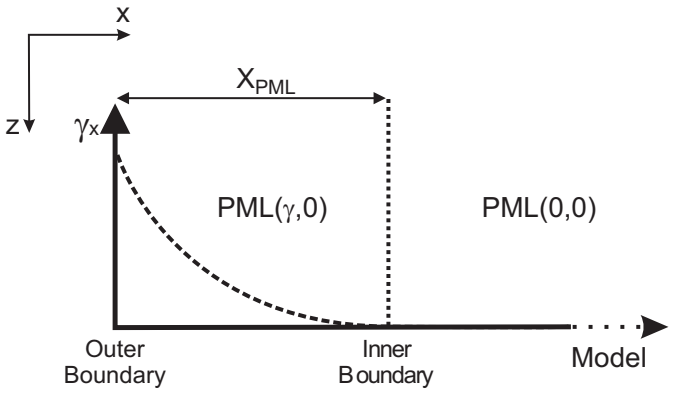

Figure 5.15: Illustration of the PML damping function.

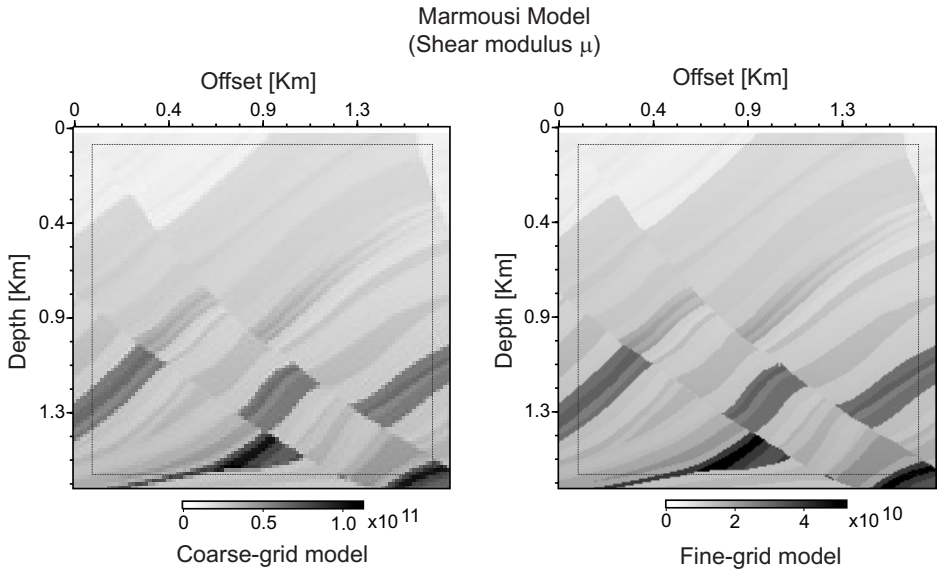

Figure 5.16: The *Marmousi Model*.

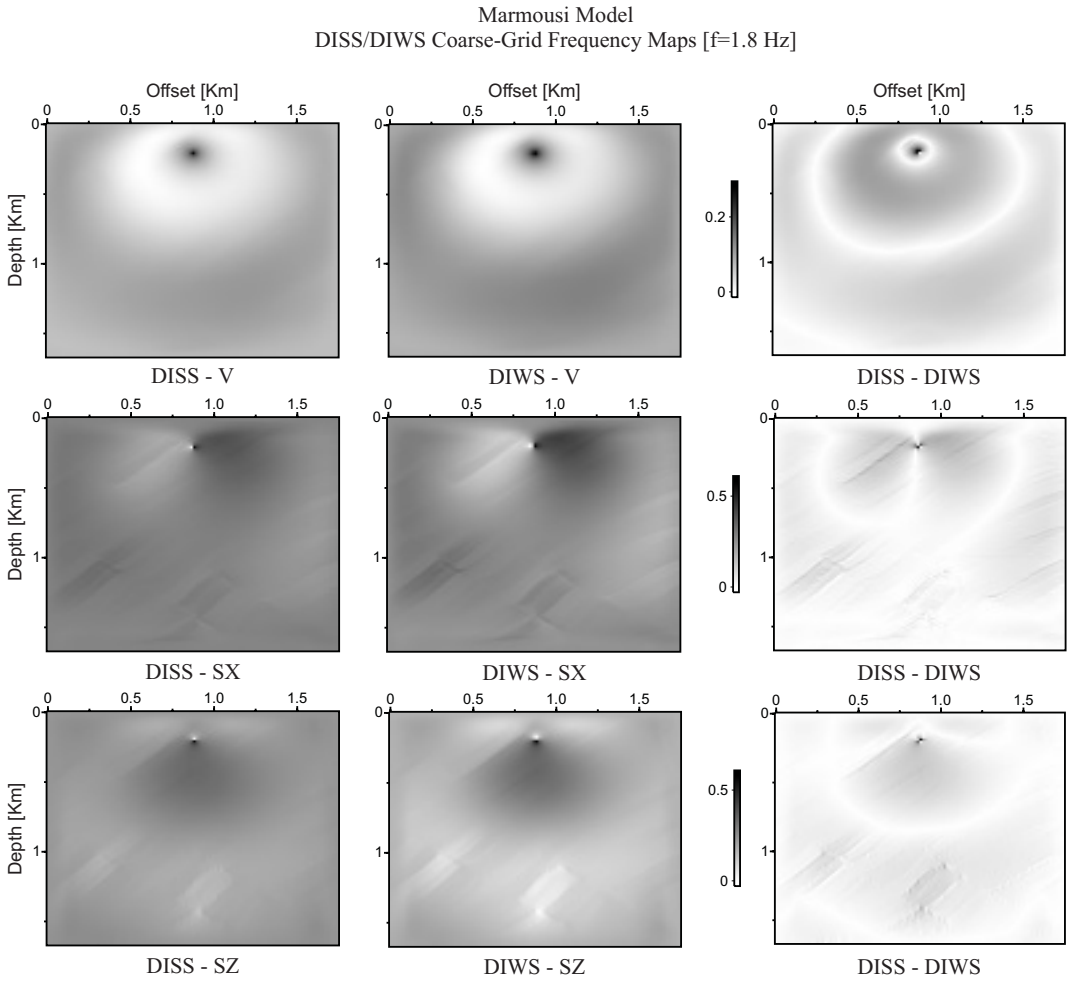

Figure 5.17: Frequency solution maps for the coarse-grid *Marmousi Model* for $f = 1.8Hz$. In the first column, I plot the DISS solution separated for each wave-field solution from top to bottom: v_y, σ_{yx} and σ_{yz}. The second column contains the DIWS solutions for the same wave-fields. The third column is the difference of the two solutions.

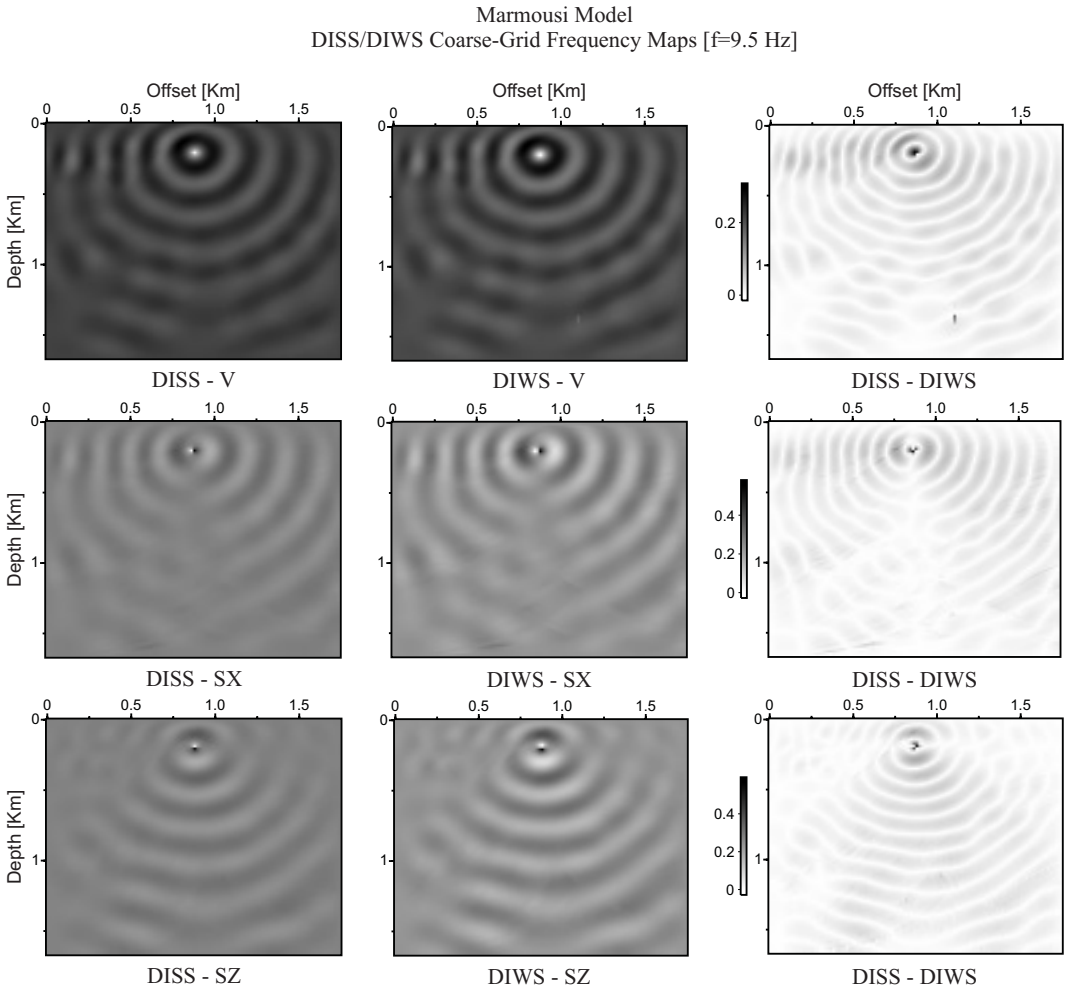

Figure 5.18: Frequency solution maps for the coarse-grid *Marmousi Model* for $f = 9.5Hz$. In the first column, I plot the DISS solution separated for each wave-field solution from top to bottom: v_y, σ_{yx} and σ_{yz}. The second column contains the DIWS solutions for the same wave-fields. The third column is the difference of the two solutions.

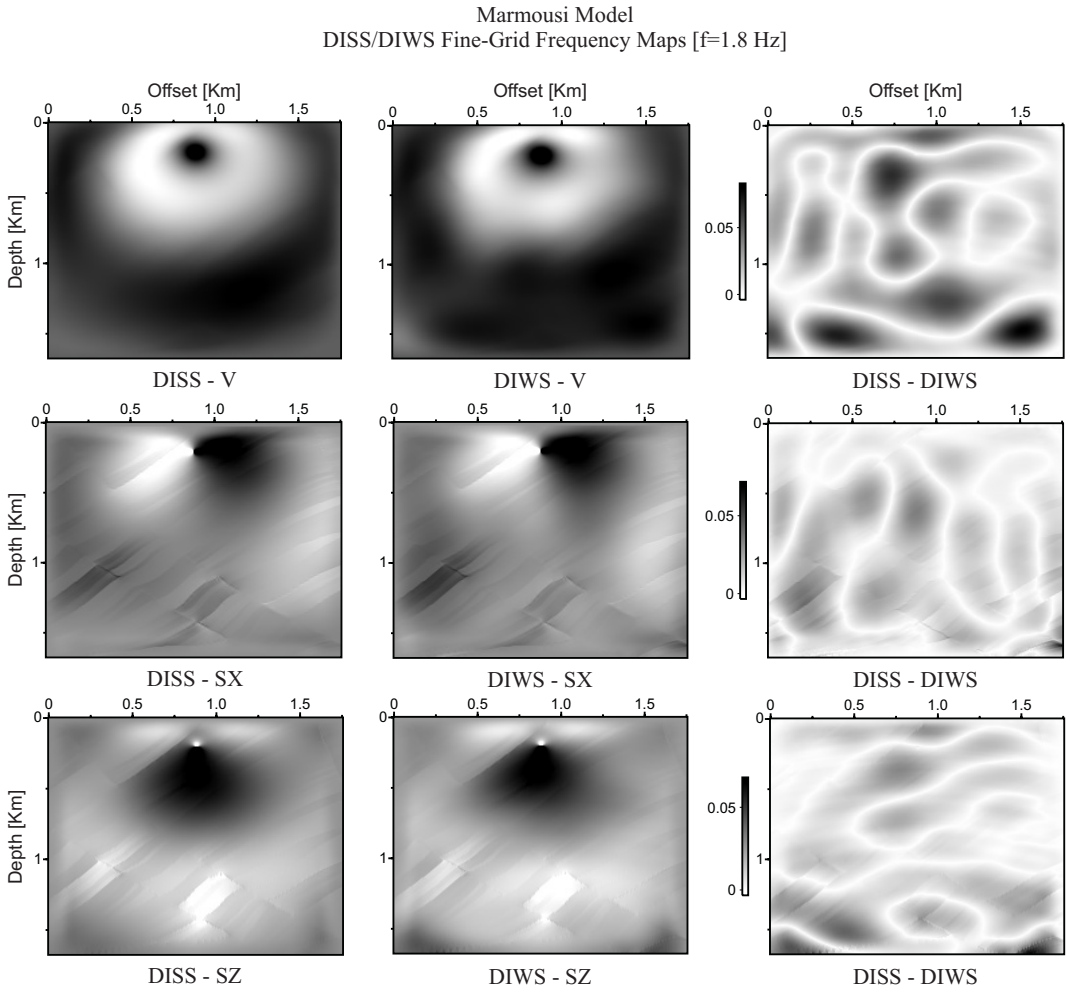

Figure 5.19: Frequency solution maps for the fine-grid *Marmousi Model* for $f = 1.8Hz$. In the first column, I plot the DISS solution separated for each wave-field solution from top to bottom: v_y, σ_{yx} and σ_{yz}. The second column contains the DIWS solutions for the same wave-fields. The third column is the difference of the two solutions.

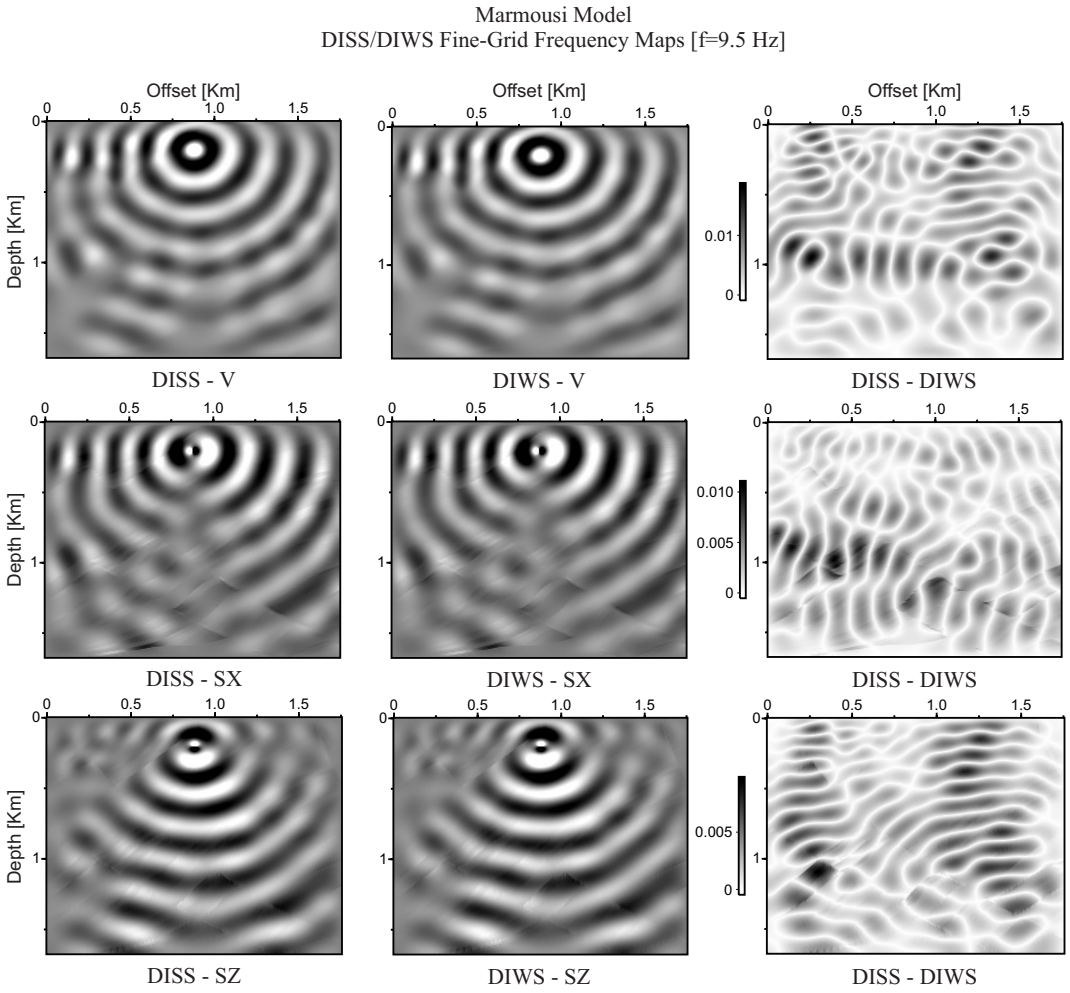

Figure 5.20: Frequency solution maps for the fine-grid *Marmousi Model* for $f = 9.5Hz$. In the first column, I plot the DISS solution separated for each wave-field solution from top to bottom: v_y, σ_{yx} and σ_{yz}. The second column contains the DIWS solutions for the same wave-fields. The third column is the difference of the two solutions.

Chapter 6

Frequency Domain Finite-Difference Modelling in 3D Acoustic Media

6.1 Résumé

Dans ce chapitre, je développe les méthodes "*Direct-Iterative-Space Solver*" (DISS-3D) et "*Direct-Iterative-Wavelet Solver*" (DIWS-3D) pour des modélisations des ondes acoustiques dans des milieux 3D fortement hétérogènes. Les approches suivent exactement les développements présentés au chapitre 4 pour les cas 2D, sauf que dans le cas 3D l'équation d'onde acoustique est traitée alors que l'équation SH était abordée en 2D.

Dans un premier temps, plusieurs exemples de simulation d'ondes dans des milieux 3D de complexité variable (homogène et hétérogène) sont présentés. A titre de validation, je compare, à une fréquence donnée, la solution de l'approche DISS-3D dans un milieu homogène pour une ligne de sources avec celle de l'approche DISS-2D calculée dans une section du modèle 3D. Une carte en fréquence d'une modélisation par l'approche DIWS-3D sur une échelle (J=1) est présentée pour illustrer la décomposition sur 2 échelles de résolution du champ d'onde 3D. Le dernier exemple présente une simulation pour une fréquence dans un modèle *Corner Edge 3D*. Ces exemples permettent une première évaluation respective des méthodes DISS-3D et DIWS-3D. La taille des applications 3D présentées est limitée considérablement par l'utilisation de programmes séquentiels.

Par conséquent, plusieurs stratégies d'implémentation des approches DISS-3D et DIWS-3D dans un environnement de mémoire distribuée sont explorées. Tout d'abord, un langage de de programmation en parallèle est choisi fondé sur le Fortran77/90 et MPI ("*Message Passing Interface*") afin de garantir une large portabilité des logiciels.

La parallélisation intervient à différents niveaux dans les algorithmes DISS-3D et DIWS-3D. Plus précisément, trois différentes types de calcul doivent être optimisés: la transformée en ondelettes, la méthode de résolution directe (factorisation de la matrice), la méthode de résolution itérative (produit matrice-vecteur et vecteur-vecteur). Pour la transformée en ondelettes plusieurs algorithmes adaptés à différentes architecture d'ordinateurs parallèles ont été publiés. La méthode de résolution directe (MUMPS) utilisé initialement pour les simulations 3D séquentielles a été initialement développé

spécifiquement pour des calculs sur des machines à mémoire distribué si bien que le seul travail à faire comporte la construction de la matrice en parallèle. Pour la méthode de résolution itérative, une approche par décomposition en sous-domaines est préférée à des approches de parallélisation purement numériques.

A ce jour, le travail de parallélisation des approches DISS-3D et DIWS-3D n'est pas terminé si bien que le chapitre se termine par une discussion sur les différentes approches possibles de parallélisation des codes sur une machine à mémoire distribuée.

6.2 Introduction

In this Chapter, I extend the DISS and DIWS approaches that have been presented for 2D problems in the Chapter 4, for wave propagation simulations in complex heterogeneous 3D media. For simplicity, I only treat solutions to the partial differential wave equation that are gradients of a 3D scalar. Waves of this sort are compressional waves where the corresponding wave equation is called acoustic wave equation. Despite of little differences between the 2D SH-wave and 3D acoustic-wave formulations, the concept of the DIS strategy in 3D media is exactly similar to the 2D developments presented before.

Introducing the third dimension significantly increases the necessary computer structure requirements to run 3D wave simulations, because of the extremely large impedance matrix for 3D media. Even though the sequential code may be extended to three dimensions, its application to wave simulations are limited to very small model sizes only. Therefore, the main difficulty faced to perform 3D FDFD modelling is the development of an appropriate DIS implementation that allows wave simulations on distributed memory super computers.

This chapter will formulate the finite-difference DISS-3D and DIWS-3D frequency domain acoustic wave equations. The DISS-3D and DIWS-3D schemes for 3D simulations are first developed in sequential mode which are directly comparable to the 2D formulations. Then different parallelization strategies are introduced and discussed, with respect to the complexity of implementation and the computational gain expected.

6.3 Frequency domain forward modelling in 3D

In this Section, I introduce the acoustic wave equation for pressure wave propagation in 3D media and formulate the DISS-3D and DIWS-3D approaches. The first-order

hyperbolic system of equations for the pressure field P writes,

$$\begin{aligned}
\frac{\partial P_x(x,y,z,t)}{\partial t} + \gamma_x(x) P_x(x,y,z,t) &= K(x,y,z)\frac{\partial Q(x,y,z,t)}{\partial x} + S(x,y,z,t) \\
\frac{\partial P_y(x,y,z,t)}{\partial t} + \gamma_y(y) P_y(x,y,z,t) &= K(x,y,z)\frac{\partial R(x,y,z,t)}{\partial y} \\
\frac{\partial P_z(x,y,z,t)}{\partial t} + \gamma_z(z) P_z(x,y,z,t) &= K(x,y,z)\frac{\partial T(x,y,z,t)}{\partial z} \\
\frac{\partial Q(x,y,z,t)}{\partial t} + \gamma_x(x) Q(x,y,z,t) &= b(x,y,z)\frac{\partial P(x,y,z,t)}{\partial x} \\
\frac{\partial R(x,y,z,t)}{\partial t} + \gamma_y(y) R(x,y,z,t) &= b(x,y,z)\frac{\partial P(x,y,z,t)}{\partial y} \\
\frac{\partial T(x,y,z,t)}{\partial t} + \gamma_z(z) T(x,y,z,t) &= b(x,y,z)\frac{\partial P(x,y,z,t)}{\partial z}
\end{aligned} \tag{6.1}$$

where I introduce three pressure wave-fields P_x, P_y and P_z to account for the PML absorbing boundary conditions (see Berenger, 1994, for details). The PML damping functions for each spatial direction are denoted by γ_x, γ_y and γ_z.

I introduce three additional functions Q, R and T in order to formally construct the acoustic analogues of the first-order velocity-stress formulation of the hyperbolic wave equation. The buoyancy, inverse of the density $\rho(x,y,z)$ is denoted by $b(x,y,z)$, and the Bulk modulus that describes the stress-strain relation under hydrostatic pressure is $K(x,y,z)$. The pressure wave-field decomposition P_x, P_y and P_z can be combined into the physical P wave-field by simple addition $P(x,y,z,t) = P_x(x,y,z,t) + P_y(x,y,z,t) + P_z(x,y,z,t)$. The external source function is denoted by $S(x,y,z,t)$.

The system of Equations 6.1 is transformed in the Fourier domain:

$$\begin{aligned}
i\omega\xi(x,\omega)\frac{1}{K(x,y,z)} \cdot P_x(x,y,z,\omega) + \frac{\partial Q(x,y,z,\omega)}{\partial x} &= -S(x,y,z,\omega) \\
i\omega\xi(y,\omega)\frac{1}{K(x,y,z)} \cdot P_y(x,y,z,\omega) + \frac{\partial R(x,y,z,\omega)}{\partial y} &= 0 \\
i\omega\xi(z,\omega)\frac{1}{K(x,y,z)} \cdot P_z(x,y,z,\omega) + \frac{\partial T(x,y,z,\omega)}{\partial z} &= 0 \\
i\omega\xi(x,\omega)\rho(x,y,z) \cdot Q(x,y,z,\omega) + \frac{\partial P(x,y,z,\omega)}{\partial x} &= 0 \\
i\omega\xi(y,\omega)\rho(x,y,z) \cdot R(x,y,z,\omega) + \frac{\partial P(x,y,z,\omega)}{\partial y} &= 0 \\
i\omega\xi(z,\omega)\rho(x,y,z) \cdot T(x,y,z,\omega) + \frac{\partial P(x,y,z,\omega)}{\partial z} &= 0
\end{aligned} \tag{6.2}$$

where I introduce the frequency dependent PML damping terms $\xi_{x,y,z,\omega} = 1 + i\gamma_{x,y,z}/\omega$ to keep the presentation clear.

The system of equations is recast into a matrix-type equation of the form $A \cdot x = b$. The complex impedance matrix is denoted by A and the wave-field solution by x. The external source term is b, which is also called right-hand side (RHS).

I construct the complex impedance matrix, such that complex- and frequency-dependent terms are confined to the diagonal matrix blocks only. Spatial derivative operators in off-diagonal blocks are real-valued and need to be computed only once before the modelling starts. Matrix constructions for varying frequency components are easily performed by replacing diagonal matrix contributions:

$$\begin{pmatrix} i\omega\xi_x 1/K & 0 & 0 & \partial/\partial x & 0 & 0 \\ 0 & i\omega\xi_y 1/K & 0 & 0 & \partial/\partial y & 0 \\ 0 & 0 & i\omega\xi_z 1/K & 0 & 0 & \partial/\partial z \\ \partial/\partial x & \partial/\partial x & \partial/\partial x & i\omega\xi_x\rho & 0 & 0 \\ \partial/\partial y & \partial/\partial y & \partial/\partial y & 0 & i\omega\xi_y\rho & 0 \\ \partial/\partial z & \partial/\partial z & \partial/\partial z & 0 & 0 & i\omega\xi_z\rho \end{pmatrix} \begin{pmatrix} P_x \\ P_y \\ P_z \\ Q_x \\ R_y \\ T_z \end{pmatrix} = \begin{pmatrix} -S \\ 0 \\ 0 \\ 0 \\ 0 \\ 0 \end{pmatrix} \tag{6.3}$$

The overall size of the matrix is $(6 \times nx \times ny \times nz)^2$, where the physical model dimensions are $nx \times ny \times nz$ grid-nodes.

6.3.1 The Direct-Iterative-Space Solver

In order to find wave-field solutions to the matrix Equation 6.3, I extend the DISS-2D strategy for SH-wave simulations to heterogeneous acoustic 3D media. From a conceptional point of view, the DISS-3D only differs from the 2D-version with respect to the number of equations enlarged by one additional spatial dimension. The direct-iterative solver combination and resolution strategy are similar to the 2D case.

The DISS-3D computes a coarse-grid solution by computing the *LU* factorization of the complex impedance matrix A using the *MUMPS* direct solver (see Equation 6.3). Note that the coarse-grid size, in general, is determined by the computer resources available rather than by wave-field simulation constraints. The *LU*-factors of A are computed separately for all necessary frequency components. Then, coarse-grid wave-field solutions (x_{f_i}) can be computed for numerous RHSs at practically no computational cost (Štekl, 1997).

The combination of the direct coarse-grid solutions with the fine-grid iterative solver is obtained by a simple space bilinear interpolation procedure. The interpolated wave-field solutions serve as initial solutions for the iterative scheme. As for the DISS-2D scheme, the computed 3D fine-grid wave-field solutions suffer from spatial phase-shift artefacts caused by the interpolation process. Additional V- and W-cycles or large amounts of iteration steps are necessary to efficiently eliminate the interpolation artefacts.

6.3.2 The Direct-Iterative-Wavelet Solver

The Direct-Iterative-Wavelet Solver (DIWS-3D) solves the matrix Equation 6.3 in the spectral wavelet domain. The matrix is projected on the orthogonal Daub4 wavelet basis. Necessary wavelet expansions follow exactly similar computation procedures as

developed for the DIWS-2D. Each term in Equation 6.2 is transformed using the wavelet projection operators W and W^T. Since the Daub4 wavelet expansion is an orthogonal transform, the inverse projection operator is equivalent to the transpose of the forward operator $W^{-1} = W^T$.

The following equations are transformed in the wavelet domain:

$$\begin{aligned}
W[i\omega\xi_x \frac{1}{K} \cdot P_x]W^T + W[\frac{\partial Q}{\partial x}]W^T &= W[-S]W^T \\
W[i\omega\xi_y \frac{1}{K} \cdot P_y]W^T + W[\frac{\partial R}{\partial y}]W^T &= 0 \\
W[i\omega\xi_z \frac{1}{K} \cdot P_z]W^T + W[\frac{\partial T}{\partial z}]W^T &= 0 \\
W[i\omega\xi_x \rho \cdot Q]W^T + W[\frac{\partial P}{\partial x}]W^T &= 0 \\
W[i\omega\xi_y \rho \cdot R]W^T + W[\frac{\partial P}{\partial y}]W^T &= 0 \\
W[i\omega\xi_z \rho \cdot T]W^T + W[\frac{\partial P}{\partial z}]W^T &= 0
\end{aligned} \tag{6.4}$$

For the complex-valued diagonal terms that hold medium and frequency relevant parameters, I obtain:

$$\begin{aligned}
&W[i\omega\xi_x \frac{1}{K} \cdot P_x]W^T = \\
&\sum_{u,v} \sum_{\alpha,\beta} \sum_{i,j} < P_x, \psi_j\psi_\beta\psi_v >< \psi_j\psi_\beta\psi_v, i\omega\xi_x \frac{1}{K}\psi_i\psi_\alpha\psi_u > \psi_i\psi_\alpha\psi_u
\end{aligned} \tag{6.5}$$

where indices (i, j), (α, β) and (u, v) represent wavelet projections with respect to the x-, y-, and z-directions. The corresponding wavelet basis functions are denoted by $\psi_{i,j}$, $\psi_{\alpha,\beta}$, and $\psi_{u,v}$. I reintroduce the initial PML damping function γ in Equation 6.5 and obtain:

$$\begin{aligned}
&W[i\omega(1 + i\frac{\gamma_x}{\omega})\frac{1}{K} \cdot P_x]W^T = \\
&\sum_{u,v} \sum_{\alpha,\beta} \sum_{i,j} < P_x, \psi_j\psi_\beta\psi_v >< \psi_j\psi_\beta\psi_v, (i\omega\frac{1}{K} - \gamma_x\frac{1}{K})\psi_i\psi_\alpha\psi_u > \psi_i\psi_\alpha\psi_u
\end{aligned} \tag{6.6}$$

Equation 6.6 is split up with respect to terms depending on the frequency ω:

$$\begin{aligned} & W[i\omega(1+i\frac{\gamma_x}{\omega})\frac{1}{K}\cdot P_x]W^T = \\ i\omega \quad & \sum_{u,v}\sum_{\alpha,\beta}\sum_{i,j} < P_x, \psi_j\psi_\beta\psi_v >< \psi_j\psi_\beta\psi_v, (\frac{1}{K})\psi_i\psi_\alpha\psi_u > \psi_i\psi_\alpha\psi_u \\ - \quad & \sum_{u,v}\sum_{\alpha,\beta}\sum_{i,j} < P_x, \psi_j\psi_\beta\psi_v >< \psi_j\psi_\beta\psi_v, (\gamma_x\frac{1}{K})\psi_i\psi_\alpha\psi_u > \psi_i\psi_\alpha\psi_u \end{aligned} \tag{6.7}$$

In order to obtain an efficient DIWS-3D algorithm, I calculate the two convolution projections of $W[\gamma_x\frac{1}{K}]W^T$ and $W[\frac{1}{K}]W^T$ before the modelling starts. The algorithm to obtain the coefficients $c_{i,\alpha,u} = W[i\omega(1+i\frac{\gamma_x}{\omega})\frac{1}{K}]W^T$ then writes:

```
do i = 1, n_x
do α = 1, n_y
do u = 1, n_z
   do j = 1, nnz_i
   do β = 1, nnz_α
   do v = 1, nnz_u
      c^1_{i,α,u} = [1/K(j,β,v)] · ψ_i(j) · ψ_α(β) · ψ_u(v)
      c^2_{i,α,u} = [γ_{i,α,u} 1/K(j,β,v)] · ψ_i(j) · ψ_α(β) · ψ_u(v)
   end do
   end do
   end do
   call WT3D(c^1_{i,α,u})
   call WT3D(c^2_{i,α,u})
end do
end do
end do
```

(6.8)

I underline the importance of the appropriate choice of wavelet basis functions in order to guarantee fast and efficient spectral transformation algorithms. One coefficient $c_{i,\alpha,u}$ is computed by the multiplication of physical media parameters at the grid point (i,α,u) with the corresponding wavelet basis functions in all three dimensions. In case the wavelet basis functions are sparse, which is equivalent to the wavelets having small number of vanishing moments and quadrature mirror filter coefficients, the products and the subsequent wavelet projections can be computed efficiently. The Daub4 wavelet basis fulfills these requirements and is therefore used throughout.

Nevertheless, the convolution projections need to be computed only once before the modelling starts. During wave propagation simulation, I construct the complex impedance matrix for the corresponding angular frequency components ω_i by simple multiplications and subtractions of precomputed projection terms (Equation 6.7), which significantly reduces the computational cost of the DIWS-3D approach:

$$i\omega \cdot W[\frac{1}{K}]W^T - W[\gamma_x \frac{1}{K}]W^T \tag{6.9}$$

Off-diagonal matrix terms consists of derivative operators for all three spatial dimensions. I discretize the operators in physical domain using the standard staggered FD geometry. A typical expansion of an operator in the spectral wavelet domain e.g., for the x-direction, gives:

$$W[\frac{\partial}{\partial x}Q]W^T = -\sum_u \sum_\alpha \sum_{i,j} < \frac{\partial}{\partial x}\psi_i, \psi_j >< Q, \psi_j \psi_\alpha \psi_u > \psi_i \psi_\alpha \psi_u \tag{6.10}$$

Similar projections can be performed for spatial operators in y- and z-directions. The matrix formulation in Equation 6.3 results in real-valued and frequency independent derivative operators. Therefore, they are constructed only once before the modelling starts.

6.4 Benchmark tests for sequential code

I implement the acoustic DISS-3D and DIWS-3D approach for 3D wave simulations in a sequential version. The 3D sequential code is tested for a simple homogeneous model using the DISS-3D and DIWS-3D in order to verify the correct implementation and moreover to evaluate the largest possible model size that still could be simulated on a single desktop Linux PC. The principal purpose of the sequential 3D wave simulation tests presented here, is to serve as comparison for possible parallel implementations of the DIS strategies.

6.4.1 Homogeneous cube

The first numerical tests for the DISS-3D and DIWS-3D were performed for a simple homogeneous cube. The medium velocity is $v = 4000m/sec$ and the density $\rho = 2500kg/m^3$. PML absorbing boundary conditions are defined on all edges of the cube. The PML layer size for the direct coarse-grid and iterative fine-grid, is 2 and 4 grid-nodes, respectively. The source function S is the derivative of a Gaussian exactly similar to the one defined in Chapter 4 for the Corner Edge simulation. In order to keep the matrix size small, at this stage, I only use second-order derivative approximations rather than fourth-order used for the 2D simulations.

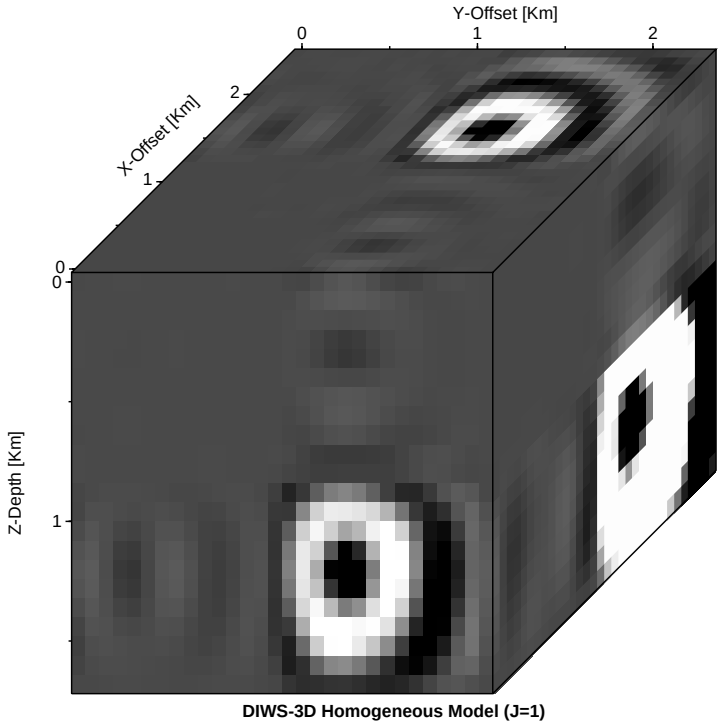

Figure 6.1: 3D Pressure wave-field component calculated by the DIWS-3D on $J = 1$ wavelet resolution scales. The frequency is $f = 9.5Hz$. The wave-field has been recombined from the three PML contributions $P = P_x + P_y + P_z$.

All simulations were run on a single desktop Linux PC with $1GByte$ of RAM memory and processor speed of $1MHz$. At the current stage, the largest DISS-3D wave simulation that can be performed, uses a coarse-grid of size $34 \times 30 \times 14$ grid-nodes. Using a *two-step* grid combination gives a fine-grid of size $68 \times 60 \times 28$, where PML absorbing layers are included. Note that larger 3D models require larger RAM memory available for the direct matrix factorization.

The largest DIWS-3D model simulation is performed on a coarse-grid $16 \times 15 \times 11$. As for the DISS-3D, I use a *two-scales* geometry which gives a fine-grid of size $32 \times 30 \times 22$. Note that the DIWS-3D implementation is not optimised in order to model the largest possible 3D model in sequential mode. Therefore, the largest DIWS-3D model size is limited by the RAM memory available to expand the impedance matrix in the spectral wavelet domain.

In Figure 6.1, I illustrate a DIWS-3D simulation result for the frequency component $f = 9.5Hz$ on $J = 1$ resolution scales. The model is the largest DIWS-3D model mentioned earlier. The plot shows only the recombined pressure wave-field component $(P = P_x + P_y + P_z)$. The spatial discretization step for the coarse-grid and fine-grid, is

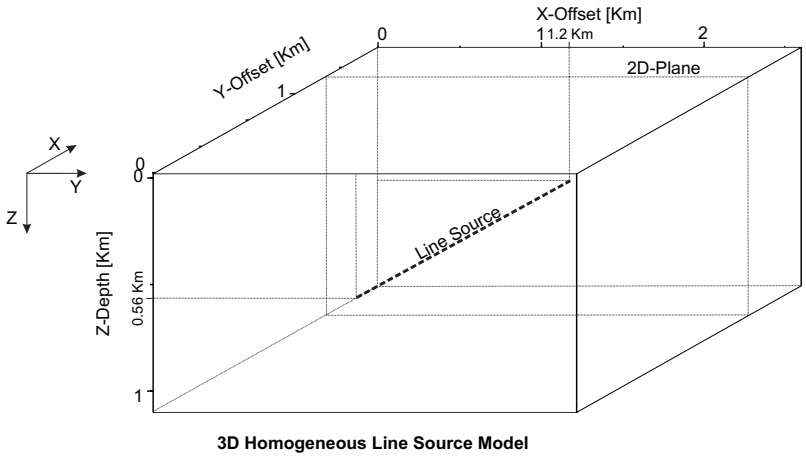

Figure 6.2: 3D Line Source model.

$dx = dy = dz = 80m$ and $40m$, respectively.

6.4.2 Line Source simulation

In order to verify the correct computation of the 3D wave propagation, I perform a DISS-3D wave simulation in a homogeneous model that is excited by a line source. Then, the obtained solution may be directly compared to a DISS-2D wave-field simulation.

The line source is placed in y-direction at the coordinates ($nz = 0.56Km, ny = 0 - 1.44Km, nx = 1.2Km$) in the 3D model. The fine-grid has a size of $60 \times 44 \times 28$ and a spatial discretization step of $40m$. This corresponds to a 3D model with dimensions $2.4Km \times 1.76Km \times 1.12Km$. The *Line Source* model geometry setup is illustrated in Figure 6.2. Overall godd agreement of the two solutions is observed.

In Figure 6.3, I show the re-combined pressure wave-field component ($P = P_x + P_y + P_z$) for the frequency $f = 9.5Hz$. Clearly visible is the *2D frequency map* on the xz-plane of the cube.

In order to compare the DISS-3D solution, I cut a 2D slice out of the cube in the xz-plane as indicated in Figure 6.2. The 2D slice frequency map and the corresponding DISS-2D simulation results for a homogeneous 2D model having similar properties, are shown in Figure 6.4.

6.4.3 3D Corner Edge model

I perform a 3D Corner Edge simulation using the DISS-3D approach. The Corner Edge model in 3D media separates two homogeneous volumes, where the corner edge volume is a sub-block in the cube. An illustration of the 3D Corner Edge model is given in Figure 6.5.

The surrounding media has a velocity and density of $v = 2000m/sec$, $\rho = 2000kg/m^3$, while the corner edge volume physical parameters are $v = 5000m/sec$ and $\rho = 2500kg/m^3$,

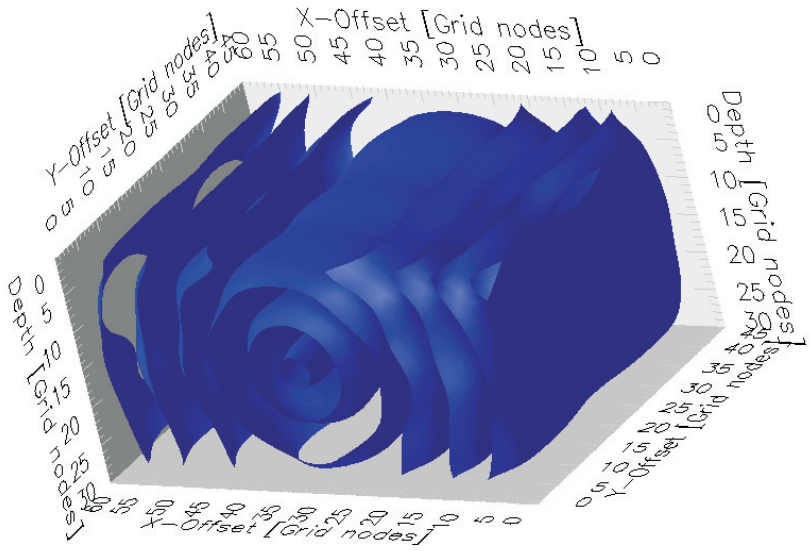

Figure 6.3: 3D frequency map ($f = 9.5Hz$) of the recombined pressure wave-field $P = P_x + P_y + P_z$ computed by the DISS-3D scheme. The source is a line source in the y-direction placed in the middle of the xz-plane ($i_z = 0.4Km, j_y = 1, .., ny, k_x = 1.04Km$). Note that the frequency map is plotted with PML absorbing boundary layers included.

respectively. The DISS-3D simulation is run for a *two-step* scenario, where the fine-grid is the largest possible sequential grid ($68 \times 60 \times 28$). The fine-grid discretization step is $dx = dy = dz = 20m$.

A wave-field simulation for the frequency component $f = 9.5Hz$ is illustrated in Figure 6.6. The source is located at ($nx = 0.76Km, ny = 0.56Km, nz = 0.16Km$). I show the pressure wave-field component that has been recombined from its PML contributions.

6.4.4 Discussion

Frequency-domain (FD) modelling for large-scale complex 3D media is difficult to perform on single desktop workstations, because of the massive computer resources required. A large 2D model that incorporates strong structural complexity is, in general, already too large to be treated by a direct matrix factorization and iteration procedure.

The actual physical model size of a 3D wave simulation that can be computed by the DISS-3D sequential mode (for second-order derivative approximations) on a stand-alone Linux-PC consists of $68 \times 60 \times 28$ grid-nodes. Even though the combination of both solver

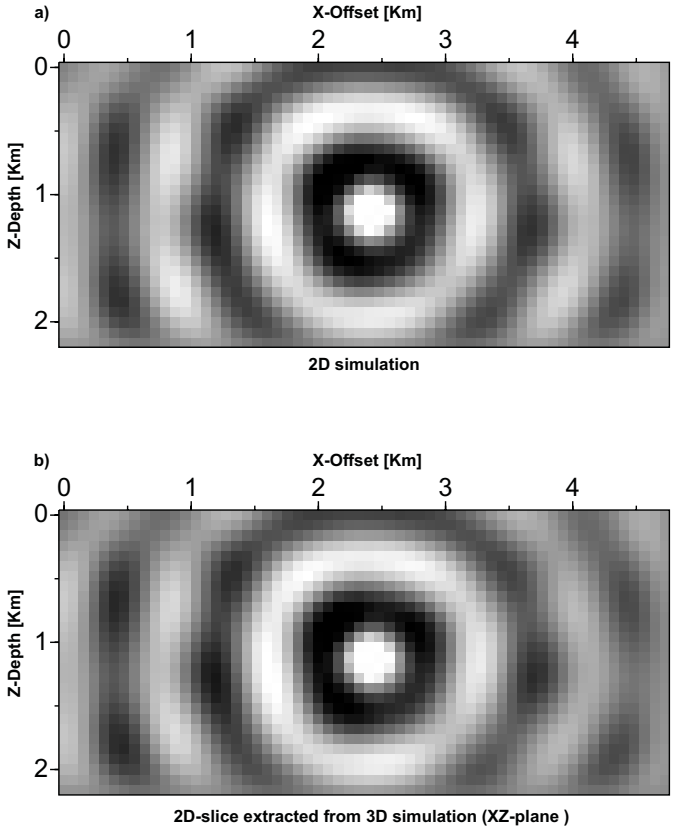

Figure 6.4: 3D line source simulation performed by the DISS-3D scheme compared to the 2D simulation for the pressure wave-field shown in Figure 6.3. The 2D solution in (a) was computed for exactly the same model parameters using the DISS-2D code. The sliced-out frequency map is shown in (b).

schemes in the DISS and DIWS approaches increases the dimension of the model that can be simulated, the gain obtained is not sufficient to treat realistic large-scale earth models.

Ideally, I would like to model 3D simulations for acoustic wave propagation using the DISS-3D and DIWS-3D strategies for a realistic model configuration shown in Table 6.1. I assume the model to have a physical size of $10Km \times 10Km \times 10Km$, where the minimal wave-speed in the model is $c_{min} = 2000m/sec$. I would like to model frequencies in a range from $0Hz - 5Hz$ which gives a shortest wavelength of $400m$. In order to provide a sufficiently accurate and stable modelling result, I define a spatial discretization that guarantees at least 10 grid points per shortest wavelength. Therefore, I set the spatial discretization to $dx = dy = dz = 40m$ which gives a computational grid of $256 \times 256 \times 256$ grid-nodes.

The overall matrix size for the DISS-3D and DIWS-3D scheme is $6 \cdot 256^3 \times 6 \cdot 256^3$.

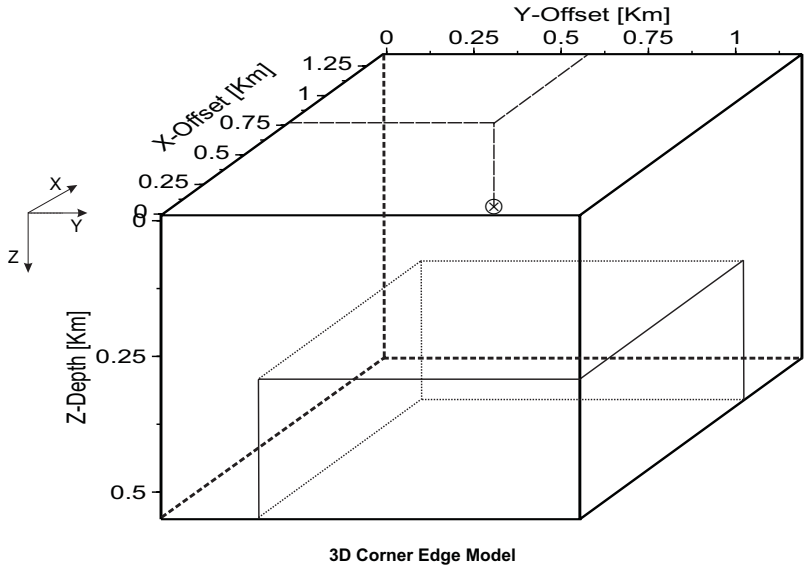

Figure 6.5: 3D Corner Edge model that consists of two homogeneous volumes, where the corner edge volume is a sub-block in the cube. The media surrounding the corner edge has a velocity and density of $v = 2000m/sec$, $\rho = 2000kg/m^3$, while the corner edge volume physical parameters are $v = 5000m/sec$ and $\rho = 2500kg/m^3$, respectively.

If I assume fourth-order derivative approximations, the DISS-3D and DIWS-3D matrices contain approximately 9×10^8 and 3.5×10^9 coefficients different from zero, respectively. Note that the number of non-zero coefficients in the DIWS-3D matrix are estimated for $J = 2$ wavelet resolution scales. Therefore, I would need at least $7GBytes$, $28GBytes$ memory to hold the non-zero coefficients of the DISS-3D and DIWS-3D matrix in RAM memory. The extremely large memory demand directly excludes any sequential FDFD modelling schemes on common single desktop workstation configurations.

Because of the estimated computer resources required for realistic 3D FDFD simulations, I propose to transfer the DISS-3D and DIWS-3D sequential code to large-scale distributed memory PC-Clusters. The deduced parallel algorithm shall construct blocks of the complex impedance matrix on a group of processors, independently. The matrix blocks are defined with respect to local memory and CPU configurations of a single processor in the parallel environment.

When the matrix blocks have been constructed locally, we ideally would like each processor to perform local parts of a global computation using only matrix information a processor holds in its proper RAM memory. Moreover, expensive communications between single or groups of processors shall be reduced to the minimum in order to obtain the maximum possible speed. In case each processor successfully terminates its task, the parallel code performs one single global communication between processors in order to combine local solutions to the overall global problem solution. Since local problems on each processor are greatly reduced in size, I expect their computation to be fast and

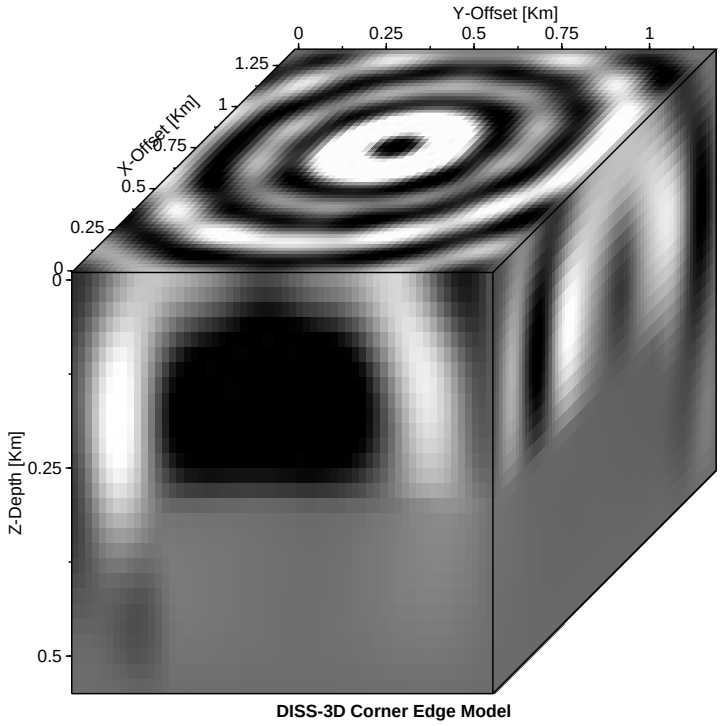

Figure 6.6: Frequency map ($f = 9.5Hz$) computed by the DISS-3D in the 3D Corner Edge model. The source is excited at ($nx = 0.76Km, ny = 0.56Km, nz = 0.16Km$). The frequency map corresponds to the pressure wave-field, that is recombined from its PML components.

efficient.

Typical computational tasks in the DISS and DIWS strategies that need to be parallelized are the matrix construction and factorization, as well as the matrix-vector and dot-products in the iterative scheme.

Another possibility to overcome computer hardware limits for a large-scale FDFD wave propagation simulations is the matrix construction *on-the-fly*. As before, I assume the complete matrix to be too large to be constructed directly in RAM memory. In an iterative scheme, the complete matrix A only takes part in the iteration process through matrix-vector products. Therefore, the matrix coefficients that are required by the matrix-vector product at an instant of the computation may be constructed only when needed. Once a matrix coefficient has been derived and subsequently been used in the matrix-vector product, its memory space is set free to be accessed by the next required coefficient. In this case, the complete impedance matrix is never constructed and memory constraints become negligible (Pessel, 2000).

From a strict memory constraints point of view, large wave simulation problems may

Model Dim. [Km]	$10 \times 10 \times 10$	
P-Velocity $[m/sec]$	2000	
Frequency $[Hz]$	5	
Wavelength $[m]$	400	
Discretization $[m]$	40	
Grid	$256 \times 256 \times 256$	
Scheme	DISS-3D	DIWS-3D
Non-zero Coef.	0.9×10^9	3.5×10^9
RAM $[GBytes]$	**7**	**28**

Table 6.1: Computer resources requirements for a desired 3D wave propagation simulation using the Direct-Iterative Strategy

be treated using the matrix construction *on-the-fly*, since RAM memory is only needed to construct single matrix coefficients and to hold wave-field and RHS vectors. However, the approach is extremely expensive in CPU-time demands. Matrix coefficients need to be re-constructed at each step of the iteration process when a matrix-vector product is required. Moreover, iterations are repeated for multiple RHSs and additional frequency components. With respect to the estimated matrix size of a realistic 3D wave simulation (number of non-zero coefficients of the order of 1×10^9), the approach is not considered here.

6.5 Parallelization

A brief look at FDFD modelling schemes suggest a parallelization approach that distributes the simulation of several frequency components to a group of processors, where each processor computes one frequency component. Even though this parallelization approach is rather simple to implement and also effective to cut down required CPU-time, it does not permit large-scale wave simulations, since required RAM memory and CPU-time are restricted to the performance of a single processor PC. I rather suggest to speed-up the principal numerical expensive computations, such as matrix constructions, factorizations, and iterative processes, that have to be computed inside the frequency loop. Thus, computations for one frequency component will be significantly accelerated, which implies an overall CPU-time gain for the whole scheme. Moreover, distribution of single frequency components to distinct processors or, in parallel to a group of procssors, may still be performed if necessary.

Many different techniques to parallelize a numerical code exist, where the main difference, to my knowledge, is related to code-portability aspects. One of the standard tools out of the group of parallel languages that provides stable and repeatable numerical simulations is the MPI (Message Passing Interface Forum, 1994) standard. Similar approaches, such as High Performance Fortran (HPF), are easier to implement, though they are still under development, and therefore not considered here.

In addition to parallelizing the principal computational processes on a distributed memory system, one may include OpenMP (Dagum and Menon, 1998) to further optimise computations on shared memory structures. A typical example is a combination of the general code parallelization on a distributed memory PC-Cluster using MPI with applications of OpenMP to parallelize the CPUs combined at one node in the Cluster.

In the first stage of the DIS parallelization, I restrict the developments to the MPI standard formulation that provides large code-portability. Moreover, the sequential DISS-3D and DIWS-3D codes rely entirely on Fortran 77/90 programming language. Since the MPI standard is easily combined with Fortran code, I decide to develop the DISS-3D and DIWS-3D parallel versions using Fortran 77/90 together with MPI. Any further code optimisation is not hindered by this approach and may be pursued in the future.

An effective parallelization of the DIS approach requires three different strategies corresponding to the principal processes that need to be computed during wave simulation modelling. In Figure 6.7, I illustrate the computationally expensive procedures that appear in either the DISS and DIWS approaches, or in both.

6.5.1 Parallel convolution computation

The DIWS approach suffers from expensive convolution-type expansion algorithms that have to be computed to transform physical media property-terms in the orthogonal Daub4 wavelet basis (see Equation 6.8). Approximately $60\% - 70\%$ of the dispensed CPU-time for the convolution computations is due to wavelet transformations that may be easily parallelized on a group of processors (Homlström, 1995).

Despite of the wavelet transform, both space- and wavelet solvers require the computation of the complex impedance matrix LU-factorization and the iterative solver i.e., matrix-vector and dot-products, to obtain coarse-grid and fine-grid wave-field solution. The direct and iterative solvers are the principal CPU-costly computations and it is desirable to parallelize both in an optimal way. This is explained in the following.

6.5.2 Parallel direct solver

The direct solver software *MUMPS* for the matrix factorization was especially developed for parallel applications. Therefore, parallelization of the coarse-grid computations are restricted to construct the complex impedance matrix in the format required by *MUMPS* in a distributed manner.

MUMPS provides several options to enter the matrix into the factorization phase, such as *centralised* and *distributed* input. Since my principal concern is the overall size of the impedance matrix for a 3D simulation, I choose the distributed matrix input for the DISS and DIWS schemes.

The complex impedance matrix in Equation 6.3 and its DIWS wavelet expansion are constructed in a row-wise manner. Since the row-wise matrix construction is natural to the DIS-FDFD approaches, I distribute blocks of matrix rows to every processor that contributes to the parallel factorization process. Each processor then constructs the matrix parts that correspond to the number and position of rows it is *responsible* for.

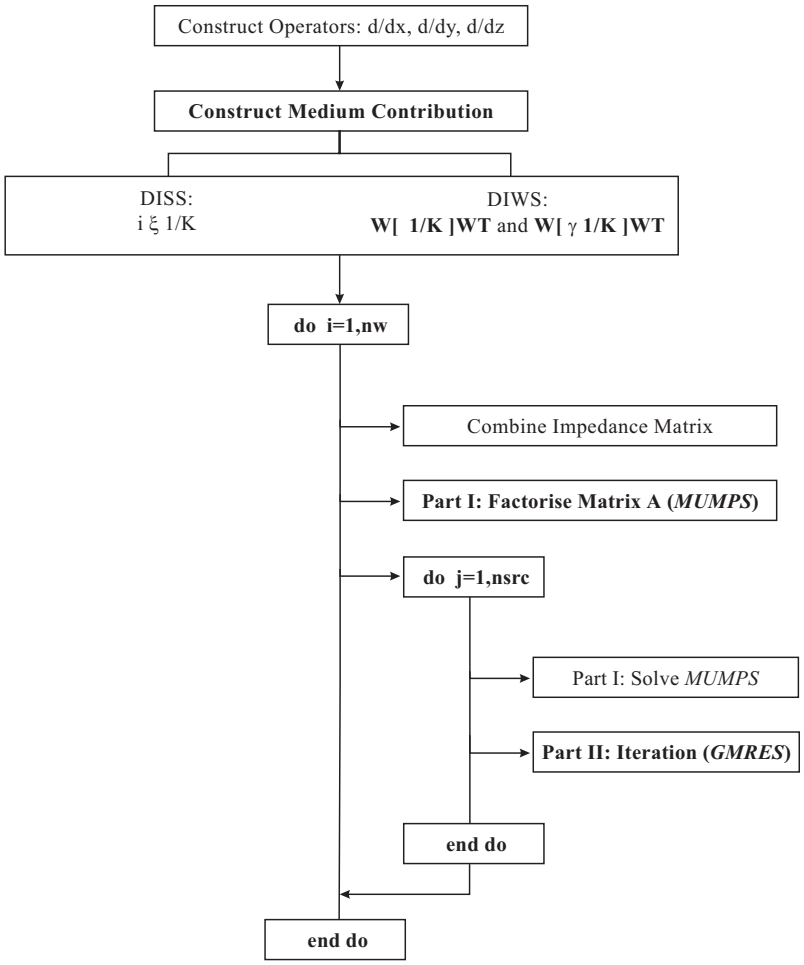

Figure 6.7: Flowchart of the DIS approach. Only computational expensive procedures are shown, where bold type parts are possible candidates for parallelization.

MUMPS demands the distributed matrix blocks in a sparse Harwell-Boeing type format, that consists of three arrays storing the actual non-zero matrix values and their row and column indices. The complete matrix in centralised form is never constructed.

The block structure information of the matrix distribution on all (*slave*-) processors in the group is passed to *MUMPS* on the *host* processor. *MUMPS* then performs an analysis phase where the distributed input matrix is ordered with respect to a minimum degree pivot strategy. Therefore, I neglect any manual pre-ordering of the impedance matrix. Note that in the new *MUMPS* version the user will have the choice between different ordering strategies, such as minimum degree or nested dissection (Amestoy and Giraud, 2002), while for the current simulations the minimum degree ordering is used throughout.

When the analysis phase is successfully terminated, *MUMPS* performs the distributed

matrix factorization. Even though *MUMPS* may choose all computational related parameters automatically, the software also provides extensive possibilities for the user to interact in order to provide additional relevant information, such as predefined pivot vectors, etc.

For initial DISS and DIWS wave simulation tests on parallel computer structures, I increased the matrix-block buffer size to allow increased fill-in during the matrix factorization phase. This modification becomes necessary when low frequency components are modelled ($f < 1 - 2Hz$), since, otherwise, the required memory to account for increased matrix fill-in caused by the numerical pivoting is insufficient. All other parameters are left with theirs default values.

6.5.3 Parallel iterative solver

The third DIS procedure that requires efficient computations is the iterative solver applied to compute fine-grid wave-field solutions in the space (DISS) and wavelet domain (DIWS). As for the direct matrix factorization part, I use an external software developed by Frayssé et al. (1997) to compute the iterative solution. I use a *GMRES* (Saad and Schultz, 1996) iterative solver that belongs to the class of Krylov based iterative methods, since the DISS- and DIWS impedance matrices are complex-valued and asymmetric.

The *GMRES* implementation computes only the strictly iterative part. Subroutines for computational costly procedures that appear during the iteration steps, such as matrix-vector and dot-products, as well as preconditioning, are left to the user's responsibility. Note that until now, I did not investigate any numerical preconditioning strategies. Therefore, parallelization strategies investigated for the iterative scheme are restricted to solve the matrix-vector and dot-products as efficiently as possible. Since the matrix-vector are the heaviest computations to be performed, I prioritize possible parallelization strategies for distributed matrix-vector products.

Column matrix distribution

The first matrix-vector parallelization strategy is of purely mathematical nature. Any constraints imposed by the physics of the underlying wave simulation problem are not considered for the parallelization process.

As I illustrate in Figure 6.8, I assume that the matrix A and the vector x are distributed over a group of distributed memory processors. Each processor in the group holds a vertical slice of matrix columns and the corresponding slice of the vector x_{loc}. The size of the slice is denoted by m. Then each processor may perform a local matrix-vector product ($A_{loc} \times x_{loc}$) corresponding to the distributed matrix-vector-slice it is responsible for. The obtained result on each processor (b_{loc}) is of length n. When all processors terminate the local product computations, two global communication steps are required to collect and pass on the locally computed information to the whole group of processors.

At first, all local results need to be collected from each processor and recombined on e.g., the host processor to obtain the global matrix-vector result (b_{glb}). Since the matrix-vector product in an iterative scheme is an intermediate step to update the iterative

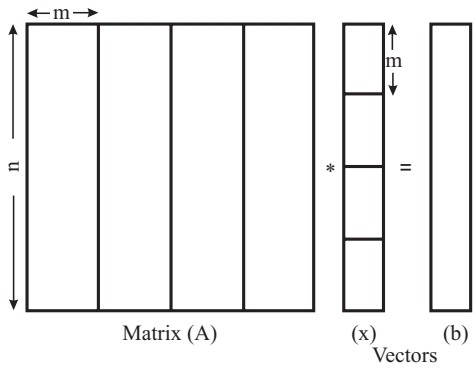

Figure 6.8: Parallelization of a matrix-vector product on a group of processors. The matrix A and the vector x are distributed in slices of size m over a group of processors. Each processor performs a local matrix-vector product ($A_{loc} \times x_{loc}$), that gives a part of the global RHS result (b_{glb}). The final result may be constructed through a global communication step that collects the local solution from each processor in the group.

solution approximation, the computed RHS vector b_{glb} needs to be distributed to the group of processors with respect to the slice each processor is responsible for. The two global communication steps are easily implemented using MPI-based message passing subroutines.

The main drawback of this matrix-vector product parallelization comes from the column-wise matrix decomposition. As I mentioned earlier, the complex impedance matrices for the DISS and DIWS approaches are naturally constructed in a row-wise manner. Moreover, blocks of rows rather than columns are easily constructed in a distributed environment.

The development of a direct column-wise matrix construction algorithm is possible, though excessive processor communications are required, which renders the approach inefficient. Because of the mentioned handicaps, I did not further pursue a column-wise matrix implementation.

Row matrix distribution

The second parallelization strategy considered is similar to the first one, though now I distribute the DISS-3D and DIWS-3D matrices by packets of rows to the group of processors rather than columns. The row-wise distribution strategy obliges each processor to hold the entire wave-field solution in memory (see Figure 6.9).

Local matrix-vector products are performed on each processor which results in the global RHS vector solution being distributed over the group of processors. In the *GMRES* scheme we therefore have to collect the RHS_i vector components from each processor, combine the information, and redistribute the result to all processors after each iteration step.

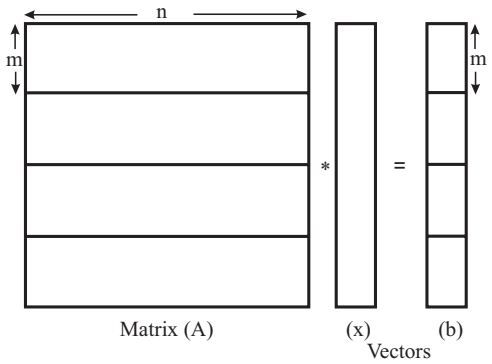

Figure 6.9: Parallelization of a matrix-vector product on a group of processors. The matrix is distributed in slices of rows over the group of processors. Then each processors performs a local matrix-vector product that constructs separate slices of the global RHS result. The global matrix-vector product is obtained by first collecting and then recombining all slices from all processors in the group.

Compared to the column-wise matrix distribution, the row-wise decomposition is favourable since it follows natural DISS and DIWS matrix constructions. Moreover, the transfer from the sequential to parallel implementation is not arduous to perform. The main drawback of this approach is related to a large number of expensive global processor communications. Thus, the approach may be superior to the first column-wise parallelization strategy, but the computational load for communications and to hold the complete wave-field in memory is not optimal. Also, the iterative *GMRES* solver is applied to the global wave-field approximation solution. Allocation of iterative working arrays relate to the iterative problem size, which for the row-wise ordering is similar to the sequential load. Thus, the strict iterative part will have similar performance as the sequential version. Therefore, the row-wise ordering does not provide an optimal parallelization startegy, and may only be implemented to perform simple initial tests for parallel computations.

Domain decomposition

The third parallelization approach is based on a domain decomposition concept, which is widely used for efficient parallelization strategies of finite-element and time-domain FD modelling approaches. Domain decomposition breaks up the physical model into a number of sub-domains that are distributed over an existing group of parallel processors.

The idea of the model decomposition is the partition of a global, computational expensive procedure to a number of local problems of significantly reduced size, such that each processor in the group easily performs its attributed local process. Moreover, the decomposition has to be performed in a manner that guarantees parallel computations, with inter-processor communications kept to a minimum. Thus, the initially large com-

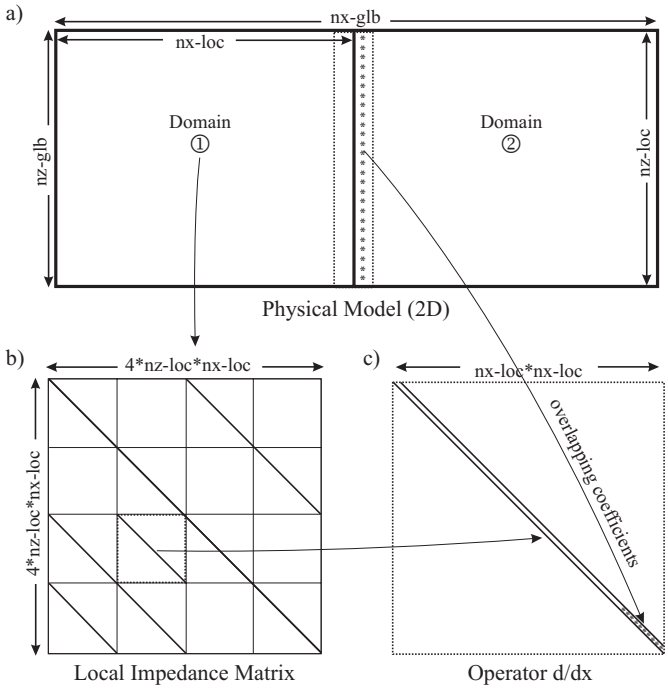

Figure 6.10: Parallelization by domain decomposition for a FDFD modelling scheme. In this example, the physical model is subdivided into 2 sub-domains (a), which implies a parallel computation using 2 processors. Each processor constructs a local impedance matrix corresponding to the sub-domain it is responsible for (b). Computations of partial derivatives require coefficients in neighbouring sub-domains that need to be sent by an inter-processor communication step (c).

putation is split into a set of local problems that are easily solved in a fast and efficient manner using known sequential algorithms.

In order to obtain the desired model decomposition, we need to formulate local FDFD matrix equations for each sub-domain. Moreover, the deduced model decomposition subsequently induces a similar decomposition of the approximated wave-field solution x_i and the RHS vector b. Note that, in general, it is desirable to formulate the domain decomposition in such a way that the initial sequential code for the global problem is only adapted to local sub-domains, while the computational structure remains unchanged.

Once local systems of equations are defined, we can run local iterative schemes on each processor for each sub-domain *independently*. The distributed iterative solver is then similar to a parallel iterative computation, where the initial global procedure is distributed over the group of sub-domains on each processor.

In oversimplified terms, I said the parallel iterations to be domain-independent. This is only true for the inner sub-domain body. Since derivative operators require grid-node information from neighbouring points in order to precisely estimate spatial derivatives,

sub-domain interactions exist near the interfaces of domains.

Krylov-based iterative solvers, such as *GMRES*, update the approximate iterative solution through matrix-vector or dot-product computations. In order to guarantee the correct evaluation of a global iterative solution e.g., for the matrix-vector product $z = A \times y$, processors require information passing from neighbouring sub-domains to compute the corresponding local product $z^j = A^j \times y^j$ they are *responsible* for. The message passing is implemented by an overlap of a given sub-domain into the neighbouring domains, where the dimension of the overlap is controlled by the order or spatial size of the partial derivative operator used.

In Figure 6.10, I illustrate a domain decomposition situation for the DISS-2D approach. The physical model is decomposed into two sub-domains building a vertical interface (a). For each sub-domain a local matrix equation is formulated that is similar to Equation 6.3. The local impedance matrix (see Figure 6.10b) holds discretized derivative operators that require grid-node information from the neighbouring domain (denoted by stars near the interface in Figure 6.10c). Since the overlapping data is defined on the next processor only, MPI message passing is performed to guarantee exact matrix-vector computations.

Dot-product computations follow a similar parallelization induced by the domain decomposition. Each processor performs a local product corresponding to the data of its sub-domain. Once all processors in the group terminate their calculations, a MPI processor communication step constructs the global wave-field approximation solution for the given iteration step. The iteration process is continued by updating corresponding vector slices for all processors in the group.

Domain decomposition may be directly applied to the DISS approach for parallelising the iterative scheme. For the DIWS approach, this may not be true since the decomposition into sub-domains, similar to the approach presented here, is not natural to the global wavelet projection of the computational domain.

Discussion

Three different parallelization strategies for matrix-vector products resulting from a FDFD-DISS or DIWS formulation have been discussed. The main problem underlying all approaches is to find a good matrix decomposition strategy that respects the physical characteristics of the DISS and DIWS formulation.

The first column-wise matrix distribution is in contrast to the sequential matrix construction algorithm. I therefore expect large additional work to be performed in order to construct the impedance matrix directly in distributed mode, which is why this approach is considered not being appropriate for the FDFD-DIS formulation.

The same kind of parallelization strategy is followed for the second approach, called row-wise parallelization. As the name indicates, this approach is better adapted to the problem at hand and, moreover, the implementation of the parallel code is estimated to stay rather simple. Still, this approach requires large processor communications and the strict iterative scheme is not parallelized in an optimal way. Therefore the row-wise matrix distribution is not the ideal solution for large-scale wave simulation modelling.

The third parallelization strategy relies on a physical domain decomposition approach. The inherent structure and expected algorithms for a domain decomposition fulfil the desired parallelization constraints, since large-scale global computation for the sequential code are efficiently split-up in a large number of practically independent problems. Therefore, domain decomposition shall be investigated in greater detail for an optimized DISS-3D implementation.

For now, the question remains how the domain decomposition approach may be applied to the wavelet-based DIWS scheme. Although it might be possible to apply the DIWS resolution strategy to each sub-domain in the decomposition, this does not lead to a proper wavelet-based parallelization strategy, since the underlying physics of the wavelet formulation are disregarded.

In my opinion, the DIWS parallelization of the iterative scheme should build on the intrinsic multi-scale decomposition provided by the wavelet expansion. Unfortunately, I did not have enough time to further pursue these ideas and I will therefore end the discussion here.

6.6 Conclusion

I demonstrate acoustic wave propagation modelling in homogeneous and heterogeneous 3D media using the space DISS-3D and wavelet-based DIWS-3D FDFD approaches. The 3D approaches are exactly similar to the 2D developments discussed in Chapter 4.

The current sequential implementation of both DIS schemes limits significantly the 3D grid sizes that may be modelled. Nevertheless, DISS-3D and DIWS-3D were compared to simple 2D wave simulations to guarantee correct numerical wave simulations. In fact, I compute 3D wave-field simualtions that are excited by an external line source linearly spread out over one spatial coordinate direction. Then extracted 2D-planes out of the 3D solution provide wave-field frequency maps exactly similar to standard 2D computations. In case numerical or implementation errors exist, they can be detected easily following this comparison test.

In order to permit acoustic wave modelling in large-scale earth models, the parallelization of the DISS-3D and DIWS-3D approaches is unavoidable. Therefore, different parallelization strategies for different computational aspects are discussed with respect to their feasibility and expected performance.

I choose MPI-based Fortran programming for all DIS parallelization aspects in order to guarantee large code-portability on numerous distributed memory computer structures.

I detect three principal CPU-time expensive computations that may be parallelized in a DIS approach. The first is the wavelet transform applied during convolution-type spectral wavelet expansions performed in the DIWS approach. The transformation algorithm may be parallelized on multi-processors structures using wavelet-adapted parallelization strategies developed by mathematicians (Homlström, 1995).

The second computational expensive calculation is the coarse-grid LU-matrix factorization. Since I apply a minimum degree ordering solver that was developed especially for parallel applications, the principal task is an optimised matrix construction algorithms for

the solver software. I implement a distributed parallel matrix construction scheme, where each processor constructs a pre-defined number of rows of the global impedance matrix. The distributed matrix blocks are analysed and subsequently re-ordered by the factorization software following minimum pivot strategies. The combined global impedance matrix is never constructed.

Finally, I discuss parallelization strategies for the iterative *GMRES* computations of the fine-grid wave-field solutions. I find the domain decomposition approach promising to provide a powerful DISS-3D parallelization strategy. This shall be implemented in the near future.

A domain decomposition parallelization for the DIWS approach requires significant modifications to the spatial DISS approach due to the global view of the wavelet transform. Different strategies may be imagined that, in my opinion, should profit from the natural wavelet-based multi-scale decomposition. This needs to be investigated in further detail.

Chapter 7

Conclusions

7.1 Résumé

La modélisation de la propagation des ondes est essentielle pour évaluer le risque sismique d'un site donné, comme outil numérique dans des algorithmes d'inversion des données sismiques, ou pour effectuer des simulations des ondes pour des expériences multi-sources. Parmi l'ensemble des méthodes de modélisation existantes, les méthodes par différences finies (FD) ont un intérêt particulier dans la mesure où elles fournissent la réponse complète du champ d'onde sur un ensemble de points d'une grille numérique pour des structures hétérogènes complexes arbitraires. Des phénomènes réalistes de propagation des ondes peuvent être reproduits dans des modèles complexes tridimensionnelles de grande taille (par exemple, 10x10x10 Km) et des excitations de source de bande passante élevée (par exemple, 0-10 Hz).

Les algorithmes standard FD fournissent un outil puissant pour la modélisation des ondes en deux dimensions (2D). Dans le cas de la propagation en trois dimensions (3D), les discrétisations FD classiques des équations aux dérivés partielles (PDE) sur des grilles cartésiennes nécessitent des temps CPU et des volumes de mémoire vive prohibitifs, qui excèdent considérablement les capacités actuelles des ordinateurs. L'utilisation de grilles numériques uniformes conduisent à des algorithmes stables et des implémentations aisées. Néanmoins, les performances limitées de ces approches dans les cas de modélisations en 3D ont motivé le développement d'approches multi-grilles utilisant des combinaisons de grilles ayant des résolutions variables. Ces développements ont permis d'améliorer les performances des méthodes par différences finies, bien que d'autres méthodes basées sur des éléments finies (FE) et des éléments spectraux (SE) sont clairement supérieures aux méthodes FD optimisées.

Les techniques FE et SE définissent une grille numérique irrégulière pour un niveau de précision donné. La grille numérique est construite de manière à représenter parfaitement les frontières ou discontinuités du modèle. Par conséquent, les problèmes liés à la modélisation tendent plutôt à être reportés au niveau de la construction de la maille irrégulière. Malheureusement, *mailleurs* (AMR) sont plutôt difficiles à contrôler par l'utilisateur et, en général, sont loin d'être évidents à mettre en oeuvre.

Cette thèse étudie le potentiel d'une approche utilisant l'analyse multirésolution fournie par la transformée en ondelettes (WT) dans une formulation classique par FD pour des simulations de la propagation des ondes dans des milieux 2D et 3D fortement hétérogènes. La formulation en ondelettes fournit un outil puissant pour représenter le champ d'onde modélisé et le milieu de propagation sur plusieurs grilles numériques de résolution différente moyennant la projection de l'équation d'onde sur une base de fonctions orthogonales, les ondelettes. Cette approche relève de ce fait des méthodes spectrales. Avant de faire des remarques de conclusion, je récapitulerai brièvement différentes étapes du travail présenté dans la thèse.

Après la présentation de différentes approches de discrétisation spatiale des équations aux dérivés partielles, j'ai présenté un nouveau schéma basé sur une géométrie des grilles en quinconce pour la modélisation des ondes acoustiques par FD dans le domaine des fréquences (FDFD). Ce schéma, qui est appelé *croix 13-points* à cause de sa forme géométrique, a été comparé à l'approche classiquement utilisée pour les modélisations dans le domaine des fréquences fondée sur des grilles tournées de 45 degrés par rapport au repère cartésien. Les deux schémas ont été comparés analytiquement par analyse de dispersion et numériquement via des simulations des ondes dans des milieux 2D homogènes et hétérogènes en ce qui concerne la rapidité et la précision. Par ailleurs, j'ai étendu l'implémentation séquentielle des deux approches au cas des architectures parallèles à mémoire distribuée de manière à accélérer les calculs numériques.

La stratégie sélectionnée d'optimisation des modélisations des ondes FDFD propose une extension des approches multigrilles classiques. La nouvelle approche, appelée "*Direct-Iterative Solver*" (DIS), combine des calculs de simulation sur des grilles numériques de résolution variable. La stratégie de l'approche DIS est sudivisée en trois principales étapes de calcul:

- la solution sur la grille grossière est calculée de manière exacte par une méthode directe (factorisation LU de la matrice d'impédance)
- la solution grossière est prolongée sur la grille fine
- la solution prolongée est corrigée pour obtenir la solution finale sur la grille fine par une méthode itérative

J'ai présenté deux procédures différentes de prolongation de la solution de la grille grossière sur la grille fine qui sont fondées respectivement sur une interpolation bilinéaire en espace, dénommée le "*Direct-Iterative-Space Solver*" (DISS), et sur une décomposition multi-échelles en ondelettes, dénommée "*Direct-Iterative-Wavelet Solver*" (DIWS). Les deux approches de simulation sont mises en oeuvre pour modéliser des ondes SH dans des milieux 2D fortement hétérogènes et structurellement complexes. Des exemples divers de simulation de propagation des ondes ont été présentés afin d'évaluer l'efficacité et la précision des méthodes DIS.

Les deux approches DIS ont été alors étendues à la propagation d'onde acoustique dans des milieux 3D. Mis à part la construction de la matrice d'impédance, l'implémentation des approches DIS en 3D et en 2D repose sur les mêmes principes. Les codes séquentiels ont été validés sur des modèles 3D de taille limitée.

L'utilisation de la stratégie DIS pour des simulations de la propagation des ondes à grande échelle nécessite la parallélisation du code afin de le rendre opérationnel sur des architectures parallèles en mémoire distribuée. Différentes stratégies de parallélisation des méthodes DIS ont été discutées et en partie implémentées. Par manque de temps, la parallélisation des approches DISS et DIWS n'a pu être complètement implémentée durant cette thèse.

Résultats

Je présente les principaux résultats de cette thèse dans deux paragraphes séparés, corespondant respectivement aux recherches sur la discrétisation par différences finies des dérivés partielles spatiales (schémas en quinconce versus schémas combinés suivant plusieurs systèmes d'axes) et sur les développements d'optimisation en espace et en ondelettes dédiés aux simulations FDFDs.

Discrétisation spatiale de l'équation d'onde

Le schéma résultant de la géométrie de grilles en quinconce pour les approximations d'ordre 2 des dérivées est identique au schéma à 5-points tel qu'il a été introduit il y a une dizaine d'année dans les modélisations en fréquence. Les approximations d'ordre 4 des dérivées pour des simulations FDFD en 2D conduisent à un schéma à 13-points. La comparaison de l'étoile 9-points, qui résulte d'une approche par rotation de grille, avec le schéma à 13-points montre que l'approche en quinconce est moins efficace. La géométrie en quinconce conduit à un schéma qui contient les contributions de 13 points de la grille numérique, par rapport aux 9 points pour l'approche par rotation de grille.

Par conséquent, les factorisations de la matrice d'impédance dans la modélisation par FDFD sont moins efficaces. D'ailleurs, la combinaison des grilles en rotation avec une approche de condensation de masse fournit des relations optimisées de dispersion pour l'étoile de 9-points. La précision du schéma 13-points peut également être améliorée en appliquant des optimisations de courbe de dispersion. Néanmoins, cette optimisation n'a pas permis d'obtenir des résultats supérieurs à ceux obtenus par la combinaison de la condensation de masse avec la rotation des grilles. J'en conclus que la recherche d'une approche numérique qui combine des grilles en quinconce avec une rotation pour des simulations de la propagation des ondes par FD mériterait d'être menée également dans le domaine du temps (TDFD).

Dans le cas des modélisations en 3D, l'approche par rotation de grille conduit à une étoile de 27-points. Le schéma résultant des grilles en quinconce contient seulement 19 coefficients. Bien que le schéma de 19-points soit moins compact (distance entre la diagonale et la frange externe de la matrice d'impédance), le nombre de coefficients du schéma 3D est sensiblement réduit. Par conséquent, nous pouvons anticiper différentes conclusions sur les performances respectives des schémas 3D correspondant à l'étoile 27-points et la croix 19-points.

Optimisation dans le domaine spatial et des ondelettes

L'approche DIS combine des solutions du champ d'onde calculées sur une grille grossière et sur une grille fine. Les solutions sur la grille grossière sont utilisées pour construire, par prolongation, la solution intiale d'une approche itérative calculée sur la grille fine. Bien que les simulations des ondes par FDFD peuvent être calculées par méthode itérative en partant d'une solution initiale nulle, le préconditionnement fourni par l'approche DIS, sous forme d'une solution initiale *proche* de la solution finale, accélère de manière significative la convergence du processus itératif.

Les approches DISS et DIWS fournissent des simulations des ondes stables et précises pour des modèles hétérogènes complexes, telles que le modèle Marmousi. La différence principale entre la formulation spatiale (DISS) et la formulation en ondelettes (DIWS) est liée aux algorithmes de construction de la matrice et à la performance de la méthode de résolution itérative.

L'approche DISS fournit naturellement des approches de construction rapides et efficaces de la matrice dans l'espace physique. La principale limite de l'approche DISS est comparable à celle des méthodes multigrilles classiques. J'ai noté que le nombre d'itérations pour faire converger le processus itératif variait significativement d'une simulation à l'autre. Ce comportement instable est attribué à l'interpolation bilinéaire utilisée pour prolonger la solution grossière sur la grille fine. Par conséquent, l'utilisation de l'approche DISS se révèle peu conviviale dans la mesure où il est difficile d'anticiper le nombre minimal d'itérations nécessaire à la convergence de l'algorithme. Dans les approches multigrilles classiques, la convergence est accélérée en utilisant des cycles en V et W consistant à résoudre séquentiellement le problème itératif sur des grilles de résolution variable. Néanmoins, le nombre de cycles à utiliser n'est pas facile à déterminer a priori.

L'approche de DIWS effectue des itérations sur une base orthogonale d'ondelettes. J'ai limité l'analyse à l'utilisation des ondelettes de Daubechies-4 (Daub4).

La construction de la matrice d'impédance dans le domaine spectral des ondelettes nécessite des calculs coûteux sous forme de convolutions multidimensionnelles (temps CPU). Bien que ces calculs soient coûteux, ils ne sont effectués qu'une fois avant que la modélisation sensu stricto ne commence.

Par ailleurs, la matrice d'impédance dans l'espace des ondelettes contient un plus grand nombre de coefficients non nuls comparativement à la matrice discrétisée dans l'espace physique. L'augmentation du nombre de coefficients non nuls, qui résulte de la prise en compte des intéractions entre les différentes résolutions, dépend du nombre d'espaces (ou de grilles) d'approximation utilisées dans l'analyse multirésolution. Cette augmentation du nombre de coefficients non nuls peux être compensés en appliquant des masques dans le domaine des ondelettes dont l'objectif est d'adapter localement le nombre de grilles utilisées aux propriétés locales du milieu (les grilles fines ne sont utilisées que dans les parties du modèle où se propagent des phénomènes de courte longueur d'onde). Cette stratégie d'adaptabilité spatiale exploite la double localisation spatiale et spectrale fournie par la représentation en ondelettes.

L'apport observé de l'approche itérative DIWS est l'accélération de la convergence vers la solution désirée du champ d'onde sur la grille fine ainsi qu'une certaine stabilité

de la convergence par rapport au nombre de résolutions utilisées. La représentation multigrilles fournie par la transformée en ondelettes se substitue efficacement et de manière automatique aux cycles en V et W des approches multigrilles classiques. En effet, la représentation en ondelettes fournit la représentation multigrille mais est capable en plus de résoudre le problème itératif simultanément sur chacune des grilles. La résolution simultanée du problème itératif sur chaque grille est rendue possible par le fait que la transformée en ondelettes prend en compte les intéractions entre les différentes échelles lorsque par exemple un opérateur différentiel est appliqué à un champ d'onde. La prise en compte de ces intéractions entre grilles se substitue aux opérations de prolongation et de restriction des approches multigrilles classiques.

D'ailleurs, j'ai constaté que l'itération DIWS fournit une solution homogénéisé du champ d'onde pour un nombre considérablement réduit d'itérations. En d'autres termes, les principaux composants du champ d'onde sont déjà présents dans la solution rapprochée.

Des simulations d'ondes acoustiques dans des milieux hétérogènes 2D et 3D ont été effectuées par les méthodes DISS et DIWS en mode séquentiel. La taille maximale de la grille numérique (nombre des noeuds) de l'approche DISS-3D est limitée par la mémoire vive nécessaire au calcul de la solution du champ d'onde par une factorisation de la matrice d'impédance. En revanche, l'approche DIWS-3D séquentielle a permis des modélisations des ondes dans des modèles 3D ayant la taille de la moitié des modèles de DISS-3D, puisque l'attribution des espaces mémoire liées à la construction et stockage de la matrice d'impédance dans le domaine d'ondelette, excède les ressources d'informatique locales disponibles.

Des simulations de la propagation des ondes en 3D ont été validées par comparaison avec des simulations calculées en 2D avec les programmes DISS-2D et DIWS-2D. Pour effectuer ces comparaisons, j'ai utilisé une ligne de sources orientée perpendiculairement au plan dans lequel les simulations 2D ont été calculées. Les simulations 3D pour une ligne de sources et 2D pour une source ponctuelle ont fourni les mêmes résultats.

Future

Pour conclure, je propose quelques idées dans la perspective de futurs développements des méthodes de modélisation des ondes par FDFD. La discussion concerne les stratégies de discrétisation spatiale et d'optimisation des FDFD par l'approche DIS.

7.2 Summary

Seismic wave propagation modelling is essential to quantify site effects and local seismic risk, as a numerical tool in seismic data inversion algorithms, or to perform wave simulations for multi-source experiments. Finite-difference (FD) methods are of particular interest as they provide the complete wave-field response on a discrete numerical set of grid points for arbitrary complex heterogeneous structures. Realistic wave propagation phenomena are accounted for when large complex 3D models (e.g., $10Km \times 10Km \times 10Km$) and high frequency ranges (e.g., $0Hz - 10Hz$) are modelled.

Standard finite-difference algorithms provide a powerful tool for 2D simulations. For 3D modelling, natural FD discretizations of the partial differential equations (PDEs) on Cartesian grids require massive amounts of CPU-time and memory, which greatly exceeds available computer hardware systems. In general, simple grids are desirable since they lead to numerical stable algorithms and simple implementation schemes. However, the limitations due to computational inefficiencies have been reduced through the introduction of irregular grids, combinations of grids having varying resolution, and optimized implementation schemes for parallel super computers. These developments increased the computational efficiency, though other methods based finite elements (FE) and spectral elements (SE) spatial discretizations clearly outperform optimized FD methods.

FE and SE techniques, by default, define an irregular numerical grid that, for a given accuracy level, needs to be constructed to perfectly fit the internal model structures. Therefore, problems related to accurate and efficient forward modelling are shifted to the development of an appropriate mesh generation algorithm. Unfortunately, powerful (automatic) mesh refinement techniques are rather difficult to control by the user and, in general, are far from being obvious to implement.

This thesis investigates potentials of the wavelet transform combined in a classic FD formulation for 2D and 3D wave propagation simulations, with respect to the CPU-time performance and accuracy. The study was motivated by shortcomings of existing forward modelling techniques to deliver synthetic results for large-scale wave simulation scenarios. Moreover, the wavelet formulation seemed to provide a powerful tool that nicely introduces the, in general, difficult multi-grid combination at the cost of a transformation in the spectral wavelet domain. Before making concluding remarks, I will briefly summarise different steps of the work presented in the thesis.

After introducing different spatial discretization schemes for general PDE formulations, I presented a new staggered cross stencil for frequency domain finite difference (FDFD) acoustic wave modelling. The deduced stencil, called 13-points cross stencil because of its geometrical shape, was compared to the state-of-the-art grid rotation approach in FDFD modelling. Both stencils have been compared for wave simulations in 2D homogeneous and heterogeneous media with respect to computational efficiency and accuracy. Moreover, I extended the initially sequential implementations for both grid-rotation and staggered-grids to run on a distributed memory computer environment in order to accelerate numerical computations.

I proceeded the research by developing a new FDFD modelling approach that provides an alternative optimization for standard multi-grid simulation strategies. The new approach, called Direct-Iterative Solver (DIS), combines wave simulations on coarse-grid and fine-grid discretizations. The DIS strategy is based on three different computation steps:

1. compute coarse-grid solution by direct matrix factorization

2. project coarse-grid solution on fine-grid

3. extend projected solution to desired fine-grid solution by iterative solver

Two different coarse-grid projection procedures have been introduced that, either rely on a space bilinear interpolation, denoted by Direct-Iterative Space Solver (DISS), or on a wavelet-based multi-scale decomposition, called Direct-Iterative-Wavelet Solver (DIWS). Both solver approaches are implemented for SH-wave simulations in strongly heterogeneous and structurally complex 2D model scenarios. Various wave propagation simulation examples have been presented in order to evaluate the computational efficiency and accuracy of the DIS schemes.

Both DIS approaches are then extended to acoustic wave propagation in 3D media. Besides the matrix construction, the DIS concept for the 3D and 2D implementation are exactly identical. The sequential codes are evaluated for limited 3D models.

The extension of the DIS strategy to allow large-scale wave simulations requires a complete parallelization of the code in order to run on distributed super computer environments. Different DIS parallelization strategies have been discussed and partly implemented. Due to time constraints, the complete parallelization of the DISS and DIWS approaches could not fully implemented in this thesis.

7.3 Results

I present the principal outcomings of the work in two separate subsections that correspond to investigations related to space discretizations by the staggered-grid and grid-rotation strategies, and to space and wavelet optimization developments performed for FDFD modelling.

7.3.1 Space discretization

The deduced staggered cross stencil for second-order derivative approximations is exactly similar to the 5-points stencil strategy. Fourth-order staggered derivative approximations in 2D FDFD modelling lead to the 13-points cross stencil. Compared to the 9-points star stencil that results from a grid rotation approach, the 13-points cross stencil is less efficient. The staggered geometry gives a computational stencil that incorporates grid contributions from 13 points, rather than 9-points for the grid rotation approach.

Therefore, required matrix factorizations in FDFD modelling are less efficient. Moreover, the combination of the grid rotation geometry with a lumped mass approach provides optimized dispersion relations for the 9-points star. The accuracy of the 13-points cross stencil may be increased by applying dispersion curve optimizations, though I do not find superior results compared to the rotation-lumped mass combination. Therefore, I propose the investigation of a staggered grid rotation approach for 2D time domain finite difference (TDFD) wave propagation simulations.

In case of 3D modelling, the grid rotation approach leads to a 27-points star. The corresponding staggered stencil incorporates only 19 grid nodes. Even though the 19-points stencil is less compact, the number of stencil coefficients in 3D is significantly reduced. Therefore, we may expect different results for the 3D stencil comparison between the 27-points star and the 19-points cross.

7.3.2 Space and wavelet optimization

The Direct-Iterative Solver approach combines coarse-grid and fine-grid wave-field solutions, thereby extending the dimensions of numerical grids in FDFD modelling. Even though FDFD wave simulations may be performed using an iterative solver with zero initial solution, the DIS preconditioning strategy significantly accelerates the convergence of the iteration process.

The DISS and DIWS provide stable and accurate wave simulations for complex heterogeneous model structures, such as the Marmousi model. The main difference between the space and the wavelet formulation is related to the matrix construction algorithms and to the performance of the iterative scheme.

The DISS approach, that is similar to a multi-grid nested iteration scheme, naturally provides fast and efficient matrix construction schemes in the physical space. The main drawback that prohibits stable wave simulations comes from known shortcomings of standard full multi-grid methods. The performance of the space bilinear interpolation as preconditioner for an iterative matrix solver was found to be strongly dependent on the maximum number of iteration steps performed. Therefore, dispersion-free wave simulations become a cumbersome task to evaluate, since a given simulation problem may, or may not be performed efficiently. The DISS ambiguity related to the space interpolation phase-shifts may be reduced by the use of V- and W-cycles.

The DIWS approach performs iterations on an orthogonal wavelet basis. I restricted investigations to the Daub4 wavelet basis, since it leads to fast and efficient numerical algorithms while providing accurate and stable approximation properties.

The construction of the complex impedance matrix in the spectral wavelet domain requires extensive wavelet expansion computations that have CPU-expensive convolution-type structure. Even though convolutions are heavy to compute, they are only performed once before the modelling starts and provide several optimization possibilities that, until now, have not been investigated. Typical approaches to speed-up wavelet transform algorithms include e.g., optimized parallelization techniques.

In addition to convolution-type expansions, the DIWS matrix in the wavelet space contains an increased number of non-zero coefficients compared to the corresponding DISS matrix in the physical space. The increase of coefficients depends on the number of wavelet resolution approximation spaces applied and may slow down the performance of the spectral approach. However, space adaptivity can be incorporated in the matrix construction process, which is expected to largely eliminate shortcomings caused by increasing matrix entries. From a conceptual point of view, the multi-scale wavelet decomposition of the DIWS is similar to a Full Multi-Grid method.

The main advantage of the DIWS iteration process is the possibility to perform restriction and prolongation steps simultaneously at each iteration step through the wavelet multi-scale formulation. Therefore fast and stable convergence to the desired fine-grid wave-field solution may be obtained. The multi-scale preconditioning efficiently accounts for grid interactions and interpolation phase-shifts intrinsic to a numerical grid-combination technique. Moreover, I find that the DIWS iteration provides a *homogenized* wave-field solution for a greatly reduced number of iteration steps. Homogenized, as I

used here implies that the principal wave-field components are present in the approximated solution.

Acoustic wave simulations in 3D heterogeneous media are performed by the DISS-3D and DIWS-3D approaches in sequential mode. The largest possible DISS-3D grid model size is limited by the required RAM memory for the direct matrix factorization solver. In contrast, the sequential DIWS-3D approach permitted 3D models having only half size of the largest DISS-3D model, since allocation of working arrays related to the construction and storage of the complex impedance matrix in wavelet domain, exceed the available local computer resources.

Correct 3D wave simulations have been verified by comparisons with DISS-2D and DIWS-2D modelling examples. I excite the 3D simulations in simple homogeneous media by a line source function parallel to one of the principal axis of the 3D space. The wave-field extractions from 2D-planes perpendicular to the line source are compared to corresponding 2D simulations. I find good fit of the two solutions.

7.4 Future work

In this section, I give some ideas for future developments of the FDFD forward modelling schemes. The discussion is subdivided with respect to the space discretization developments and DIS FDFD optimization strategies. At the end, I make a final remark concerning the principal aims of this work.

7.4.1 Staggered grids versus grid rotation

FD and grid rotation

To start with, I comment on the space discretization scheme used for second-order FDFD modelling of the acoustic wave equation. As I have shown, in 2D media the grid-rotation approach gives superior results over the staggered grid geometry. Since the principal difference between the frequency and time domain FD modelling is a Fourier transform, I suggest the investigation of a corresponding staggered grid-rotation approach for standard TDFD wave simulations.

In view of the FDFD results, I mainly expect increasing stability during wave propagation. Computational speed-up, as obtained for FDFD modelling due to the compactness of the 9-points star stencil, may not be achieved in a time domain grid-rotation scheme.

The staggered-grid-rotation strategy may then be extended to the FDFD modelling described in Chapter 3 and Chapter 4.

3D investigation

For 3D modelling, the conclusions for 2D FDFD modelling might not be true anymore. The grid rotation strategy in 3D media leads to a 27-points star. In contrast, the staggered grid geometry in 3D gives a 19-points cross stencil. Therefore, the number non-zero matrix coefficients of the grid-rotation approach is approximately 30% larger than for the

staggered scheme. In contrast, the grid-rotation approach guarantees a compact stencil, while the cross stencil is naturally enlarged. Which of the two approaches provides better CPU-performance and less memory requirements for the direct matrix factorization in case of a 3D wave simulation example, will be investigated in the near future.

Parallelization

The current star and cross stencil implementations for 2D acoustic wave propagation exist in sequential and parallel form. The parallel implementation simply constructs blocks of matrix rows on a group processor in a distributed computer environment. Given the result of the stencil comparison i.e., 19-points cross versus 27-points star, the most efficient approach should be parallelized using a domain decomposition strategy rather than simple block-row distributions. In the same context, numerical preconditioning may be investigated in order to optimize the overall convergence performance of the modelling scheme.

Realistic wave propagation

Both space discretization approaches may be extended to allow elastic wave propagation modelling including visco-elastic effects for models including free-surface boundary conditions with complex topography, that have important implication for real-case wave simulation examples.

DIS strategy

The DISS strategy that was developed in Chapter 4 for the first-order hyperbolic wave equation may easily be applied for the staggered cross and grid rotation approaches. Then, FDFD wave simulation for largely extended grid-models may be performed. In contrast, the wavelet-based DIWS for second-order hyperbolic equations was estimated to be computational expensive due to convolution calculations, and shall therefore not be considered.

Applications

Once the parallel code optimization has been implemented, large-scale 3D frequency domain wave simulations may be performed. A typical application is a wave-form inversion processing flow where the forward problem has to be solved for numerous external source positions.

7.4.2 Direct-Iterative-Solver approach in 3D

More important for large-scale 3D FDFD wave propagation simulations is the optimal extension of the sequential DISS and DIWS algorithms to parallel super computer structures. I propose a combination of Fortran90 and MPI based implementation to allow large code portability.

Iteration

In a first step, the behaviour of the DISS and DIWS iterative scheme have been investigated for fixed numbers of iteration steps. In order to better evaluate the difference between the simple space nested iteration (DISS) and the wavelet full multi-grid scheme (DIWS), the convergence of iterative solver needs to be studied for a fixed tolerance level rather than number of iteration steps.

Parallelization

Since the direct matrix factorization parallelization is included in the *MUMPS* solver, in principal parallel wavelet transform algorithms and a parallel iterative *GMRES* scheme should be developed. Ideally, the DISS iterative solver should be parallelised using a standard domain decomposition approach. In case of the DIWS, a similar parallelization strategy based on a wavelet domain decomposition is desirable and should be investigated.

Space adaptivity

The CPU-time performance of the DIWS is largely accelerated through the definition of space adaptive strategies. Computational mask should optionally be defined on each resolution approximation grid with respect to a physical parameter characterizing the local accuracy of the solution. Ideally, different physical parameters shall be evaluated in order to study the influence on the overall performance of the optimization approach.

Matrix ordering

Moreover, both DIS approaches should be evaluated with respect to their performance when additional numerical pivoting strategies for the iterative scheme and different matrix ordering techniques for the direct matrix factorization (e.g., minimum ordering, nested dissection, etc.) are applied.

Absorbing boundary conditions

Once a fast and efficient implementation is obtained, a set of necessary and interesting implementation related problems may be studied in further detail. At first, the PML absorbing boundary conditions need modifications in order to suppress any artificial reflections from the model-PML boundary.

Elastic wave propagation

In orer to allow wide-spread applications to numerous geophysical and geological problems, the DISS and DIWS approaches shall be extended for visco-elastic wave propagation modelling. From a conceptional point of view, elasticity and viscocity are fast and easy implemented. I suggest that the extension shall be performed for the final optimized DISS and DIWS versions, since memory and CPU-time constraints will become even

more important than in the acoustic case due to an increase in the number of equations and therefore the number of non-zero coefficients in the complex impedance matrix.

Free surface

An important feature required to perform realistic wave propagation simulations is the implementation of a stable free-surface boundary condition with topography in the DISS and DIWS approaches. In general, the exact verification of the free surface boundary condition is a difficult task for strong formulation PDE discretizations, since equations are verified on discrete grid points. FD methods are extremely sensible to the strongly changing physical parameters at the boundary, which often causes numerical instabilities. Because of the great implementation difficulties of a stable boundary condition, the FDFD DISS and DIWS investigation may even re-consider other, more stable, discretization stencils. For example, we might investigate the stability performance for a staggered grid-rotation approach combined in the DISS and DIWS modelling schemes.

3D applications

The deduced DISS and DIWS approaches may then be applied to a realistic 3D wave propagation simulation scenario, such as a multi-source experiment carried on the Vesuvius volcano in 1998 (Auger, 2000). Also, the parallel implementation should be compared to other high performance modelling schemes (e.g., spectral element code). The 3D parallel benchmark tests for acoustic wave propagation will provide important constraints on possible extensions to DISS and DIWS approaches for elastic wave propagation modelling.

Frequency interpolation

For now, all FDFD approaches presented in this thesis were set up to compute a predefined number of discrete frequency components. Although I did not comment on exact details, a set of frequencies was assumed to be computed by repeated applications of the e.g., DISS or DIWS approach. Clearly, this is only one possibility to obtain the required frequency component solutions. Other strategies that rely on intermediate interpolation and iteration procedures should be tested.

For example, we might assume the wave-field solution for a given frequency component to resemble slightly higher and lower *neighbouring* frequencies. The DISS and DIWS implementations could be modified to allow exact DIS computation of distinct frequency components only, while all remaining wave-field frequencies are determined through interpolation and subsequent iterations of the interpolated solutions.

7.4.3 Final remark

Altogether, the current DISS and DIWS implementations provide a first development step of a powerful wave simulation strategy based on optimized FD space discretizations. All the above suggestions for future work are mainly related to the necessary developments to render the principal DIS approach stable and efficient.

Even though I only considered applications in seismology, the general problematic to solve efficiently matrix-type equations resulting from discretization of PDEs is encountered in many sciences. Therefore, this DIS approach should be widely distributed which, in my opinion, includes free access to all developments I performed.

Thus, the final outcome should be a free distributed modelling tool that can be applied to numerous interesting geophysical and geological problematics. Typical applications are strong ground motion site-effect studies, large-scale wave-form inversions, etc..

Appendix A

Wavelets and PDEs

A.1 Multi-resolution analysis and wavelet transform

I illustrate the basic principles that define the orthogonal Daubechies wavelet basis and multi-resolution analysis. The aim of this Appendix is to provide the background information regarding wavelet definitions used in the thesis and, moreover, to define the wavelet notations I applied throughout. For detailed mathematical developments, I refer the reader to the original works by Daubechies (1988); Mallat (1989); Daubechies (1992); Mallat (1999). For simplicity, wavelet explanations are given on 1D examples only, since 2D and 3D generalisations may be derived through repeated application of 1D processes for each spatial dimension.

The orthogonal wavelet transform, that leads to the Daubechies wavelets, is based on two functions: the scaling function $\phi(x)$ and the wavelet function $\psi(x)$. The scaling function defines a dilation relation of the form,

$$\phi(x) = \sqrt{2} \sum_{k=0}^{L-1} h_k \phi(2x - k), \tag{6.1}$$

where h_k is one of two *quadrature mirror filters*. In addition to the dilation property, the scaling function is normalized $\int_{-\infty}^{\infty} \phi(x)dx = 1$.

I define the corresponding wavelet function in terms of the scaling function to be,

$$\psi(x) = \sqrt{2} \sum_{k=0}^{L-1} g_k \phi(2x - k), \tag{6.2}$$

where g_k is the second *quadrature mirror filter*.

With the help of dilating and translating the scaling and wavelet function, one can

build an orthonormal basis of $L^2(R)$:

$$\phi_k^j(x) = 2^{-j/2} \cdot \phi(2^{-j}x - k),$$
$$\psi_k^j(x) = 2^{-j/2} \cdot \psi(2^{-j}x - k), \tag{6.3}$$

where $j \epsilon Z$ is the dilation and $k \epsilon Z$ the translation parameter, respectively. The *quadrature mirror filter* coefficients $H = \{h_k\}_{k=0}^{L-1}$ and $G = \{g_k\}_{k=0}^{L-1}$ are related by $g_k = (-1)^k h_{L-k}$ for $k = 0, ..., L-1$. All wavelet properties can be specified through the *quadrature mirror filters*, which therefore allows the computation of the discrete orthogonal wavelet transform (OWT) without constructing the basis functions. In this sense, the OWT is similar to the Fourier transform, where Fourier coefficients are obtained through a subdivision process, without constructing the Fourier basis functions.

The accuracy of the transform is defined by the number of *vanishing moments* (M) of the wavelet function $\psi(x)$. It is,

$$\delta_{kl}\delta_{jm} = \int_{-\infty}^{\infty} \psi_k^j(x)\psi_l^m(x)dx, \tag{6.4}$$

where δ_{kl} denotes the *Kronecker symbol*. Then the *vanishing moments* require that $\psi(x) = \psi_0^0(x)$, which is similar to,

$$\int_{-\infty}^{\infty} \psi(x)x^m dx = 0, \tag{6.5}$$

with $m = 0, ..., M-1$. For Daubechies wavelets, the number of filter coefficients in H and G, denoted by L, is related to the number of *vanishing moments* by $2M = L$.

The two basic functions that define the wavelet transform, $\phi_k^j(x)$ and $\psi_k^j(x)$, span spaces for a fixed parameter k, called *scaling* (V_j) and *wavelet* (W_j) spaces, respectively,

$$V_j = \operatorname*{span}_{k \epsilon Z} \phi_k^j(x) \tag{6.6}$$
$$W_j = \operatorname*{span}_{k \epsilon Z} \psi_k^j(x) \tag{6.7}$$

The spaces V_j and W_j build a chain of subspaces and are related by

$$.... \subset V_1 \subset V_0 \subset V_{-1} \subset V_{-2} ....., \tag{6.8}$$

and

$$V_j = V_{j+1} \oplus W_{j+1} \tag{6.9}$$

where $V_{j+1} \oplus W_{j+1}$ is the direct sum, which is equivalent to the vectors in V_{j+1} being orthogonal to the vectors in W_{j+1}. One step in a wavelet transform simply decomposes the given V_j-space into two disjoint subspaces. The decomposition procedure can be repeated by storing the wavelet space coefficients in W_{j+1} and continuing the subdivision process with the next coarser V_{j+1}-space, until the coarsest resolution space is reached.

I remind that the latter Equations 6.8 and 6.9 express the fact that the scaling functions, which build the basis to the multi-resolution analysis, only form a proper basis on each resolution approximation space, since bases of the V_j-spaces are linear dependent (see Equation 6.8). The combination of the V_j-space with the wavelet space W_j on a given resolution level, permits the construction of a basis on the next finer level (Equation 6.9), which can be repeated until V_0 is reached. Note that I denote V_0 as being the finest resolution space throughout.

It is the extension of the scaling basis functions with the wavelet functions that build the desired linear independent set of functions, that together form the wavelet basis. In case Daubechies wavelets are used, the wavelet basis is also orthogonal. In practice, the wavelet transformation of a signal on a Daubechies wavelet basis can be performed through a convolution type procedure using the *quadrature mirror filters*. Therefore, the number of filter coefficients is crucial to provide fast transform algorithms. I used the wavelet transform algorithm developed in Press et al. (1992).

A.2 1D wave propagation on a wavelet basis using the Non-Standard Form

I give a brief review of the Non-Standard Formulation (NSF) in a Daubechies wavelet basis. By means of the NSF, I show the development of a 1D finite-difference (FD) wave propagation algorithm in the wavelet domain. Moreover, I will discuss the problematics related to scale interaction in the wavelet domain representation with respect to a time-adaptivity implementation, which guided me to work on frequency-domain rather than time-domain wave propagation modelling. For a detailed discussion of the NSF, I recommend the original articles by Beylkin et al. (1991). In addition to the example shown here, I refer to the wave propagation simulation developments, using a wavelet-FD approach in standard form, by Operto et al. (2002).

A.2.1 The Non-Standard Form

The NSF is a signal representation that results from a wavelet-based projection procedure, though the final transformed signal does not lie in the wavelet domain.

The Standard Form (STF) of a signal holds coefficients that are decomposed on a series of discrete *wavelet*-spaces plus a *scaling*-space. I denote with $P_{V_0} f(x)$ the projection of a

continuous signal $f(x)$ in the wavelet domain. Then the STF gives,

$$P_{V_0}^{STF} f(x) = \sum_{k \epsilon Z} f_k^J \phi_k^J(x) + \sum_{j=1}^{J} \sum_{k \epsilon Z} f_k^j \psi_k^j(x), \tag{6.10}$$

where f_k^J are the scaling function coefficients on the coarsest approximation space V_J, and f_k^j the wavelet function coefficients on all finer spaces W_j,

$$\begin{aligned} f_k^J &= \int_{-\infty}^{\infty} f(x) \phi_k^J(x) dx \\ f_k^j &= \int_{-\infty}^{\infty} f(x) \psi_k^j(x) dx. \end{aligned} \tag{6.11}$$

In contrast to the STF representation, the NSF projects the signal $f(x)$ in another domain since, not only *wavelet* contributions on all approximation spaces are stored, but also the corresponding *scaling* informations:

$$P_{V_0}^{NSF} f(x) = \sum_{j=1}^{J} (\sum_{k \epsilon Z} f_k^j \phi_k^j(x) + \sum_{k \epsilon Z} f_k^j \psi_k^j(x)). \tag{6.12}$$

As was shown by Beylkin (1992), the transformation of an operator into the NSF domain can be obtained by an expansion into a *telescopic series*. The resulting operator can then be applied to the NSF vector defined in Equation 6.12.

In Figure A.1, I show the matrix-vector product in NSF without repeating the strict mathematical development of the NSF. Each resolution approximation subspace is encoded by three different blocks, denoted by $T = \{\{A_j, B_j, C_j\}_{j \epsilon Z : j < J}, T_J\}$, that build the *telescopic series* of the operator T. These blocks act on the wavelet subspaces V_j and W_j,

$$\begin{aligned} A_j &: W_j \longrightarrow W_j, \\ B_j &: V_j \longrightarrow W_j, \\ C_j &: W_j \longrightarrow V_j. \end{aligned} \tag{6.13}$$

The operator A_j describes the interaction on the scale j only, while B_j and C_j define the interaction between the scale j and all coarser scales $j' > j$.

As for a standard wavelet transform, the *telescopic series* admits a recursive definition on subsequent coarser resolution levels,

$$T_j = \begin{pmatrix} A_{j+1} & B_{j+1} \\ C_{j+1} & T_{j+1} \end{pmatrix} \tag{6.14}$$

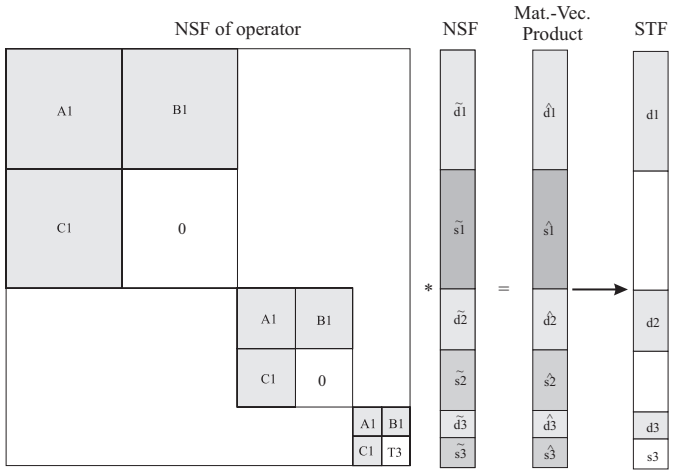

Figure A.1: Multi-resolution matrix-vector product in the Non-Standard Form. The result from the standard matrix-vector product does not give a vector that lies in a wavelet domain since contributions from wavelet- and scaling-spaces are stored (coefficients $\tilde{d}_j$ and $\tilde{s}_j$). Additional wavelet projections may transform the vector in the standard wavelet basis.

where $T_j = V_j \longrightarrow V_j$ is an averaged version of the operator T_{j-1} . Note that T_0 is the operator discretized on the finest resolution level.

In a similar way, I construct the NSF of a vector (see Figure A.1 and Equation 6.12) which, in addition to coefficients in the wavelet spaces ($\tilde{d}_j$) also stores the corresponding scaling coefficients in $\tilde{s}_j$. I set the initial vector size in the physical domain to be np and the size of the coarsest approximation space in the NSF to $n0$. Then, the NSF of a vector has the length $n = 2 \times np - n0$.

In order to compute a multi-resolution matrix-vector product, I first apply standard matrix-vector multiplications on each resolution scale separately. The resulting coefficients, denoted by $\hat{d}_j$ and $\hat{s}_j$, belong to the following subspaces,

$$\begin{aligned} \hat{d}_j &= A_j\tilde{d}_j + B_j\tilde{s}_j \; \varepsilon \; W_j, \\ \hat{s}_j &= C_j\tilde{d}_j \; \varepsilon \; V_j, \end{aligned} \tag{6.15}$$

for $j = 1, 2, ..., J$, and on the coarsest scale

$$\hat{s}_J = C_J\tilde{d}_J + T_J\tilde{s}_J \; \varepsilon \; V_J. \tag{6.16}$$

I underline that the NSF representation of the operator *decouples* the different approximation spaces, since a standard matrix-vector product is applied independently on each resolution scale. The apparent *scale-decoupling*, noted by Beylkin (1992), first motivated my work on a time domain FD approach.

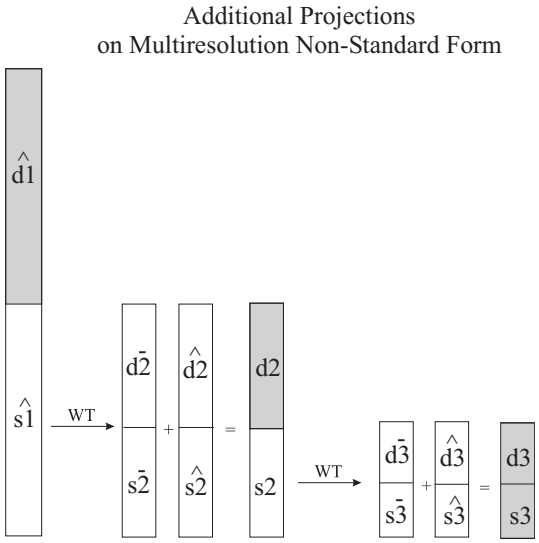

Figure A.2: Additional multi-resolution projection procedure to obtain a vector in standard form. The result of the standard matrix-vector product is denoted by $\hat{d}_j$ for wavelet, and $\hat{s}_j$ for scaling coefficients. The expansion vector $(\{\bar{d}_j, \bar{s}_j\}_{1\leq j\leq J})$ is computed via one step of the discrete wavelet transform. The final result of the multi-resolution matrix-vector product i.e., a vector in the standard form, is shown in grey. Note that the finest scale produces pollution on all coarser scales.

The NSF of an operator can be stored in a compressed form respecting the initial operator dimensions $(np \times np)$, since coefficients from coarser scales can be injected in the 0-blocks of the next finer scale (see Figure A.1). Then, only the NSF-vector requires additional storage of $n = 2 \times np - n0$, rather than np. However, the vector that results from the NSF matrix-vector product $(\{\hat{d}_j\}_{1\leq j\leq J}\ ,\ \hat{s}_J)$ still needs to be further expanded in order to give the desired proper representation in a basis $(\{d_j\}_{1\leq j\leq J}, s_J)$. Except from the finest scale, intermediate expansion vectors appear at each scale, denoted by $\{\bar{d}_j, \bar{s}_j\}_{2\leq j\leq J}$.

In Figure A.2, I show the recursion that needs to be computed for all scales $j = 2, ..., J$ in order to map currently missing fine-scale information to the coarser scales,

$$\hat{s}_{j-1} + \bar{s}_{j-1} \quad \stackrel{WT}{\longrightarrow} \quad (\bar{d}_j\ ,\ \bar{s}_j) \tag{6.17}$$

The sum of the intermediate and the expansion vectors allows the construction of standard wavelet coefficients,

$$\begin{aligned} d_j &= \hat{d}_j + \bar{d}_j \\ s_J &= \hat{s}_J + \bar{s}_J. \end{aligned} \tag{6.18}$$

A.2.2 Finite-difference scheme in NSF

The 1D SH-wave equation can be written as follows (Virieux, 1984),

$$\begin{aligned} \frac{\partial u(x,t)}{\partial t} &= \frac{1}{\rho(x)} \frac{\partial \sigma(x,t)}{\partial x} \\ \frac{\partial \sigma(x,t)}{\partial t} &= \mu(x) \frac{\partial u(x,t)}{\partial x}, \end{aligned} \tag{6.19}$$

where $u\,(x,t)$ is velocity of the displacement, $\sigma\,(x,t)$ the shear stresses, $\rho(x)$ the density, and $\mu(x)$ the first Lamé parameter. Following the developments of Virieux (1984), I discretize the wave equation on spatially staggered grids:

$$\begin{aligned} u^{n+1} &= u^n + \Delta t \, \frac{1}{\rho} \, \frac{\partial \sigma}{\partial x} \\ \sigma^{n+1} &= \sigma^n + \Delta t \, \mu \, \frac{\partial u}{\partial x}, \end{aligned} \tag{6.20}$$

where n is the time index and Δt the time stepping. Each term discretized in Equation 6.20, is projected in the Daub4 wavelet domain:

$$\begin{aligned} \sum_{\alpha} < u^{n+1}, \psi_\alpha > \; \psi_\alpha &= \sum_{\alpha} < u^n, \psi_\alpha > \; \psi_\alpha \\ &\quad -\Delta \; t \, \frac{1}{\rho} \sum_{\alpha} \sum_{\beta} < \sigma^n, \psi_\beta > < \psi_\beta, \frac{\partial \psi_\alpha}{\partial x} > \\ \sum_{\alpha} < \sigma^{n+1}, \psi_\alpha > \; \psi_\alpha &= \sum_{\alpha} < \sigma^n, \psi_\alpha > \; \psi_\alpha \\ &\quad -\Delta \; t \; \mu \sum_{\alpha} \sum_{\beta} < u^n, \psi_\beta > < \psi_\beta, \frac{\partial \psi_\alpha}{\partial x} >, \end{aligned} \tag{6.21}$$

where ψ_α and ψ_β are two wavelet bases. The term $< \psi_\beta, \frac{\partial \psi_\alpha}{\partial x} >$ is the projection of the derivative operator in the wavelet basis, which is independent of the time evolution. A detailed discussion concerning the projection of an operator in a wavelet basis is given by Operto et al. (2002).

In order to verify the NSF-based FD scheme, I implemented Equations 6.21 for the first-order hyperbolic SH-wave equation in one spatial dimension. In Figure A.3, I show the seismogram obtained from a wave propagation simulation using the NSF-FD scheme for a simple heterogeneous model example.

A.2.3 Time-adaptivity in the NSF

In order to increase the performance of a wavelet-based FD scheme, we ideally would like to adapt the, in general unique, time evolution step with respect to the local stability

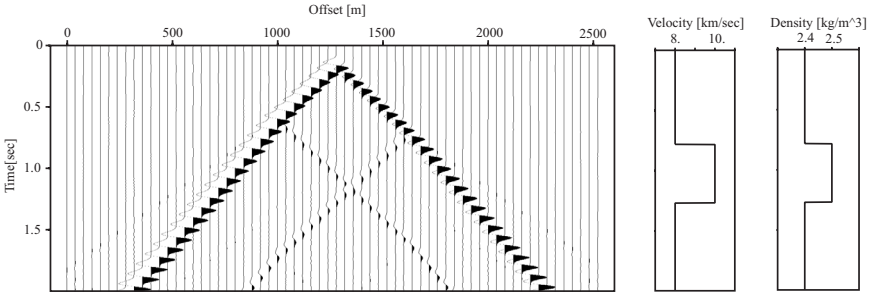

Figure A.3: Seismogram for a $1D$ SH-wave propagation in a heterogeneous media using the Non-Standard Form Finite-Difference method. To the right, I plot the SH-wave velocity and density models.

requirements (spatial discretization) on each resolution grid in the wavelet expansion. Since at each time step, the wave-field solution is advanced by performing an operator-wave-field product (see Equation 6.21), we require this product to be independent from the actual resolution scale. If we assume to find such a representation, the Daub4 wavelet basis would provide us with a tool to perform adaptive FD wave simulations independently on several resolution scales.

Although for Equation 6.20, I mentioned transforming the terms on a wavelet basis without any loss of information, I can also perform a projection in a NSF domain. Then, different resolution scales are *decoupled* since the matrix-vector product in the NSF is performed separately on each resolution scale. The desired time-adaptivity for a NSF-FD scheme is shown in Figure A.4

Unfortunately, we require more than just decoupling of scales. In order to perform FD-time evolution on each scale independently, we ask for a wavelet representation where the outcome of the extrapolation (the matrix-vector product) lies in the wavelet domain, not in the NSF. As I noted before, this is not case the for the NSF since additional projections need to be performed that contain interactions from the finest scale. Therefore, time-adaptivity applied independently for each resolution scale, to my knowledge, is not possible using the NSF. Only if the *NSF-pollution* from the fine-grid is extrapolated in time, a different time-step can be assigned to each resolution scale. Unfortunately, this requires the storage of a large amount of additional coefficients in the operator, as well as numerous additional wavelet projections and matrix-vector products which renders the approach inefficient.

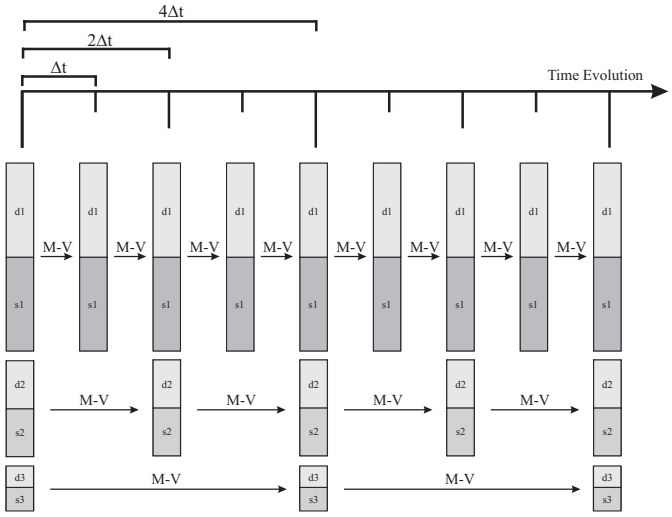

Figure A.4: Cartoon showing the desired time evolution scheme for a Non-Standard Form Finite-Difference method. In the Non-Standard Form, a matrix-vector product can be performed on each resolution scale independently. Therefore, we would like to assign an independent time-step to each resolution scale that propagates wavelet and scaling coefficients with respect to their local stability criterium. The matrix-vector product in NSF on one resolution scale is denoted by $M - V$.

Appendix B

Le Nouveau Chapitre de Thèse

B.1 Généralités

Nom: **Bernhard Hustedt**

Mentor: **Nadjia Hohweiller**

Titre de la thèse:
Propagation des ondes: approches espace et ondelette
(Wave Propagation Modelling : Space and Wavelet Approaches)

Ecole doctorale:
Sciences Fondamentales et Appliquées

Discipline:
Sciences de la Terre

Laboratoire d'Accueil:
UMR Géosciences Azur

B.2 Place et Enjeux de la Thèse

B.2.1 Résumé

Dans le domaine de la sismologie, la propagation des ondes sismiques est importante pour analyser des informations du sous-sol. Les enregistrements à la surface de la Terre donnent, après un traitement du signal adéquat, une image du sous-sol détaillée dépendante de l'échelle caractéristique des ondes utilisées pendant le traitement. Pour créer cette image, il est souvent nécessaire de reproduire synthétiquement le trajet suivi par des ondes pendant leur propagation, du point d'excitation, par exemple, un tremblement de terre, jusqu'à la surface. La modélisation synthétique des ondes permet également de quantifier, de façon déterministe, le niveau du risque sismique d'un site donné, par exemple la ville de Nice.

Des simulations réalistes doivent remplir un certain nombre de conditions qui sont à la limite de ce que les ordinateurs puissants actuels peuvent faire. Mon travail de thèse comprend donc la recherche et la mise en place de nouveaux schémas numériques qui permettent de dépasser les limites présentes. Par exemple, une modélisation des ondes d'un modèle de $20 \times 20 \times 20 Km$ et une fréquence maximale de $10 Hz$ n'est pas faisable actuellement.

B.2.2 Motivations personnelles

Mes motivations personnelles pour faire une thèse en France ont été à la fois influencées par des attentes professionnelles mais aussi, de façon plus importante, par le désir de vivre dans un pays autre que l'Allemagne. Pour comprendre l'origine de ce qui m'a poussé à ce désir, il faut savoir que j'ai commencé mes études en Géophysique en Allemagne en 1993. Après quatre années d'études non-validées, je suis allé en 1997 en Angleterre à l'*University of Leeds* pour m'inscrire dans un programme d'études *Master of Science by Research*. C'est un programme de recherche d'un an en interaction avec le monde industriel, ce qui a l'avantage de favoriser pour les étudiants des contacts avec leur futur éventuel employeur : l'industrie pétrolière. Pour pouvoir m'inscrire dans ce programme, j'ai dû surmonter des obstacles : l'autorisation de mon inscription à l'Université et le financement de mon année d'étude. Pour cela, j'ai effectué de nombreuses démarches qui m'ont permis de rencontrer un responsable de l'Université qui a été séduit par mon initiative et a donc favorisé mon inscription. Par la même, il m'a mis en contact avec un employeur potentiel avec qui j'ai signé un CDD de 6 mois pour pouvoir financer mes frais d'étude et d'inscription à l'Université (4500 Euro). La qualité des rapports que j'ai établis avec mon employeur m'a permis de bénéficier de son soutien jusqu'à la fin de mon Master.

J'ai donc pendant mon séjour en Angleterre, pour la première fois de ma vie, effectué un vrai travail de recherche d'un an, mais aussi un travail contractuel pour gagner de l'argent. Cette expérience m'a bien montré les deux scénarios possibles pour la suite du Master. Finalement, après deux années en Angleterre, j'ai décidé de poursuivre des études de Géophysique en faisant une thèse. A la fois, ce choix était poussé par un désir de continuer un travail de recherche plus fondamental, plus long et plus intensif, mais

également et à mon avis le plus important, par la liberté d'aller dans un autre pays de mon choix pour apprendre une autre langue et vivre une autre culture. Ce pays était la France dont la manière de vivre, les arts, la culture, etc. m'ont toujours intéressé. Il y avait plusieurs handicaps liés à ce choix : je ne savais pas parler français à l'époque, je n'avais pas de contact en France, et je n'avais pas de bourse pour faire une thèse ni des possibilités d'en récupérer une allemande ou anglaise. En plus, je ne voulais pas faire une thèse financée par l'industrie pétrolière, parce que la recherche dans ce milieu me semblait trop proche d'un travail contractuel, travail que j'avais déjà effectué. Pendant ma recherche d'un laboratoire d'accueil et d'un sujet de thèse en France, j'ai rencontré mon futur responsable, le Professeur Jean Virieux, à Géosciences Azur, qui a été tout de suite très motivé pour me proposer un sujet de recherche. La seule difficulté était de trouver encore une fois un financement de trois ans en France. A cause de nombreux problèmes administratifs et financiers, j'ai d'abord fait un stage de recherche d'un an à Naples, en Italie, dans le cadre du projet européen TOMOVES (TOMOgraphie VESuvious) pour bien préparer le début d'une thèse à l'Université de Nice. Ce stage m'a aussi aidé à obtenir l'équivalence de mon Master avec le DEA en France, qui est obligatoire pour s'inscrire à l'Université.

B.2.3 Ressources humaines et financières

Mon travail de thèse a été financé par une bourse du Ministère de Recherche (MENRT). Il s'inscrit dans un programme de recherche en géophysique établi par le CEA. Le sujet fait partie d'un effort de développement méthodologique des approches de la simulation numérique des ondes sismiques dans des milieux tridimensionnels fortement hétérogènes et complexes pour étudier les phénomènes comme les effets de site et le risque sismique (ProSIS3D).

En terme de ressources humaines, ce programme de travail regroupe des chercheurs (5) et étudiants (2) : un chercheur et un étudiant de CEA/DASE à Paris (Commissariat d'Energique Atomique/Département Analyse Surveillance et Environnement), deux chercheurs de LGIT à Grenoble (Laboratoire de Géophysique Interne et de Tectonophysique), trois chercheurs et un étudiant de l'UMR Géosciences Azur. Les chercheurs et étudiants sur chaque site ont suivi différents axes de recherche pour développer des approches numériques pour la simulation des ondes en 3D. Les groupes de recherche des trois sites se sont réunis tous les 6 mois où chacun des groupes a présentés ces principaux résultats suivis par une discussion sur des éventuels point communs, des comparaisons à faire, etc..

Le montant du financement fourni par le CEA pour supporter le projet de recherche ProSIS3D (achat des ordinateurs, financement des missions des conférences et *workshops* nationaux et internationaux, etc.) est de 30.500 Euro par an. Le travail a nécessité principalement des ressources humaines ainsi que des moyens et systèmes informatiques. Le travail de recherche a bénéficié de l'aide de mon Professeur, Jean Virieux (environ 5 heures par semaine), et d'un chercheur CNRS, Stéphane Operto (environ 1.25 heures par semaine) en moyenne sur 3 ans : Autres frais sur 3 ans: On peut estimer le coût total de ce travail de thèse à 164.200 Euro.

Personnel	Temps / mois	Salaire (net) / mois	Salaire (net) / 3 ans
Professeur	$20h$	$\sim$ 800 Euro	19200 Euro
Chercheur CNRS	$5h$	$\sim$ 200 Euro	4800 Euro
Doctorant	$240h$	$\sim$ 1000 Euro	25000 Euro

Table B.1: Resources humaines de la thèse

Formation (éducation continue)	1200 Euro
Congrès nationaux et internationaux	1200 Euro
Moyens informatiques	4000 Euro
Calculs parallèles	$200h$ / IDRIS (difficilement évaluable)
Fonctionnement	10800 Euro

Table B.2: Resources financières de la thèse

B.3 Gestion du Projet

Durant mon stage de recherche à l'*Universita di Napoli* en Italie, une question clé m'a été posée concernant la simulation 3D de la propagation des ondes dans des milieux comme les volcans, une question qui a servi à déterminer mon futur travail de thèse. De manière à me former à des questions de modélisation numérique avant de commencer ma thèse, j'ai également suivi une école d'été européenne à Marseille (*Multiscale approaches for partial differential equations, 1999*) pour obtenir une version différente sur les approches de la modélisation numérique utilisées actuellement par des mathématiciens.

Le titre initial de ma thèse était : *Modélisation 3D des Effets de Site : Application à la quantification du Risque Sismique*. Ce projet de thèse était prévu pour une durée de trois ans qui se décomposait de la manière suivante : la première année était consacrée à l'étude et le choix d'un schéma numérique le plus prometteur pour étudier les effets de site, en interaction avec des mathématiciens lorsque cela serait nécessaire. Puis une deuxième année de mise en forme numérique, probablement sur une machine de calcul massivement parallèle pour permettre des modélisations à grande échelle. Enfin, la troisième année était réservée à l'étude des confrontations entre les résultats numériques et les données réelles des sites intéressants.

Au début de ma thèse, j'ai mis en place l'approche standard de modélisation dans le domaine espace-fréquence de manière à comprendre les subtilités de l'état de l'art dans ce domaine. Par exemple, un code de modélisation des ondes sismiques acoustiques en deux dimensions spatiales (2D) est utilisé d'une manière routinière dans mon équipe scientifique. Ensuite, j'ai continué à approfondir cette approche en utilaisant les techniques nouvelles de factorisation des matrices, de compression du maillage, de schémas itératifs, de décomposition sur plusieurs échelles de résolution différentes (ondelettes), développées par des mathématiciens. J'ai eu de la chance de pouvoir approfondir personnellement ma connaissance de ces techniques dans le cadre de deux écoles que j'ai suivis : l'une à Trieste en Italie (*Workshop on three-dimensional modelling of seismic wave generation, propaga-*

tion and their inversion, 2000), l'autre à l'INRIA Roquencourt (*Écoles des ondes, 2001*). Cette partie de la mise en place de l'approche développée a eu lieu par une coopération entre l'équipe locale de l'UMR Géosciences Azur, le CERFACS de Toulouse, et de l'INRIA à Sophia-Antipolis. Pendant les deux premières années de ma thèse, l'approche scientifique développée était définie et partiellement mise en place à Géosciences Azur sans des interactions avec d'autres équipes de recherche. Pour maintenir une discussion vivante et une échange régulière entre mes directeurs de thèse (Jean Virieux, basé à Sophia Antipolis, et Stéphane Operto de Villefranche-sur-Mer) et d'autres chercheurs et étudiants du laboratoire éventuellement intéressés par notre projet, j'ai organisé une réunion scientifique une fois par semaine. En général, les sujets de discussion d'une réunion fixée étaient déterminés au fur et à mesure des demandes actuels. A part des thèmes spécifiques, j'ai toujours profité de ces réunions pour présenter l'état actuel de mon travail ou bien des éventuels problèmes qui ont bloqué un avancement de mon projet de recherche. Dans la troisième année de ma thèse, les réunions scientifiques ont eu lieu occasionnellement avec mes directeurs de thèse (environ une fois tous les mois). Par contre, le travail de recherche a renforcé des interactions avec des chercheurs du CERFACS et d'INRIA principalement par courrier électronique et également par des visites des différentes sites, des échanges de logiciels (CERFACS) et des permissions d'accès à des ressources informatiques (INRIA).

En utilisant l'ensemble des techniques, deux nouvelles approches de modélisation ont été analysées en 2D et 3D qui permettent la simulation des modèles de taille élevée par rapport à l'approche classique. J'ai estimé les besoins de temps de calcul et d'espace mémoire pour des modèles 3D, qui m'ont permis de faire appel à des moyens nationaux de gros calculateurs (IDRIS, CEA, INRIA) pour calculer, à partir des codes de modélisation, des exemples réalistes. La dernière étape, notamment l'application du code à un modèle réaliste, n'a pas été mise en place, en raison de nombreuses difficultés rencontrées pendant l'implémentation parallèle de l'approche numérique. Le titre de ma thèse était donc modifié en *Propagation des ondes : approches espace et ondelette*. L'état actuel de mon travail était présenté régulièrement à des conférences *workshops* et a donné lieu à deux publications importantes dans des revues internationales.

A côté de la recherche liée au développement d'une approche de modélisation numérique, j'ai participé à de nombreuses campagnes de sismologie, à la fois dans le département des Alpes-Maritimes (GéoFrance3D, SALAM), au Chili en Amérique du Sud (Ovalle99), et aussi au Japon sur un bateau de recherche (Kaiyo2001).

B.4 Compétences Dévelopées dans le Cadre du Projet

B.4.1 Domaine d'Expertise

- **Physique:** pour conduire ce sujet de recherche, j'ai acquis et approfondi l'ensemble des connaissances liées aux phénomènes de la propagation des ondes dans un milieu géologique.

- **Mathématique:** pour mettre en place une approche de modélisation numérique de la propagation des ondes, j'ai dû maîtriser les bases de la mathématique liées aux

équations partielles. Mon sujet de thèse spécifique utilise également une approche basée sur une transformation ondelette qui n'était pas incluse dans mon parcours universitaire en Allemagne. La maîtrise de cette discipline mathématique spécifique était donc incontournable pour aborder le problème posé.

- **Numérique:** la modélisation de la propagation des ondes nécessite la connaissance et la compréhension des méthodes numériques de représentation d'une équation partielle d'une manière discrète dans un code de programmation d'un ordinateur.

- **Programmation:** une grande partie de ma thèse comporte la mise en oeuvre d'un logiciel de simulation numérique, ce qui m'a conduit à apprendre des langages de programmation tels que Fortran77/90 et MPI, en séquentiel et parallèle.

B.4.2 Autres Compétences

- **Résolution d'un problème:** initialement je n'avais aucune connaissance du domaine afférent au sujet de thèse. J'ai dû dans un premier temps intégrer et maîtriser les fondements théoriques (mathématiques, modélisations numériques, propagation des ondes) de manière à résoudre le problème scientifique.

- **Abstraction des résultats:** durant le travail de recherche, il était souvent nécessaire d'abstraire les points et contraintes clés des résultats intermédiaires pour, ensuite, les présenter à mes responsables de recherche, et qui me permettaient de mieux cerner les axes principaux à suivre au cours du travail.

- **Organisation des réunions de travail:** régulièrement, j'étais chargé de planifier et d'animer des réunions de groupe de travail avec plusieurs chercheurs du laboratoire. Ces réunions ont servi de débats entre tous les chercheurs et étudiants intéressés par la modélisation des ondes. Ces occasions m'ont permis de mettre en oeuvre mes capacités de communication et mon sens critique, de présenter les résultats et problèmes rencontrés, et de me forcer à développer mon point vu et à le défendre.

- **Communication pluridisciplinaire:** la manière de présenter mon travail théorique à des communautés différentes, l'une formée en géologie / géophysique, l'autre en mathématique et informatique, m'a permis de m'ouvrir et de m'adapter à d'autres cultures scientifiques. A l'issue de ma thèse, je pense avoir perfectionné et consolidé mes acquis de base même si certaines lacunes subsistent.

- **Langue anglaise:** la rédaction de mon manuscrit de thèse et les articles soumis à des journaux de publication scientifique ont été rédigés en anglais.

- **Langue française:** au début de mon séjour en France je ne maîtrisais pas la langue française. Pendant une durée de trois mois j'ai appris les bases de la grammaire et de la communication orale et écrite en suivant deux cours de français au CNRS et à l'Alliance Française.

- **Enseignement:** j'ai assuré pendant un certain temps des enseignements en programmation informatique en Fortran et C au niveau Licence des Sciences de la Terre.

B.5 Evaluation des Retombées de la Thèse

De manière générale, la thèse a apporté des résultats scientifiques intéressants. Même si le but initial de la thèse n'a pas été entièrement atteint, le travail de recherche a montré de nouvelles approches qui, à long terme, vont rendre envisageable la simulation numérique des ondes dans des milieux 3D complexes. Tout de même, jusqu'à aujourd'hui, deux publications dans des journaux scientifiques internationaux et de nombreuses présentations de recherche ont montré l'intérêt de la communauté par rapport au sujet traité. Par ailleurs, des coopérations entre plusieurs équipes de géophysiciens, mathématiciens et informaticiens qui vont, à ma connaissance, continuer à travailler dans cet axe de recherche.

D'un autre côté, la question se pose: quel bénéfice ai-je moi-même tiré de ces trois années de thèse et comment vont elles être profitables pour mon avenir professionnel. Bien entendu, la nécessité d'apprendre un savoir-faire lié à mon travail de recherche est une grande réussite et peut certainement être utile si mes axes de recherche futurs sont les mêmes que ceux de la thèse. Bien souvent, c'est par d'autres qualités, plutôt de nature personnelle, qui deviennent les points clés pour les réussites futures. A mon avis, les aspects de la culture générale que j'ai pu consolider au cours de ces trois années en France sont d'une valeur extrêmement importante. Des diverses présentations à des conférences et réunions, des participations à des campagnes de terrain, l'organisation et la motivation pour le travail, la communication avec d'autres étudiants et chercheurs, m'ont donné une bonne préparation pour l'après thèse, que ce soit dans la vie universitaire ou bien dans le secteur privé. Pour résumer, la thèse m'a donné le temps nécessaire pour avoir une réflexion profonde sur la vie professionnelle à suivre, que ce soit comme Chercheur au CNRS, Maître de Conférences à l'Université, ou intégrer un département de recherche et développement dans l'industrie. Mon expérience personnelle à travers ces années de thèse m'a permis de me rendre compte que ni le sujet de thèse, ni le titre de Docteur, me permet de garantir un accès systématique dans le monde du travail. Mais bien souvent le choix professionnel est dépendant de la capacité du thésard à se représenter et à se projeter dans des environnements professionnels différents de ceux auxquels il est habitué. A la fin de la thèse il ne faut pas rester cantonné à un seul choix qui est celui de son domaine scientifique, mais accepter de s'ouvrir à d'autres choix possibles qui peuvent constituer un réel enrichissement. Par exemple, pour la suite de ma thèse, j'ai obtenu un poste de recherche dans l'industrie où, pendant le processus de sélection, mon sujet de thèse n'a joué aucun rôle. Bien sûr, pour trouver un certain poste, peut-être faut-il envisager de partir dans une autre ville ou même un autre pays, mais je suis convaincu que la thèse a bien servi à me former.

Bibliography

Amestoy, P. R., Duff, I. S., Koster, J., and L'Excellent, J.-Y. (2001). A fully asynchronous multifrontal solver using distributed dynamic scheduling. *SIAM Journal of Matrix Analysis and Applications*, 23:15–41.

Amestoy, P. R. and Giraud, L. (2002). On the implementation of a direct and an iterative matrix solver scheme. Personal communication.

Arntsen, B., Nebel, A., and Amundsen, L. (1998). Visco-acoustic finite-difference modeling in the frequency domain. *Journal of Seismic Exploration*, 7:45–64.

Auger, E. (2000). *Imagerie sismique du Vesuve*. PhD thesis, Université de Nice Sophia-Antipolis.

Bacry, E., Mallat, S., and Papanicolaou, G. (1992). A wavelet based space-time adaptive numerical method for partial differential equations. *Mathematical modelling and numerical analysis*, 26:793–834.

Berenger, J. P. (1994). A perfectly matched layer for the absorption of electromagnetic waves. *Journal of Computational Physics*, 114:185–200.

Berger, M. J. and LeVeque, R. (1998). Adaptive mesh refinement using wave propagation algorithms for hyperbolic systems. *SIAM*, 35:2298–2316.

Berger, M. J. and Oliger, J. (1984). Adaptive mesh refinement for hyperbolic partial differential equations. *Journal of Computational Physics*, 53:484–512.

Beylkin, G. (1992). On the representation of operators in bases of compactly supported wavelets. *SIAM J. Numer. Anal.*, 6:1716–1740.

Beylkin, G. (1998). On multiresolution methods in numerical analysis. *Documenta Mathematica*, Extra Volume ICM III:481–490.

Beylkin, G., Coifman, R., and Rokhlin, V. (1991). Fast wavelet transforms and numerical algorithms. *Comm. Pure Appl. Math.*, 44:141–183.

Beylkin, G. and Keiser, J. M. (1995). On the adaptive numerical solution of nonlinear partial differential equations in wavelet bases. *J. Comp. Phys.*, 132:233–259.

Bourgeois, A., Bourget, M., Lailly, P., Poulet, M., Ricarte, P., and Versteeg, R. (1991). Marmousi, model and data. In *The Marmousi Experience*, pages 5–16. Eur. Ass. Expl. Geophys.

Briggs, W. L. (1987). *A Multigrid Tutorial*. SIAM.

Briggs, W. L. and Henson, V. E. (1993). Wavelets and multigrid. *SIAM J. Comput.*, 14(2):506–510.

Červený, V., Molotkov, I. A., and Psencik, I. (1977). *Ray theory in Seismology*. Charles University Press, Praha.

Charton, P. (1996). *Produits de matrices rapides en bases d'ondelettes: application à la résolution numérique d'équations aux dérivés partielles*. PhD thesis, University of Paris Nord.

Chiavassa, G. (1997). *Algorithmes adaptatifs en ondelettes pour la résolution d'équations aux dérivés partielles*. PhD thesis, University of Méditerranée Aix Marseille II.

Cohen, G. and Fauqueux, S. (2000). Mixed finite elements with mass-lumping for the transient wave equation. *J. of Computational Acoustics*, 8:171–188.

Dagum, L. and Menon, R. (1998). OpenMP: An industry-standard api for shared-memory programming. *IEEE Computational Science and Engineering*, 1.

Daubechies, I. (1988). Orthonormal bases of compactly supported wavelets. *Comm. Pure and Appl. Math.*, XLI:909–996.

Daubechies, I. (1992). *Ten lectures on Wavelets*. SIAM CBMS61.

Davis, T. A. and Duff, I. S. (1997). A combined unifrontal/multifrontal method for unsymmetric sparse matrices. *Technical Report TR-97-016, University of Florida*.

Debicki, M. P. (1999). *A low-frequency hyperthermia system for malignant cervic melanoma treatment*. PhD thesis, Technical University of Gdańsk.

Dormy, E. and Tarantola, A. (1995). Numerical simulation of elastic wave propagation using a finite volume method. *Journal of Geophysical Research*, 100:2123–2133.

Duff, I. S., Erisman, A. M., and Reid, J. K. (1997). *Direct Methods for Sparse Matrices*. Oxford Science Publications, Oxford.

Faccioli, E., Maggio, F., Quarteroni, A., and Tagliani, A. (1996). Spectral-domain deomposition methods for the solution of acoustic and elastic wave equations. *Geophysics*, 61(4):1160–1174.

Falk, J., Tessmer, E., and Gajewski, D. (1998). Efficient finite-difference modelling of seismic waves using locally adjustable time steps. *Geophysical Prospecting*, 46:603–616.

Frayssé, V., Giraud, L., and Gratton, S. (1997). A set of GMRES routines for real and complex arithmetics. *CERFACS Technical Report TR/PA/97/49.*

Fuchs, K. and Muller, K. (1971). Computations of synthetic seismograms with the reflectivity method and comparison with observations. *Geophys. J. R. Astron. Soc.*

Gines, D. L., Beylkin, G., and Dunn, J. (1999). Lu factorization of non-standard forms and direct multiresolution solvers. http://amath.colorado.edu/pub/wavelets/papers.

Golub, G. H. and van Loan, C. F. (1996). *Matrix Computations.* The John Hopkins University Press, 3^{rd} edition.

Graves, R. W. (1996). Simulating seismic wave propagation in 3-D elastic media using staggered-grid finite differences. *Bull. Seismol. Soc. Am.*, 86:1091–1106.

Hackbusch, W. (1978). On the multi-grid method applied to difference equations. *Computing*, 20:291–306.

Hestholm, S. and Ruud, B. (1998). 3-D finite-difference elastic wave modeling including surface topography. *Geophysics*, pages 613–622.

Holberg, O. (1987). Computational aspects of the choice of operator and sampling interval for numerical differentiation in large-scale simulation of wave phenomena. *Geophys. Prosp.*, 35:629–655.

Homlström, M. (1995). Parallelizing the fast wavelet transform. *Parallel Computing*, 21:1837–1848.

Hong, T.-K. and Kennett, B. L. N. (2002). A wavelet-based method for simulation of two-dimensional elastic wave propagation. *Geophys. J. Int.*, 150:610–638.

Igel, H. (1999). Wave propagation in three-dimensional spherical sections by the Chebyshev spectral method. *Geophys. J. Int.*, 136:559–566.

Jameson, L. (1993). On the wavelet based differentiation matrix. *Journal of Scientific Computing*, 8:267–305.

Jameson, L. and Miyama, T. (1999). Wavelet analysis and ocean modeling: A dynamically adaptive numerical method WOFD-AHO. *Monthly Weather Review*, 128:1536–1548.

Janod, F. (1999). *Propagation des ondes large bande dans des milieux élastiques 3D: méthodes d'Eléments de Frontière et couplage avec les Différences Finies.* PhD thesis, Université Joseph Fourier - Grenoble I.

Jastram, C. and Behle, A. (1992). Acoustic modelling on a grid of vertically varying spacing. *Geophysical Prospecting*, 40:157–169.

Jianfeng, Z. and Tielin, L. (1999). P-SV-wave propagation in heterogeneous media: grid method. *Geophys. J. Int.*, 136:431–438.

Jianfeng, Z. and Tielin, L. (2002). Elastic wave modelling in 3D heterogeneous media: 3D grid method. *Geophys. J. Int.*, 150:780–799.

Jo, C. H., Shin, C., and Suh, J. H. (1996). An optimal 9-point, finite-difference, frequency-space, 2D scalar wave extrapolator. *Geophysics*, 61(2):529–537.

Joly, P., Komatitsch, D., and Vilotte, J. (1995). The solution of the wave equation by wavelet basis approximation. In *Proceedings of the Enumath'95 conference*.

Joly, P., Maday, Y., and Perrier, V. (1994). Towards a method for solving partial differential equations by using wavelet packet bases. *Comput. Meth. Appl. Mech. Eng.*, 116:301–307.

Kelly, K. R., Ward, R. W., Treitel, S., and Alford, R. M. (1976). Synthetic seismograms: a finite difference approach. *Geophysics*, 41:2–27.

Komatitsch, D. and Tromp, J. (1999). Introduction to the spectral element method for three-dimensional seismic wave propagation. *Geophysical Journal International*, 139:806–822.

Komatitsch, D. and Tromp, J. (2001). Modeling seismic wave propagation using linux on a 156-gigabyte PC cluster. *Linux Journal*, 10:38–45.

Komatitsch, D. and Vilotte, J. P. (1998). The spectral element method: an efficient tool to simulate the response of 2D and 3D geological structures. *Bull. Seismol. Soc. Am.*, 88:368–392.

Kosloff, D. and Baysal, E. (1982). Forward modeling by a fourier method. *Geophysics*, 47:1402–1412.

Kristek, J., Moczo, P., and Archuleta, R. J. (2002). Efficient methods to simulate planar free surface in the 3D 4th-order staggered-grid finite-difference schemes. *Stud. geophys. goed.*, 46:355–381.

Lazaar, S., Liandrat, J., and Tchamitchian, P. (1994). Algorithmes à base d'ondelettes pour la résolution numériques d'équations aux dérivés partielles à coefficients variables. *C. R. Acad. Sci. Paris*, 319:1101–1107.

Levander, A. R. (1988). Fourth-order finite-difference p-sv seismograms. *Geophysics*, 53:1425–1436.

LeVeque, R. J. (1997). Wave propagation algorithms for multidimensional hyperbolic systems. *Journal of Computational Physics*, 131:327–353.

Liandrat, J. and Tchamitchian, P. (1990). Resolution of the 1D regularized Burgers equation using a spatial wavelet approximation. *NASA Report, ICASE Report 90-83.*

Luo, Y. and Schuster, G. (1990). Parsimonious staggered grid finite differencing of the wave equation. *Geophysical Research Letters*, 17(2):155–158.

Madariaga, R. (1976). Dynamics of an expanding circular fault. *Bull. Seism. Soc. Am.*, 73:765–780.

Maday, Y., Perrier, V., and Ravel, J.-C. (1991). Adaptivité dynamique sur bases d'ondelettes pour l'approximation d'équations aux dérivés partielles. *C. R. Acad. Sci. Paris*, I:405–410.

Mallat, S. (1989). Multiresolution approximation and wavelets. *Trans. Amer. Math. Soc.*, 315:69–88.

Mallat, S. (1999). *A wavelet tour of signal processing.* Academic Press.

McGeary, D. and Plummer, C. (1998). *Physical geology: Earth revealed.* McGraw-Hill, Boston, MA. 3rd ed.

Message Passing Interface Forum, M. (1994). A message-passing interface standard. *International Journal of Supercomputer Applications and High Performance Computing*, 8:3/4.

Meyer, Y. (1992). *Ondelettes et algorithmes concurrents.* Hermann.

Mikhailenko, B. G. (2000). Seismic modelling by the spectral-finite difference method. *Physics of the Earth and Planetary Interiors*, 119:133–147.

Moczo, P. (1980). Finite difference technique for sh waves in 2-D media using irregular grids. *Geophys. J. R. Astr. Soc.*, 99:321–329.

Moczo, P., Lucká, M., Kristek, J., and Kristeková, M. (1999). 3D displacement finite differences and a combined memory optimization. *Bull. Seismol. Soc. Am.*, 89:69–79.

Moore, G. E. (1965). Cramming more components onto integrated circuits. *Electronics*, 8.

Morse, P. and Feshbach, H. (1953). *Methods of Theoritical Physics.* McGraw-Hill, New York, NY.

Mulder, W. and Plessix, R.-E. (2002). Time- versus frequency domain modelling of seismic wave propagation. In *Extended Abstracts.* Eur. Ass. of Geosc. and Eng.

Olsen, K. B. and Archuleta, R. J. (1996). Three-dimensional simulation of earthquakes on the Los Angeles fault system. *Bull. Seismol. Soc. Am.*, 86(3):575–596.

Olsen, K. B., Archuleta, R. J., and Matarese, J. R. (1995). Magnitude 7.75 earthquake on the San Andreas fault: three-dimensional ground motion in Los Angeles. *Science*, 270:1628–1632.

Operto, S., Virieux, J., Hustedt, B., and Malfanti, F. (2002). Adaptive wavelet-based finite-difference modelling of SH-wave propagation. *Geophysical Journal International*, 148:1–28.

Owen, S. J. (1998). A survey of unstructured mesh generation technology. In *Proceedings*. Dearborn, MI.

Patera, A. T. (1984). A spectral element method for fluid dynamics: laminar flow in a channel expansion. *J. Comput. Phys.*, 54:468–488.

Perrier, V. and Basdevant, C. (1988). La décomposition en ondelettes périodiques, un outil pour l'analyse de champ inhomogènes. théorie et algorithmes. *La recherche aérospatiale*, 3:53–67.

Pessel, M. (2000). *Tomographie électrique: Dévelopements méthodologiques et application*. PhD thesis, Universite de Rennes 1.

Pitarka, A. (1999). 3-D elastic finite-difference modeling of seismic motion using staggered grids with nonuniform spacing. *Bull. Seismol. Soc. Am.*, 89(1):54–68.

Pratt, R. G. (1990). Frequency-domain elastic wave modeling by finite-differences: A tool for crosshole seismic imaging. *Geophysics*, 55:626–632.

Pratt, R. G. and Worthington, M. H. (1990). Inverse theory applied to multi-source cross-hole tomography, part i: Acoustic wave-equation method. *Geophys. Prosp.*, 38:287–310.

Press, W. H., Teukolsky, S. A., Vetterling, W. T., and Flannery, B. P. (1992). *Numerical Recipes in Fortran 77 - Second Edition - The Art of Scientific Computing*. Cambridge University Press.

Rewienski, M. (1999). *High performance algorithms for large scale electromagnetic modeling*. PhD thesis, Technical University of Gdańsk.

Robertsson, J. O. A. (1999). A numerical free-surface condition for elastic/viscoelastic finite-difference modeling in the presence of topography. *Geophysics*, 61(6):1921–1934.

Robertsson, J. O. A. and Chapman, C. H. (2000). An efficient method for calculating finite-difference seismograms after model alterations. *Geophysics*, 65:907–918.

Saad, Y. and Schultz, M. (1996). GMRES: A generalized minimal residual algorithm for solving non-symmetric linear systems. *SIAM J. Sci. Stat. Comput.*, 7:856–869.

Saenger, E. H., Gold, N., and Shapiro, A. (2000). Modeling the propagation of elastic waves using a modified finite-difference grid. *Wave Motion*, 31:77–92.

Sambridge, M., Braun, J., and McQueen, H. (1995). Geophysical parametrization and interpolation of irregular data using natural neighbours. *Geophysical Journal International*, 122:837–857.

Sanchez-Sesma, F. J. (1983). Diffraction of elastic waves by three-dimensional surface irregularities. *Bull. Seism. Soc. Am.*, 73:1621–1636.

Štekl, I. (1997). *Frequency domain seismic forward modelling: a tool for waveform inversion.* PhD thesis, Department of Geoloy, Royal School of Mines, Imperial College London.

Štekl, I. and Pratt, R. G. (1998). Accurate viscoelastic modeling by frequency-domain finite differences using rotated operators. *Geophysics*, 63(5):1779–1794.

Strang, G. and Nguyen, T. (1996). *Wavelet and filter banks.* Wellesley-Cambridge Press, Box 812060, Wellesley MA 02181.

Tessmer, E. (2000). Seismic finite-difference modeling with spatially varying time steps. *Geophysics*, 65:1290–1293.

Tessmer, E. and Kosloff, D. (1994). 3-D elastic modeling with surface topography by a chebychev spectral method. *Geophysics*, 59:464–473.

Virieux, J. (1984). SH wave propagation in heterogeneous media, velocity-stress finite difference method. *Geophysics*, 49:1259–1266.

Virieux, J. (1986). P-SV wave propagation in heterogeneous media, velocity-stress finite difference method. *Geophysics*, 51:889–901.

Wells, R. O. (1994). Adaptive wave propagation modeling. *Technical Report Rice University - Department of Mathematics*, pages TX 77251–1892.

Wu, Y. and McMechan, G. (1998). Wave extrapolation in the spatial wavelet domain with application to postack reverse-time migration. *Geophysics*, 63:589–600.

Xie, Z., Chan, C.-H., and Zhang, B. (2002). An explicit fourth-order orthogonal curvilinear staggered-grid FDTD method for maxwell's equations. *Journal of Computational Physics*, 175:739–763.

Zienkiewicz, O. C. and Morgan, K. (1982). *Finite elements and approximation.* John Wiley and Sons.